

2.0 STRUCTURAL EVALUATION

This section presents evaluations demonstrating that the ATR FFSC package meets all applicable structural criteria. The ATR FFSC packaging, consisting of the body and closure, is evaluated and shown to provide adequate protection for each payload listed in Section 1.2.2, *Contents*. Each payload fuel element is transported in a fuel handling enclosure (FHE) within the ATR FFSC package. The loose fuel plate basket (LFPB) is evaluated to contain only loose fuel plates associated with the ATR fuel element. The small quantity payload loose fuel plates, fuel elements, or foils are contained within a small quantity fuel handling enclosure.

Normal conditions of transport (NCT) and hypothetical accident condition (HAC) evaluations are performed to address 10 CFR §71¹ performance requirements primarily through physical testing. Physical demonstration by testing, including the free drop and puncture events, consists of certification testing utilizing two full-scale certification test units (CTU-1 and CTU-2). CTU-1 included the ATR fuel element payload and CTU-2 included the ATR LFPB and loose plates payload. Certification testing has demonstrated that the key performance objective of criticality control will be met by the ATR FFSC package. Details of the certification test program are provided in Appendix 2.12.1, *Certification Tests on CTU-1*, and Appendix 2.12.2, *Certification Tests on CTU-2*. The evaluation for the MIT and MURR fuel elements is provided in Appendix 2.12.3, *Structural Evaluation for MIT and MURR Fuel*.

2.1 Structural Design

2.1.1 Discussion

The ATR FFSC is a two part packaging consisting of the body and the closure. The body is a single weldment that features square tubing as an outer shell and round tubing for the payload cavity. The closure engages with the body using a bayonet style design. There are four lugs, uniformly spaced on the closure that engages with four slots in the mating body feature. The closure is secured by retracting two spring loaded pins, rotating the closure through approximately 45°, and releasing the spring loaded pins such that the pins engage with mating holes in the body. When the pins are properly engaged with the mating holes the closure is locked.

With the exception of several minor components, all steel used in the ATR FFSC packaging is of a Type 304 stainless steel. Components are joined using full-thickness fillet welds (i.e., fillet welds whose leg size is nominally equal to the lesser thickness of the parts joined) and full and partial penetration groove welds. The fuel containers for the package, the FHEs and the LFPB, are principally of aluminum construction and secured with stainless steel fasteners. The FHEs are a fabrication and the LFPB consists of four machined aluminum components.

A comprehensive discussion of the ATR FFSC packaging design and configuration is provided in Section 1.2, *Package Description*.

¹ Title 10, Code of Federal Regulations, Part 71 (10 CFR §71), *Packaging and Transportation of Radioactive Material*, 01-01-21 Edition.

2.1.2 Design Criteria

The ATR FFSC package has been designed to meet the majority of applicable structural requirements of 10 CFR §71 through physical testing. The design objectives for the package are threefold:

1. For NCT, demonstrate that the ATR FFSC package contains the payload without dispersal and that it does not experience a significant reduction in its effectiveness to withstand HAC; and
2. For HAC, demonstrate that the ATR FFSC package contains the payload without dispersal, consistent with conservative bounding assumptions utilized in the criticality analysis.
3. For HAC, demonstrate that the insulation used in the ATR FFSC package remains in place, to protect the payload from excessive heat from the thermal test, within the assumptions utilized in the thermal analysis.

Consequently, the design criteria for NCT are that the ATR FFSC package exhibit only minor damage subsequent to the NCT conditions and tests, including no damage that would materially affect the outcome of the subsequent HAC tests.

For HAC, the design criteria is that the payload will be retained within the packaging subsequent to the HAC test series of free drop, puncture, thermal, and the immersion test of 10 CFR §71.73(c)(5), or subsequent to immersion of an undamaged specimen per 10 CFR §71.73(c)(6).

Material properties are controlled by the acquisition of critical components to ASTM standards, testing, and process control, as described in Section 2.2, *Materials*. Lifting devices that are a structural part of the package are designed with a minimum safety factor of three against yielding. The index lugs located at the top of the package are considered a tiedown devices and are designed to withstand the loading requirements per 10 CFR §71.45(b)(1).

2.1.2.1 Miscellaneous Structural Failure Modes

2.1.2.1.1 Brittle Fracture Assessment

The steel materials utilized in the ATR FFSC package provide adequate fracture toughness. All critical structural components of the packaging are made of Type 304 stainless steel and have a nil ductility transition temperature less than -40°F (-40°C). Therefore, brittle fracture is not a concern for the ATR FFSC packaging.

To confirm the performance of the uranium aluminide (UAl_x) fuel types at reduced temperatures, the ATR fuel element in CTU-1, was subjected to two HAC drops with the payload at approximately -20°F (-29°C). Following all CTU-1 testing, as discussed in Appendix 2.12.1, *Certification Tests on CTU-1*, the package was disassembled and the payload inspected. Upon inspection, the performance of both the payload and packaging, including the reduced temperature tests, was satisfactory. Following all testing, the payload remained within the assumptions presented in Section 6.0, *Criticality Evaluation*.

2.1.2.1.2 Fatigue Assessment

Normal operating cycles do not present a fatigue concern for the ATR FFSC. The packaging does not retain pressure, and consequently fatigue due to pressure cycling cannot occur. Since all structural components of the packaging are made of the same alloy, and since thermal

gradients are small, thermally-induced fatigue is not of concern. Since the packaging is normally handled on a pallet, the lifting features of the packaging are infrequently used, and fatigue of the lifting load path is not of concern.

The only components which are routinely handled are the closure and the fuel handling enclosures and loose plate basket. The closure is designed as a bayonet-type attachment with two spring-loaded locking pins which prevent rotation during transport. Neither the bayonet lugs nor the locking pins experience any significant loading (such as preload or other repeating mechanical loads) in routine usage. If damage to these components were to occur, it will be identified during the inspections discussed in Section 7.1.1, *Preparation for Loading*. Consequently, fatigue of the closure components is not of concern.

The fuel handling structures (fuel handling enclosures and loose plate basket) are simple structures that do not have significant handling loads. These structures are fully exposed to view during loading and unloading, and can be inspected to ensure integrity.

For these reasons, normal operating cycles are not a failure mode of concern for the ATR FFSC packaging. Fatigue associated with normal vibration over the road is discussed in Section 2.6.5, *Vibration*.

2.1.2.1.3 Buckling Assessment

Certification testing has demonstrated that buckling of the ATR FFSC package does not occur as a result of any normal conditions of transport or as a result of the HAC primary test sequence (e.g., the free drop and puncture tests). Buckling of the ATR FFSC body is also shown to not be a concern during the 50 ft immersion test specified under 10 CFR §71.73(c)(6). A discussion of the response to the 50 ft immersion test is provided in Section 2.7.6, *Immersion – All Packages*.

2.1.3 Weights and Centers of Gravity

The maximum gross weight of the ATR FFSC package is 290 lb. The packaging component weights are summarized in Table 2.1-1 and payload and maximum package weights are summarized in Table 2.1-2. The Cobra HEU fuel element is bounded by a weight of 16 lb and the Cobra LEU fuel element is bounded by a weight of 20 lb. The greater of these is shown in Table 2.1-2. Due to symmetry of design, the center of gravity (CG) of the package is located essentially at the geometric center of the package. Regardless of payload, the center of gravity remains 35 inches from the face of the closure end and 4 inches from the bottom and sides of the package. The packaging components are illustrated in Figure 2.1-1 through Figure 2.1-9.

Table 2.1-1 – ATR FFSC Component Weights

Item	Weight, lb	
	Component	Assembly
ATR FFSC Packaging (empty)	---	240
Body Assembly	230	---
Closure Assembly	10	---

Table 2.1-2 – ATR FFSC Payload and Maximum Package Weights

Case	FHE Drawing	Weight, lb			
		Fuel Element	FHE	Total Contents	Total Package
ATR HEU	60501-30	25	15	40	280
ATR LEU	60501-110	44	6	50	290
MIT HEU	60501-40	10	25	35	275
MIT LEU ^①	60501-40	19	25	44	284
MURR HEU	60501-50	15	30	45	285
MURR LEU ^①	60501-111	29	21	50	289
RINSC	60501-60	17	28	45	285
ATR Loose Plates ^②	60501-20	20	30	50	290
Small Quantity ^③	60501-70	20	30	50	290
Cobra (bounding)	60501-90	20	28	48	288
NBSR LEU DDE	④	23	④	32 ^④	272 ^④

Notes:

1. Weight of LEU element bounds the weight of the corresponding DDE.
2. Includes optional dunnage.
3. Small Quantity Payload defined in Section 1.2.2.4, *Small Quantity Payload*.
4. NBSR DDE may be blocked with up to 4 kg of cardboard (8.8 lb) or other disposable packing material.

2.1.4 Identification of Codes and Standards for Package Design

As a Type AF package, the ATR FFSC is designed to meet the performance requirements of 10 CFR 71, Subpart E. Compliance with these requirements is demonstrated via full scale testing of the package under both NCT and HAC, as documented in Section 2.12, *Appendices*. In addition, structural materials which are important to safety are specified using American Society for Testing and Materials (ASTM) standards as shown on the drawings in Appendix 1.3.2, *Packaging General Arrangement Drawings*. Welding procedures and personnel are qualified in accordance with the ASME Code, Section IX. All welds are visually examined on each pass per the requirements of AWS D1.6:1999² for stainless steel and AWS D1.2:2003³ for aluminum. All welds which are important to safety are examined by liquid penetrant test on the final pass using procedures compliant with ASTM E165-02⁴.

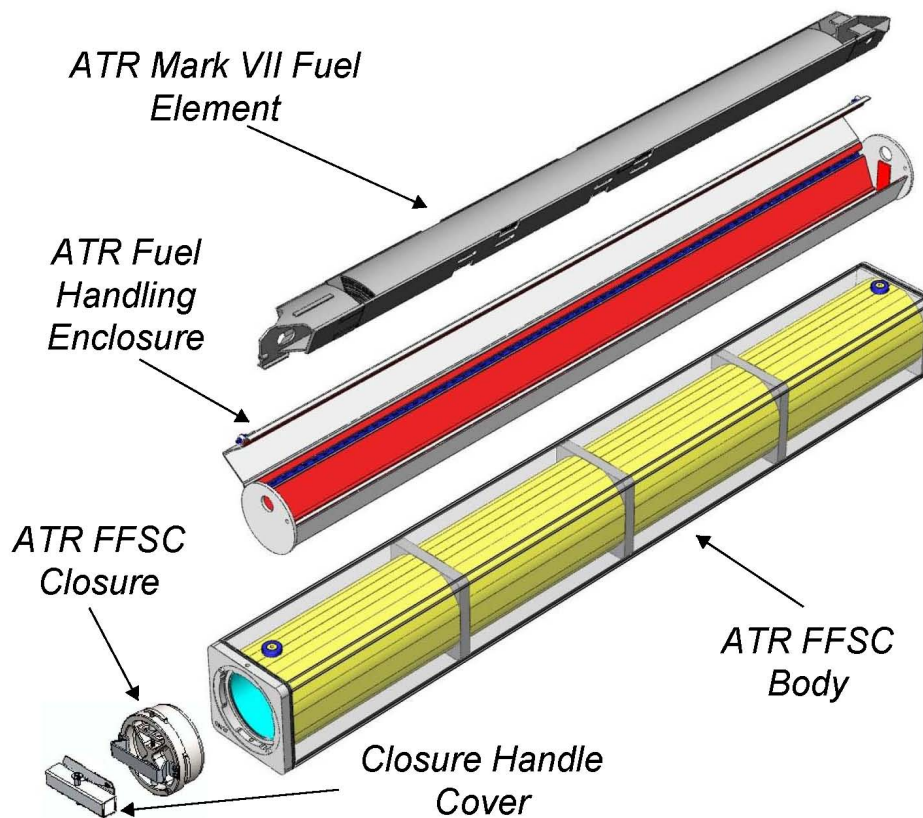


Figure 2.1-1 –Package Components (With ATR HEU Fuel Element)

² ANSI/AWS D1.6:1999, *Structural Welding Code – Stainless Steel*, American Welding Society (AWS).

³ ANSI/AWS D1.2:2003, *Structural Welding Code – Aluminum*, American Welding Society (AWS)

⁴ American Society for Testing and Materials (ASTM International), ASTM E165-02, *Standard Test Method for Liquid Penetrant Examination*, Feb 2002.

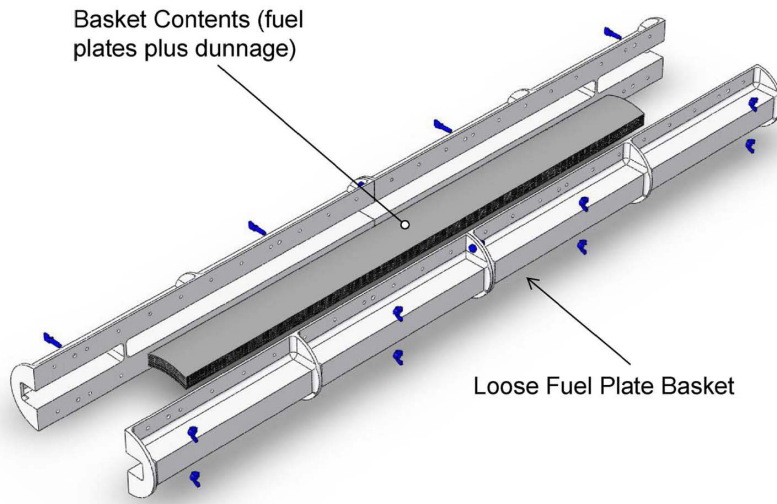


Figure 2.1-2 – Loose Fuel Plate Basket Components

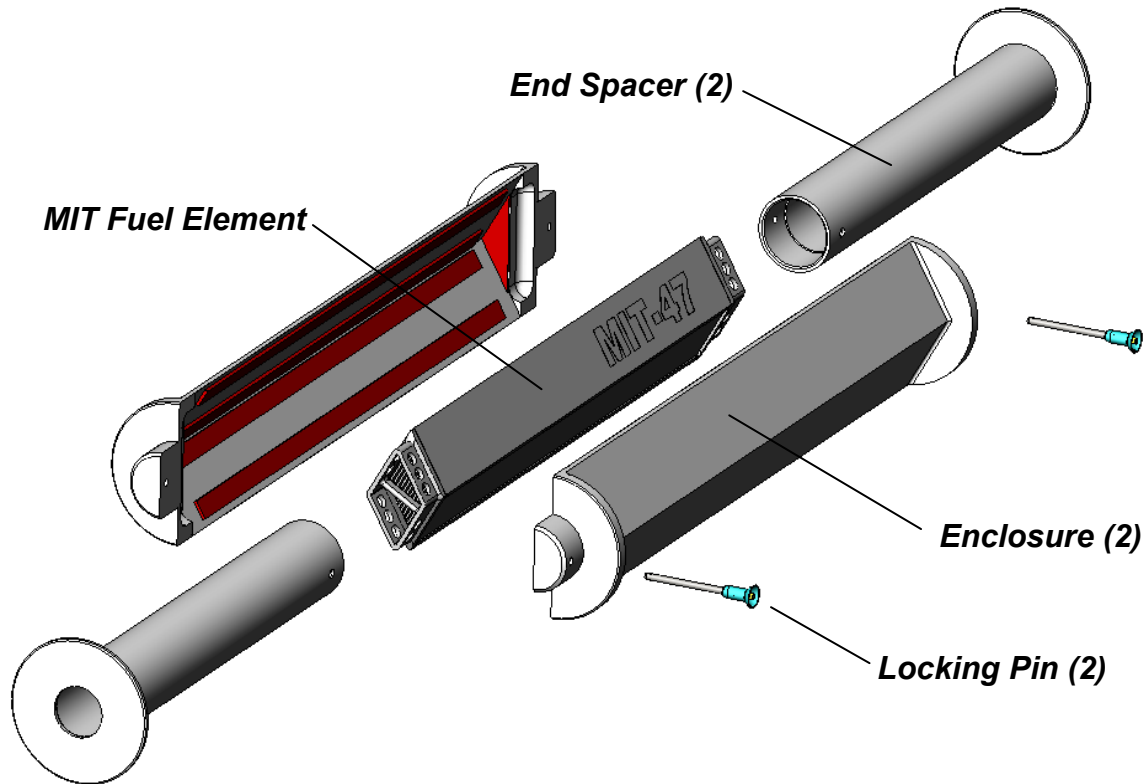


Figure 2.1-3 – MIT HEU or LEU Fuel Handling Enclosure

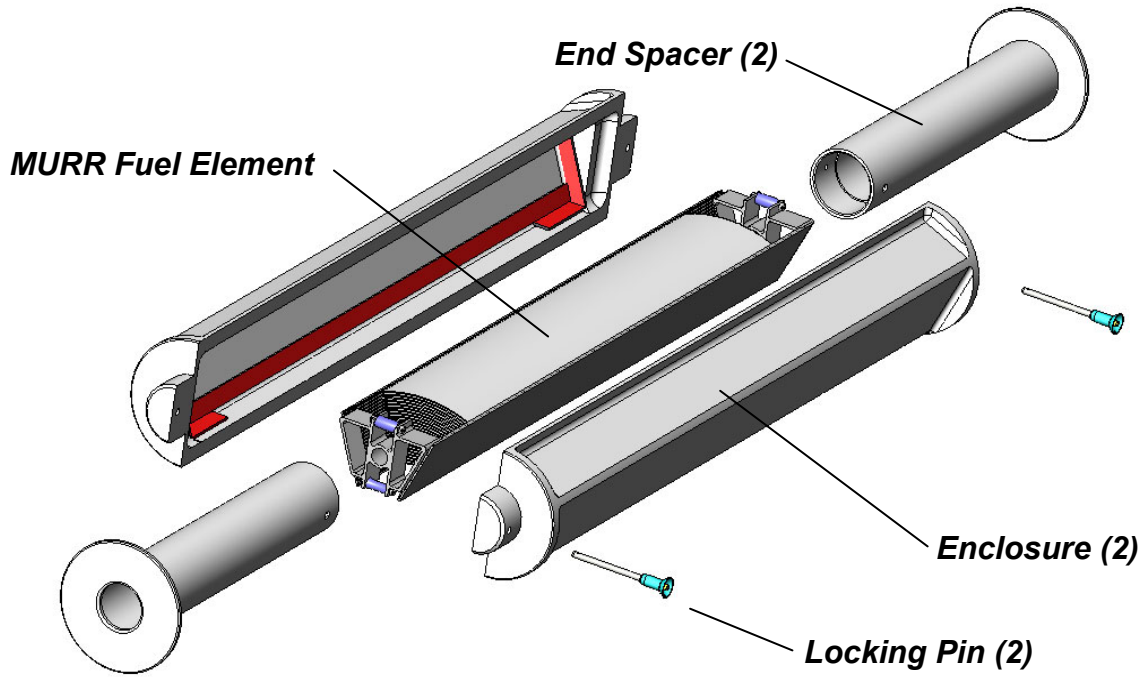


Figure 2.1-4 – MURR HEU Fuel Handling Enclosure

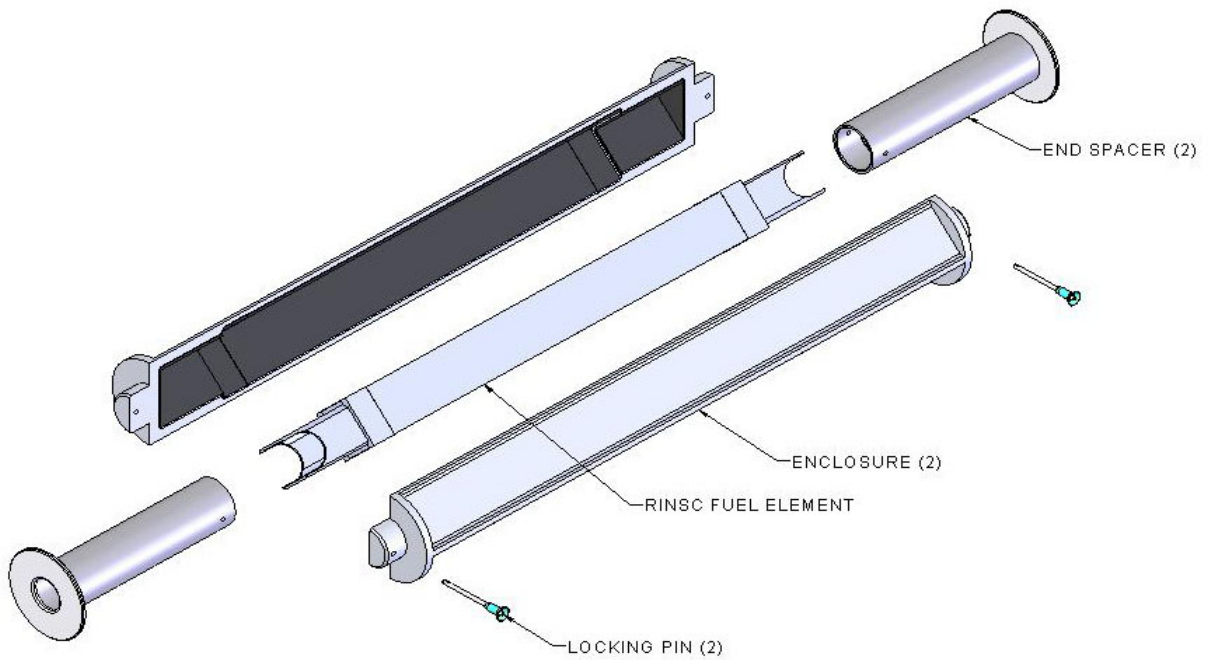


Figure 2.1-5 – RINSC Fuel Handling Enclosure

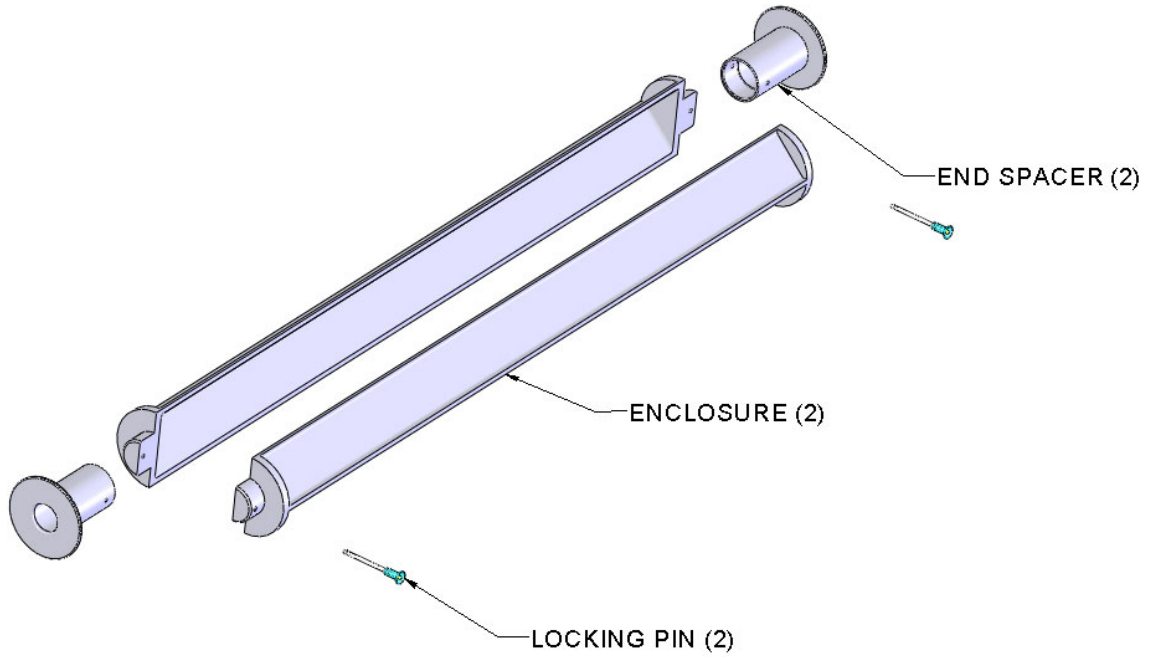


Figure 2.1-6 – Small Quantity Fuel Handling Enclosure

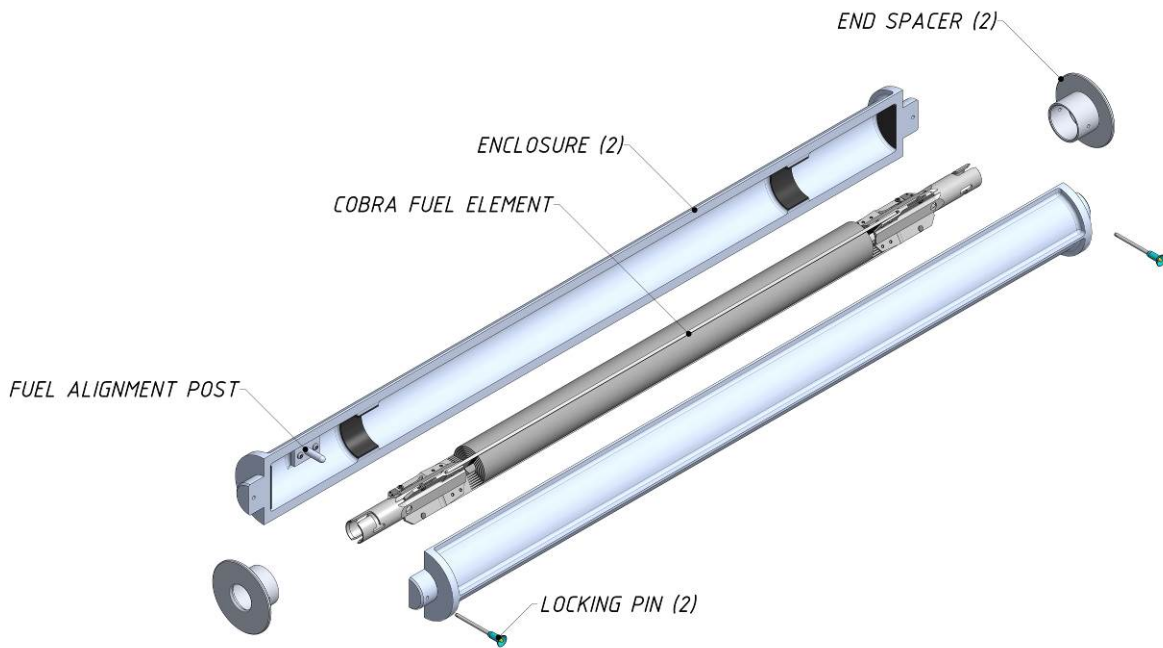


Figure 2.1-7 – Cobra Fuel Handling Enclosure

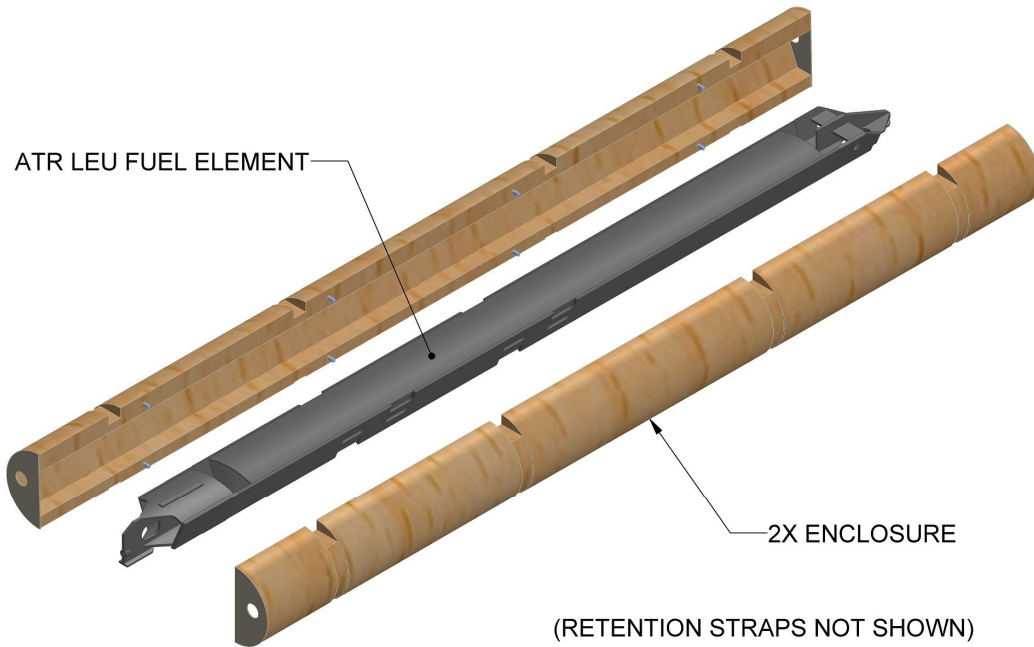


Figure 2.1-8 – ATR LEU Fuel Handling Enclosure

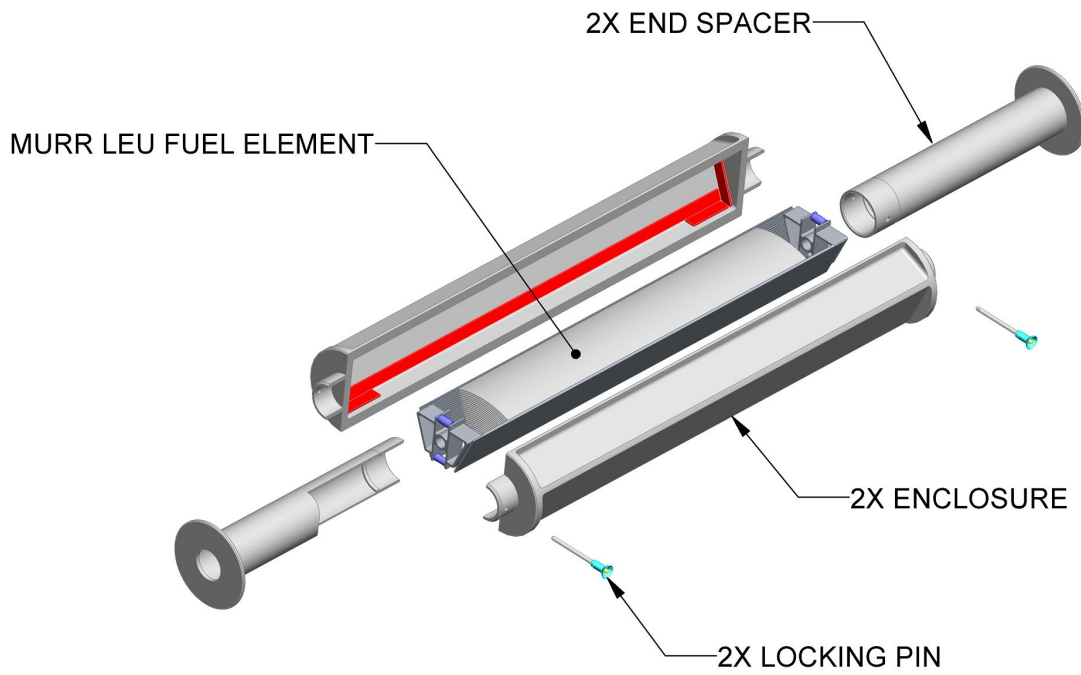


Figure 2.1-9 – MURR LEU Fuel Handling Enclosure

2.2 Materials

The ATR FFSC package is constructed primarily from Type 304 stainless steel structural materials. The drawings presented in Appendix 1.3.1, *Packaging General Arrangement Drawings*, delineate the specific materials used for each ATR FFSC packaging components.

2.2.1 Mechanical Properties and Specifications

Since the demonstration of compliance with the regulations is primarily via performance testing of full-scale prototypes, analytical structural evaluations are in general not performed. Properties of structural materials are controlled either by purchase to an ASTM or other standard or via a written specification.

2.2.1.1 Stainless Steel

All of the structural steel used in the ATR FFSC packaging is an ASTM grade stainless steel. The weld consumable material is ASTM Type 308-308L, which results in weld metal deposits which have properties at least as great as the base metal. The minimum properties of the stainless steel items are given in Table 2.2-1.

Table 2.2-1 –Material Properties of Stainless Steel

Material	Yield Strength, minimum, psi	Ultimate Strength, minimum, psi
ASTM A240 Type 304	30,000	75,000
ASTM A269 Type 304	30,000	75,000
ASTM A276 Type S21800	50,000	95,000
ASTM A479 Type 304	30,000	75,000
ASTM A554 Grade MT-304	30,000	75,000

2.2.1.2 Aluminum

The internal FHEs and LFPB are fabricated from aluminum alloy. Minimum material properties are given in Table 2.2-2.

Table 2.2-2 –Material Properties of Aluminum

Material	Yield Strength, minimum, psi	Ultimate Strength, minimum, psi
ASTM B209, Alloy 5052 – H32	23,000	31,000
ASTM B209, Alloy 6061 – T651, 4" Plate	35,000	40,000
ASTM B210, Alloy 6061 – T6 ¼" Thick	35,000	42,000
ASTM B211, Alloy 6061 – T6 or 6061 – T651	35,000	42,000
ASTM B221 or B241, Alloy 6061 – T6, T6510, or T6511	35,000	38,000

2.2.2 Chemical, Galvanic, or Other Reactions

The materials of construction of the ATR FFSC packaging are primarily Type 304 stainless steel and refractory insulation. Since these materials are relatively unreactive, no excessive corrosion or other reactions will occur during normal use. The package is normally transported in a closed van, and is not subject to immersion or exposure to water or chemicals other than occasional precipitation or mild cleaning agents. In addition, all of these materials have been used in Type A and Type B packagings for many years without incident. If unusual corrosion of the stainless steel components occurs, it can be readily detected during preparation of the packaging for use. The refractory insulation is sealed within the body and is not subject to chemical degradation or corrosion during normal use.

The payloads, consisting of either the FHE and corresponding fuel element or the LFPB and fuel plates, are constructed primarily of aluminum alloy. There is no galvanic or other reactions between the stainless steel package and aluminum alloy payload. Furthermore, the FHEs and LFPB are inspected prior to placement within the packaging.

2.2.3 Effects of Radiation on Materials

Since the payload of the ATR FFSC consists of contact handled un-irradiated fuel elements (or loose fuel plates), enriched to a maximum of 94% U-235, the radiation from the payload is insignificant. Consequently, there will be no radiation effects on the materials of construction and the requirements of 10 CFR §71.43(d) are met.

2.3 Fabrication and Examination

2.3.1 Fabrication

The metallic components of the ATR FFSC packaging are fabricated using conventional metal forming and welding techniques. Structural materials which are important to safety are specified using American Society for Testing and Materials (ASTM) standards as shown on the drawings in Appendix 1.3.2, *Packaging General Arrangement Drawings*. All materials and components are procured and assembled under a 10 CFR 71, Subpart H quality assurance program. Welding procedures and personnel are qualified in accordance with the ASME Code, Section IX. Each packaging and its components are fabricated in accordance with the requirements delineated on the drawings in Appendix 1.3.2, *Packaging General Arrangement Drawings*.

2.3.2 Examination

Each packaging and its components are examined per the requirements delineated on the drawings in Appendix 1.3.2, *Packaging General Arrangement Drawings*. All welds are visually examined on each pass per the requirements of AWS D1.6:1999 for stainless steel and AWS D1.2:2003 for aluminum. All welds which are important to safety are examined by liquid penetrant test on the final pass using procedures compliant with ASTM E165-02. Personnel performing NDE shall be qualified in accordance with ASNT SNT-TC-1A⁵. Any deviations from SAR drawing requirements will be dispositioned and corrected under a 10 CFR 71, Subpart H quality assurance program prior to the application of the model number, per 10 CFR §71.85(c).

2.4 General Requirements for All Packages

This section defines the general standards for all packages. The ATR FFSC package meets all requirements of this section.

2.4.1 Minimum Package Size

The minimum dimension of the ATR FFSC package is 8 inches square. Thus, the 4 inch minimum requirement of 10 CFR §71.43(a) is satisfied.

2.4.2 Tamper-Indicating Feature

A tamper-indicating device (TID) lock wire and seal is installed through a small post on the closure provided to receive the wire. An identical post is located on the body for the TID wire. For ease in operation, there are two TID posts on the body. There are only two possible angular orientations for the closure installation and the duplicate TID post on the body enables TID installation in both positions. Thus, the requirement of 10 CFR §71.43(b) is satisfied.

⁵ American Society for Nondestructive Testing (ASNT), Recommended Practice No. ASNT SNT-TC-1A, 2001 Edition.

2.4.3 Positive Closure

The ATR FFSC package cannot be opened unintentionally. The closure engages with the body using a bayonet style design. There are four lugs, uniformly spaced on the closure, that engage with four slots in the mating body feature. The closure is secured by retracting two spring loaded pins, rotating the closure through approximately 45°, and releasing the spring loaded pins such that the pins engage with mating holes in the body. When the pins are properly engaged with the mating holes the closure is locked. Thus, the requirements of 10 CFR §71.43(c) are satisfied.

2.4.4 Valves

The ATR FFSC does not contain any valves.

2.4.5 External Temperatures

As discussed in Section 3.3.1.1, *Maximum Temperatures*, the maximum accessible surface temperature with no insolation is 100°F (38°C). Since the maximum external temperature does not exceed 122°F (50°C), the requirements of 10 CFR §71.43(g) are satisfied.

2.5 Lifting and Tiedown Standards for All Packages

2.5.1 Lifting Devices

The ATR FFSC package may be lifted from beneath utilizing a standard forklift truck when the package is secured to a fork pocket equipped pallet, or in a package rack. Swivel lift eyes can be installed in the package to enable package handling with overhead lifting equipment. The swivel eyes are installed after removing the 3/8-16 socket flat head cap screws and index lugs used for stacking.

Assuming both lift eyes carry half the load, the weight at each lug is:

$$P = \left(\frac{290}{2}\right) = 145 \text{ lbf}$$

Applying a minimum horizontal sling angle of 30°, the maximum load on each sling is:

$$T = \frac{145}{\sin(30)} = 290 \text{ lbf}$$

Therefore, all lifting devices shall have a minimum working load limit of 300 lb.

2.5.1.1 Attachment Capacity

Per 10 CFR §71.45(a) any lifting attachment that is a structural part of the package must be designed with a minimum safety factor of three against yielding. This evaluation verifies the adequacy of the groove weld securing the threaded bar to the wall of the 8 inch square tube. By inspection, the groove weld is the weakest point of the lifting point and all other items will have a greater margin of safety. The lift eye is required to have a minimum working load limit of 300 lb. The lift eye components are therefore assumed to meet the lifting requirements.

The allowable force on the groove weld is equal to the shear strength of the base material, $0.6 \cdot \sigma_{yield}$.

Allowable weld stresses:

$$\sigma_{yield} = 30,000 \text{ psi}$$

$$w_{allow} = 0.6 \cdot 30,000 = 18,000 \text{ psi}$$

Maximum tension in each of the two lift slings is 290 lbf at an angle of 30°.

$$T_y = P = 145 \text{ lbf}$$

$$T_x = 290 \cdot \cos(30) = 251 \text{ lbf}$$

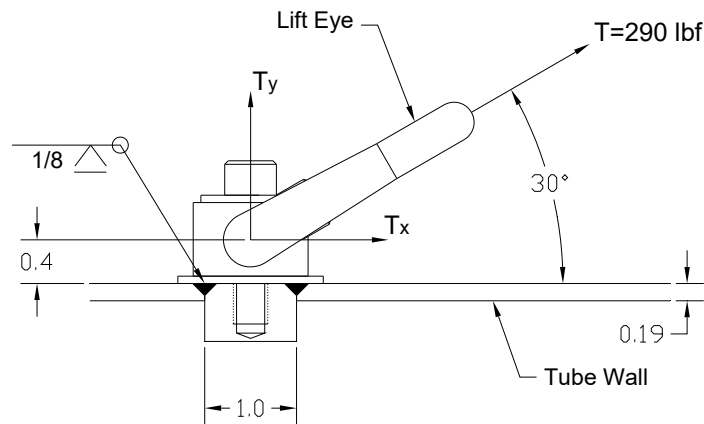


Figure 2.5-1 – Lift Attachment Diagram

Including the safety factor of three, the maximum horizontal and vertical forces are:

$$P_h = 3 \cdot T_x = 753 \text{ lbf}$$

$$P_v = 3 \cdot T_y = 435 \text{ lbf}$$

Using Blodgett⁶, the given load is divided by the length of the weld to arrive at the applied unit force, lb per linear inch of weld. From this force, the proper throat of the groove weld is determined.

The properties of the weld, treated as a line, are:

$$A_w = \pi \cdot d$$

$$S_w = \frac{\pi \cdot d^2}{4}$$

⁶ Omer Blodgett, *Design of Welded Structures*, 1982, The James F. Lincoln Arc Welding Foundation, Cleveland, Ohio.

Where,

$d = \text{diameter of weld} = 1.0 \text{ inch}$

$$A_w = \pi \cdot (1) = 3.14 \text{ in}$$

$$S_w = \frac{\pi \cdot (1)^2}{4} = 0.785 \text{ in}^2$$

Vertical tension on the weld is:

$$f_v = \frac{P_v}{A_w} = \frac{435}{3.14} = 139 \frac{\text{lb}f}{\text{in}}$$

Horizontal shear on the weld is:

$$f_h = \frac{P_h}{A_w} = \frac{753}{3.14} = 240 \frac{\text{lb}f}{\text{in}}$$

The bending force on the weld is

$h = \text{height of applied load from lift eye} = 0.4 \text{ in, plus half of the weld thickness of } 0.125/2$

$$h = 0.4 + (.125 / 2) = 0.463 \text{ in}$$

$$M = P_h \cdot h = 753 \cdot 0.463 = 349 \text{ in} \cdot \text{lb}$$

$$f_b = \frac{M}{S_w} = \frac{349}{0.785} = 445 \frac{\text{lb}f}{\text{in}}$$

The vertical tension and bending forces are in the same direction and additive:

$$f_{v+b} = f_v + f_b = 139 + 445 = 584 \frac{\text{lb}f}{\text{in}}$$

The vertical and horizontal loads are perpendicular, therefore the combined load is:

$$f_r = \sqrt{(f_{v+b})^2 + f_h^2} = \sqrt{(584)^2 + (240)^2} = 631 \frac{\text{lb}f}{\text{in}}$$

The required groove weld is:

$$w = \frac{f_r}{w_{allow}} = \frac{631}{18,000} = 0.035 \text{ in}$$

Thus the weld margin of safety is:

$$MS_{weld} = \frac{.125}{.035} - 1 = +2.6$$

2.5.1.2 Conclusion

From the above analyses, the lifting attachment points adequately lift the fully loaded package with a margin of safety of 2.6. The conservative minimum lifting angle of the slings is 30° above horizontal. Failure of this lifting component under excessive load would not impair the ability of

this package to meet other requirements of 10 CFR §71, per the requirements of 10 CFR §71.45(a).

2.5.2 Tiedown Devices

For transport, the package will be strapped or otherwise restrained inside or on the transport vehicle. Any features used to lift the ATR FFSC will be removed or rendered unusable for tiedown. The index lugs used to align the package during stacking are evaluated for the tiedown loads. Per 10 CFR §71.45(b)(1) the tiedown system must withstand a vertical loading of 2g, horizontal for/aft loading of 10g, and horizontal lateral loading of 5g. Because there is no vertical restraint capability of the index lug, the 2g vertical load is neglected. Combining the loads, the maximum horizontal g loading is $\sqrt{10^2 + 5^2} = 11.18g$. The loaded ATR FFSC package weighs 290 lb.

2.5.2.1 Tiedown Method

The ATR FFSC may be stacked in a 4 wide by 3 high array during transport. The packages are secured by means which resist the vertical loading. However, any axial/lateral restraint is conservatively neglected.

The index lugs at each end of the packages are used to align and secure the packages within the array and are subjected to g-loads from neighboring packages. The index lugs are attached to the package by a single flat head, socket cap screw such that horizontal loading causes shearing in the threaded area of the screw as shown in Figure 2.5-2.

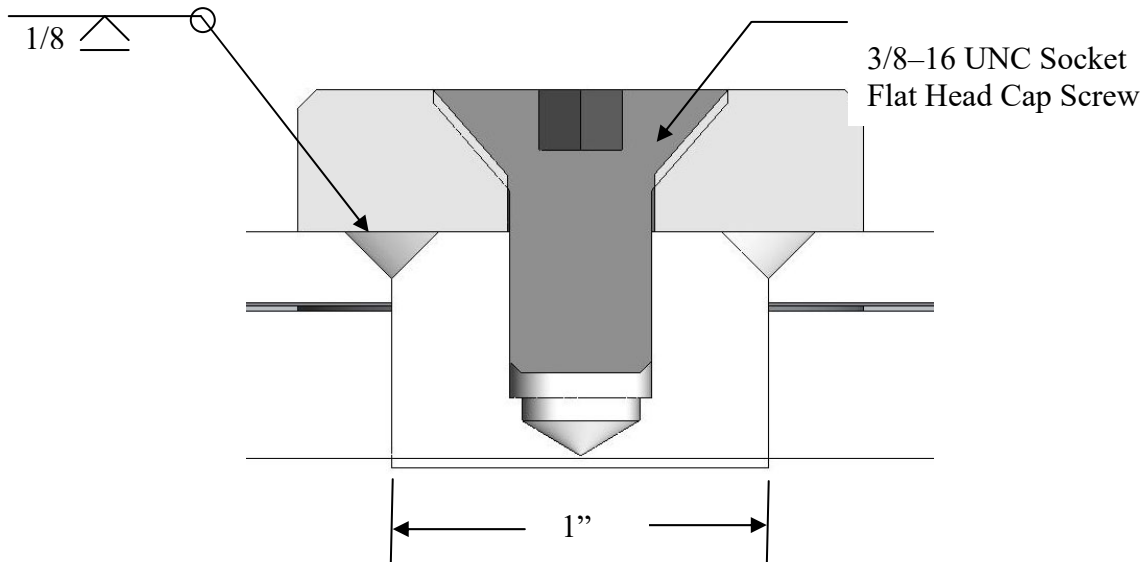


Figure 2.5-2 – Index Lug

2.5.2.2 Tiedown Capacity

By assuming the package is not restrained horizontally, the index lugs of the first tier must resist the horizontal loading of the middle and top tiers. The maximum load on each button is 2W times the g loading.

$$P_h = \frac{(2)(290)(11.18)}{2} = 3,242 \text{ lbf}$$

2.5.2.3 Fasteners

The screw thread shear area is 0.0775 in^2 and the screw material is ASTM F835 which has minimum tensile strength of 145 ksi. The yield strength is 116 ksi; conservatively assuming yield to be 80% of tensile strength for alloy steel. The shear force allowable is $0.6\sigma_{\text{yield}}$.

$$\text{Fastener shear stress} = \frac{3,242}{0.0775} = 41,832 \text{ psi}$$

$$MS = \frac{(116,000)(.6)}{41,832} - 1 = +0.66$$

The load required to fail the screw is:

$$P_{h\text{-failure}} = 0.6 \cdot \sigma_{\text{ult}} \cdot A = (0.6 \cdot 145,000) \cdot (0.0775) = 6,743 \text{ lbf}$$

2.5.2.4 Weld Structure

The allowable force on the groove weld is equal to the shear strength of the base material, $0.6\sigma_{\text{yield}}$.

Allowable weld stresses:

$$\sigma_{\text{yield}} = 30,000 \text{ psi}$$

$$w_{\text{allow}} = 0.6 \cdot 30,000 = 18,000 \text{ psi}$$

Using Blodgett, the given load is divided by the length of the weld to arrive at the applied unit force, lb per linear inch of weld. From this force, the proper throat of the groove weld is determined.

The properties of the weld, treated as a line, are:

$$A_w = \pi \cdot d$$

$$S_w = \frac{\pi \cdot d^2}{4}$$

Where,

d = diameter of weld = 1.0 inch

$$A_w = \pi \cdot (1) = 3.14 \text{ in}$$

$$S_w = \frac{\pi \cdot (1)^2}{4} = 0.785 \text{ in}^2$$

Horizontal shear on the weld is:

$$f_h = \frac{P_h}{A_w} = \frac{3,242}{3.14} = 1,033 \text{ lbf / in}$$

Assume for simplicity that the index lug diameter matches that of the weld (conservative). The moment on the weld is equal to the applied load times the distance from the weld c.g. to the mid-height of the 3/8 inch high index lug, or:

$$\frac{0.125}{2} + \frac{0.375}{2} = 0.25 \text{ in}$$

The bending force on the weld, as a vertical component, is

$$h = \text{height of applied load to index lug} = 0.25 \text{ in}$$

$$M = P_h \cdot h = 3,242 \cdot 0.25 = 811 \text{ in} \cdot \text{lb}$$

$$f_b = \frac{M}{S_w} = \frac{811}{0.785} = 1,033 \text{ lbf / in}$$

The vertical and horizontal loads are perpendicular, therefore the combined load is:

$$f_r = \sqrt{f_b^2 + f_h^2} = \sqrt{(1,033)^2 + (1,033)^2} = 1,461 \text{ lbf / in}$$

The required groove weld is:

$$w = \frac{f_r}{w_{allow}} = \frac{1,461}{18,000} = .081 \text{ in}$$

Thus the weld margin of safety is:

$$MS_{weld} = \frac{.125}{.081} - 1 = +0.54$$

The load required to fail the weld is:

$$f_r = w \cdot (0.6 \cdot w_{ult}) = (0.125) \cdot (0.6 \cdot 75,000) = 5,625 \text{ lbf / in}$$

$$\text{Since } f_b = f_h: f_h = \sqrt{f_r^2 / 2} = \sqrt{(5,625)^2 / 2} = 3,977 \text{ lbf / in}$$

The load required to fail the weld is:

$$P_{h-failure} = f_h \cdot A_w = (3,977) \cdot (3.14) = 12,488 \text{ lbf}$$

2.5.2.5 Conclusion

From the above analysis, the index lugs adequately withstand the combined horizontal tiedown g-loads for the fully loaded package. Furthermore, it is shown that the index lug screw will fail prior to the weld. This satisfies the requirements of 10 CFR §71.45(b)(1).

2.5.3 Closure Handle

The closure handle, deemed a structural part of the package, must be rendered inoperable for lifting and tiedown during transport in compliance with 10 CFR §71.45. To satisfy this requirement, a cover will be secured over the closure handle during transport to prevent any straps or hooks from being attached to the handle or to prevent any hardware from being placed between the handle and closure as illustrated in Figure 1.2-5. As an option, the handle may also be removed during transport.

The attachment of the closure handle to the closure assembly is evaluated here to show that its failure will not impair the ability of the package to meet other requirements. A lifting or tiedown load applied to the closure handle is expected to deform the handle and fail the closure screws causing the handle to become detached from the closure assembly. The closure handle is used only for operator convenience in handling the 10 lb closure assembly by hand. The four small fasteners securing the handle to the closure are designed to fail under light loads and well before impairment of any safety related packaging feature.

This evaluation conservatively neglects any tension (pulling) on the handle and handle screws since a load in this direction would pull on the closure locking tabs and not the locking pins. A simple comparison between the area of the closure tabs and the area of the handle screws shows that the closure tabs consist of significantly more material and the screws will fail well before any significant loads are applied to the closure tabs.

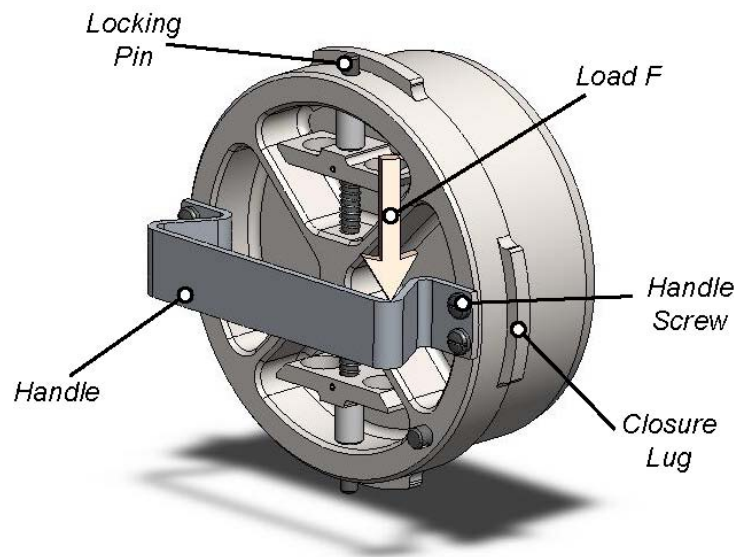


Figure 2.5-3 – Closure Assembly Handle

2.5.3.1 Handle Fasteners

The closure handle is secured by four #10-24 UNC screws (two per side). For this evaluation the load F is applied at the outside edge of the handle: 0.5 inches radially out from the screws and 0.5 inches above the face of the closure assembly.

This evaluation is based on the load F necessary to fail the handle screws. The load will be a function of the ultimate strength of the handle screws, which are given as a minimum of 72,000 psi for 18-8 material. To account for possible strain hardening due to the manufacturing process, that value will be conservatively multiplied by a factor of 2. Therefore:

$$\sigma_{\text{ultimate}} = 144,000 \text{ psi}$$

For the handle screws, the area across the threads is equal to the area of the minor diameter. For a #10-24UNC screw the minor diameter is 0.1389 inches.

$$A_s = \frac{\pi d_m^2}{4} = \frac{\pi (0.1389)^2}{4} = 0.0152 \text{ in}^2$$

The shear force in each screw is now determined. The largest forces will be at the two screws closest to the applied force. See Figure 2.5-4.

$$M = F \cdot r = 3.25 F \text{ in} \cdot \text{lb}$$

$$r = 3.25 \text{ in (dist. to centroid)}$$

Where r is taken as the maximum distance possible for any handle configuration.

The primary shear is:

$$n = 4 \text{ (number of screws)}$$

$$S' = \frac{F}{n} = \frac{F}{4} = 0.25F \text{ lb}$$

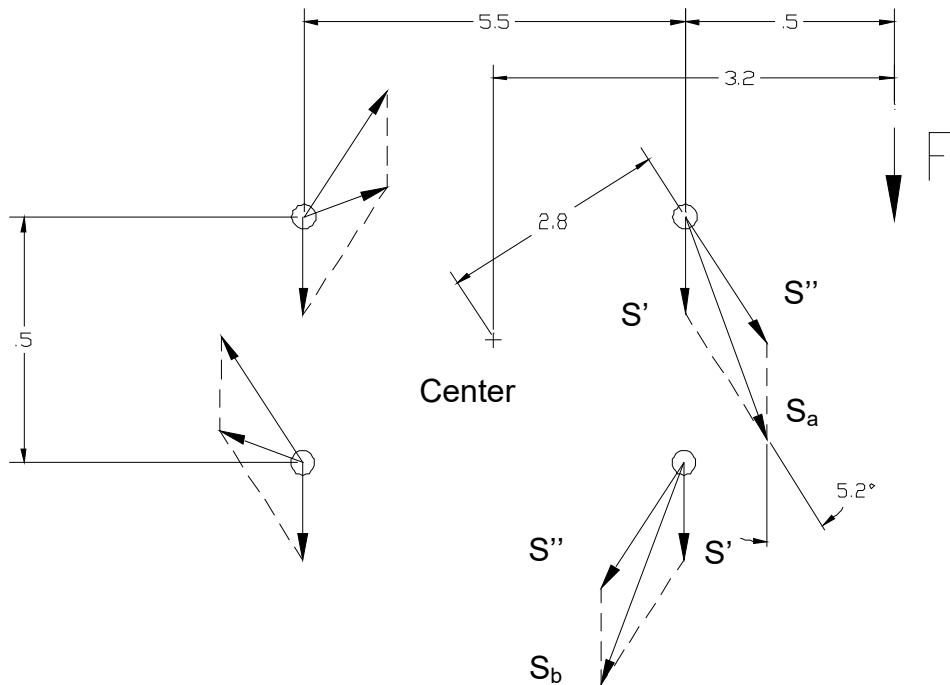


Figure 2.5-4 – Screw Pattern Diagram

The secondary shear is:

$$S'' = \frac{M}{4 \cdot R} = \frac{3.25F}{4 \cdot 2.8} = 0.29F \text{ lb}$$

$$R = 2.8 \text{ in. (dist. to centroid)}$$

The combined shear force is:

$$S_a = S_b = 0.29F + 0.25F(\cos 5.2) = 0.29F + 0.249F = 0.539F$$

The shear stress is:

$$\tau = \frac{S_a}{A_s} = \frac{0.539F}{0.0152} = 35.46F \text{ psi}$$

The tensile load on the screws due to the load F is applied to only two of the four screws, since the handle, due to its flexibility, cannot effectively transfer the load to the screws on the opposite side of the handle. The tensile load on the two screws closest to the load is:

$$\sum M_A = F \cdot (0.5) - R_1 \cdot (0.25) - R_2 \cdot (0.75) = 0$$

$$F = 0.5R_1 + 1.5R_2$$

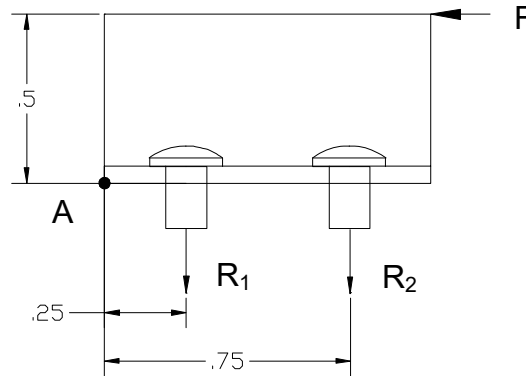


Figure 2.5-5 – Screw Prying Diagram

The relation between the screws is:

$$\frac{R_1}{R_2} = \frac{0.25}{0.75}$$

$$R_1 = \frac{1}{3}R_2$$

Substitute into the sum of moments equation:

$$F = 0.5R_1 + 1.5R_2$$

$$F = \left(\frac{1}{3} 0.5R_2\right) + 1.5R_2$$

$$R_2 = 0.6F \text{ lb}$$

$$R_1 = 0.2F \text{ lb}$$

The peak tension appears in R_2 . The maximum tensile stress is:

$$\sigma = \frac{R_2}{A_s} = \frac{0.6F}{0.0152} = 39.47F \text{ psi}$$

Combine the shear and tensile stresses to find the force necessary to fail the screws:

$$\sigma_{\text{ultimate}} = \sqrt{\sigma^2 + 4\tau^2} = \sqrt{(39.47F)^2 + 4(35.46F)^2}$$

$$144,000 = \sqrt{6,588F^2} = 81.17F$$

$$F = 1,774 \text{ lb}$$

2.5.3.2 Locking Pin Loading

To show that the handle attachment fails prior to the closure components of the package, the force necessary to fail the screws is applied to the two locking pins. The yield strength of the locking pins is conservatively used in the comparison.

The locking pins are 0.25 inch in diameter and made of ASTM A276, Type S21800 material, having a yield strength of $\sigma_{\text{yield}} = 50,000$ psi. The pin area is:

$$A_p = \frac{\pi d^2}{4} = \frac{\pi (.25)^2}{4} = 0.049 \text{ in}^2$$

The load P must be calculated from the screw failure load F . The distance from the center of the closure assembly to the point of shear in the locking pin is half of the diameter of the closure at the location of the pin, or $r_p = 5.97/2 = 2.99$ inches. The distance from the center of the closure assembly to the load F is 3.25 inches.

$$P = \frac{3.25F}{2.99} = 1,928 \text{ lb}$$

The shear stress for each pin is:

$$\tau = \frac{1}{2} \cdot \frac{P}{A} = \frac{1,928}{2(.049)} = 19,673 \text{ psi}$$

The margin of safety on the locking pins (against pin yield) at the point of handle screw failure is:

$$MS = \frac{0.6\sigma_{\text{yield}}}{\tau} - 1 = \frac{0.6 \times 50,000}{19,673} - 1 = +0.52$$

where the factor of 0.6 converts the tensile yield of the pin material to shear yield. Thus, should the closure handle be incorrectly used as a tiedown device, the handle screws will break off before the pins yield.

2.5.3.3 Conclusion

From the above analysis, should a force be applied to the closure handle, the handle screws will fail before the closure locking pins yield. Therefore, adverse loading of the closure handle does not impair the ability of the package to meet other requirements.

2.6 Normal Conditions of Transport

2.6.1 Heat

2.6.1.1 Summary of Pressures and Temperatures

As presented in Table 3.1-1 of Section 3.1.3, *Summary Tables of Temperatures*, the maximum ATR FFSC package temperature under conditions of 100°F ambient temperature and full insolation is 186°F on the outer shell. As presented in Table 3.1-2 of Section 3.1.4, *Summary Table of Maximum Pressures*, the maximum normal operating pressure (MNOP) of the ATR FFSC package is zero. This is assured because there are no seals provided between the body and closure to retain pressure.

The ATR FFSC body cavity is also discussed in Section 3.1.4, *Summary Table of Maximum Pressures*. The maximum pressure that may develop between the inner and outer shells will be limited to that achieved due to ideal gas expansion. The maximum pressure rise within the sealed cavity under NCT will be less than 4 psi gauge.

2.6.1.2 Differential Thermal Expansion

Because of the simple design of the ATR FFSC package, there are no features, such as rigid lids and containment seals, which could be affected by the differential thermal expansion of the package components. In addition, since the package has a negligible internal decay heat, any temperature differences will arise only from the solar loading, and consequently be modest in nature.

The nominal end gap between the package cavity and the FHEs or the LFPB is 0.63 inches and 0.38 inches respectively. The nominal end gap for the ATR LEU (balsa) FHE is 1.0 inch. These gaps are large enough to prevent the payload from expanding enough to load the closure. Therefore, differential thermal expansion is not of concern.

2.6.1.3 Stress Calculations

Since the MNOP is zero and the maximum sealed cavity pressure is 4 psi gauge, stresses due to NCT pressures and temperatures are negligible.

2.6.1.4 Comparison with Allowable Stresses

Since NCT stresses are negligible, this section does not apply.

2.6.2 Cold

With an internal decay heat load of zero, no insolation, and an ambient temperature of -40°F, the average package temperature will be -40°F. None of the materials of construction (i.e., stainless

steel) undergo a ductile-to-brittle transition at temperatures of -40 °F or higher. Therefore, the minimum NCT temperature is of negligible consequence.

2.6.3 Reduced External Pressure

As discussed in Section 2.6.1.1, *Summary of Pressures and Temperatures*, the ATR FFSC packaging is not capable of retaining pressure. Therefore, there is no effect of a reduced external pressure on the package of 3.5 lbf/in² (25 kPa) absolute, per 10 CFR §71.71(c)(3).

2.6.4 Increased External Pressure

10 CFR §71.71(c)(4) requires exposure of the ATR FFSC package to an increased external pressure of 20 psi (140 kPa) absolute. Since there are no sealing surfaces, there is no effect of an increased external pressure to the ATR FFSC package.

Section 2.7.6.1, *Cavity Evaluation*, evaluates the effect of pressure on the sealed cavity between the outer 8 inch tube and inner 6 inch diameter pipe. This cavity is welded closed during fabrication and has no relation to the payload. The cavity evaluation conservatively considers the satisfactory performance of a 22 psi gauge external pressure to the packaging.

2.6.5 Vibration

The effects of vibration normally incident to transport are not significant for the ATR FFSC packaging. Table 2 of ANSI N14.23⁷ shows peak vibration accelerations of a trailer bed as a function of package and tie-down system natural frequency. For the frequency range 0 to 5 Hz, assuming a light package, Table 2 of ANSI N14.23 gives peak accelerations (99% level) of 2g in the vertical direction, and 0.1g in both the lateral and longitudinal directions. All other frequency ranges give significantly lower acceleration levels.

The ATR FFSC is very resistant to damage from transportation vibration. The closure is subject to the ± 0.1g longitudinal (axial) loading, but since friction between the closure and its opening will exceed 0.1, the closure is not expected to apply any vibrational loadings to the bayonet lugs. The insulating material located between the inner, round tube and the outer, square tube is retained in place by a jacket of 28 gauge stainless steel. The resistance to displacement of the insulation was demonstrated in the testing program (see Section 2.12.2.5.1, *CTU Inspection*). When exposed to axial impacts which were many times larger than the vibration load of 0.1g, the insulation displaced an insignificant distance which was bounded by the assumptions made in the thermal analysis. Therefore, vibration will have no effect on the placement or condition of the insulation.

When supported on the shipping rack, the package is supported near index lugs which interface with the two pockets on the lower face of the package. Conservatively, an analysis of the package as a simply supported beam, supported at the extreme ends, is performed. The overall length of the package is $L = 72.5$ inches, and the maximum weight, from Table 2.1-1, is 290 lb. The distributed load is therefore $290/72.5 = 4$ lb/in. The outer square tube has a square

⁷ ANSI N14.23, *Design Basis for Resistance to Shock and Vibration of Radioactive Material Packages Greater Than One Ton in Truck Transport*, 1980, American National Standards Institute, Inc. (ANSI).

dimension of 8 inches and a wall thickness of 0.188 inches. AISC⁸ gives the moment of inertia of the tube as 58.2 in⁴. The c-distance is 4 inches. The bending moment is:

$$M = \frac{wL^2}{8}(2) = 5,256 \text{ in} \cdot \text{lb}$$

where the factor of 2 accounts for the inertia loading of $\pm 2g$. The reversing bending stress in the outer square tube is:

$$\sigma = \frac{Mc}{I} = 361 \text{ psi}$$

This value is well below the fatigue limit for stainless steel. Since the inner round tube is supported at three places along its length, the unsupported length is much shorter than for the outer square tube. In addition, the distributed weight, which consists of only the self-weight and payload weight, is significantly less than for the outer square tube. For these reasons, the stress in the inner round tube will be bounded by the stress in the outer square tube.

The FHEs and loose fuel plate basket are designed to be form fitting and supported by the inner stainless steel round tube. Furthermore, the FHEs and loose fuel plate basket are completely removed and in view at both the shipping and receiving sites, and consequently, a complete fatigue failure of either basket due to transportation vibration is not to be expected.

For these reasons, the effect of vibration normally incident to transport is not of concern for the ATR FFSC package.

2.6.6 Water Spray

The external surfaces of the ATR FFSC package are made from stainless steel, whose properties are not affected by water spray. For this reason, the effect of water spray, per 10 CFR §71.71(c)(6), is not of concern for the ATR FFSC package.

2.6.7 Free Drop

10 CFR §71.71(c)(7) requires a free drop for the ATR FFSC package. Since the package gross weight is less than 11,000 lb, the applicable free drop distance is 4 ft. As discussed in Appendix 2.12.1, *Certification Tests on CTU-1*, one NCT free drop preceded the HAC drop tests performed on CTU-1. The damage from the NTC drop case was minor as illustrated in Figure 2.12.1-5 through Figure 2.12.1-7. There was no loss or dispersal of package contents, and no substantial reduction in the effectiveness of the packaging. The latter result was confirmed by the successful completion of the subsequent HAC testing.

From the test results, the amount of deformation in the top corner was approximately 1/8 inch. Because there are no crushable materials of construction, the deformation of the package in any other NCT drop orientation is assumed to be the same or less than this CG over top corner orientation. This assumption is verified by the degree of damage recorded during the HAC drop orientations discussed in Section 2.7, *Hypothetical Accident Conditions*.

⁸ American Institute of Steel Construction, *Manual of Steel Construction, Allowable Stress Design*, Ninth Edition, 1989.

By observation, the NCT damage is much less than 5% of the total effective volume of the package, approximately 230 in³, based on 5% of the volume of the 72.5-inch long, by 8-inch square tube. Therefore, the requirement of 10 CFR §71.55(d)(4)(i) is met. Further, the effective spacing between fissile contents is 8 inches, based on a center-to-center distance between packages which are in side to side and top to bottom contact. Five percent of this distance is 0.4 inches, and therefore the requirement of 10 CFR §71.55(d)(4)(ii) is met. Finally, no opening capable of admitting a 4-inch cube was created, and the requirement of 10 CFR §71.55(d)(4)(iii) is also met. Thus, the effect of the free drop test, per 10 CFR §71.71(c)(7), is not of concern.

2.6.8 Corner Drop

This test does not apply, since the ATR FFSC package is a rectangular fissile material package weighing more than 110 lb, as specified in 10 CFR §71.71(c)(8).

2.6.9 Compression

As specified in 10 CFR §71.71(c)(9), the ATR FFSC must be subjected, for a period of 24 hours, to a compressive load applied uniformly to the top and bottom of the package in the normal transport position. The greater of the following uniformly distributed loads is to be used: (a) the equivalent of 5 times the weight of the package, or (b) the equivalent of 2 lbf/in² multiplied by the vertically projected area of the package. For these two cases, the loads are:

$$P_{(a)} = 5 \cdot W = 5 \cdot 290 \text{ lbf} = 1,450 \text{ lbf}$$

$$P_{(b)} = 2 \text{ psi} \cdot L \cdot w = 2 \text{ psi} \cdot (72.5 \text{ in}) \cdot (8 \text{ in}) = 1,160 \text{ lbf}$$

Where,

W is the maximum weight of one package

w is the overall width of the package

L is the overall length of the package.

Thus, it is seen that case (a) governs with a compressive load of 1,450 lbf.

The exterior side of the ATR FFSC packaging is a reinforced 8 inch by 8 inch square stainless steel tube with a 0.188 inch wall thickness. The closure end includes a 1.5 inch thick stainless steel plate and the bottom end includes a 0.88 inch thick stainless steel plate. By observation, buckling of the outer tube is not a concern due to its reinforcement, short height, wall thickness, and the relatively small load applied. A conservative evaluation is performed in the following section to demonstrate the adequacy of the design under the compression load.

2.6.9.1 Compression Evaluation

To conservatively evaluate the compressive load, buckling of the square tube under a uniform load is evaluated neglecting the reinforcing end plates and interior ribs. The applied load, as determined in Section 2.6.9, *Compression*, is 1,450 lbf. The average stress in the 8 inch tube is:

$$\sigma_{\text{tube}} = \frac{P}{A_{\text{tube}}}$$

Where,

$P = \text{applied load} = 1,450 \text{ lbf}$

$A_{\text{tube}} = \text{area of vertical legs of the tube} = 2 \times t \times L = 2 \cdot (0.19) \cdot 72.5 = 27.6 \text{ in}^2$

$t = \text{thickness} = 0.19 \text{ in}$

$L = \text{length of tube} = 72.5 \text{ in}$

Therefore:

$$\sigma_{\text{tube}} = \frac{P}{A_{\text{tube}}} = \frac{1450}{27.6} = 52.5 \text{ psi}$$

Using Roark⁹, Table 35 Case 1a, a rectangular plate under equal uniform compression, all edges simply supported, the critical unit compressive stress σ' is:

$$\sigma' = K \cdot \frac{E}{1 - \nu^2} \cdot \left(\frac{t}{L} \right)^2$$

Where,

$E = \text{modulus of elasticity for stainless steel} = 27.6 \text{ Mpsi}$

$\nu = \text{Poisson's ratio} = 0.3$

$K = \text{conservatively chosen as equal to } 10.9$

$$\sigma' = 10.9 \cdot \frac{27600000}{1 - (.3)^2} \cdot \left(\frac{0.19}{72.5} \right)^2 = 2,271 \text{ psi}$$

By comparison:

$$\sigma_{\text{tube}} \ll \sigma'$$

Therefore, buckling of the outer tube due to the compression load is not a concern.

2.6.10 Penetration

10 CFR §71.71(c)(10) requires that a bar of hemispherical end, weighing at least 13 lb be dropped from a height of 40 inches onto the most vulnerable part of the packaging. As documented in Appendix 2.12.1, *Certification Tests on CTU-1*, the ATR FFSC package, weighing approximately 290 lb, was subjected to the much more demanding test of being dropped from 40 inches onto the puncture bar described in §71.73(c)(3) without experiencing any damage which could compromise confinement or criticality control. Therefore, this test does not need to be performed, and the penetration test requirement is satisfied.

2.7 Hypothetical Accident Conditions

When subjected to the hypothetical accident conditions of 10 CFR §71.73, the ATR FFSC prevents loss or dispersal of the enriched uranium payload. The analysis given in Chapter 6, *Criticality*, which includes conservative assumptions regarding damaged geometry and

⁹ Young, Warren C., *Roark's Formulas for Stress and Strain*, Sixth Edition, 1989, McGraw Hill, New York, New York.

moderation, demonstrates the criticality safety of the ATR FFSC under hypothetical accident conditions.

10 CFR §71.55 requires that packages containing fissile material be evaluated for criticality with the inclusion of any damage resulting from the NCT tests specified in §71.71 plus the damage from the HAC tests specified in §71.73. The ATR FFSC was subjected to accident condition loadings by means of full scale certification testing. Each test specified by §71.73 was applied sequentially, as specified in Regulatory Guide 7.8¹⁰. One full scale certification test unit (CTU-1) using the ATR fuel element as the payload was subjected to the full series of free drop and puncture testing. A second full scale certification test unit (CTU-2) using the loose fuel plates as the payload was subjected to a series of worst case free drops. Puncture drops were not performed on CTU-2 because the testing focused on the performance of the insulation and payload, which would not be affected by any puncture damage. The puncture testing performed on CTU-1 demonstrated that the effects of the puncture test on the insulation and on the payload are negligible. Utilizing the results of drop testing, the fire test was evaluated analytically. The immersion tests are also evaluated analytically.

The payload for CTU-1 used during testing was an un-irradiated ATR fuel element, enriched to a maximum of 94% U-235. The ATR fuel element used was a rejected production fuel element. The defects were considered cosmetic only and had no structural significance for purposes of the certification tests. Further discussion of the CTU-1 payload is provided in Appendix 2.12.1, *Certification Tests on CTU-1*.

The simulated loose fuel plate payload for CTU-2 was a combination of 2- and 4-inch wide, 0.06-inch thick, 5052H32 aluminum flat plates. All plates were 49.5 inches long. There were 15, 2-inch wide plates and 10, 4-inch wide plates. The weight of the aluminum plates totaled 20.7 lb. Further discussion of the CTU-2 payload is provided in Appendix 2.12.2, *Certification Tests on CTU-2*.

Rationale for the selection of the test series is given below. The tests actually performed, and their sequence, are summarized in Table 2.7-1. Test results are summarized in the sections which follow and in Section 2.7.8, *Summary of Damage*, with details given in Appendix 2.12.1, *Certification Tests on CTU-1* and Appendix 2.12.2, *Certification Tests on CTU-2*.

HEU Fuel Elements, ATR Loose Plates, Small Quantity Payloads, and Cobra Fuel Elements.

The performance of the MIT and MURR fuel elements is bounded by the test results using the ATR fuel element. A full discussion and comparison of the three fuel elements is given in Appendix 2.12.3, *Structural Evaluation for MIT and MURR Fuel*. As with the ATR fuel element, the criticality evaluation performed in Section 6.10, *Appendix B: Criticality Analysis for MIT and MURR Fuel*, makes conservative assumptions designed to encompass a wide range of damage exceeding the actual damage observed during testing of the ATR fuel element. Since Section 6.11, *Appendix C: Criticality Analysis for Small Quantity Payloads* conservatively models the fuel as a homogeneous mixture of uranium and water, a structural evaluation of the RINSC and other small quantity payloads, and the corresponding FHE is not required. For Cobra fuel, Section 6.13, *Appendix E: Criticality Analysis for the Cobra Fuel Element* conservatively models the Cobra fuel as follows: for NCT, both the fuel and the FHE are

¹⁰ U. S. Nuclear Regulatory Commission, Regulatory Guide 7.8, *Load Combinations for the Structural Analysis of Shipping Casks for Radioactive Material*, Revision 1, March 1989.

considered as intact, consistent with the approach used for ATR, MURR, and MIT fuel. For HAC, the Cobra fuel is considered as both intact within an intact FHE, as well as conservatively reconfigured in the absence of an FHE. Since the Cobra fuel and the Cobra FHE are modeled as both intact and as fully reconfigured to the most reactive extent (including total absence of the FHE), a structural evaluation of the Cobra fuel and the Cobra FHE is not required.

LEU Fuel Elements and DDEs. Section 6.14, Appendix F: *Criticality Analysis for ATR, MURR, MIT, and NBSR LEU Fuel Elements and/or DDEs* conservatively models the LEU fuel elements and DDEs as follows: based on the performance of the ATR HEU fuel element in physical testing, the fuel plates of all fuel elements will remain intact. In the criticality evaluation, the separation of the plates is maximized in accordance with the physical space available within the package by assuming complete loss of attachment of the plates from the fuel element side combs. For MIT LEU and MURR LEU fuel elements and DDEs, the available space utilized is the same as was calculated in Appendix 2.12.3, *Structural Evaluation for MIT and MURR Fuel*. For the ATR LEU fuel element and the NBSR DDE, the balsa wood FHE of the ATR LEU fuel element and the packing material of the NBSR DDE are assumed not to be present, and the available space for plate separation is the entire cavity of the ATR FFSC package.

2.7.1 Free Drop

10 CFR §71.73(c)(1) requires a free drop of the specimen through a distance of 30 ft onto a flat, essentially unyielding surface in the orientation for which maximum damage is expected. The primary mode of failure of the ATR FFSC would be loss of the ability of the closure to retain the payload. This could occur through loss of the bayonet style lugs, or through failure of the retracting pins allowing the lid to rotate, or through excessive deformation of the closure area which could cause separation of the body from the closure. If a sufficient gap is formed between the body and closure, the payload may no longer be retained, consequently possibly affecting criticality safety.

The object of the free drop tests in the current instance is to create the maximum amount of damage in critical locations and components. Therefore, free drop orientations are selected which would result in the greatest amount of critical damage and which would render the package most vulnerable to damage from the puncture drop test.

The ability of the payload to remain in a critically safe geometry is also confirmed through the free drop tests. Following all drop tests, the fuel assembly in CTU-1 and the simulated loose fuel plates in CTU-2, are inspected to confirm the geometries remain within the assumptions used in Section 6.0, *Criticality Evaluation*.

To confirm the performance of the payload at reduced temperatures CTU-1 was subjected to two HAC drops with the payload temperature at approximately -20°F (-29°C). Following all CTU-1 testing, as discussed in Appendix 2.12.1, *Certification Tests on CTU-1*, the package was destructively disassembled and the payload inspected.

Upon inspection of both CTU-1 and CTU-2, the performance of both the payload and packaging, including the reduced temperature tests, was satisfactory.

2.7.1.1 Side Drop

The horizontal side drops for CTU-1 include CD1-1, CD2-1, and CD3-1. The first three HAC drops primarily address the packaging closure and shell response to the free drops. Also, the side

drop orientations represent large impact loads to the ATR fuel element for geometry control. CD1-1 presents the highest acceleration to the locking pins when the pins are oriented vertically with respect to the target surface. CD2-1 is directed at challenging the outer shell in the vicinity of the index lugs. The intent is to demonstrate that the outer shell is not penetrated by the impacted index lugs which could represent a thermal concern. In CD3-1, the locking pins are oriented horizontally with respect to the target surface presenting the worst case bending load to the locking feature.

The horizontal side drops for CTU-2 include CD1-2 and CD3-2. These two HAC drops address the performance of the LFPB in maintaining the geometry of the loose plates. Furthermore, the intent is to demonstrate the similar performance of the outer packaging in response to the LFPB as the payload.

2.7.1.2 CG Over Bottom Drop

The CG over bottom drop for CTU-1 includes CD4-1. This vertical orientation is expected to have the greatest potential for deformation to the insulation cavity at the bottom end. CD4-1 is considered to present the worst case loading to the 3/8 inch thick plate located at the bottom of the payload cavity. The intent of the drop is to demonstrate the insulation cavity at the bottom end of the package is not breached or significantly reduced. Additionally, the CD4-1 drop presents the worst case buckling load to the ATR fuel element.

For CTU-2, the CG over bottom drop includes CD4-2. As with CD4-1, this orientation is expected to have the greatest local deformation to the bottom end plate and insulation cavity and present the worst case buckling load to the LFPB and loose plates.

2.7.1.3 CG Over Corner Drop

The CG over corner drop was only performed on CTU-1. CD5-1, the CG over top corner drop, produces the greatest deformation in the closure region and also presents the greatest challenge for the closure locking tabs. The intent of the drop is to demonstrate the effectiveness of the closure in retaining the payload.

2.7.1.4 Oblique Drops

An oblique free drop orientation, also known as a slap-down drop, was not performed for this package. Consequences from the slap-down event are considered bounded by the CG over bottom (CD4-1/CD4-2) and CG over corner (CD5-1) drop tests performed. The slap-down drop challenges the closure and the fuel by producing high angular velocities and accelerations to the packaging and contents. However, in the case of the ATR FFSC, the end drops present a greater challenge to the closure and the fuel than the slap-down condition. In bolted closure designs, the slap-down side loads have the tendency to shear the closure bolts. Since the ATR FFSC closure is secured by a bayonet type design rather than bolts, this is not a concern. The axial load imparted to the closure in a slap-down drop will be lower than the axial loading developed in an end drop. And the greater the axial load, the greater the challenge to the locking tabs on the closure. The CD5-1 drop therefore presents the greatest challenge to closure retention, and the CD4-1/CD4-2 drop presents the greatest potential for fuel buckling.

2.7.1.5 Results of the Free Drop Tests

CD1-1 Flat Side Drop (CTU-1). See Figure 2.12.1-8 through Figure 2.12.1-13. The visible damage resulting from the 30 ft flat side drop, pocket side down, was negligible. There were minor visible exterior scratches resulting from the drop. The areas showing the greatest impact marks are at each end plate and near the three internal stiffening ribs. There was no significant bowing or other visible deformation. There was no visible deformation or rotation of the closure and the locking pins remained in the locked position.

Following the CD1-1 drop, CTU-1 was opened and the FHE and fuel element payload were visually inspected for damage. As illustrated in Figure 2.12.1-11 in Section 2.12.1, there were no major deformations and no cracked welds noticed. As illustrated in Figure 2.12.1-12, there was no visible damage to the fuel element.

With the closure assembly removed from the body of the CTU, one locking pin was noticeably bent approximately 1/32 inch as illustrated in Figure 2.12.1-13. It was noticed that the bent locking pin tended to bind when compressed to the open position. The other locking pin was not deformed and there was no other visible deformation of the closure assembly.

CD2-1 Flat Side Drop (CTU-1). Due to CTU-1 not impacting square on the index lugs, this orientation was tested three different times. The three tests in this orientation are identified as CD2.A-1, CD2.B-1, and CD2.C-1 throughout this section. For CD2.A-1, CTU-1 rotated during its descent and impacted at a slight angle causing the package to bounce and spin somewhat on the longitudinal axis after impact. The visible damage resulting from the CD2.A-1 drop was minor with the index lugs at each end pressed into the body approximately 1/8 inch. See Figure 2.12.1-14 through Figure 2.12.1-17.

For CD2.B-1 the package again rotated during its decent and impacted at an angle causing the package to bounce and spin on the longitudinal axis after impact. Also, a gust of wind blew the rigging straps into the adjacent stadia board during the drop. The visible damage resulting from the CD2.B-1 drop was minor with the index lugs at each end now pressed into the body approximately 3/16 inch. See Figure 2.12.1-18 through Figure 2.12.1-20.

CD2.C-1, which was performed after CD5-1, impacted in the correct orientation directly on the index lugs; see Figure 2.12.1-37 through Figure 2.12.1-40. The index lug near the closure end was flush with the original surface, pressed in approximately 3/8 inch (the height of the lug) as seen in Figure 2.12.1-39. The index lug at the bottom end was pushed in to approximately 1/8 inch from the original surface. A cracked weld was found under the index lug near the closure end as shown in Figure 2.12.1-40. The length of the cracked weld was approximately 1/2 inch.

CD3-1 Flat Side Drop – Reduced Temperature (CTU-1). See Figure 2.12.1-22 through Figure 2.12.1-25. The visible damage resulting from the 30 ft flat side drop performed with the payload at reduced temperature (-20°F) was negligible. Similar to CD1-1, the impact side exhibited scratches and impact marks near the locations of the internal ribs. Upon inspection of the closure assembly, one of the two locking pins was found sheared off from the outside edge of the closure as it interfaces with the package body. There was no other visible damage or any signs of rotation to the closure assembly as the second locking pin remained in the locked position.

CD4-1 CG Over Bottom End – Reduced Temperature (CTU-1). See Figure 2.12.1-26 through Figure 2.12.1-28. The visible damage resulting from the 30 ft CG over bottom end drop performed with the payload at reduced temperature (-20°F) was minor. The outer shell of CTU-1

exhibited minor bowing near the impact end with the greatest deformation measuring approximately 1/8 inch on one side. The overall length of the package body was compared with the initial measurements at eight locations and found to have compressed a maximum of approximately 1/8 inch. There was no visible deformation or rotation of the closure following the drop and the remaining locking pin remained in the locked position.

CD5-1 CG Over Top Corner Drop (CTU-1). See Figure 2.12.1-32 through Figure 2.12.1-36. The visible damage resulting from the 30 ft CG over top corner drop was prominent in the closure area. The impact corner was deformed in approximately 5/8 inch. There was modest deformation on the sides of the package near the impact location bulging in approximately 1/2 inch near the index lug pocket and bulged out approximately 5/8 inches on the adjoining side.

Following the drop, the closure assembly exhibited deformation with the end of the package and was unable to be rotated more than 1/8 inch in either direction. The locking pins showed no visible signs of deformation and the remaining locking pin remained in the locked position.

CD1-2 Flat Side Drop (CTU-2). See Figure 2.12.2-5 through Figure 2.12.2-7. This drop is a repeat of CD1-1 using the loose fuel plate payload rather than the ATR fuel element. The orientation of the LFPB parting lines is shown in Figure 2.12.2-3 through Figure 2.12.2-4. There was minor visible exterior damage, principally scuff marks, resulting from the drop. There was no bowing or other significant visible deformation. There was no visible deformation or rotation of the closure assembly, and the locking pins were unaffected by the drop.

Following the CD1-2 drop, CTU-2 was opened and the LFPB and payload were inspected. The basket was not affected by the drop, however the finger operated screws securing the two basket halves were loosened slightly. One tie wrap was broken but the simulated loose fuel plates were not damaged. The broken tie wrap was not replaced for the subsequent drops.

CD3-2 Flat Side Drop (CTU-2). See Figure 2.12.2-8 through Figure 2.12.2-10. This drop is a repeat of CD3-1 but at ambient temperature and using the loose fuel plate payload rather than the ATR fuel element. As with the other side drop events, the outer shell exhibited minor impact marks at the stiffening rib locations. There was no visible deformation or rotation of the closure assembly, and the locking pins were undamaged and in good working order.

The closure was opened and the payload inspected following the CD3-2 drop. The basket exhibited no signs of deformation and again the basket screws were loosened slightly. The second plastic tie wrap was broken and the simulated fuel plates exhibited no significant damage as seen in Figure 2.12.2-10. The broken tie wrap was not replaced for the subsequent drop.

CD4-2 CG Over Bottom End (CTU-2). See Figure 2.12.2-11 through Figure 2.12.2-16. This drop orientation is a repeat of CD4-1 but at ambient temperature and using the loose fuel plate payload rather than the ATR fuel element. CTU-2 appeared to impact slightly off of true vertical and impacted near one corner of the package. The impact caused one side to dent inward approximately 1/2 inch and the adjacent side to bulge out approximately 1/2 inch. There was no overall bowing of the package or other significant visible deformation. There was no visible damage to the closure or the locking pins.

The closure was removed and the basket extracted following the CD4-2 drop. The basket damage was minor and limited to a small dent at the end of the basket that was situated closest to the package bottom and a small deformation to the basket end plate from the package inner shell. As illustrated in Figure 2.12.2-15 and Figure 2.12.2-16, the simulated fuel plates experienced

localized deformation at the end of the basket closest to the package bottom. The remaining area above the localized deformation was not deformed.

The gap between the thermal shield and the stiffening rib, where the shield pulls away from the rib was found to be less than 1/16-inch during the disassembly of CTU-2 discussed in Section 2.7.8.2, *CTU-2 Package Disassembly – Results*. With the thermal shields removed the maximum compaction for all insulation sections ranged from 1 inch to 1¾ inches.

2.7.2 Crush

10 CFR §71.73(c)(2) requires that the crush test be performed on fissile material packages which have a mass not greater than 1,100 lb and a density not greater than 62.4 lb/ft³. The ATR FFSC package has a maximum weight of 290 lb and a volume of 2.69 ft³ (based on outside dimensions of 8 in x 8 in x 72.5 in), leading to a maximum density of 290/2.69 = 108 lb/ft³. Therefore, the crush test is not applicable.

2.7.3 Puncture

10 CFR §71.73(c)(3) requires the drop of the package onto a 6-inch diameter steel bar from a height of 40 inches. The primary modes of failure of the ATR FFSC would be closure damage, closure rotation, and penetration of the outer shell. The object of the puncture drop tests in the current instance is to create the maximum amount of damage in critical locations and components. Therefore, drop orientations are selected which would result in the greatest amount of critical damage and which would render the package most vulnerable to the thermal event. For the ATR FFSC, these are the CG over center of closure, 30° oblique CG over side, and an oblique drop onto the closure.

The CG over center of closure position was chosen to confirm the performance of the closure assembly and verify at least one locking pin remained locked to prevent rotation. The 30° oblique CG over side was chosen to confirm the resistance of the outer shell to penetration from the puncture bar. The oblique drop onto the closure assembly confirms that the puncture bar can not cause rotation of the closure and was added after the CD3-1 drop sheared one of the locking pins.

CTU-2 was not subjected to puncture, since the purpose of the CTU-2 test unit was to demonstrate the effectiveness of the LFPB and the performance of the thermal insulation. The puncture test would have no impact on these features.

2.7.3.1 Results of the Puncture Tests

CG Over Center of Closure, Vertical (CP1-1). See Figure 2.12.1-44 through Figure 2.12.1-46. The puncture bar impacted directly on the closure assembly (the handle was removed during previous free drop tests). The drop resulted in only minor damage with the TID post deformed into the closure and the closure assembly exhibiting minor scratches from the puncture bar. The locking pins showed no visible signs of deformation and the remaining functional locking pin remained in the locked position.

CG Over Side, 30° Oblique (CP2-1). See Figure 2.12.1-41 through Figure 2.12.1-43. The initial impact caused a deformation of approximately 1/2 inch deep by 5 inches across with a radius the

same as the puncture bar. There were no tears or fissures in the ATR FFSC outer skin and there was no change to the closure assembly.

Oblique Drop onto Closure (CP3-1). See Figure 2.12.1-29 through Figure 2.12.1-31. CP3-1 was an unscheduled puncture drop with the purpose of causing rotation to the closure assembly. This extra drop was chosen due to the failure of one of two locking pins during CD3-1. The puncture bar squarely impacted the closure rib and the CTU bounced away from the puncture bar onto the drop pad. Following the drop, the closure assembly rib exhibited minor deformations at the impact point made by the puncture bar. There was no rotation of the closure, and the remaining functional locking pin remained in the locked position and showed no visible signs of deformation.

2.7.4 Thermal

10 CFR §71.73(c)(4) requires the exposure of the ATR FFSC packaging to a hypothetical fire event. Performance of the package under the thermal event is addressed analytically in Chapter 3, *Thermal Evaluation*. Disassembly of the package following the structural tests confirmed that the compaction to the insulation features, as assumed in the thermal analyses, was shown to still perform in a satisfactory manner.

2.7.4.1 Summary of Pressures and Temperatures

As shown in Section 3.4.3, *Maximum Temperatures and Pressures*, the maximum peak temperature of the outer shell was evaluated to be 1,471°F. The annular space between the outer shell and inner shell pressurized to a maximum 39 psi gauge during the HAC thermal event. The payload cavity of the ATR FFSC is vented to the atmosphere and therefore the inner shell (6 inch diameter pipe) experiences an external pressure of 39 psi gauge. Since the ATR FFSC does not provide leaktight containment, this pressure is not significant to the package.

2.7.4.2 Differential Thermal Expansion

The thermal analysis presented in Section 3.4.4, *Thermal Evaluation under Hypothetical Accident Conditions*, identifies that the peak temperature difference between the inner and outer shells occurs approximately six minutes into the thermal event and results in a free differential thermal expansion of approximately 0.9-inches between the two shells. This places the outer shell in compression and the inner shell in tension. The packaging could respond structurally to the forces developed by this differential expansion by:

- failure of one of the two inner shell to end plate welds (allowing free expansion of the outer shell relative to the inner shell), or
- no weld failure, but buckling of the outer shell, or
- a combination of the above two scenarios.

In any case, none of these scenarios results in a geometry change to the packaging that leads to an increase in reactivity. The only concern is a condition that could allow an increase in heat transfer to the fuel such that the fuel approaches the melting point.

As identified in Section 3.4.4, *Thermal Evaluation under Hypothetical Accident Conditions*, the thermal consequences of the above events results in insignificant changes to the fuel temperature. The fuel does not approach the melting point and therefore there will be no impact to reactivity.

The effect of differential thermal expansion on the various packaging components is therefore considered negligible.

At 72°F, the nominal length of the packaging cavity is 67.88 inches, the nominal length of the FHE is 67.25 inches and the nominal length of the LFPB is 67.5 inches. Both the LFPB and the FHE are fabricated from aluminum so the worst case for potential interference due to thermal expansion is with the LFPB. From Figure 3.4-5 it can be seen that above 700°F the inner shell temperature is much greater than the LFPB temperature and so the inner shell thermal expansion rate exceeds that of the LFPB. During the cooling period below 700°F, the temperatures of the two components track within about 50 °F with the inner shell temperature always less than the LFPB. The worst condition for potential thermal expansion interference is near the peak temperature of the LFPB. For this evaluation, conservatively assume the LFPB temperature is 750°F and the inner shell is at 700°F. The length of the two components at these temperatures is calculated as follows:

$$L = \alpha \cdot L_{Original} \cdot (\Delta T) + L_{Original}$$

Where,

$L_{Original}$ = the original length of the component at 72°F

α = the coefficient of thermal expansion¹¹

For aluminum: $\alpha_{Al} = 14.7(10^{-6})$ in/in/°F at 750 °F

For stainless steel: $\alpha_{SST} = 10.0(10^{-6})$ in/in/°F at 700 °F

ΔT = the change in temperature from 72°F

L = the length of the component at the elevated temperature

Loose fuel plate basket length at 750°F is:

$$L_{LFPB} = 14.7(10^{-6})(67.5)(750 - 72) + 67.5 = 68.17 \text{ inches}$$

Inner shell length at 700°F is:

$$L_{IS} = 10.0(10^{-6})(67.88)(700 - 72) + 67.88 = 68.31 \text{ inches}$$

$L_{IS} > L_{LFPB}$, therefore there is no interference under worst case conditions.

2.7.4.3 Stress Calculations

Since there is no differential thermal expansion interference between FHE or LFPB and the packaging, and since the packaging internal pressure is zero, there are no stresses to report.

2.7.4.4 Comparison with Allowable Stresses

Since there are no stresses to report, this section does not apply.

¹¹ Coefficients of thermal expansion are taken from ASME B&PV Code, Section II, Part D, coefficient B. For aluminum, Table TE-2, and for stainless steel, Table TE-1, Group 3.

2.7.5 Immersion – Fissile Material

10 CFR §71.73(c)(5) requires performance of the immersion test for packages containing fissile material. The criticality evaluation presented in Chapter 6.0, *Criticality Evaluation*, assumes optimum hydrogenous moderation of single ATR FFSC packages and arrays of packages. Since the criticality consequences of water in-leakage are accounted for, and leakage of the payload from the packaging did not occur, the immersion test of 10 CFR §71.73(c)(5) is not of concern.

2.7.6 Immersion – All Packages

10 CFR §71.73(c)(6) requires performance of an immersion test on an undamaged specimen under a head of water of at least 50 ft or 21.7 psig. The package payload cavity does not provide a leak tight containment. Since the criticality consequences of water in-leakage are accounted for, and leakage of the payload from the packaging did not occur, the immersion test of 10 CFR §71.73(c)(6) is not of concern.

The ATR FFSC does contain a sealed annular space between the outer square tube and the inner pipe where the insulation is located. The possible consequence of a 21.7 psig pressure applied to the outside surface of the square tube and the inside surface of the 6 inch diameter tube are considered insignificant to both the packaging and the payload.

2.7.7 Deep Water Immersion Test

The ATR FFSC package is a Type A Fissile package; hence, this requirement does not apply.

2.7.8 Summary of Damage

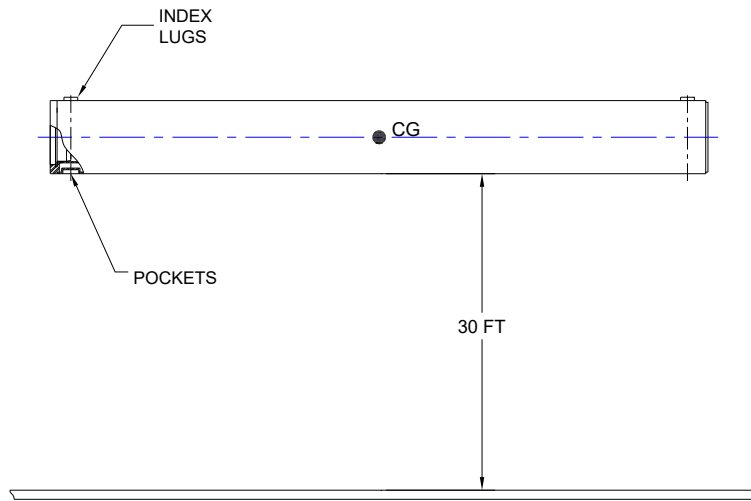
The discussions of sections 2.7.1, *Free Drop*, through 2.7.7, *Deep Water Immersion Test*, demonstrate that the ATR FFSC package prevents loss or dispersal of the payload when subjected to all applicable hypothetical accident tests. In addition, the ATR fuel element and loose fuel plates retain a geometry consistent with the analysis presented in Section 6.0, *Criticality Evaluation*. The physical test series consisted of multiple 30 ft free drop and puncture drop tests conservatively applied to two CTUs. Following the drop tests, each CTU was destructively disassembled to inspect various aspects of the packaging. Table 2.7-1 presents the certification drop test series in the sequential order performed for both CTU-1 and CTU-2.

Table 2.7-1 – ATR FFSC Certification Drop Test Series

Test No.	Test Description	Purpose of Test
CN1-1 (CTU-1)	CG over top corner	Confirm: <ul style="list-style-type: none"> • Fuel element does not penetrate the closure insulation pocket. • Fuel retains geometry necessary to maintain sub-criticality. • Closure is retained on the body and has not rotated relative to the package body.
CD1-1 (CTU-1)	Flat side drop, pocket side down.	Confirm: <ul style="list-style-type: none"> • Closure is retained and has not rotated relative to the package body. • Fuel retains geometry necessary to maintain sub-criticality.
CD2.A-1 (CTU-1)	Flat side drop, index lugs down	Confirm: <ul style="list-style-type: none"> • Impact on index lugs does not cause a fracture in the outer shell. • Closure is retained and has not rotated relative to the package body.
CD2.B-1 (CTU-1)	Flat side drop, index lugs down	Same purpose as CD2.A-1. This test was repeated due to the impact during CD2.A-1 being slightly rotated on the longitudinal axis and not fully impacting the index lugs.
CD3-1 (CTU-1)	Flat side drop, pocket and index lugs on side (-20°F)	Confirm: <ul style="list-style-type: none"> • Closure is retained and does not rotate relative to the package body. • Fuel element performance at cold temperature. • Fuel retains geometry necessary to maintain sub-criticality.
CD4-1 (CTU-1)	CG over bottom end (-20°F)	Confirm: <ul style="list-style-type: none"> • Fuel element does not penetrate into the packaging bottom end insulation pocket. This is a thermal performance requirement. • Fuel element performance at cold temperature. • Fuel retains geometry necessary to maintain sub-criticality.
CP3-1 (CTU-1)	Oblique drop onto closure assembly	Confirm: <ul style="list-style-type: none"> • Closure is retained on the body and does not rotate relative to the package body. This was an unscheduled test to confirm the performance of the remaining locking pin after the failure of the other pin during CD3-1.

Table 2.7-1 – ATR FFSC Certification Drop Test Series (continued)

Test No.	Test Description	Purpose of Test
CD5-1 (CTU-1)	CG over top corner (same orientation as CN1)	Confirm: <ul style="list-style-type: none"> • Fuel element does not penetrate the closure insulation pocket. • Fuel retains geometry necessary to maintain sub-criticality. • Closure is retained and does not rotate relative to the package body.
CD2.C-1 (CTU-1)	Flat side drop, index lugs down	Same purpose as CD2.A-1. This test was repeated for a third time due to the impact during CD2.B-1 being slightly rotated on the longitudinal axis and not fully impacting the index lugs.
CP2-1 (CTU-1)	CG over side, 30° oblique	Confirm: <ul style="list-style-type: none"> • Resistance of outer shell to puncture bar penetration.
CP1-1 (CTU-1)	CG over center of closure (Vertical)	Confirm: <ul style="list-style-type: none"> • Closure is retained and does not rotate relative to the package body.
CD1-2 (CTU-2)	Flat side drop, pocket side down.	Confirm: <ul style="list-style-type: none"> • Closure is retained and has not rotated relative to the package body. • Simulated fuel plates and basket retain geometry necessary to maintain sub-criticality.
CD3-2 (CTU-2)	Flat side drop, pocket and index lugs on side	Confirm: <ul style="list-style-type: none"> • Closure is retained and does not rotate relative to the package body. • Simulated fuel plates and basket retain geometry necessary to maintain sub-criticality.
CD4-2 (CTU-2)	CG over bottom end	Confirm: <ul style="list-style-type: none"> • Simulated fuel plates or basket do not penetrate into the packaging bottom end insulation pocket. This is a thermal performance requirement. • The insulation is not excessively compacted along the axial length of the package at the inner tube. • Simulated fuel plates and basket retain geometry necessary to maintain sub-criticality.



Index lugs and pockets rotated depending on drop series.

Figure 2.7-1 – ATR FFSC Certification Tests CD1-1, CD2-1, CD3-1, CD1-2, & CD3-2 (Test CD1-1 Shown)

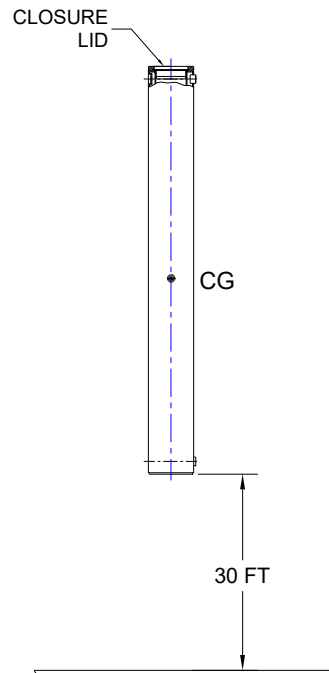


Figure 2.7-2– ATR FFSC Certification Tests CD4-1 & CD4-2

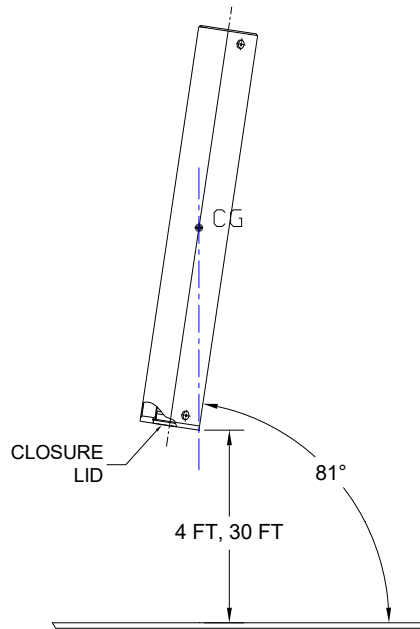


Figure 2.7-3 – ATR FFSC Certification Tests CN1-1 & CD5-1

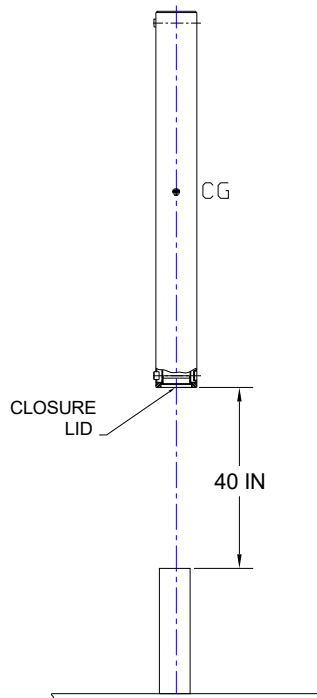


Figure 2.7-4– ATR FFSC Certification Test CP1-1

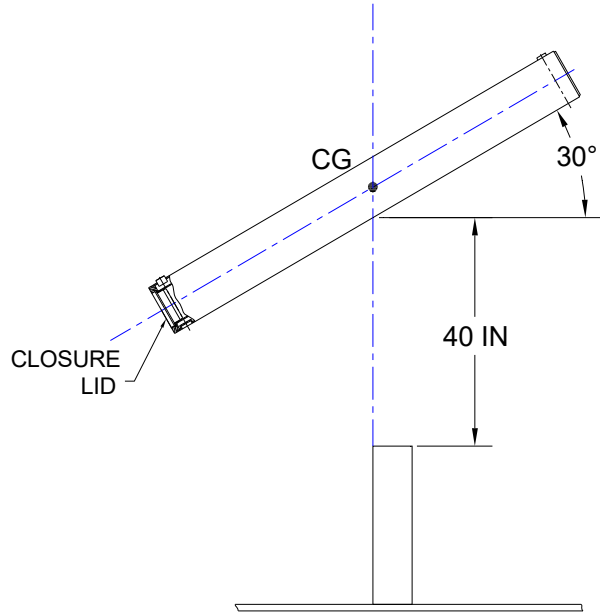


Figure 2.7-5– ATR FFSC Certification Test CP2-1

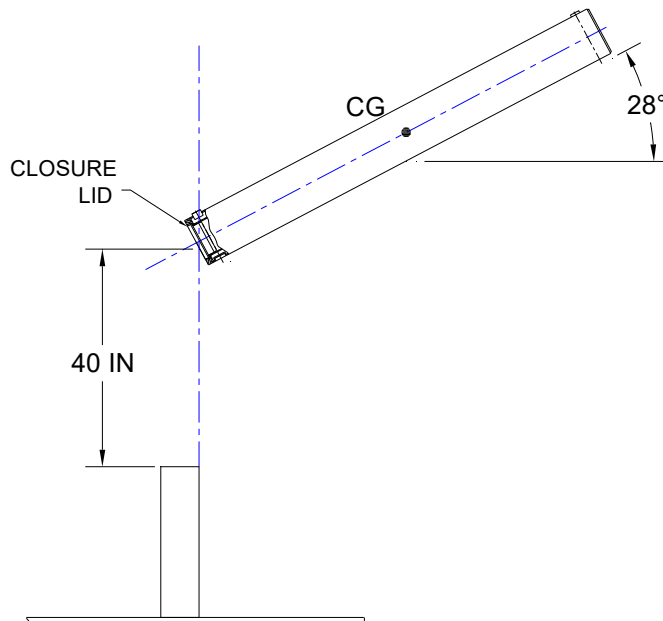


Figure 2.7-6– ATR FFSC Certification Test CP3-1

2.7.8.1 CTU-1 Package Disassembly - Results

Following the nine free drop tests and three punctures, CTU-1 was disassembled to examine the internal features. The items of critical importance focused on during the disassembly included:

- Loss or dispersal of any radioactive/fissile material
- Movement or compaction of the insulation material wrapped around the inner shell and condition of each end plate as related to the thermal evaluation.
- Deformations associated with the position and geometry of the ATR fuel element as related to the criticality evaluation.

To confirm the thermal performance features of the package the inner shell insulation and the insulation pockets at each end were visually inspected. The inner thermal shields remained in place and the maximum compaction for all insulation sections ranged from 1-1/8 inches to 1-1/2 inches. The closure end and bottom end insulation pockets were not penetrated and exhibited only minor deformation. For photographs of the disassembly see Figure 2.12.1-47 through Figure 2.12.1-51.

The inner tube was inspected as shown in Figure 2.12.1-52 and Figure 2.12.1-53. Due to the CG over corner drop deformation, CD5-1, the inner tube bowed out approximately 1/4 inch in one localized area near the closure end. In the same area the inner tube also bowed inward approximately 3/16 inch slightly deforming the FHE aluminum end plate. There were no visible signs of any weld failures associated with the inner tube.

The FHE was removed from the inner shell and visually inspected as shown in Figure 2.12.1-56. The welds joining the endplates to the FHE body had failed at both ends. There was minor bowing and deformation located near the closure end of the package and some of the neoprene padding on the inside had become detached.

The ATR fuel element end boxes were shattered as expected. The geometry of the fissile material within the fuel element was not significantly altered and clearly was within the assumptions used in the criticality analysis as illustrated in Figure 2.12.1-57 through Figure 2.12.1-62. The post test inspection of the fuel element revealed large impact marks in the fuel plates as shown in Figure 2.12.1-58 through Figure 2.12.1-59 from fragments of the fuel element end boxes deforming the ends of the fuel plates. However, the uranium aluminide fissile material within each fuel plate was not exposed and the deformations at each end did not extend to the fissile material within each fuel plate. A comparison between the pre-test and post-test inspections of the fuel element is provided in Table 2.7-2. The measurements were generally taken at five locations along the length of the fuel plates. Note that, due to the numerous free drops and punctures applied to CTU-1, the damage experienced by the ATR fuel element was much greater than is to be expected for a single, 30 ft free drop and 40-inch puncture drop. Further detail is provided in Appendix 2.12.1, *Certification Tests on CTU-1*.

Table 2.7-2 – ATR Fuel Element Measurements

Measurement Area	Pre-Test Range (in)	Post-Test Range (in)
Side Plate Flatness	±0.010	±0.075
In-Plane Bending of Side Plates	±0.011	±0.025
Side Plate Spacing - Top	4.113 – 4.130	4.015 – 4.131
Side Plate Spacing - Bottom	1.840 – 1.845	1.837 – 1.845
Height of Top Fuel Plate from Table (top side up)	2.675 – 2.691	2.655 – 2.785
Height of Bottom Fuel Plate from Table (bottom side up)	2.500 – 2.540	2.415 – 2.508
Fuel Plate to Fuel Plate Spacing	0.075 to 0.080	0.023 to 0.098 ^①

^① The minimum and maximum fuel plate spacing measurements were in localized areas near the side vents and not representative of the general spacing.

2.7.8.2 CTU-2 Package Disassembly - Results

Following the three free drop tests, CTU-2 was disassembled to examine the internal features. The items of critical importance focused on during the disassembly included:

- Loss or dispersal of any parts of the simulated loose fuel plate payload.
- Movement or compaction of the insulation material wrapped around the inner shell and condition of each end plate as related to the thermal evaluation.
- Deformations associated with the position and geometry of the simulated loose fuel plates as related to the criticality evaluation.

To confirm the thermal performance features of the package the inner shell insulation and the insulation pockets at each end were visually inspected. The gap between the thermal shield and the stiffening rib, where the shield pulls away from the rib, is less than 1/16-inch. With the thermal shields removed the maximum compaction for all insulation sections ranged from 1 inch to 1 ¾ inches. The closure end and bottom end insulation pockets were not penetrated and exhibited only minor deformation. The bottom end plate was cut open and there was no indication of compression of the insulation in that region. For photographs of the disassembly see Figure 2.12.2-18 through Figure 2.12.2-27.

The inner tube was inspected and a minor deformation occurred near the bottom end of the package as shown in Figure 2.12.2-28 and Figure 2.12.2-29. The tube was bulged out approximately 1/16-inch and, closer to the end, an inward deformation of approximately ¼ inch.

These deformations were localized and did not impair free movement of the basket in the payload cavity. There were no visible signs of any weld failures associated with the inner tube.

Following each of the three drop tests the package was opened and both the LFPB and simulated fuel plates visually inspected. The damage to the LFPB was limited to a small dent at the end of the basket that was situated closest to the package bottom and the impact point as shown in Figure 2.12.2-14. The damage was minor and did not impair the ability of the LFPB to retain the simulated fuel plates.

The simulated fuel plates within the LFPB experienced visible deformation only during the CD4-2 drop. The plates experienced localized deformation at the end of the basket closest to the package bottom as seen in Figure 2.12.2-15 and Figure 2.12.2-16. Above this area the simulated fuel plates were not deformed. Further details can be found in Appendix 2.12.2, *Certification Tests on CTU-2*.

By meeting all of the structural approval standards of Subpart E of 10 CFR §71, the ATR FFSC ensures criticality safety of the package under normal conditions of transport and hypothetical accident conditions.

2.8 Accident Conditions for Air Transport of Plutonium

The ATR FFSC package does not transport plutonium; hence, this section does not apply.

2.9 Accident Conditions for Fissile Material Packages for Air Transport

10 CFR §71.55(f) requires that a package be subcritical subsequent to the application of a series of accident condition tests applicable to the transport of fissile materials by air. The effects of these tests on the ATR FFSC have not been specifically evaluated. Instead, for purposes of the criticality evaluation, a worst-case reconfiguration of the package and contents materials is assumed. Under the bounding assumption, all of the materials of the package and of the contents are assumed to reconfigure into a spherical shape. Materials which moderate or reflect neutrons are placed in positions which lead to the greatest reactivity of the system. Materials whose presence would reduce system reactivity are not credited. The sphere is surrounded by 20 cm of water. The ATR FFSC package meets the requirements of 10 CFR §71.55(f) for the air transport of up to 2 kg of U-235. Details of the criticality analysis are given in Section 6.7, *Fissile Material Packages for Air Transport*. Details of the air transport criticality analysis for LEU fuel elements and DDEs is given in Section 6.14.5, *Fissile Material Packages for Air Transport*.

2.10 Special Form

The ATR FFSC payload is not in special form; hence, this section does not apply.

2.11 Fuel Rods

The ATR FFSC package does not carry irradiated fuel rods; hence, this section does not apply.

2.12 Appendices

2.12.1 Certification Tests on CTU-1

2.12.2 Certification Tests on CTU-2

2.12.3 Structural Evaluation for MIT and MURR Fuel

This page left intentionally blank.

2.12.1 Certification Tests on CTU-1

This report describes the methods and results of a series of tests performed on the Advanced Test Reactor (ATR) Fresh Fuel Shipping Container (FFSC) transportation package shown in Figure 2.12.1-1. The objective of testing was to conduct drop tests in accordance with the requirements of 10 CFR 71, §71.71 Normal Conditions of Transport (NCT), and §71.73 Hypothetical Accident Conditions (HAC). The verification of the loose fuel plate basket structural integrity and the performance of the package insulation are supported by the tests described in Section 2.12.1, *Certification Tests on CTU-2*.

Testing was performed at Sandia National Laboratories (SNL) in Albuquerque, New Mexico between May 21 and May 23, 2007. Data logs were maintained to track the testing that was performed. In addition, color photographs and videos were taken to document relevant events.

2.12.1.1 Overview

There are three primary objectives for the certification test program:

1. To demonstrate that, after a worst-case series of NCT and HAC free drop and puncture events, the package maintains containment of radioactive contents.
2. To demonstrate that, after a worst-case series of NCT and HAC free drop and puncture events, geometry of both the fuel and package are controlled as necessary to maintain subcriticality.
3. To demonstrate that, after the free drop and puncture bar events, the package retains the thermal protection necessary to maintain the fuel below its melting point during the thermal evaluation.

Several orientations were tested to ensure that the worst-case series of free and puncture drop events had been considered. Post-impact examination demonstrated that the package sufficiently met the design objectives. The design objectives include:

- The package closure remained attached to the body and did not become unlocked as evidenced by no rotation of the closure, thus maintaining containment.
- The package dimensions remained essentially the same providing adequate geometry control.
- Punctures and tears in the outer shell were prevented and thermal insulation was retained for protection during the fire event.
- Reconfiguration of the ATR fuel element and/or Fuel Handling Enclosure (FHE) is bounded by the criticality analysis.

2.12.1.2 Pretest Measurements and Inspections

The ATR FFSC packaging, the FHE, and ATR fuel element were received at SNL and identified as the ATR Fuel Element Certification Test Unit (CTU). The components arrived fully constructed, although not assembled, and ready for testing. The fabrication serial

number of the ATR FFSC test unit is CTU3. The serial number for the FHE is FHA 2. The packaging and payload are identified as ATR FFSC Certification Test Unit CTU-1.

The ATR fuel element is an ATR Mark VII high enriched uranium (HEU) fuel element. The ATR fuel element, serial number XA-877R, is a rejected production fuel element based on minor dimensional discrepancies. Prior to assembly of the CTU, some basic dimensions from the fuel element were recorded for post-test comparison. Figure 2.12.1-2 is a photograph of the ATR fuel element prior to testing.

The CTU was dimensionally inspected to the drawings at the fabricator and the fabrication records forwarded to PacTec. A Certificate of Compliance was issued by the fabricator of the CTUs documenting compliance with the fabrication drawings. Minor discrepancies between the drawings and the CTUs were identified and independently evaluated. The evaluations concluded that the discrepancies were minor and would not significantly affect the CTU during testing.

There were four fabrication deviations associated with the serial number CTU3 package fabrication:

- The 3/8-16 UNC index lug screws were obtained without specified ASTM F-879 certifications.
- The #10-24 UNC closure handle screws were obtained without specified ASTM F-879 certifications.
- Chemical over testing of the package body closure plate material identified manganese content 0.02% above the ASTM A479 maximum allowable.
- The handle width is specified to be 7.5 ± 0.3 -inches. When measured in the free state (not secured to the closure), the handle width was undersized by approximately 0.1-inches.

Other deviations relative to the CTU are the absence of the stainless nameplate and the use of temporary rigging attachments. These items are also insignificant relative to the weight of the CTU and their impact upon the drop tests.

2.12.1.2.1 Component Weights

Component weights were measured and recorded as shown in Table 2.12.1-1.

2.12.1.2.2 Drop Test Pad and Puncture Bar Measurement and Description

The drop pad consists of a 10.2 x 28-ft x 4 to 8-in. steel plate firmly anchored to a 300 inch reinforced concrete slab embedded in the ground. The estimated weight of the pad is greater than 2 million lbs. Thus the test pad was qualified as an essentially unyielding surface for the approximately 300 lb CTU. The puncture bar measured 6 in. (150 mm) in diameter and was 36 inches above the drop pad for the puncture drops CP1 and CP2. The puncture bar was securely mounted to the drop pad by welding.

2.12.1.2.3 Equipment and Instruments

Instrumentation used for the component weights and drop tests is given in Table 2.12.1-2. All applicable test and measurement equipment were calibrated in accordance with SNL procedures. The instrumentation used was associated with physical measurements, drop height, angle of the package, and temperature. It is noted that the SNL calibration procedures require National Institute of Standards and Technology (NIST) traceability and that SNL records adequately demonstrated that the calibrations were NIST traceable.

A few different methods were used to confirm the drop height of the package including:

- A plumb bob with a stretch resistant string.
- A tape measure.
- A surveyor theodolite.

SNL project personnel under the supervision of PacTec personnel verified the correct height prior to each drop. The angle of the CTU prior to each drop was measured using a digital level.

Photographic backdrops were fabricated and erected 54 ¼ inches away to the North and 103 ½ inches to the West from the center of the drop pad. The squares on the backdrop are approximately 10.5 inches horizontal and 14.4 inches vertical on the North stadia and 12 inches square on the West stadia.

Two high speed digital video cameras were used to record the drop events. The video views were from the front and side of the drop pad, 90 degrees apart. In addition, color photographs were taken to document the testing.

2.12.1.3 Summary of Tests and Results

2.12.1.3.1 Initial Conditions

The initial conditions for the two HAC drops CD3-1 and CD4-1 were performed at reduced temperature. All other NCT drops, HAC drops, and puncture drops were performed at ambient temperature. Figure 2.12.1-3 shows the chilling unit used to chill the CTU. The chilling unit internal temperature cycled between approximately -25 to -75°F as it circulated cold air. The CTU was in the chiller for 15 hours and 17 minutes. Just prior to removing the CTU from the chiller, the surface temperature was approximately -60°F. The target temperature for the ATR fuel element at the time of drop was -20°F. The surface temperature was recorded before CD3-1 and CD4-1 and varied due to the length of time between removal from the chilling unit to the drop. It is estimated that although the surface temperature raised quickly, the internal temperature of the fuel element was close to the target temperature.

2.12.1.3.2 Summary of Testing

Table 2.12.1-3 identifies the sequential order and testing performed on the ATR FFSC CTU.

2.12.1.4 Certification Tests

2.12.1.4.1 Drop Tests

Only one NCT drop was performed followed by seven HAC drops and three drops onto a puncture bar. The testing conditions are considered conservative due to the large number of HAC drops in various orientations on the single CTU. Relatively minor deformations were recorded due to impact attenuating devices (impact limiters) not being used in the design.

Two 30 ft HAC drops performed on the ATR fuel element CTU were at reduced temperature. These two drops were considered the worst case for the ATR fuel element payload with a targeted temperature of -20°F. The other orientations confirmed the performance of the packaging.

Figure 2.12.1-4 illustrates the orientation markings on the CTU to aid in the descriptions provided throughout this report. The test identification numbering reflects the same drop orientation as performed in CTU-2. For example, CD3-1 is the same orientation as the third HAC drop in CTU-2, test CD3-2. The “-1” identifies this drop as a CTU-1 test.

2.12.1.4.1.1 CN1-1 – CG Over Top Corner NCT Drop

A rigging attachment was welded to the bottom end of the CTU to attain the proper orientation. The drop configuration for CN1-1 was with the CG over the top corner of the closure end. Figure 2.12.1-5 illustrates the drop orientation. Initial conditions were as follows:

- Ambient temperature: 71°F
- Avg. surface temperature: 71°F
- Time: 11:21 a.m. 5/21/2007
- Drop height: 4 ft

The impact location was at corner number 5 identified in Figure 2.12.1-4. Following impact, the CTU bounced slightly and tipped over onto its side. There was minor visible exterior damage at the impact corner. The maximum deformation at the corner was approximately 1/8 inch. The closure handle was also deformed as a result of the drop. The overall length of the package did not change other than the 1/8 inch at the impact corner and compression of the closure handle of approximately 1/2 inch on one side. There was also a 1/8 inch deformation on the side corner approximately 1 ¼ inch from the impact corner. There was no visible deformation or rotation of the closure, other than the handle. Figure 2.12.1-6 and Figure 2.12.1-7 show the CTU following the NCT drop.

2.12.1.4.1.2 CD1-1 – Flat Side, Pockets Down, HAC Drop

Following CN1-1, the temporary rigging attachments were removed. To rig CD1-1 the index lugs on the CTU were removed and lifting eyes installed in their place. The drop configuration for CD1-1 was with the CTU in the typical lifting orientation, horizontal position, with the alignment pockets facing down. Figure 2.12.1-8 illustrates the drop orientation. Initial conditions were as follows:

- Ambient temperature: 76°F

- Avg. surface temperature: 78°F
- Time: 12:20 p.m. 5/21/2007
- Drop height: 30 ft

Following impact, the CTU bounced and rotated slightly in the air. The high speed video was reviewed and the impact was determined to be sufficiently flat. The justification for the determination was the large number of drops planned for the CTU, and that there were two more similar flat side drops. Also, data gathered during engineering test were consistent with the deformation exhibited from the CD1-1 drop.

There were minor visible exterior scratches resulting from the drop. The areas showing the greatest impact marks are at each end plate and near the three internal stiffening ribs. There was no significant bowing or other visible deformation. There was no visible deformation or rotation of the closure and the locking pins remained in the locked position. Figure 2.12.1-9 shows the CTU following the drop.

Upon inspection of the CTU the closure assembly was fully functional and able to be opened as illustrated in Figure 2.12.1-10. The FHE was removed and visually inspected as illustrated in Figure 2.12.1-11. There were no major deformations or cracked welds noticed. One of the spring plungers on the FHE lid was bent slightly but still functional.

As illustrated in Figure 2.12.1-12, there was no visible damage to the fuel element. The fuel element was not removed from the FHE but both end boxes were clearly visible and fully intact.

With the closure assembly removed from the body of the CTU, the locking pin was noticeably bent approximately 1/32 inch as illustrated in Figure 2.12.1-13. This locking pin was located near position number 8 identified in Figure 2.12.1-4. The other locking pin was not deformed and there was no other visible deformation of the closure assembly. It was noticed that the bent locking pin tended to bind when compressed to the open position.

2.12.1.4.1.3 CD2.A-1 – Flat Side, Index Lugs Down, HAC Drop

Following CD1-1, the FHE was reinserted with the hinged lid facing up towards the index lugs and then temporary rigging attachments were welded to the CTU to orient the package in the horizontal position with the index lugs facing down. The lifting eyes used in CD1-1 were removed and the index lugs re-installed with a 22 ft-lb torque applied to the screws. The drop configuration for CD2-1 was with the CTU in the horizontal position, with the index lugs facing down. Figure 2.12.1-14 illustrates the drop orientation. Initial conditions were as follows:

- Ambient temperature: 80°F
- Avg. surface temperature: 82°F
- Time: 2:59 p.m. 5/21/2007
- Drop height: 30 ft

Following impact, the CTU bounced and spun in the air about its longitudinal axis. After viewing the high speed video it was confirmed that the CTU impacted the drop pad at a slight angle on the longitudinal axis which caused the CTU to spin during the rebound. The index lugs did receive much of the impact but due to the angle it may not have been the worst case impact to the index lugs. There was visible exterior damage resulting from the drop at the index lugs. The index lugs were both pressed inward approximately 1/8 inch. There were no visible signs of broken welds.

The center of the package had an inward bow of about 1/16 inch. There was no other significant visible deformation. There was no visible rotation of the closure. Figure 2.12.1-15 and Figure 2.12.1-16 show the CTU following the drop. Following CD2.A-1 the closure could no longer be opened due to the body opening becoming slightly out-of-round. As illustrated in Figure 2.12.1-17, the body and closure assembly pinched in two locations.

The locking pin on the left side (near #8) of Figure 2.12.1-17 is shown stuck in the open – unlocked position. This happened during the inspection and not as a result of the drop. As the locking pins and closure assembly were inspected functionally by the test engineer, the one locking pin would bind in the open position and require a light tap from a hammer to become unstuck. The photo however, was taken before the locking pin was returned to the locked position.

2.12.1.4.2 CD2.B-1 – Flat Side, Index Lugs Down, HAC Drop

Following CD2.A-1, a second drop in the same orientation, package in the horizontal position with the index lugs facing down, was performed. The purpose of the re-test was to confirm the performance of the package in this orientation. It was felt that due to the slight incline of the package at impact, the maximum load on the index lugs was not experienced. Figure 2.12.1-18 illustrates the drop orientation which was rotated slightly to account for rotation during the drop. Initial conditions were as follows:

- Ambient temperature: 77°F
- Avg. surface temperature: 80°F
- Time: 4:07 p.m. 5/21/2007
- Drop height: 30 ft

During the drop the high speed video showed that the CTU rotated past the horizontal position in the air and impacted at an incline again. Furthermore, the rigging caught a gust of wind and blew to the side and caught the North stadia board. Following impact, the CTU bounced and spun in the air about the longitudinal axis indicating a non-flat impact. The index lugs were both pressed inward approximately 3/16 inch, at the greatest point, from the original surface of the tube. There were no visible signs of broken welds. The handle of the closure assembly broke loose at point #6 shown in Figure 2.12.1-4. The two screws both sheared off and the opposite side remained attached. There was no other significant visible deformation. There was no visible deformation or rotation of the closure and the locking pins remained in the locked position following the drop. During a functional test of the closure assembly the locking pins functioned well (with the locking pin near #8 binding in the open position) and the closure could rotate approximately ¼ inch. Figure 2.12.1-19 and Figure 2.12.1-20 show the CTU following the drop.

2.12.1.4.3 CD3-1 –Flat Side HAC Drop

The CTU was fitted with temporary rigging attachments for both CD3-1 and CD4-1 prior to chilling to minimize warming of the CTU prior to the drops. The CTU was removed from the chilling unit after 15 hours and 17 minutes with the average surface temperature reading -57°F, 14 minutes prior to CD3-1. Figure 2.12.1-21 shows the CTU in the chiller prior to removal. The CTU was oriented for a drop onto the long side with the pockets and index lugs oriented at 90° to the drop pad. The drop configuration was with the CTU's side parallel to the horizontal. Figure 2.12.1-22 illustrates the drop orientation. Initial conditions were as follows:

- Ambient temperature: 67°F
- Avg. surface temperature: +13°F
- Time: 9:31 a.m. 5/22/2007
- Drop height: 30 ft

Following impact, the CTU bounced slightly and came to rest in its standard position with the index lugs facing up. The impact side showed just minor scratches and impact marks from the drop. Figure 2.12.1-23 and Figure 2.12.1-24 show the CTU following the drop. The impact side showed a slight bowing of the ends. Using a straight edge, the maximum gap at each end was approximately 1/8 inch. There was no visible rotation of the closure and the locking pins remained in the locked position following the CD3-1 drop.

As illustrated in Figure 2.12.1-25, the closure assembly was functionally tested and upon close inspection it was found that the locking pin near point #4 (bottom of picture) had sheared off between the closure assembly and body preventing the locking pin from engaging in the body. The locking pin near point #8 was engaged following the drop but continued to bind in the open - unlocked position when depressed by hand. Figure 2.12.1-25 shows this locking pin in the open position following the attempt to open the closure. The closure assembly could partially rotate approximately ¼ inch but was unable to fully rotate to the open position. The locking pin near point #8 was returned to the locked position following the inspection. The dull gray color seen on the photographs is frost.

2.12.1.4.4 CD4-1 –CG Over Bottom End HAC Drop

Immediately after CD3-1, rigging was attached to the pre-welded lugs near the closure and the CTU prepared for the CD4-1 drop. The time between CD3-1 and CD4-1 was 33 minutes. During that time the CTU was kept elevated above the drop pad. The drop configuration was with the CTU in the vertical position, with the bottom end down (closure end up). Figure 2.12.1-26 illustrates the drop orientation. Initial conditions were as follows:

- Ambient temperature: 64°F
- Avg. surface temperature: 42°F
- Time: 10:04 a.m. 5/22/2007
- Drop height: 30 ft

Following impact the outer shell of the CTU exhibited minor bowing near the impact end with the greatest deformation measuring approximately 1/8 inch on the 90° side per Figure 2.12.1-4. The overall length of the package body was compared with the initial measurements at the eight locations and found to have compressed a maximum of approximately 1/8 inch. There was no visible deformation or rotation of the closure following the drop and the functionality of the closure assembly did not change. Figure 2.12.1-27 and Figure 2.12.1-28 show the CTU following the drop.

2.12.1.4.5 CP3-1 – Oblique, CTU Closure Over Puncture Bar

Following CD4-1 the CTU was positioned for an unscheduled puncture bar drop onto the closure. The purpose for this drop was to attempt to rotate the closure assembly prior to the CD5-1 drop which would severely deform the closure area of the body preventing any chance of

rotation. The temporary rigging attachments from CD3-1 and CD4-1 were removed and new attachments welded for this drop. The puncture bar, 36 inches in height, was welded to the drop pad. For CP3-1, the CTU was hoisted at a 28.3° orientation from horizontal and a 225° twist on the longitudinal axis so the puncture bar would impact one of the ribs in the closure assembly. The closure handle, which had broke off from one side during CD2.B-1, was bend outward to keep from interfering with the targeted impact location. Figure 2.12.1-29 and Figure 2.12.1-30 illustrate the drop orientation. Initial conditions were as follows:

- Ambient temperature: 72°F
- Avg. surface temperature: 73°F
- Time: 11:50 a.m. 5/22/2007
- Drop height: 40 inches

The puncture bar squarely impacted the closure rib and the CTU bounced away from the puncture bar onto the drop pad. Following the drop, the closure assembly rib exhibited minor deformations at the impact point made by the puncture bar. There was no rotation of the closure assembly and the locking pins showed no visible signs of deformation. The locking pin by #8 remained in the locked position. Both locking pins were functioning and able to be moved and compressed against the spring when tested by hand. Note that the locking pin by #4 was previously sheared during the CD3-1 drop. Figure 2.12.1-31 shows the CTU closure following CP3-1.

2.12.1.4.6 CD5-1 – CG Over Top Corner HAC Drop

For CD5-1, the CTU was hoisted in the same orientation as CN1 with the CG over the top corner; point #5 in Figure 2.12.1-4. The closure handle was removed for convenience since it was loose and obstructing the drops. Figure 2.12.1-32 illustrates the drop orientation. Initial conditions were as follows:

- Ambient temperature: 76°F
- Avg. surface temperature: 81°F
- Time: 1:54 p.m. 5/22/2007
- Drop height: 30 ft

Following impact, the CTU bounced slightly and tipped over onto its side. The impact corner was deformed in approximately 5/8 inch. There was modest deformation on the sides of the package near the impact location bulging in approximately 1/2 inch near the index lug pocket and bulged out approximately 5/8 inches on the adjoining side. The impacted corner deformed in approximately 5/8 inch and the opposite corner, #1, had no change in length. Figure 2.12.1-33 through Figure 2.12.1-36 show the CTU following CD5-1.

Following the drop, the closure assembly exhibited deformation with the end of the package and was unable to be rotated more than 1/8 inch in either direction. The locking pins showed no visible signs of deformation and the pin by #8 remained in the locked position. Both locking pins were functioning and able to be moved and compressed against the spring when tested by hand.

2.12.1.4.7 CD2.C-1 – Flat Side, Index Lugs Down, HAC Drop

Following CD5-1 a third drop in the same CD2 orientation, package in the horizontal position with the index lugs facing down, was performed. The purpose of third re-test was to confirm the performance of the package in this orientation. It was felt that due to the incline of the package at impact during the previous drops, the maximum load on the index lugs was not experienced. Both the release mechanism and rigging cables were changed to aid the drop. Figure 2.12.1-37 illustrates the drop orientation. Initial conditions were as follows:

- Ambient temperature: 79°F
- Avg. surface temperature: 79°F
- Time: 2:37 p.m. 5/22/2007
- Drop height: 30 ft

The third try produced a satisfactory drop orientation. Following impact, the CTU bounced and spun just slightly indicating the impact was directly on the index lugs. The index lugs were both pressed inward. The index lug at the closure end was flush with the general surface. The index lug at the bottom end was pushed in to approximately 1/8 inch from the general surface. Figure 2.12.1-38 and Figure 2.12.1-39 show the index lugs following the drop. The index lugs were removed and a cracked weld was revealed under the index lug near the closure end as shown in Figure 2.12.1-40. The length of the cracked weld was approximately 1/2 inch. There was no other significant visible deformation. There was no visible deformation or rotation of the closure as a result of the drop.

2.12.1.4.8 CP2-1 – CG Over Side, 30° Oblique, HAC Puncture Drop

For CP2-1, the CTU was hoisted at a 30° oblique angle with the CG over the edge of the puncture bar. Figure 2.12.1-41 illustrates the drop orientation. Initial conditions were as follows:

- Ambient temperature: 76°F
- Avg. surface temperature: 77°F
- Time: 3:19 p.m. 5/22/2007
- Drop height: 40 inches

As the CTU impacted the puncture bar, there was no tearing or severe deformation. The initial impact caused a deformation of approximately 1/2 inch deep by 5 inches across with a radius the same as the puncture bar. There was no fracture of the outer shell. Figure 2.12.1-42 and Figure 2.12.1-43 show the CTU following the CP2-1 drop.

2.12.1.4.9 CP1-1 – CG Over Center of Closure HAC Puncture Drop

For CP1-1, the CTU was hoisted in the vertical orientation with the closure directly over the puncture bar. Figure 2.12.1-44 illustrates the drop orientation. Initial conditions were as follows:

- Ambient temperature: 79°F
- Avg. surface temperature: 81°F
- Time: 4:06 p.m. 5/22/2007

- Drop height: 40 inches

Following impact, the CTU bounced slightly on the puncture bar, as verified by high speed video, and came to rest in the vertical position on top of the puncture bar as seen in Figure 2.12.1-45. Following the drop, the tamper indicating device (TID) post was deformed into the closure. The closure assembly exhibited minor scratches from the puncture bar. The locking pins showed no visible signs of deformation and the remaining locking pin by #8 remained in the locked position. Both locking pins were functioning and able to be moved and compressed against the spring when tested by hand. Figure 2.12.1-46 shows the CTU in the up-side-down position following CP1-1. Note that both locking pins were binding somewhat following testing and shown in the photographs in the open – unlocked position following the functional tests.

2.12.1.5 Post-test Disassembly and Inspection

The final acceptance criteria for the ATR FFSC package lies with the criticality and thermal evaluations. Any increase in reactivity of the contents resulting from the certification tests must not exceed the allowable as defined in the criticality evaluation. The inspections required to support determination of compliance with the acceptance criteria are identified as follows:

- Inspect the outer shell to verify the thermal performance of the package is unimpaired by the free drop and puncture events. The thermal analysis assumes that the outer shell is intact such that there is no significant communication between the environment and the outer/inner shell annular space during the thermal event.
- Inspect the insulation to verify compliance with the assumptions of the thermal analysis.
- Inspect the overall package to verify that the package geometry remains within the criticality analyses assumptions.
- Inspect the Mark VII fuel element to verify that the fuel geometry remains within the assumptions of the criticality analyses.

Any deviation of the test results from these acceptance criteria must be reconciled with the criticality or thermal evaluations.

2.12.1.5.1 CTU Inspection

Radiological surveys were performed after each drop test and during the disassembly of the package. The radiological survey reports confirm that there was no loss or dispersal of radioactive material from the package or from the ATR fuel element.

The ATR fuel element CTU was disassembled and inspected on May 23, 2007. Prior to disassembly the exterior dimensions were recorded for comparison to the pre-test condition. Table 2.12.1-4 lists the measured dimensions and Figure 2.12.1-4 identifies the location of the identified measurements.

The closure handle was flattened, loosened, and finally removed during testing for convenience. Due to the relatively weak nature of the handle, its presence or absence had no significant effect on any test outcome. The height of the handle changed from 1 3/8 inches to 1/2 inch on one side before being removed. There was very little bowing or change in shape of the package. The maximum

bowing of the package over its length is estimated at approximately $\frac{1}{4}$ inch. During the CD5-1, CG over corner HAC drop, deformation of the outer wall caused the width of the package to increase from 8 inches to approximately $8 \frac{5}{8}$ inches. The same CD5-1 impact caused the outer wall to deform inward approximately $\frac{1}{2}$ inch.

The CTU was disassembled systematically by cutting away the outer layers of the packaging using an abrasive saw. The destructive examination was necessary due to the deformation of the closure and the need to inspect the interior insulation. Figure 2.12.1-47 illustrates the unsuccessful attempt to rotate the closure assembly and open the package with a steel bar and 5 lb hammer. The closure could not be rotated more than approximately $\frac{3}{8}$ inch using the bar and hammer.

The package was cut with an abrasive saw lengthwise along two opposite corners and at the ends to expose the thermal shield. Figure 2.12.1-48 through Figure 2.12.1-50 show the condition of the thermal shields and insulation. The thermal shields were in relatively good shape with dents from both the index lug bosses and pockets on the shields. There was also some minor deformation at each end of the shields by the stiffening rib plates.

The insulation tended to compact towards the closure end except for the bottom end which compacted towards the bottom. The compaction was not uniform but varied around the circumference of the internal pipe. The maximum compaction for all section ranged from $1\text{-}\frac{1}{8}$ inches to $1\text{-}\frac{1}{2}$ inches.

Two thermal shield designs were used; one with a simple overlapping design and the other secured by rivets. There was no appreciable difference between the performance of either design. Both experienced minor deformation at the pockets and index lugs, and at the ends due to impacting the adjoining plates. Furthermore, the compaction of the insulation under each shield was very similar. On the riveted design, there was no failure of any rivet.

The thermal shields and insulation were removed and using an abrasive saw the bottom end plate was removed by cutting the inner tube. Figure 2.12.1-51 illustrates the condition of the bottom end plate. There were no large deformations or punctures of the stainless steel plate. There were no visual indications of broken welds or other damage near the end plate.

As shown in Figure 2.12.1-52 and Figure 2.12.1-53, the inner tube was inspected and the photographs show the areas of greatest deformation. Due to the CG over corner drop deformation, CD5-1, the inner tube bowed out approximately $\frac{1}{4}$ inch. The inner tube also bowed inward approximately $\frac{3}{16}$ inch slightly deforming the FHE aluminum end plate. There were no visible signs of any weld failures associated with the inner tube.

Figure 2.12.1-54 illustrates the relatively unchanged position of the FHE and fuel element within the CTU. Also seen in this figure are pieces of the broken end box at the bottom end and also pieces of neoprene padding from the FHE during removal. The FHE was somewhat difficult to remove and the aluminum end plate had broken off so the ATR fuel element was carefully pulled from the bottom end of the package as illustrated in Figure 2.12.1-55. Both end boxes of the fuel element had shattered into several pieces. These pieces were collected and kept with the fuel element. There were no pieces of the fuel element end boxes found outside the FHE. Once the fuel element was removed, the FHE was pulled from the inner tube. The welds securing each FHE end plate to the body were completely broken and both the end plates were loose. Figure 2.12.1-56 illustrates the area of greatest deformation to the FHE which was at the closure end.

2.12.1.5.2 ATR Fuel Element Inspection

The ATR fuel element was placed on an inspection table and compared against the same pre-test measurements for the fuel plates. Because the fuel element end boxes had shattered and bent the ends of the side plates, some of the fuel plate measurements taken from the side plates could be slightly exaggerated. The measurements included side plate flatness, in plane bending of the side plates, side plate spacing, overall fuel plate spacing, and fuel plate to fuel plate spacing. Table 2.12.1-5 provides the general change in dimensions to the fuel plates. Measurements were generally taken at five locations along the length of the fuel element. The five locations include 1 inch from the end of the fuel plate (neglecting the end boxes), 12 inches from each end of the fuel plate, and at the center of the fuel plate.

Figure 2.12.1-57 through Figure 2.12.1-62 illustrate the condition of the ATR fuel element. As shown in Figure 2.12.1-58 and Figure 2.12.1-59, fragments from the fuel element end boxes deformed and cut into the ends of the fuel plates during testing. At no point did the fuel meat, the embedded uranium within the aluminum cladding, become exposed.

In conclusion, the CTU satisfied the acceptance criteria of preventing loss or dispersal of the contents, the outer shell remained intact, the insulation remained within the assumptions of the thermal analysis, and the package and fuel geometry remained greatly unchanged. The deformations of the package and condition of the ATR fuel element were evaluated against the criticality and thermal evaluations and determined to be within the bounds of the assumptions and conditions used to ensure safety.

Table 2.12.1-1 - Component Weights

Component	Weight (lbs)
Body Assembly	225.0
Closure Assembly	9.0
Fuel Handling Enclosure	14.3
ATR Fuel Element	22.1
Package (fully loaded)	270.4

Table 2.12.1-2 - Instrumentation for Drop Tests

Item Description	Model	Serial Number	Calibration Due Date	Comments
Drop Height Indicators	N/A	N/A	N/A	String plumb bobs made specifically for this testing. The length was established using a metal tape measure.
Tape Measure	Stanley	N/A	N/A	35-ft. steel tape
Digital Level 2'	M-D Building Products	SNL 3665	1/23/09	Used to identify CTU orientation
Digital Level 4'	M-D Building Products	SNL 3666	1/23/09	Used to identify CTU orientation
Scale	NCI	D798311	2/12/08	Used to measure weights of CTU components
Hook Scale	Dively	60418/46180	Aug 2007	Used to measure the weight of the ATR FFSC body
Multilogger Thermometer	Omega Engineering	06000855	10/19/07	Handheld temperature reader for measuring ambient temperature and CTU surface temperature
Temperature Probe	N/A	56194	10/19/07	Probe which attaches to multimeter
Torque Wrench 0-25 ft-lbs	N/A	SNL 1933	2/26/09	Used to apply measured torque to index lug screws

Table 2.12.1.3 - Summary of Testing

Test No.	Test Description	Comments
CN1-1	CG over top corner	CG over top corner drop from 4 ft. Minor deformation at impact corner. Maximum change in length approximately 1/8 inch at impact point only. Closure handle deformed. Closure functions properly.
CD1-1	Flat side drop, pocket side down	Flat side drop from 30 ft. Minor visible scratches and impact marks. Closure functions properly. Package opened and inspected. One locking pin on closure bent slightly but still operable. No visible damage to fuel element.
CD2.A-1	Flat side drop, index lugs facing down	Flat side drop from 30 ft. Impact pushed index lugs into package approximately 1/8 inch. CTU impact was not level on the longitudinal axis causing the package to bounce and spin after impact. A second drop in the same orientation was chosen.
CD2.B-1	Flat side drop, index lugs facing down	Flat side drop from 30 ft. Impact pushed index lugs into package approximately 3/16 inch. CTU impact again was not level due to a gust of wind blowing the rigging straps into the stadia board.
CD3-1	Flat side drop, pockets and index lugs on side, reduced temperature	Flat side drop from 30 ft. Minor visible scratches and impact marks. One locking pin sheared during impact. No rotation of closure. Surface temperature approximately 13°F.
CD4-1	CG over bottom end (vertical), reduced temperature	Flat bottom drop from 30 ft. No appreciable deformation on impact side but minor bowing outward on side near impact end. Maximum change in length approximately 1/8 inch. Surface temperature approximately 41°F.
CP3-1	Closure assembly over puncture bar	Unscheduled drop chosen to ensure performance of closure assembly due to broken locking pin from CD3. Impact caused small deformation to closure assembly rib. There was no rotation of the closure and no other visible damage.
CD5-1	CG over top corner (same orientation as CN1)	CG over top corner drop from 30 ft. Deformation of the corner, including adjoining sides, and minor bending of the closure assembly. Maximum change in length at impact point approximately 5/8 inches.
CD2.C-1	Flat side drop, index lugs facing down	Flat side drop from 30 ft. This third drop on the index lugs was chosen to ensure performance of the outer skin and index lugs in this orientation. The previous two drops did not impact flat on the lugs. Index lug at closure end pushed in flush with general package surface, approximately 1/2 inch. A small crack in the weld between the index lug boss and square tube was recorded.
CP2-1	CG over side, 30° oblique	CG over side puncture drop from 40 in. Minor deformation from impact. Depth of impact approximately 1/2 inch. Width of impact approximately 5" across.

Table 2.12.1.3 - Summary of Testing

Test No.	Test Description	Comments
CP1-1	CG over center of closure (Vertical)	Vertical puncture drop on closure from 40 in.. The tamper indicating device stud pushed into closure assembly. No other visible damage. No rotation of closure assembly.

Table 2.12.1-4 – Package Length Measurements

Test ID	1	2	3	4	5	6	7	8
Pre-Test (in.)	72 ½	72 ½	72 ½	72 ½	72 ½	72 ½	72 ½	72 ½
Post-Test (in.)	72 5/16*	72 ½	72 7/16	72 ¼	71 11/16*	72 ¼	72 ½	72 7/16

*These locations were modified slightly due to the welding and removal of temporary rigging attachments. The change to position #5 was approximately -1/16 inch. There was approximately no change to position #1.

Table 2.12.1-5 - ATR Fuel Element Measurements

Measurement Area	Pre-Test Range (in)	Post-Test Range (in)
Side Plate Flatness	±0.010	±0.075
In-Plane Bending of Side Plates	±0.011	±0.025
Side Plate Spacing - Top	4.113 – 4.130	4.015 – 4.131
Side Plate Spacing - Bottom	1.840 – 1.845	1.837 – 1.845
Height of Top Fuel Plate from Table (top side up)	2.675 – 2.691	2.655 – 2.785
Height of Bottom Fuel Plate from Table (bottom side up)	2.500 – 2.540	2.415 – 2.508
Fuel Plate to Fuel Plate Spacing	0.075 to 0.080	0.023 to 0.098*

* The minimum and maximum fuel plate spacing were in localized areas near the side vents and not representative of the general spacing.

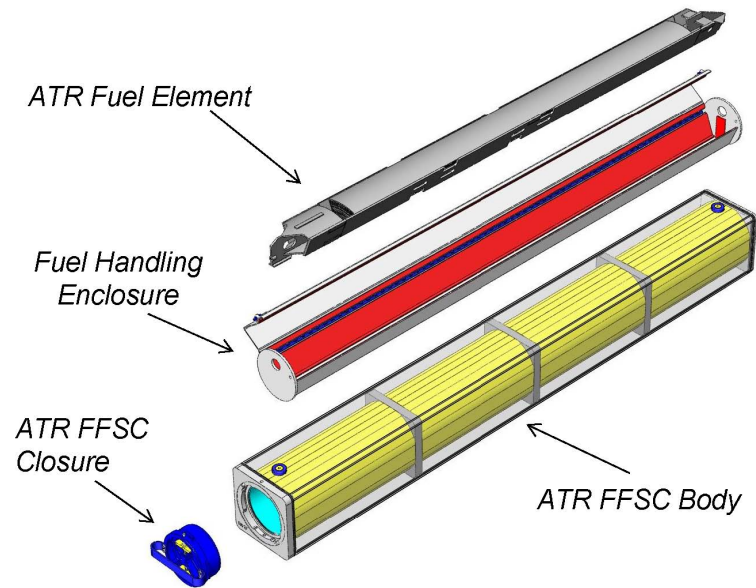


Figure 2.12.1-1 - ATR FFSC



Figure 2.12.1-2 – ATR Fuel Element



Figure 2.12.1-3 – Chilling Unit

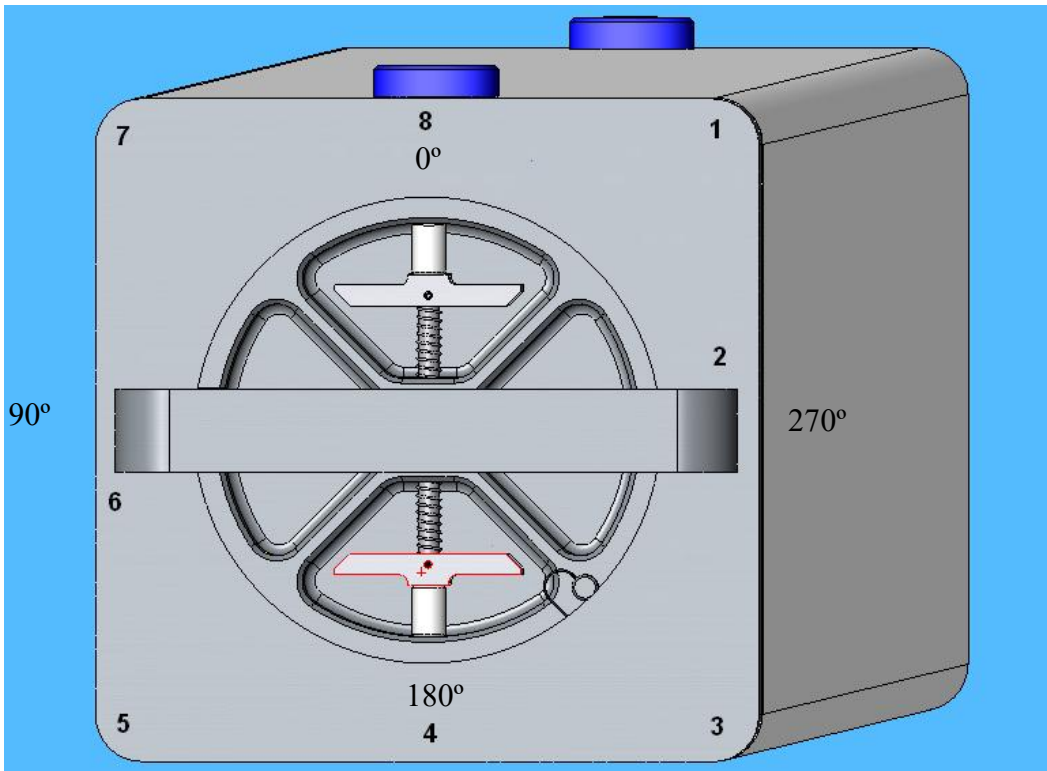


Figure 2.12.1-4 – ATR Package Orientation Markings



Figure 2.12.1-5 - CN1-1 Drop Orientation

Impact
corner



Figure 2.12.1-6 - CN1-1 Impact Damage



Figure 2.12.1-7 - CN1-1 Impact on Closure Handle

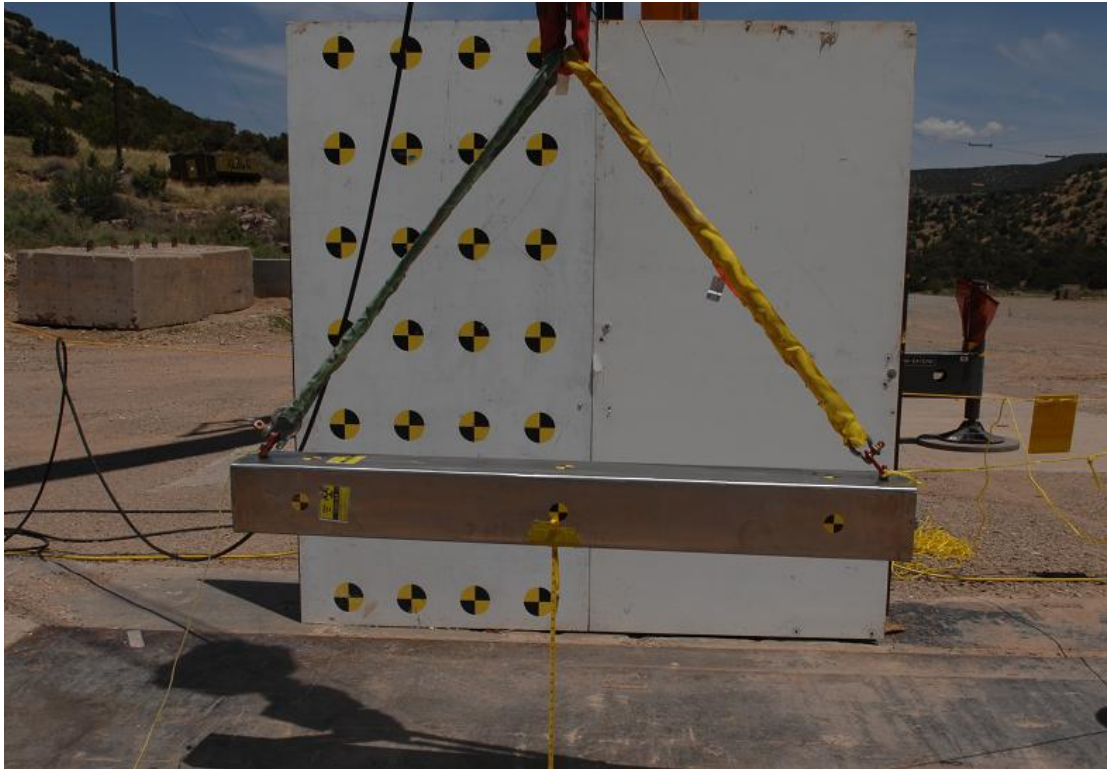


Figure 2.12.1-8 – CD1-1 Drop Orientation

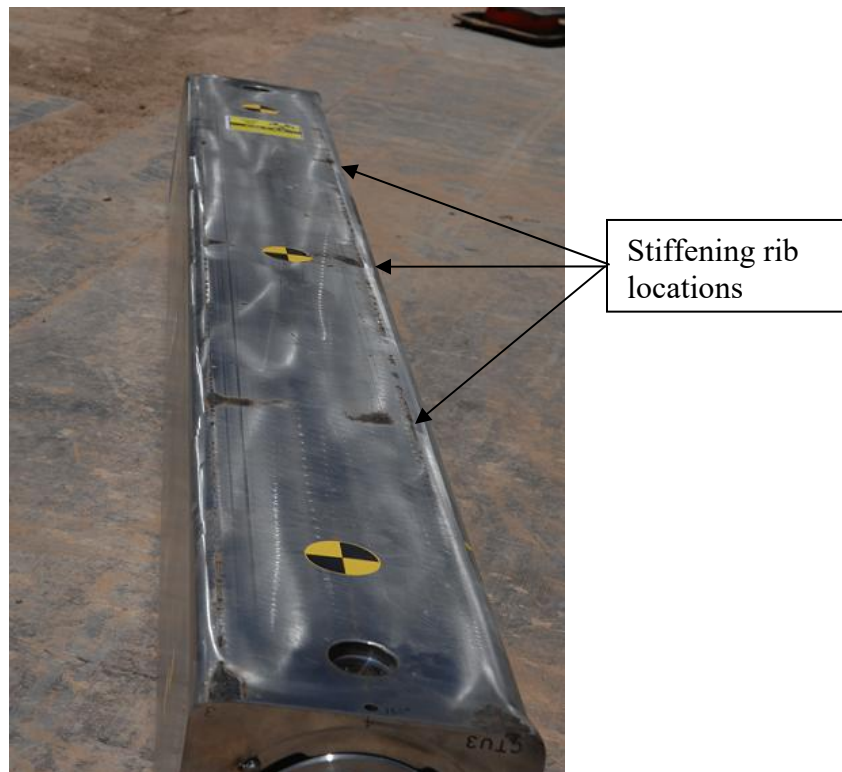


Figure 2.12.1-9 – CD1-1 Impact Side



Figure 2.12.1-10 - Opening of CTU Following CD1-1



Figure 2.12.1-11 - Inspection of Payload Following CD1-1



Figure 2.12.1-12 - Inspection of Fuel Element Following CD1-1



Figure 2.12.1-13 - Inspection of Closure Assembly Following CD1-1



Figure 2.12.1-14 – CD2.A-1

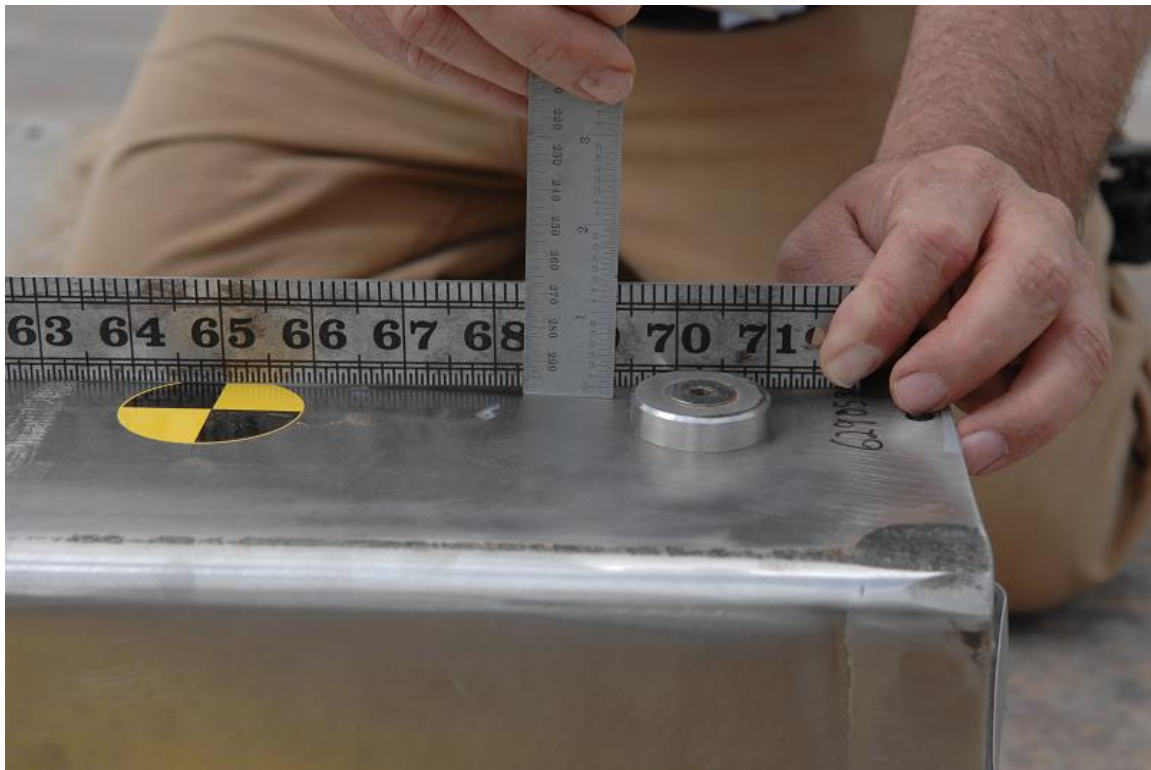


Figure 2.12.1-15 - Index Lug Near Closure End, CD2.A-1

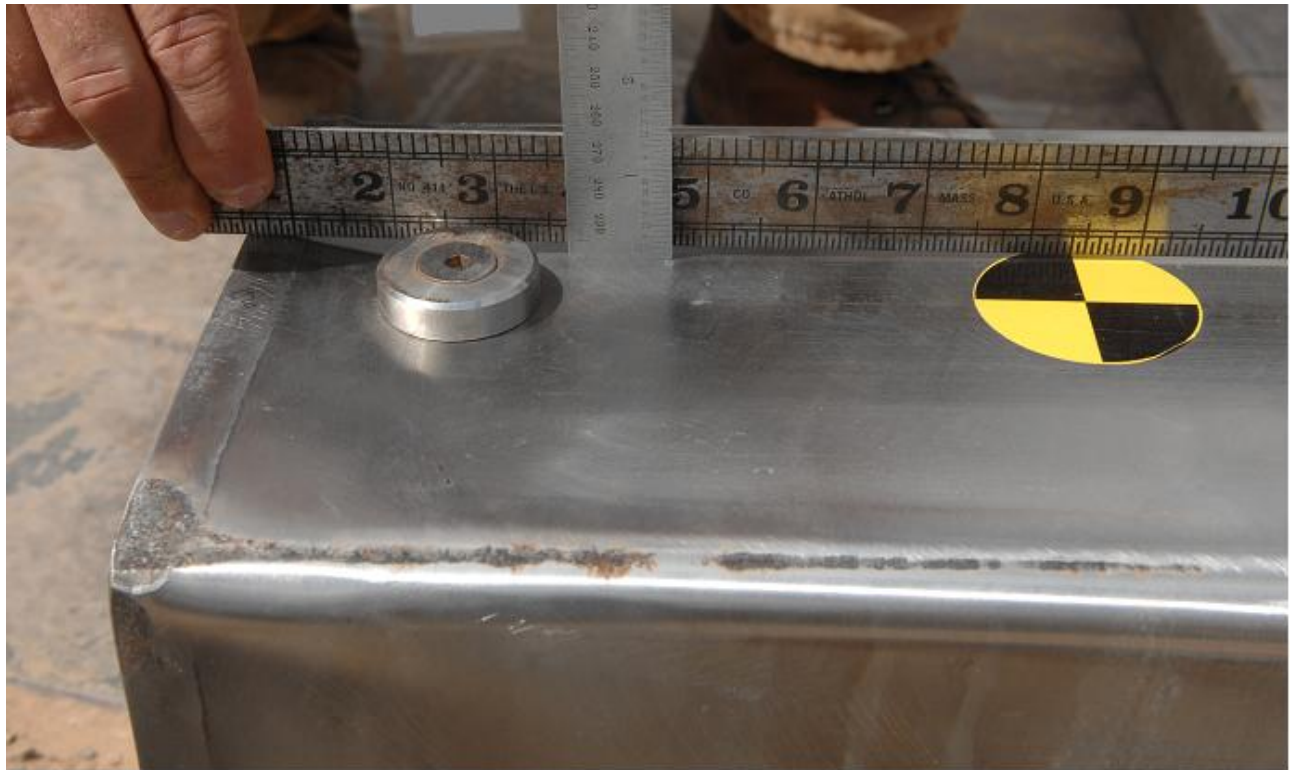


Figure 2.12.1-16 - Index Lug Near Bottom End, CD2.A-1

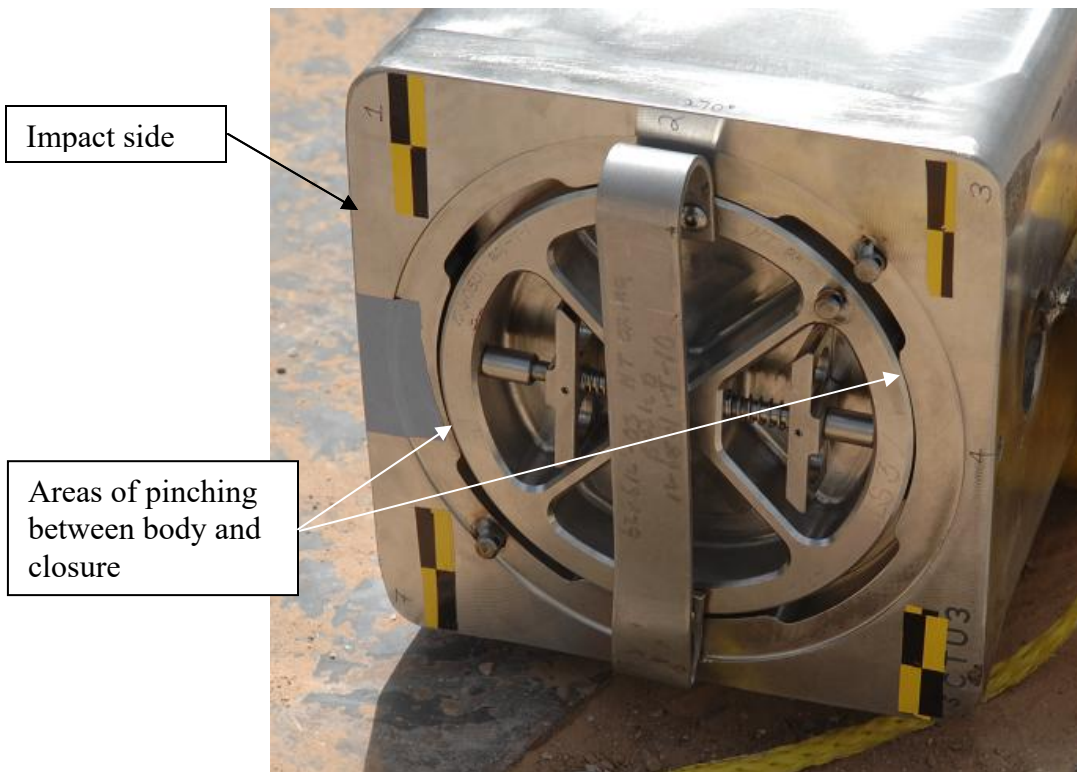


Figure 2.12.1-17 - View of Closure Following CD2.A-1



Figure 2.12.1-18 - CD2.B-1 Drop Orientation



Figure 2.12.1-19 - CTU Position Following CD2.B-1 Drop



Figure 2.12.1-20 - Index Lug Near Bottom End, CD2.B-1



Figure 2.12.1-21 - CTU in Chiller Unit



Figure 2.12.1-22 - CD3-1 Drop Orientation

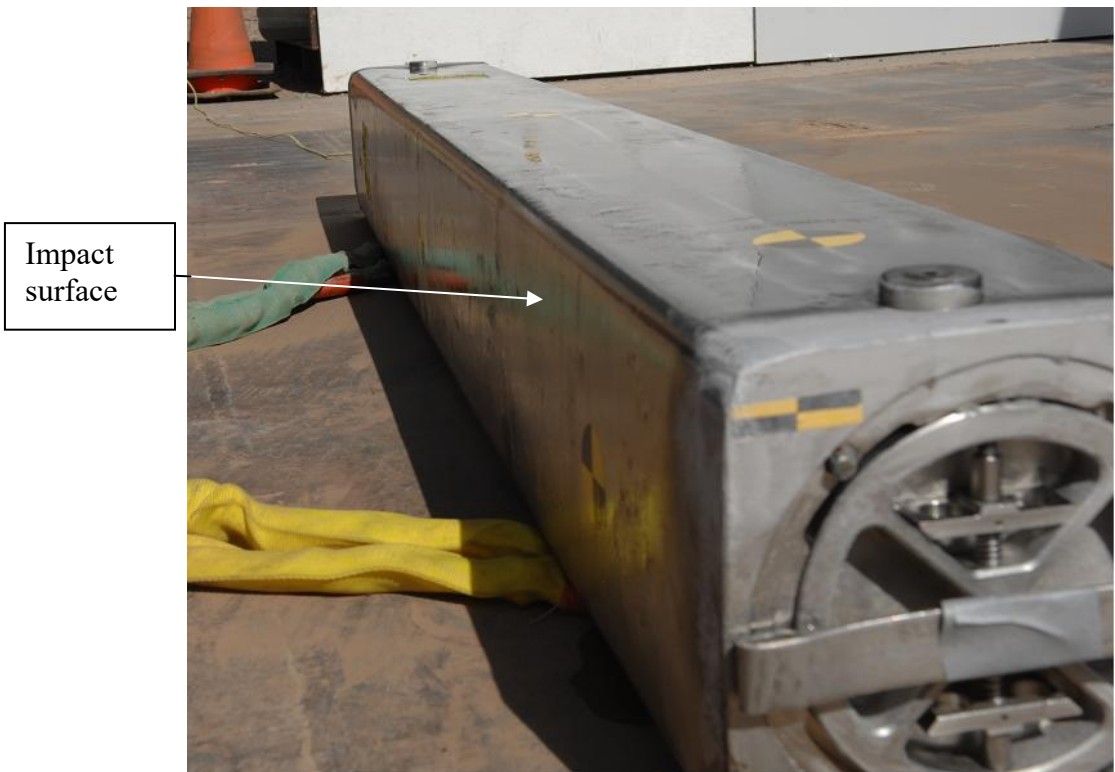


Figure 2.12.1-23 - CTU Following CD3-1 Impact



Figure 2.12.1-24 - Deformation Near Closure End Following CD3-1

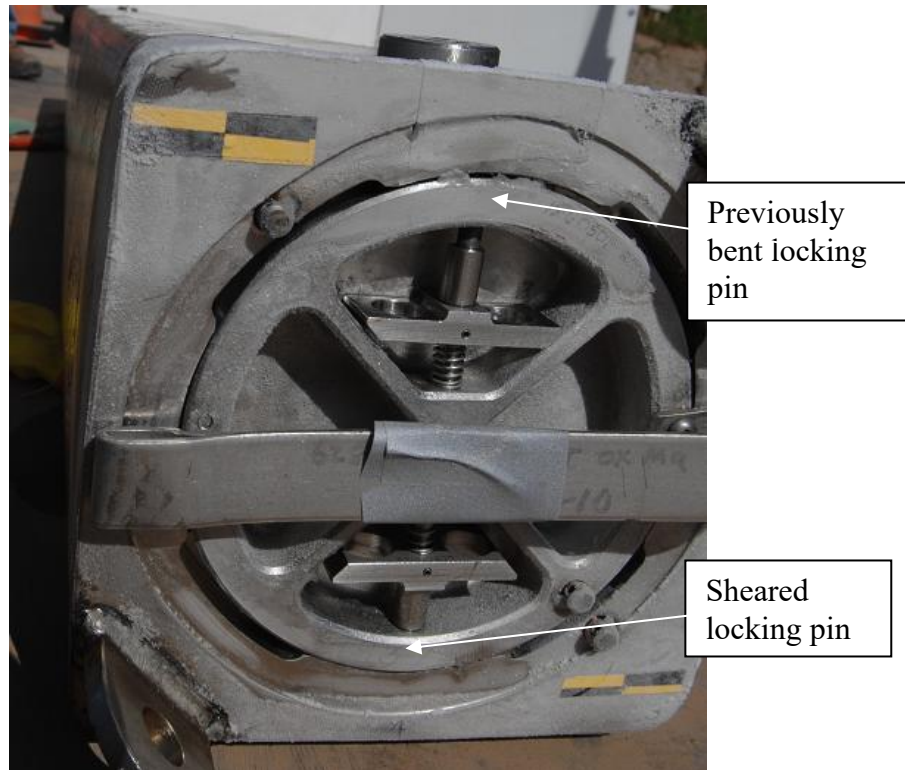


Figure 2.12.1-25 - View of Closure Following CD3-1



Figure 2.12.1-26 - CD4-1 Drop Orientation



Figure 2.12.1-27 - View of Impact End Following CD4-1



Figure 2.12.1-28 - View of Side Bowing Following CD4-1

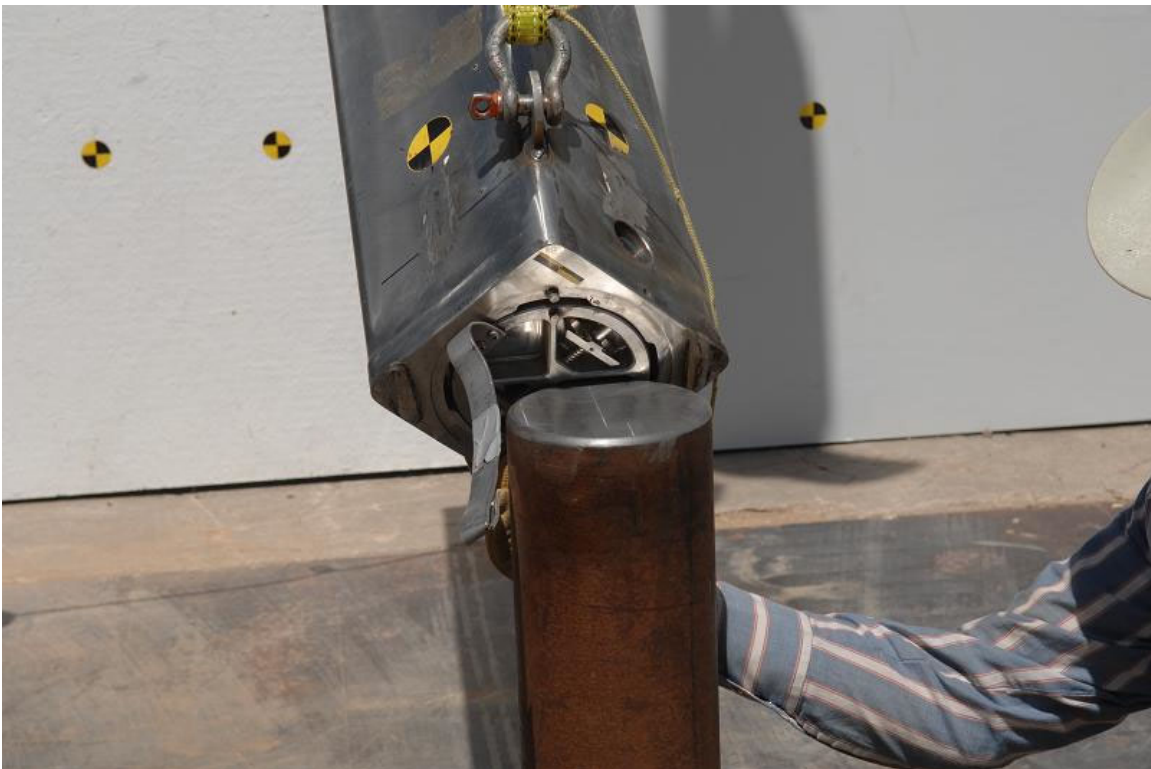


Figure 2.12.1-29 - CP3-1 Drop Orientation – Front

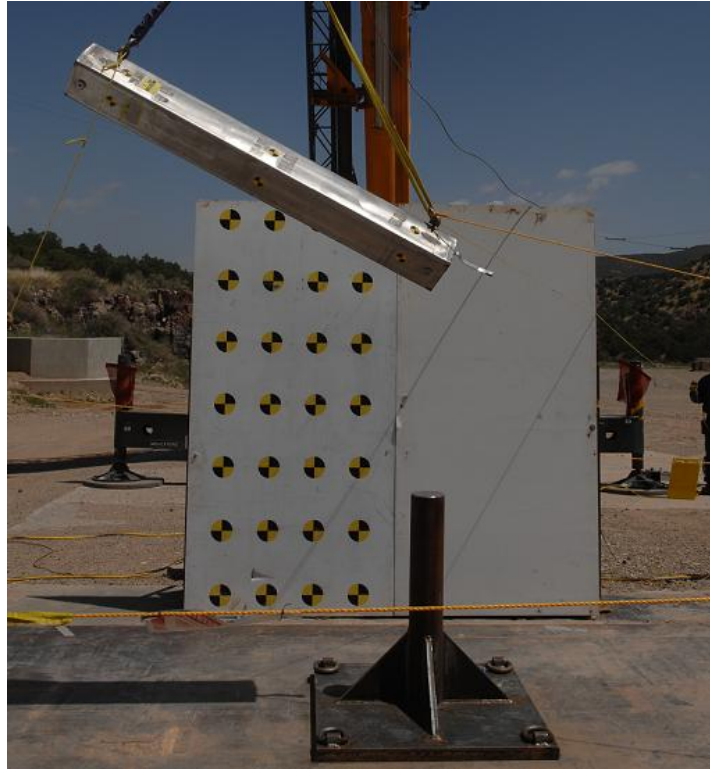


Figure 2.12.1-30 - CP3-1 Drop Orientation – Front

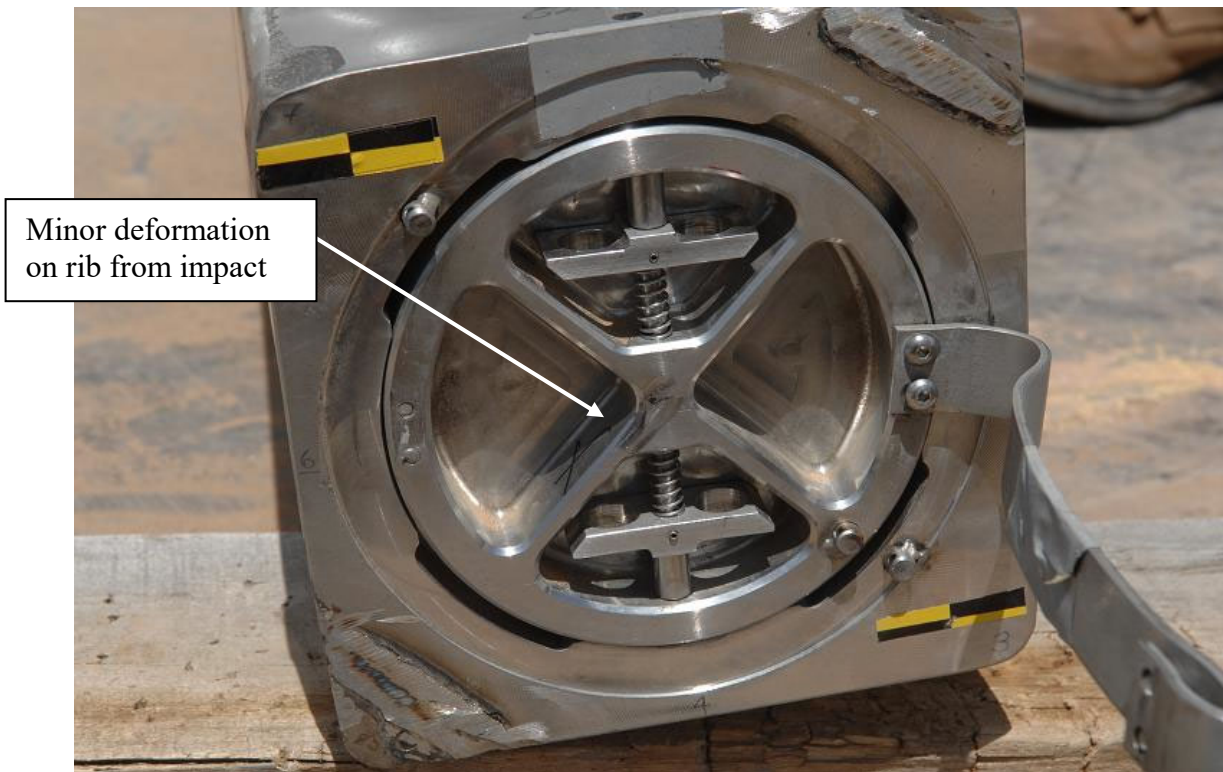


Figure 2.12.1-31 - CTU Following CP3-1 Impact



Figure 2.12.1-32 - CD5-1 Drop Orientation

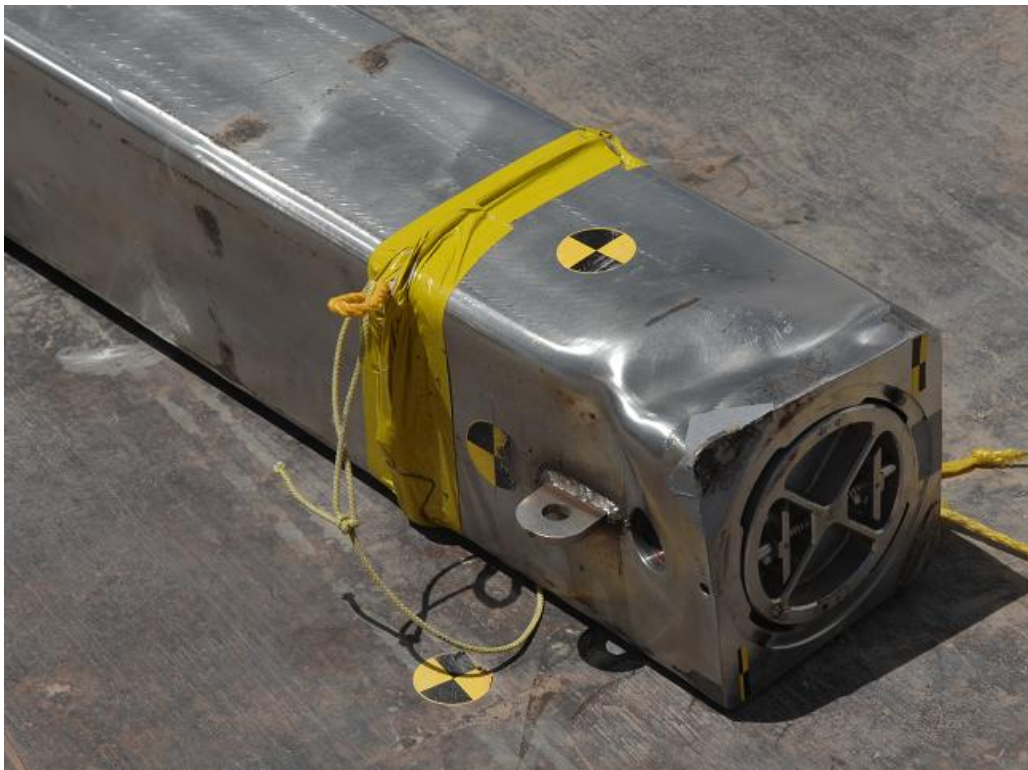


Figure 2.12.1-33 - CTU Following CD5-1 Impact



Figure 2.12.1-34 - CD5-1 Impact Damage on Bottom 180° Side



Figure 2.12.1-35 - CD5-1 Impact Damage on Closure End



Figure 2.12.1-36 - CD5-1 Impact Damage on Closure Area



Figure 2.12.1-37 - CD2.C-1 Drop Orientation



Figure 2.12.1-38 - Side View of CTU Following CD2.C-1 Drop

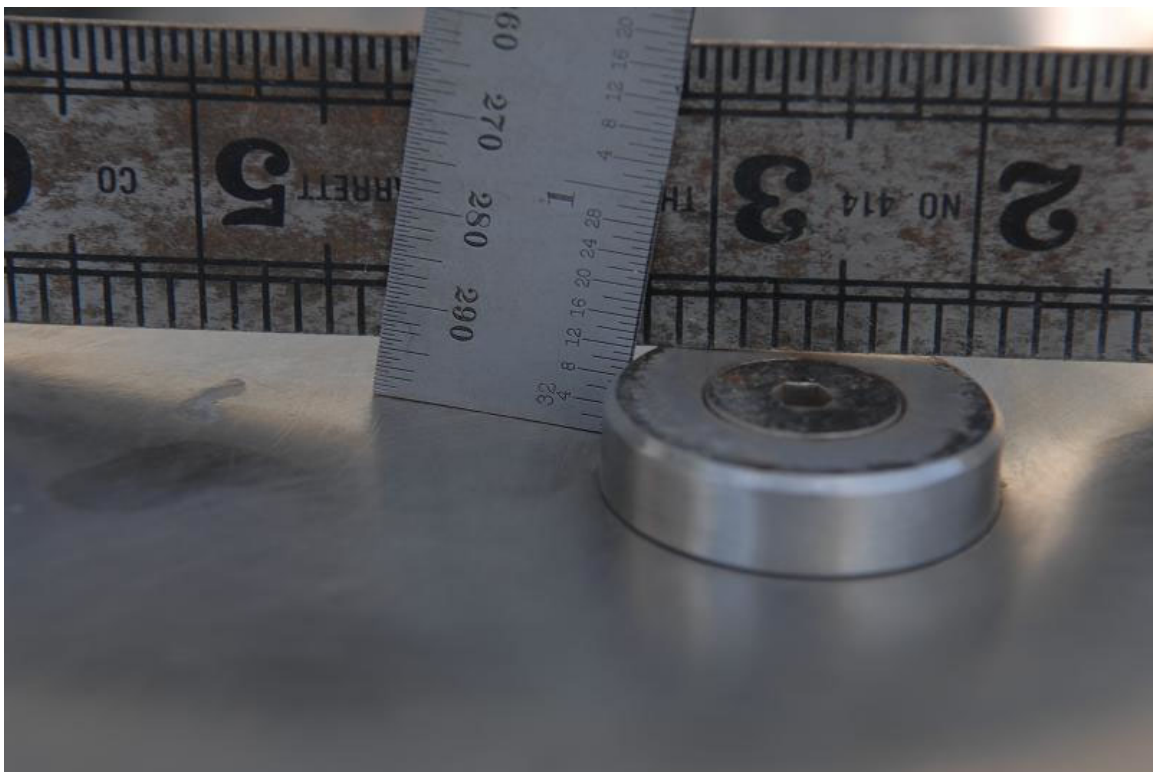


Figure 2.12.1-39 - Index Lug Near Closure End, CD2.C-1

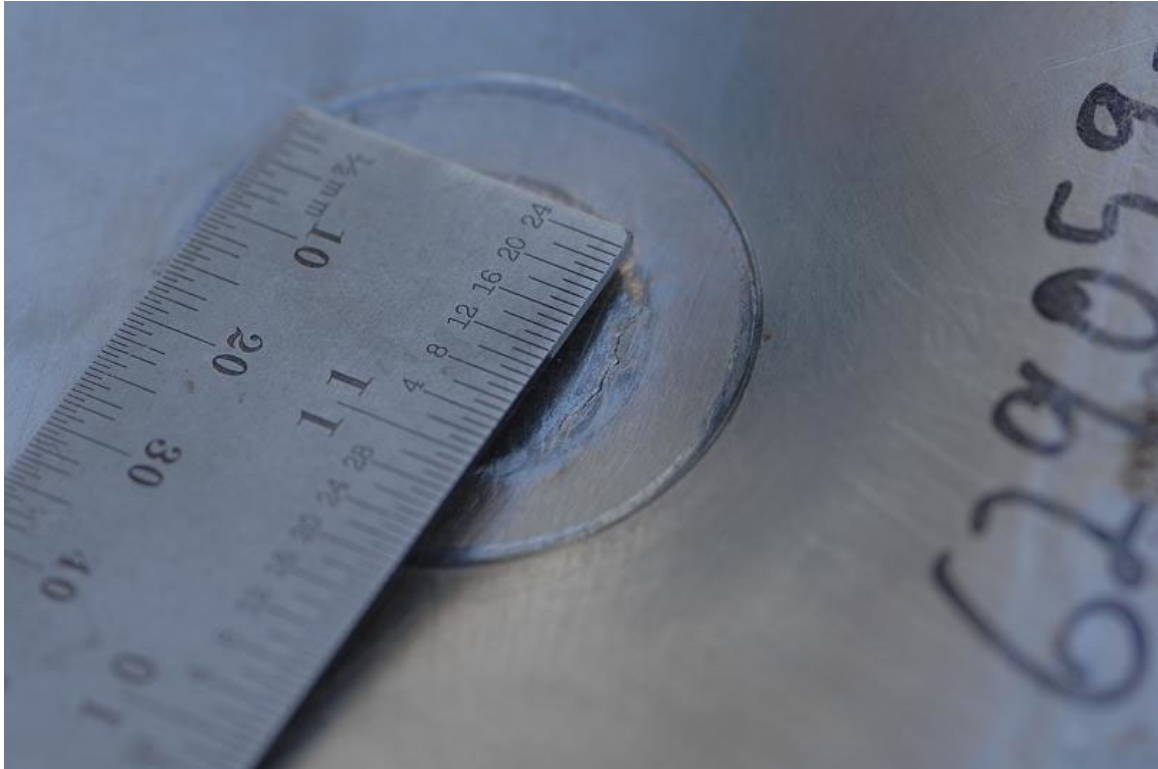


Figure 2.12.1-40 - Cracked Weld Under Index Lug, CD2.C-1



Figure 2.12.1-41 - CP2-1 Drop Orientation

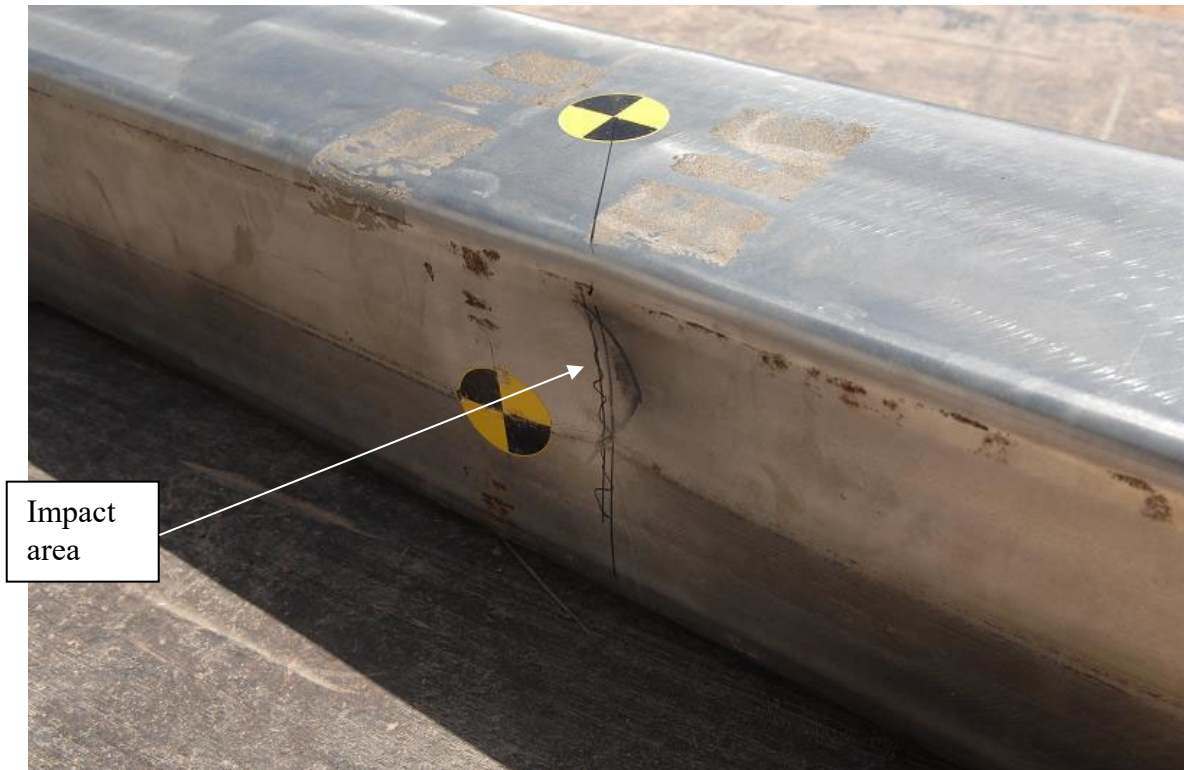


Figure 2.12.1-42 - CTU Following CP2-1 Impact

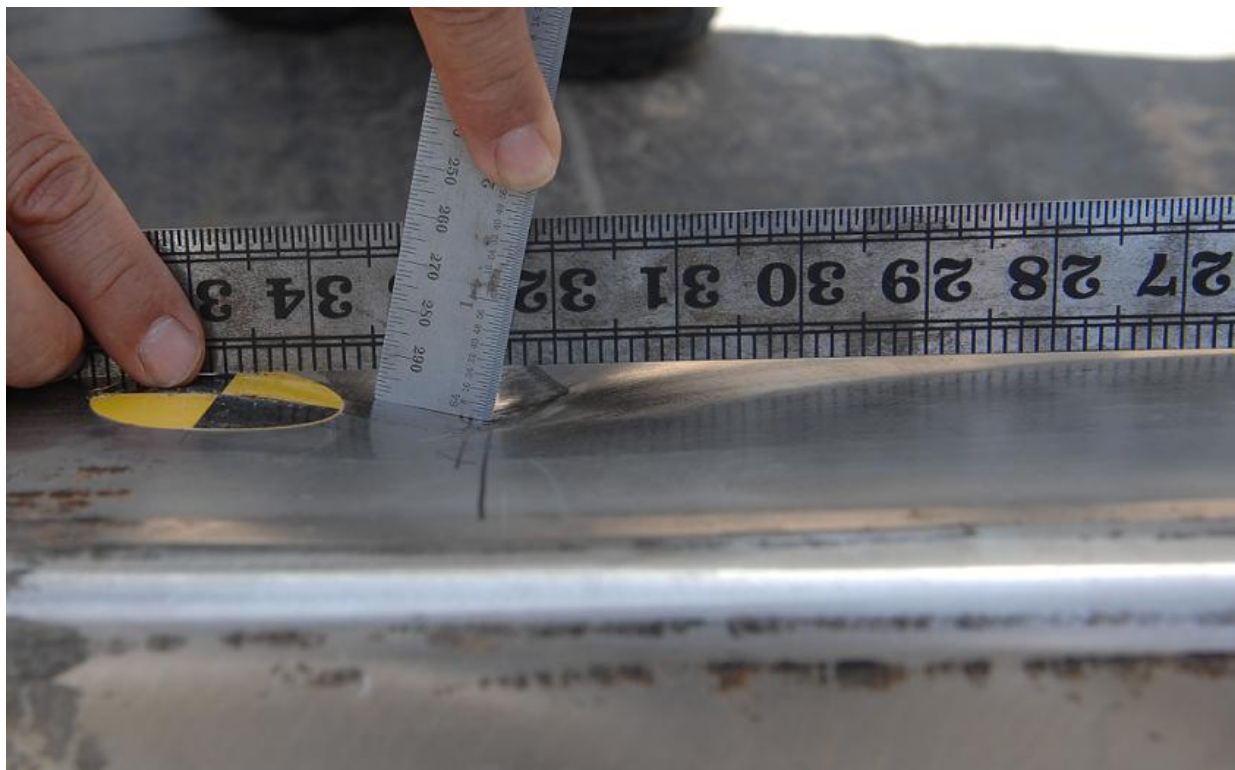


Figure 2.12.1-43 - CP2-1 Impact Damage



Figure 2.12.1-44 - CP1-1 Drop Orientation



Figure 2.12.1-45 - CTU Following CP1-1 Impact



Figure 2.12.1-46 - CP1-1 Impact Damage (Shown Index Lugs Down)



Figure 2.12.1-47 - Attempted Closure Removal



Figure 2.12.1-48 - Exposure of Thermal Shield



Figure 2.12.1-49 - Insulation After Removal of Thermal Shield



Figure 2.12.1-50 - Middle Insulation After Removal of Thermal Shield



Figure 2.12.1-51 - Bottom End Plate Condition



Figure 2.12.1-52 - View of Inner Tube at Closure End



Figure 2.12.1-53 - Inner Tube Deformation at Closure End

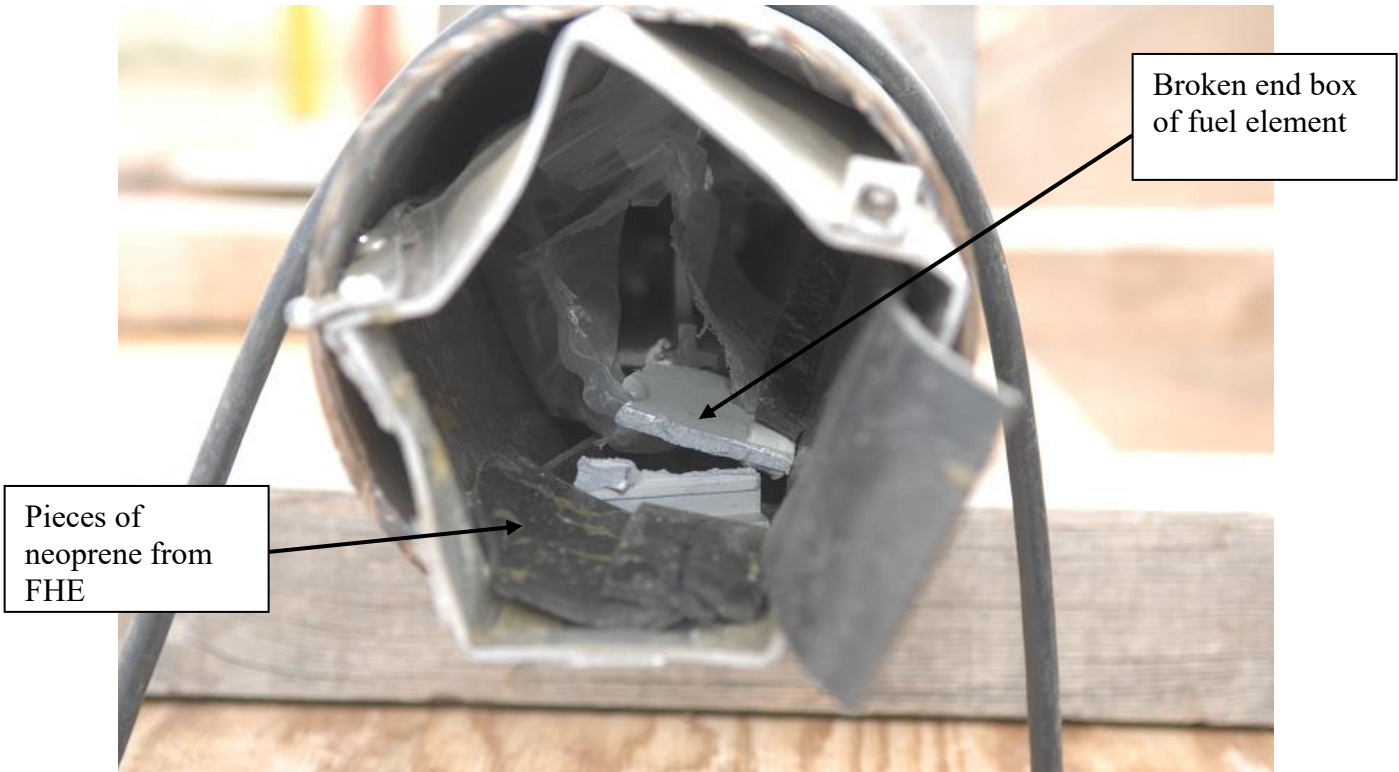


Figure 2.12.1-54 - End View (Bottom) of Opened CTU



Figure 2.12.1-55 - Removal of ATR Fuel Element

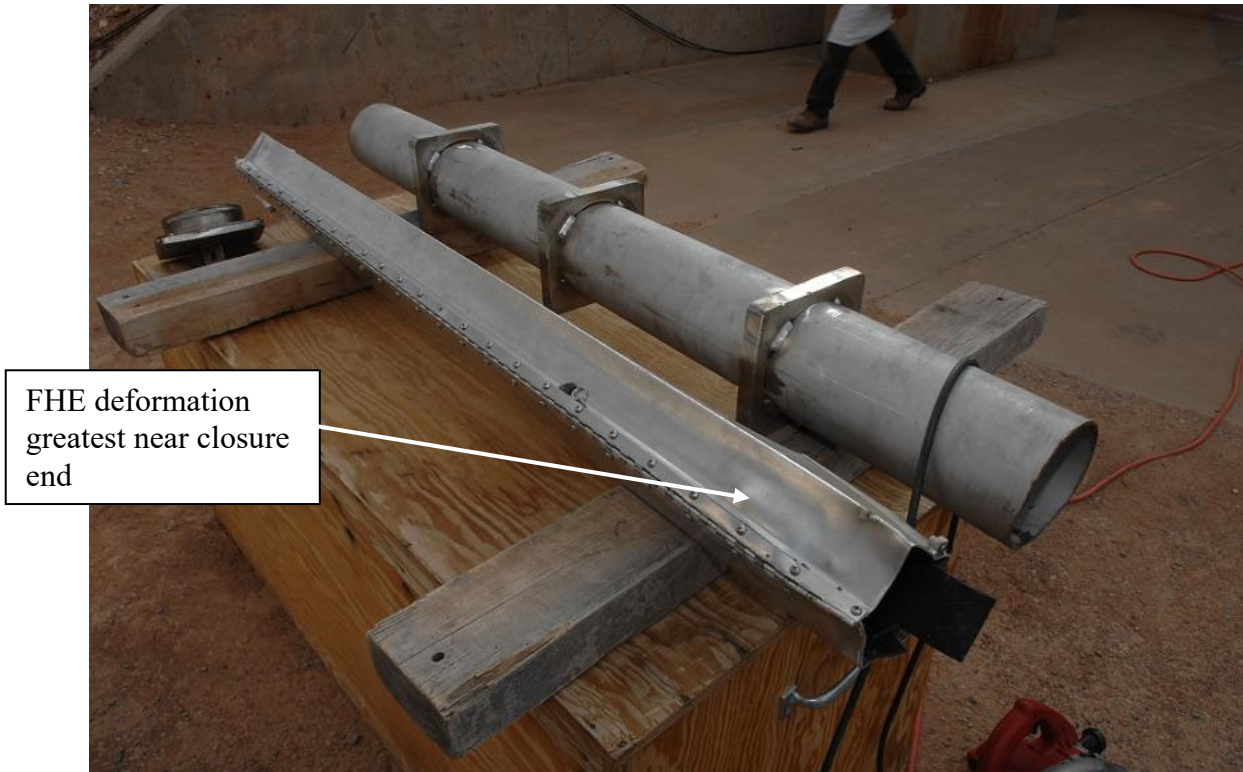


Figure 2.12.1-56 - Fuel Handling Enclosure Deformation



Figure 2.12.1-57 - ATR Fuel Element Inspection

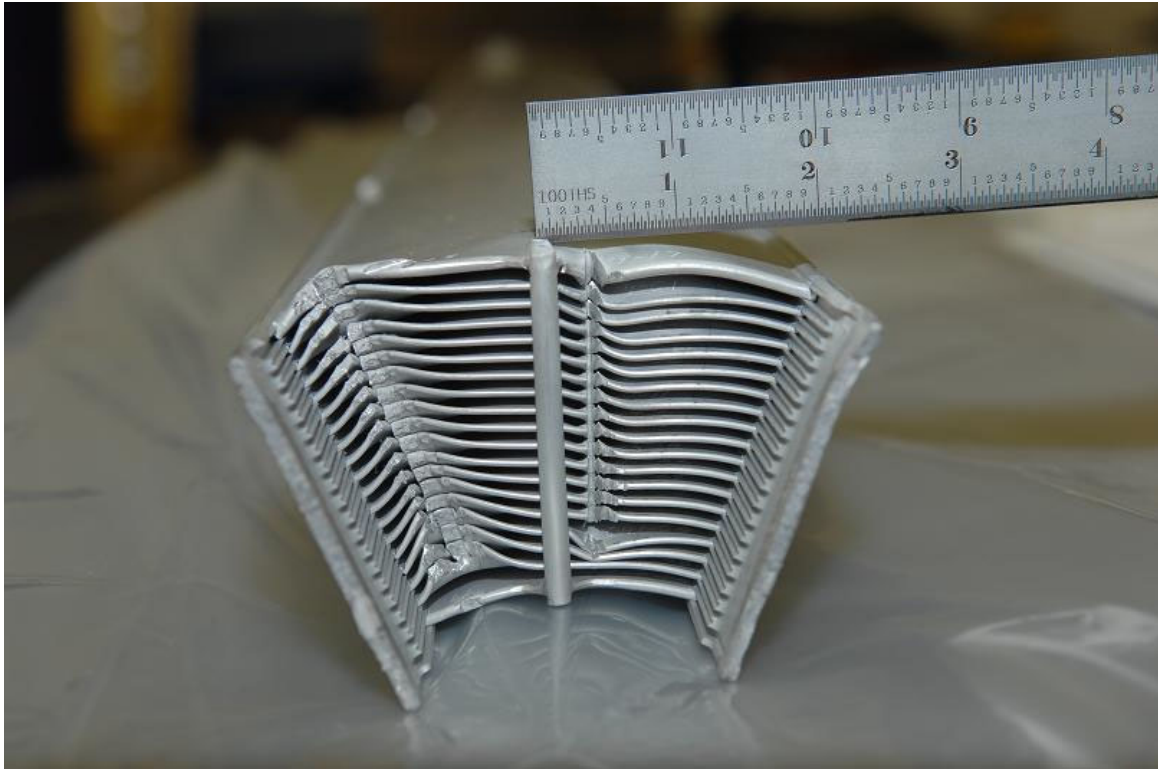


Figure 2.12.1-58 - ATR Fuel Element at Head End

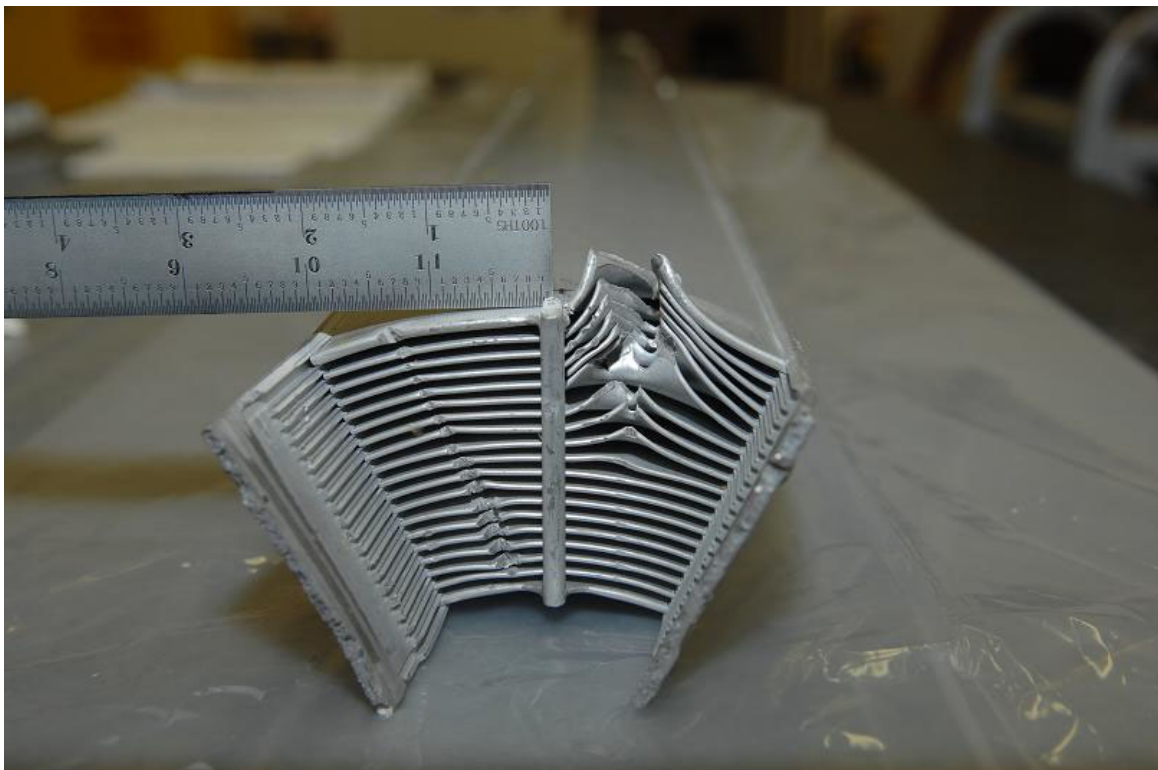


Figure 2.12.1-59 - ATR Fuel Element Damage at Bottom End



Figure 2.12.1-60 - Top View ATR Fuel Element at Bottom End

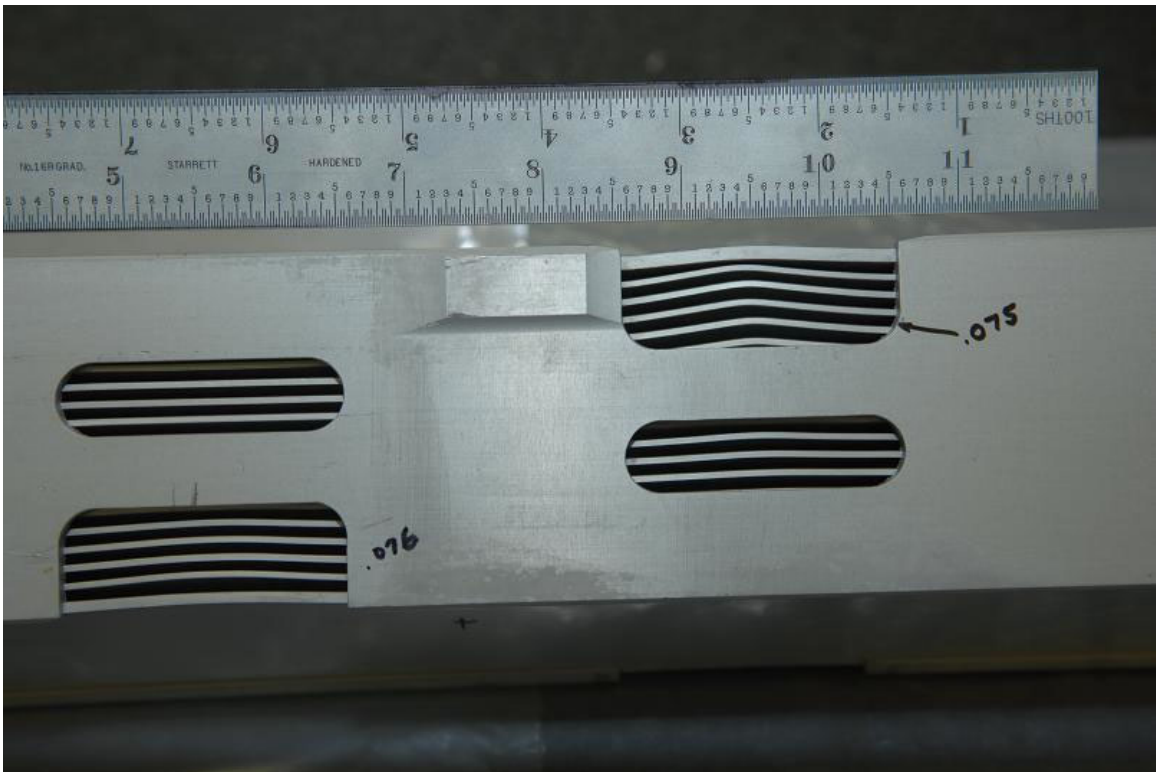


Figure 2.12.1-61 - ATR Fuel Element Fuel Plates Left Side



Figure 2.12.1-62 - ATR Fuel Element Fuel Plates Right Side

This page intentionally left blank.

2.12.2 Certification Tests on CTU-2

This report describes the methods and results of a series of tests performed on the Advanced Test Reactor (ATR) Fresh Fuel Shipping Container (FFSC) transportation package, shown in Figure 2.12.2-1. The objective of testing was to conduct drop tests in accordance with the requirements of 10 CFR 71, §71.71 Normal Conditions of Transport (NCT), and §71.73 Hypothetical Accident Conditions (HAC). This test was primarily directed at verification of the loose fuel plate basket structural integrity and the performance of the package insulation. The package and ATR fuel element payload performance are supported by the tests described in Section 2.12.1, *Certification Tests on CTU-1*.

Testing was performed at HiLine Engineering in Richland, Washington on May 17, 2007. Color photographs and videos were taken to document the test events and results.

2.12.2.1 Overview

There are three primary objectives for the certification test program:

1. To demonstrate that, after a worst-case series of HAC free drops, the package maintains containment of radioactive contents.
2. To demonstrate that, after a worst-case series of HAC free drops, geometry of both the fuel and package are controlled as necessary to maintain subcriticality.
3. To demonstrate that, after the free drops, the package retains the thermal protection necessary to maintain the fuel below its melting point during the thermal evaluation.

Several orientations were tested to ensure that the worst-case series of free and puncture drop events had been considered. Post-impact examination demonstrated that the package sufficiently met the design objectives. The specific objectives of this test were to demonstrate:

- Any displacement of package insulation and/or thermal shields are bounded in the thermal analysis,
- Reconfiguration of the loose fuel plate basket and/or loose fuel plate payload is bounded in the criticality analysis.

2.12.2.2 Pretest Measurements and Inspections

The ATR FFSC packaging (serial number CTU1), loose fuel plate basket (serial number 1), and simulated ATR loose fuel plates were received at HiLine. The packaging and payload are identified as ATR FFSC Certification Test Unit CTU-2. The components arrived fully constructed and ready for testing.

The ATR loose fuel plates were simulated. The payload was comprised of a combination of 2- and 4-inch wide, .06-inch thick, 5052H32 aluminum flat plates. All plates were 49.5-inches long. There were 15, 2-inch wide plates and 10, 4-inch wide plates making up a total payload weight of 20.7 lbs.

The CTU was dimensionally inspected to the drawings at the fabricator and the fabrication records forwarded to PacTec. A Certificate of Compliance was issued by the fabricator of the CTUs documenting compliance with the fabrication drawings. Minor discrepancies

between the drawings and CTUs were identified and independently evaluated. The evaluations concluded that the discrepancies were minor and would not significantly affect the CTU during testing.

There were five fabrication deviations associated with the S/N CTU1 package fabrication:

- The 3/8-16 UNC index lug screws were obtained without specified ASTM F-879 certifications.
- The #10-24 UNC closure handle screws were obtained without specified ASTM F-879 certifications.
- Chemical overtesting of the package body closure plate material identified a manganese content 0.02% above the ASTM A479 maximum allowable.
- The tap failed when tapping one of the four #10-24 tapped holes for the closure handle screws. As a result, one of the four tapped holes had full threads to a depth of .44-inches rather than the specified .5-inches.
- The handle width is specified to be $7.5 \pm .3$ -inches. When measured in the free state (not secured to the closure), the handle width was undersized by approximately 0.1-inches.

Other deviations relative to the CTU are the absence of the stainless nameplate and the use of temporary rigging attachments. These items are also insignificant relative to the weight of the CTU and their impact upon the drop tests.

2.12.2.2.1 Component Weights

Component weights were measured and recorded as shown in Table 2.12.2-1.

2.12.2.2.2 Drop Test Pad Measurement and Description

The drop pad consists of a 7-foot square x 5-foot thick concrete block covered with a 6-foot square x 2.5-inch thick steel plate. The estimated weight of the pad is greater than 44,000 lbs. Thus the test pad was qualified as an essentially unyielding surface for the approximately 300 lb CTU.

2.12.2.2.3 Equipment and Instruments

Instrumentation used for the component weights and drop tests is given in Table 2.12.2-2. Calibrated test and measurement equipment used were the weight scale and temperature meter. Those two instruments were calibrated in accordance with HiLine procedures. It is noted that the HiLine calibration procedures require National Institute of Standards and Technology (NIST) traceability and that the HiLine records adequately demonstrated that the calibrations were NIST traceable.

A plumb bob with a stretch resistant string was used to determine the appropriate drop height. HiLine project personnel under the supervision of PacTec personnel measured the plumb bob and string using steel tape measures. The angle of the CTU prior to each drop was measured using a mechanical inclinometer.

One low speed digital video camera was used to record the drop events. In addition, color photographs were taken to document the testing.

2.12.2.3 Summary of Tests and Results

2.12.2.3.1 Initial Conditions

All three HAC drops, CD1-2, CD3-2, and CD4-2, were performed at ambient temperature. Ambient temperature and the package surface temperature was recorded before and after each drop. After each drop the closure was removed and the basket inspected. The basket was reassembled (the basket screws tightened to the “finger tight” condition) and the package re-closed for the following test. One tie wrap (securing the loose fuel plate payload) failed in the CD1-2 test and the second tie wrap failed in the CD3-2 test. Neither of the two tie wraps were replaced between tests.

2.12.2.3.2 Summary of Testing

Table 2.12.2-3 identifies the testing performed on the ATR FFSC CTU.

2.12.2.4 Certification Tests

2.12.2.4.1 Drop Tests

The three CTU-2 HAC drop tests were performed to augment the CTU-1 tests for the package, and to demonstrate acceptable performance of the loose fuel plate basket payload. In CTU-1, the package was subjected to end drops on both the closure and the bottom ends of the package. CTU-2 restricted the end drop test to just the bottom end to properly assess axial insulation displacement.

There were no NCT or puncture bar tests performed on the package, since CTU-1 adequately demonstrates acceptable package performance under those conditions. The two side drops subjected the loose fuel plate basket and simulated fuel to worst case impact conditions with the basket oriented perpendicular and parallel to the target surface.

The test identification numbering reflects the same drop orientation as performed in CTU-1. For example, CD3-2 is the same orientation as the third HAC drop in CTU-1, test CD3-1. The “-2” identifies this drop as a CTU-2 test.

2.12.2.4.1.1 CD1-2 –Flat (pocket side down) Side HAC Drop

The CTU was fitted with swivel lift eyes, and the lift eyes were threaded into the package lift points. This configuration oriented the package such that the package pocket side impacted the target surface. Slings were used to rig the CTU from the swivel lift eyes to the crane remote release hook. Figure 2.12.2-5 illustrates the drop orientation. Initial conditions were as follows:

- Ambient temperature: 73 °F
- Avg. surface temperature: 78 °F
- Time: 10:04 a.m. 5/17/2007
- Drop height: 30 ft

Following impact, the CTU bounced slightly and landed on the impact side. There was minor visible exterior damage, principally scuff marks, resulting from the drop. Close examination of

the package, on the impacted surface side, reveals minor distortion of the outer shell localized at the stiffening ribs. Figures 2.12.2-6 and 2.12.2-7 show the CTU prior to and following the drop. There was no bowing or other significant visible deformation. There was no visible deformation or rotation of the closure, and the locking pins condition and function were unaffected by the drop.

The basket was not affected by the drop, however the finger operated screws securing the two basket halves were loosened approximately one turn. One fuel tie wrap was broken but the simulated loose fuel plates were not damaged. The simulated fuel plates were replaced in the basket without installing new tie wraps, and the basket closure screws again tightened to the finger tight condition.

2.12.2.4.1.2 CD3-2 – Flat Side HAC Drop (90° from CD1-2)

Following the CD1-2 drop, lift points were welded to the package to enable a side drop rotated 90° from CD1-2 (Figure 2.12.2-8):

- Ambient temperature: 78 °F
- Avg. surface temperature: 85 °F
- Time: 10:50 a.m. 5/17/2007
- Drop height: 30 ft

The CTU rebounded from the drop pad approximately 1 ft following the 30 ft drop and came to rest on its side (rotated 90° from the drop orientation). As with the CD1-2 event, the outer shell exhibited minor deformation at the stiffening rib locations (reference Figure 2.12.2-9). There was no visible deformation or rotation of the closure, and the locking pins were undamaged and in good working order.

The closure was opened and the basket removed following the drop. The basket exhibited no signs of any deformation but the finger tightened basket screws were loosened approximately 1 turn by the drop.

The basket was opened and it was discovered that the second plastic tie wrap was broken (Figure 2.12.2-10). The simulated fuel plates were found to exhibit no significant damage. The simulated fuel plates were replaced in the basket without installing new tie wraps, and the basket closure screws again tightened to the finger tight condition.

2.12.2.4.1.3 CD4-2 – CG over Bottom End (Vertical)

Following CD3-2, the temporary rigging attachments were removed and the CTU rigged for CD4-2 by lifting the package from the closure handle (Figure 2.12.2-11). Initial conditions were recorded as follows:

- Ambient temperature: 88 °F
- Avg. surface temperature: 90 °F
- Time: 11:20 a.m. 5/17/2007
- Drop height: 30 ft

The CTU appeared to impact slightly off of true vertical; impacting near one corner of the package. This impact dented the lift point feature inward approximately ½-inch, and on one adjacent side, bulged out the square outer tube surface by approximately ½-inch. Following impact, the CTU rebounded vertically approximately 2-feet, tipped over, and landed on the CD3-2 impact side. There was no overall bowing or of the package or other significant visible deformation. There was no visible deformation or rotation of the closure. Figure 2.12.2-12 shows the bottom end of the CTU following the drop.

There was no visible damage to the closure or the locking pins. The closure was removed and the basket extracted following CD4-2. Damaged to the basket was limited to a small dent at the end of the basket that was situated closest to the package bottom. Upon destructive examination of the package, it was discovered that the weld between the package inner shell and the component at the bottom of the payload cavity had intruded into the payload cavity in a localized area (Figure 2.12.2-13). When the package impacted in CD4-2, the basket was partially supported by that weld bead. The end plate of the basket was slightly deformed (Figure 2.12.2-14) as the basket seated on the bottom of the package payload cavity. The damage was minor and did not impair the ability of the basket to retain the fuel plates.

The simulated fuel plates experienced localized deformation at the end of the basket closest to the package bottom (Figure 2.12.2-15 and Figure 2.12.2-16). Above this area the simulated fuel plates were not deformed.

2.12.2.5 Post-test Disassembly and Inspection

The final acceptance criteria for the ATR FFSC package lies with the criticality evaluation. Any increase in reactivity of the contents resulting from the certification tests must not exceed the allowable as defined in the criticality evaluation. The inspections required to support determination of compliance with the acceptance criteria are identified as follows:

- Inspect the outer shell to verify the thermal performance of the package is unimpaired by the free drop events. The thermal analysis assumes that the outer shell is intact such that there is no significant communication between the environment and the outer/inner shell annular space during the thermal event.
- Inspect the insulation to verify compliance with the assumptions of the thermal analysis.

- Inspect the overall package to verify that the package geometry remains within the criticality analyses assumptions.
- Inspect the simulated fuel plate payload to verify that the fuel geometry remains within the assumptions of the criticality analyses.

Any deviation of the test results from these acceptance criteria must be reconciled with the criticality evaluation.

2.12.2.5.1 CTU Inspection

The CTU-2 was disassembled and inspected on May 17, 2007. Prior to disassembly the exterior dimensions were recorded for comparison to the pre-test condition. Table 2.12.2-4 lists the measured dimensions and Figure 2.12.2-17 identifies the location of the identified measurements.

The closure handle was unaffected by the first two drops. In the CD4-2 drop, the handle was dented when it was struck by the rigging shackle. During the CD4-2 CG over bottom (vertical) HAC drop, the outer wall bulged out at the bottom end of the package and caused the width of the package to increase from 8 inches to approximately 8 5/8 inches in that area.

The CTU was disassembled systematically by cutting away the outer layers of the packaging using an abrasive saw. The destructive examination was necessary due to the required inspection of the interior insulation. The package was cut lengthwise along two opposite corners and at the ends to expose the thermal shield.

The stainless steel thermal shields were all intact (Figure 2.12.2-18 through Figure 2.12.2-20). There was minor deformation of the thermal shields at the interface to the stiffening rib. This deformation resulted from the CD4-2 drop and caused the thermal shields to buckle one end and pull away from the stiffening rib at the other end. Figure 2.12.2-21 is typical of this condition. The gap between the thermal shield and the stiffening rib, where the shield pulls away from the rib, is less than 1/16-inch.

Following documentation of the thermal shields the shields were removed to enable examination of the insulation. For reference purposes the ribs are labeled 1 through 3 (Figure 2.12.2-22). The number 1 rib is closest to the bottom end of the package.

As can be seen in Figure 2.12.2-23 through Figure 2.12.2-26 the largest gap occurred at the closure end of the package. The gap ranges from 1-inch to 1 3/4 inches at that location. At the rib 3 and rib 2 locations the gap ranged from 1- to 1 1/2-inches. At the rib 3 location the gap ranged from 1/2- to 1-inch. All gaps are within the 1.85-inch gap assumed in the thermal analysis.

Following thermal shield and insulation removal an abrasive saw was used to separate the bottom end plate from the inner tube. Figure 2.12.2-13 illustrates the condition of the end plate. The endplate showed no drop related deformation and there were no visual indications of broken welds or other damage near the end plate. Using a lathe, the bottom end plate was cut from the insulation pocket to determine the extent of possible insulation compression in the insulation pocket (Figure 2.12.2-27). There was no indication of compression in that region and it was determined that there was no need to open the closure insulation pocket.

The inner tube was inspected and, in general, showed no signs of buckling or large deformations. A minor deformation occurred near the bottom end of the package (Figure 2.12.2-28 and Figure 2.12.2-29) corresponding to the same area of deformation as the outer shell. The tube was bent in that area yielding a slight outward bulge of about 1/16-inch and, closer to the weld between the inner shell and the package bottom, an inward deformation of approximately ¼-inch. These deformations were localized and did not impair free movement of the basket in the payload cavity. There were no weld failures.

The closure assembly remained fully functional throughout the test series. The only damage to the closure was the handle deformation caused by the rigging shackle. The locking pins and the engagement lugs showed no signs of any deformation. The closure could be freely removed and installed through the tests.

In conclusion, CTU-2 satisfied the acceptance criteria of preventing loss or dispersal of the contents, the outer shell remained intact, the insulation remained within the assumptions of the thermal analysis, and the package and fuel geometry remained greatly unchanged. The deformations of the package and condition of the ATR loose fuel plates were evaluated, against both the criticality evaluation and thermal analysis, and determined to be within the bounds of the assumptions and conditions used to ensure safety.

Table 2.12.2-1 - Component Weights

Component	Weight (lbs)
Body Assembly	224.1
Closure Assembly	8.9
Loose Plate Fuel Basket	29.9
Simulated Fuel Plate Weight	20.7
Package (fully loaded)	283.6

Table 2.12.2-2 - Instrumentation for Drop Tests

Item Description	Model	Serial Number	Calibration Due Date	Comments
Drop Height Indicators	N/A	N/A	N/A	String plumb bobs made specifically for this testing. The length was established using a metal tape measure.
Tape Measure	N/A	N/A	N/A	35-ft. steel tape
Mechanical inclinometer	N/A	N/A	N/A	Used to identify CTU orientation
Weight Scale	Ohaus, Model CD11	0042508-6BD	7/19/2007	Used to measure weights of CTU components. The scale calibration documents included NIST traceable records.
Temperature meter	Carson, Model 4085	41372269	3/1/2008	Handheld temperature reader for measuring ambient temperature and CTU surface temperature. Meter calibration documents included NIST traceable records.

Table 2.12.2.3 - Summary of Testing

Test No.	Test Description	Comments
CD1-2	Flat side drop, pocket side down. Fuel plates oriented perpendicular to target (see Figure 2.12.2-3).	Flat side drop from 30-feet. No visible damage to package. Both closure locking pins remained in the locked position. Closure could be freely opened and payload extracted. The eight hand tightened screws securing the basket halves together were loose (approximately one turn). No visible damage to basket or simulated fuel plates.
CD3-2	Flat side drop, pockets and index lugs on side. Fuel plates oriented parallel to target (see Figure 2.12.2-4).	Flat side drop from 30-feet. No visible damage to package. Both closure locking pins remained in the locked position. Closure could be freely opened and payload extracted. The eight hand tightened screws securing the basket were loose (approximately one turn). The plastic wire ties securing the fuel bundle failed as shown in Figure 2.12.2-10. No significant deformation was observed in the fuel plates.
CD4-2	CG over bottom end (vertical)	<p>Vertical end drop from 30-feet; bottom end of package impacting the target. Both closure locking pins remained in the locked position. Closure could be freely opened and payload extracted. The eight hand tightened screws securing the basket were loose (approximately one turn).</p> <p>The bottom end of the package was deformed on two surfaces (Figure 2.12.2-12). The surface with the threaded hole was dented inward and the adjacent surface 90° apart was bulged outward.</p> <p>The surface of the basket end plate contacting the bottom of the package was slightly dented.</p> <p>The simulated fuel plates were deformed at the bottom end of the basket (Figure 2.12.2-15 and Figure 2.12.2-16).</p>

Table 2.12.2-4 - Package Length Measurements

Test ID	1	2	3	4	5	6	7	8
Pre-Test (in.)	72 7/16	72 1/2	72 7/16	72 1/2	72 7/16	72 7/16	72 7/16	72 1/2
CD1-2 (in.)	72 7/16	72 1/2	72 7/16	72 1/2	72 7/16	72 7/16	72 7/16	72 7/16
CD3-2 (in.)	72 7/16	72 1/2	72 7/16	72 1/2	72 7/16	72 7/16	72 7/16	72 7/16
CD4-2 (in.)	72 7/16	72 1/2	72 3/8	72 7/16	72 5/16	72 5/16	72 3/16	72 3/8



Figure 2.12.2-1 - ATR FFSC CTU-2
(CTU-2 uses package S/N CTU1)



Figure 2.12.2-2 - Loose Fuel Plate Basket and Simulated Fuel Plates

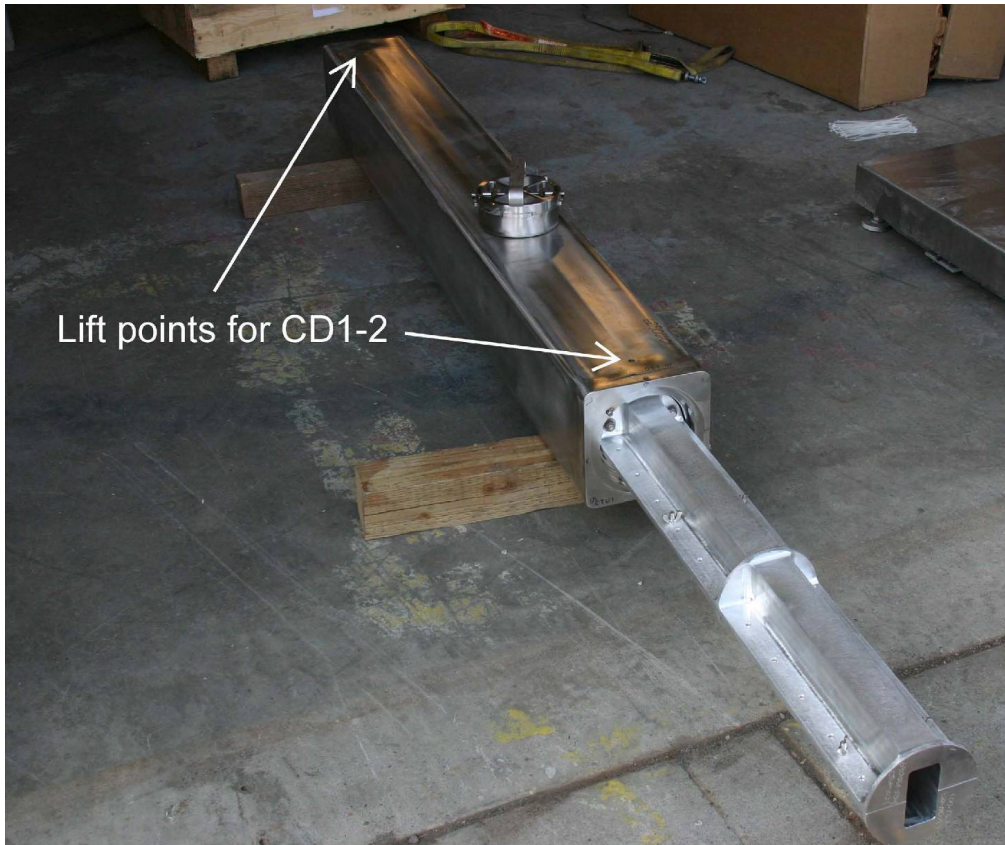


Figure 2.12.2-3 - Basket Orientation in CD1-2



Figure 2.12.2-4 - Basket Orientation in CD3-2



Figure 2.12.2-5 - CD1-2 Drop Orientation



Figure 2.12.2-6 - CTU Following CD1-2 Impact
(impact side facing up)



Figure 2.12.2-7 - CD1-2, Extracting Basket Following Drop



Figure 2.12.2-8 - CD3-2 Drop Orientation

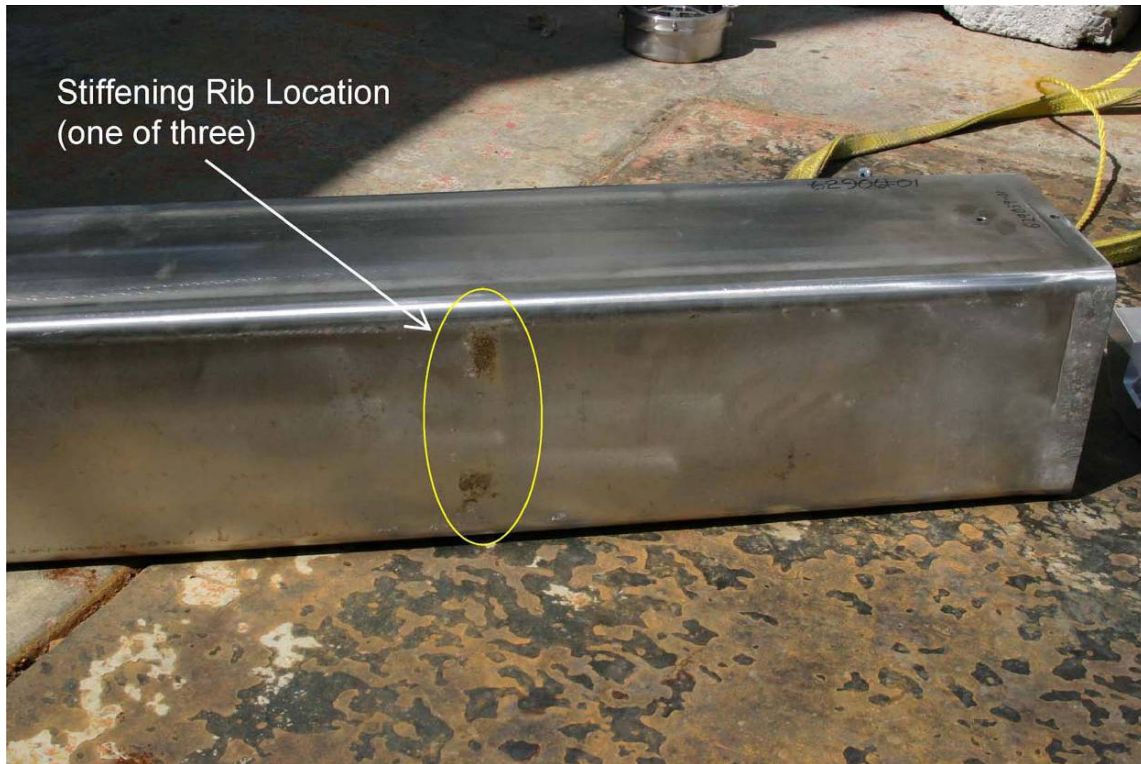


Figure 2.12.2-9 - CD3-2 Deformation at Stiffening Rib Location



Figure 2.12.2-10 - CD3-2 – Failed tie wraps



Figure 2.12.2-11 - CD4-2 – Drop Orientation

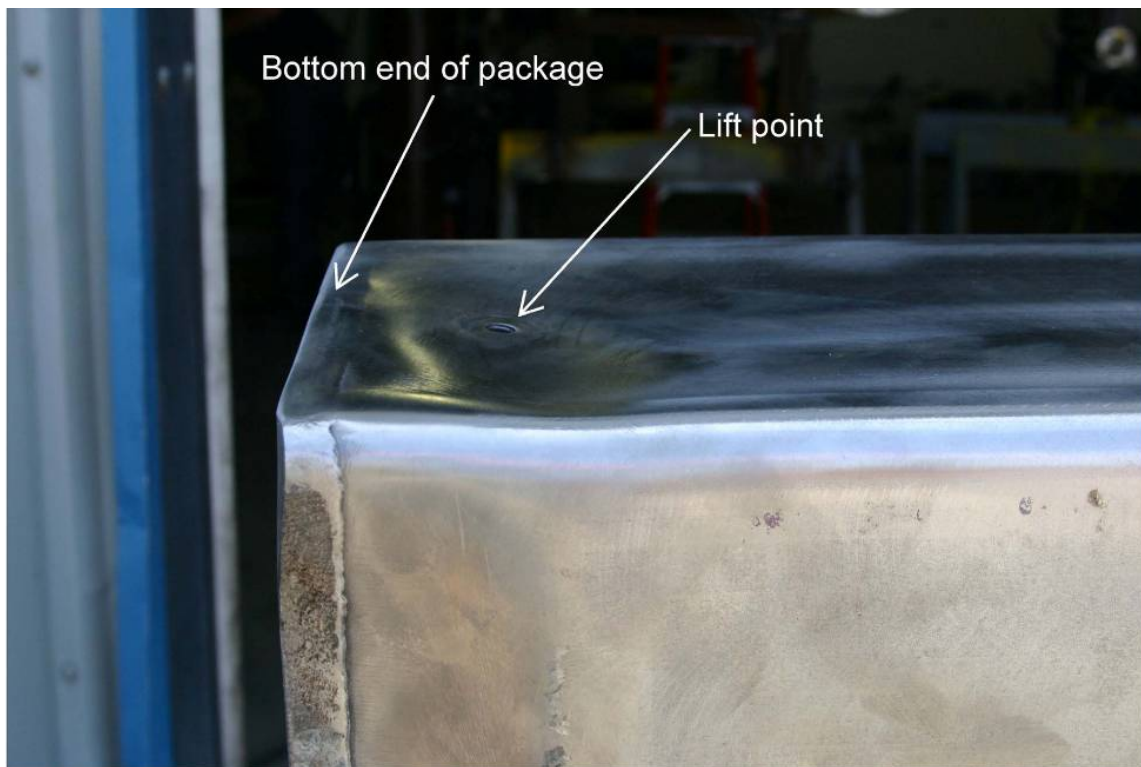


Figure 2.12.2-12 - CD4-2 Impact Damage to Package

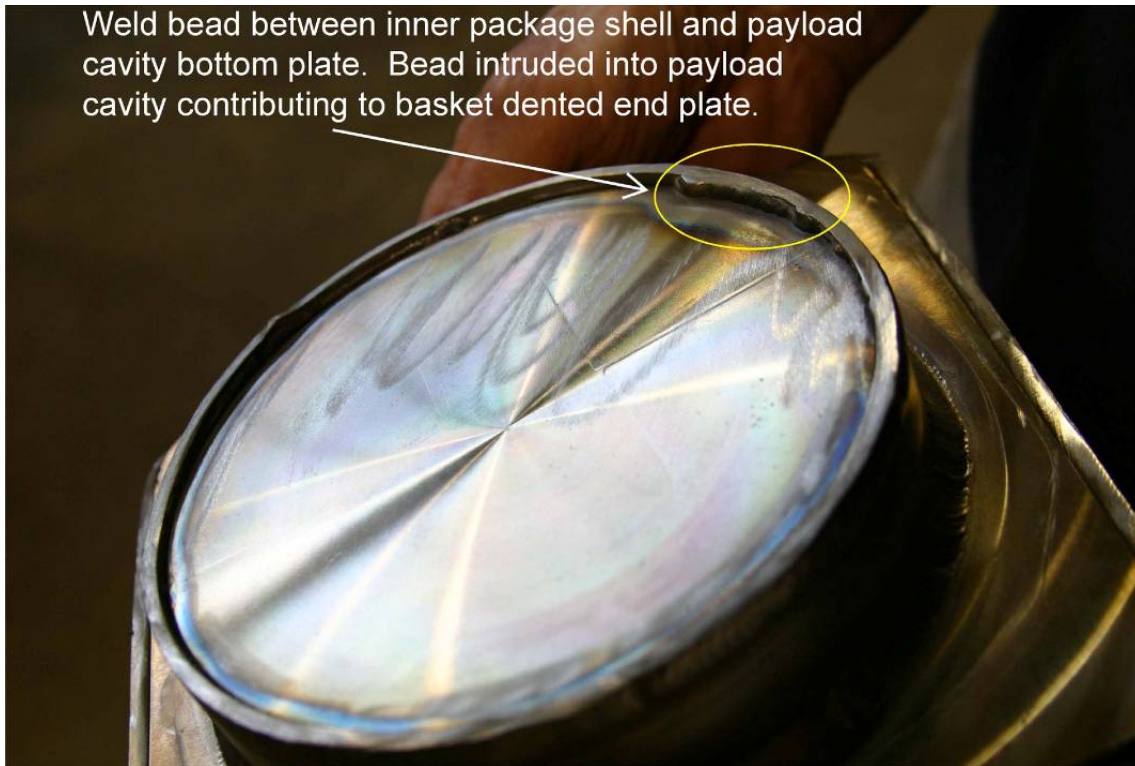


Figure 2.12.2-13 - Weld bead protruding into package payload cavity (inner shell has been removed in this photo)

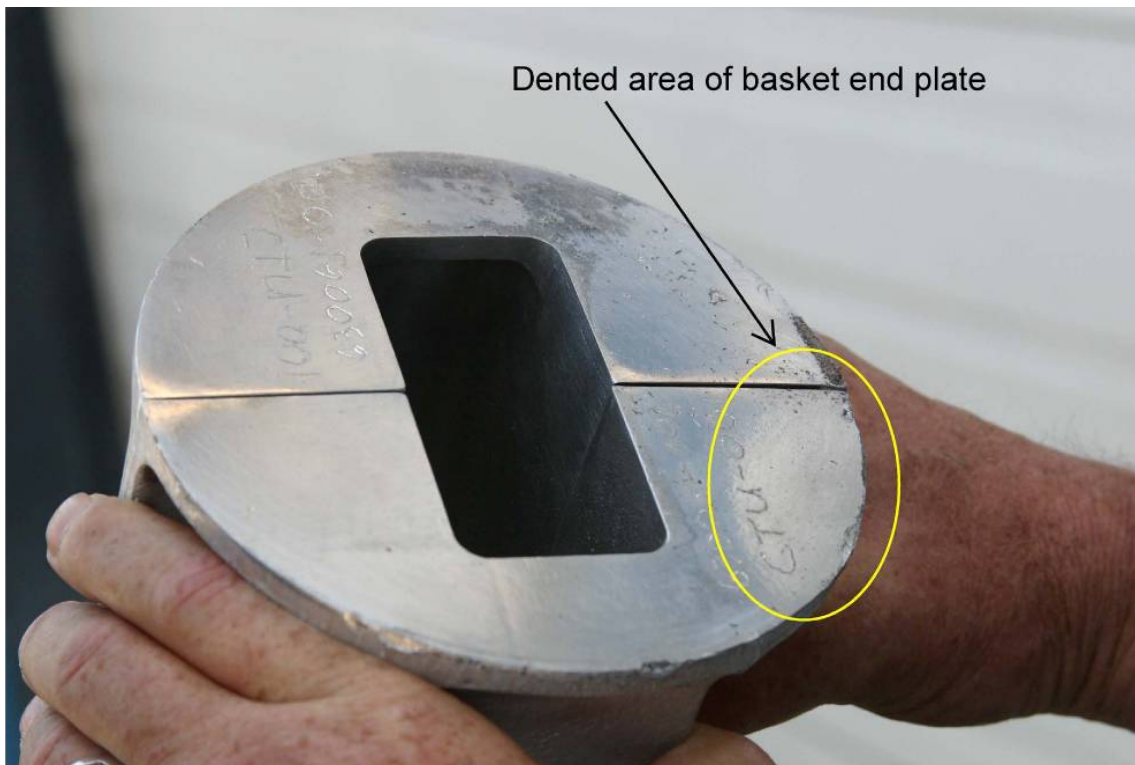


Figure 2.12.2-14 - Dented area – basket end plate



Figure 2.12.2-15 - CD4-2 Impact Damage to Simulated Fuel Plates

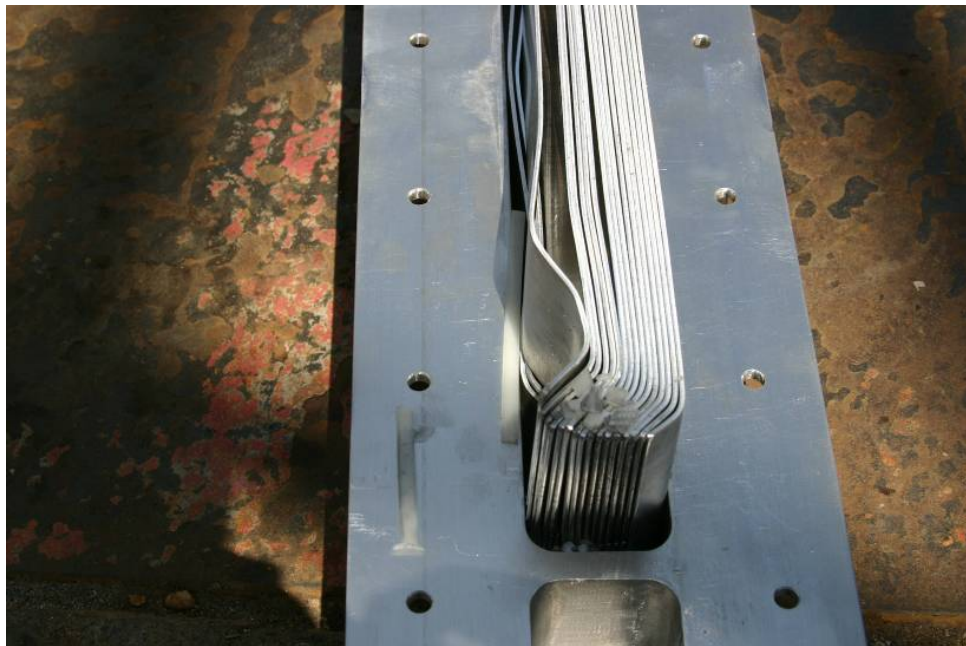


Figure 2.12.2-16 - CD4-2 Impact Damage to Simulated Fuel Plates (close up view)

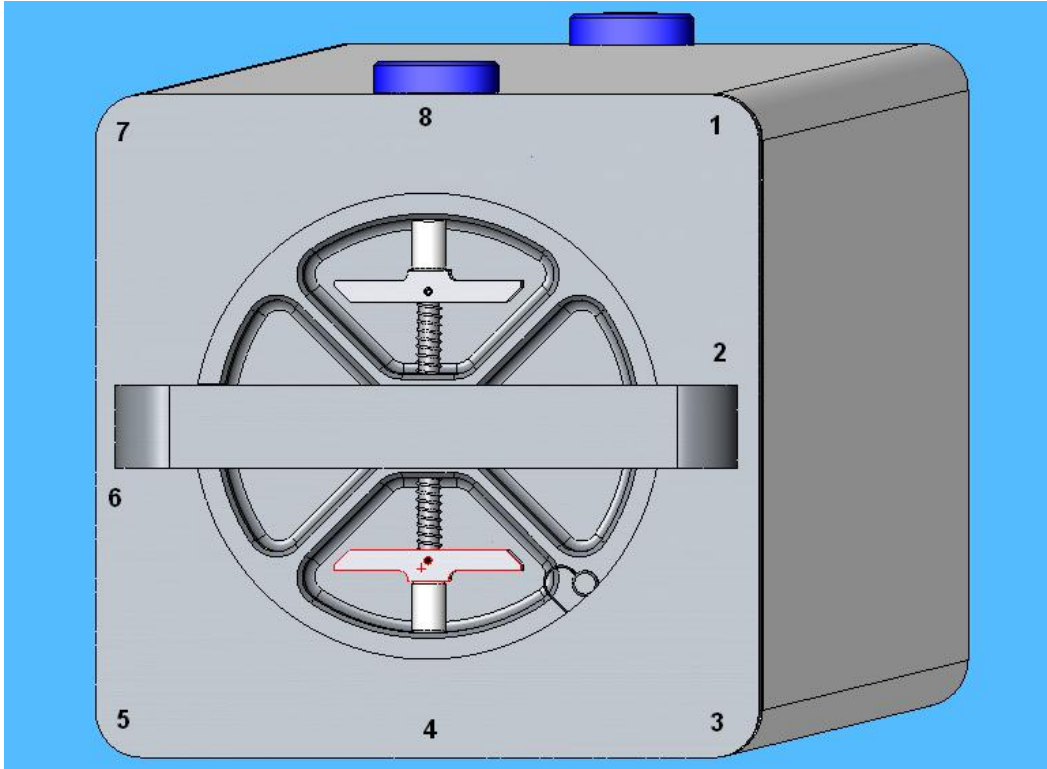


Figure 2.12.2-17 - CTU Measurement Locations



Figure 2.12.2-18 - Thermal Shield Condition, View 1



Figure 2.12.2-19 - Thermal Shield Condition, View 2



Figure 2.12.2-20 - Thermal Shield Condition, View 3



Figure 2.12.2-21 - Thermal Shields at Interface to Stiffening Rib

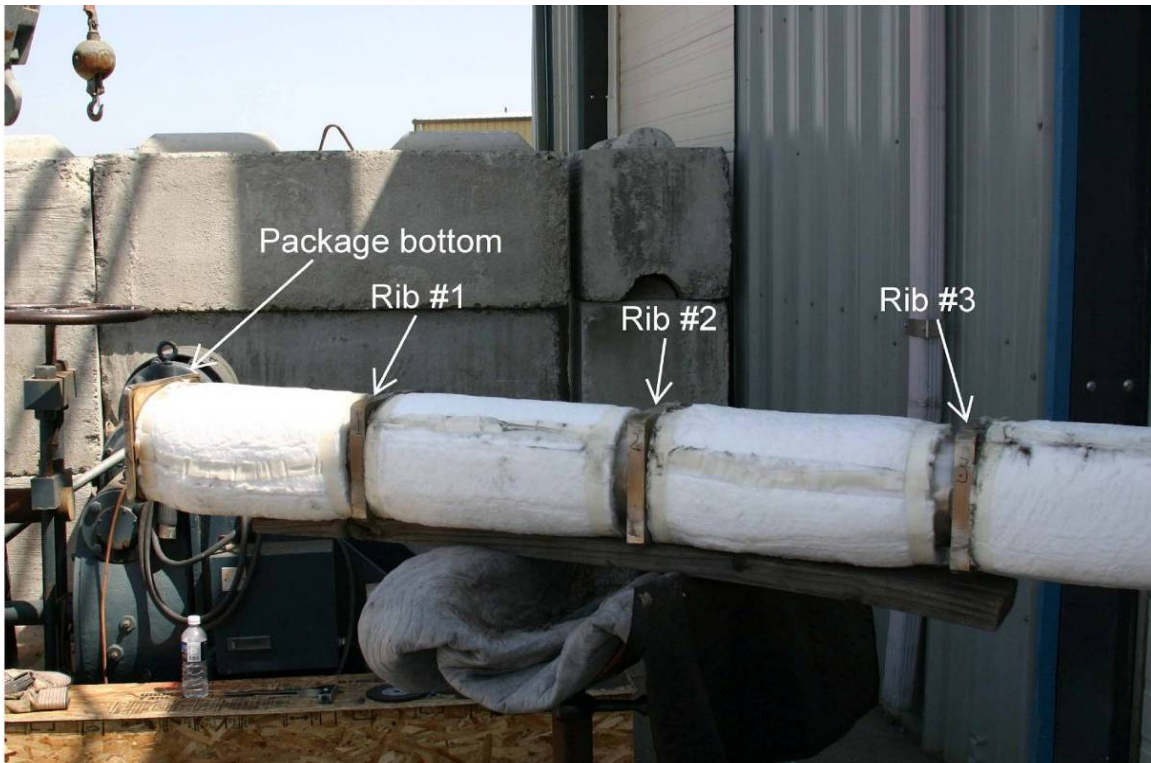


Figure 2.12.2-22 - Exposed Insulation - Overview



Figure 2.12.2-23 - Insulation Gap at Package Closure End



Figure 2.12.2-24 - Insulation Gap at Rib #3



Figure 2.12.2-25 - Insulation Gap at Rib #2



Figure 2.12.2-26 - Insulation Gap at Rib #1 (nearest impact)



Figure 2.12.2-27 - End Plate Insulation Condition



Figure 2.12.2-28 - Tube to Bottom End Plate – View 1



Figure 2.12.2-29 - Tube to Bottom End Plate – View 2

2.12.3 Structural Evaluation for MIT and MURR Fuel

The ATR FFSC may be utilized to transport a MIT fuel assembly or a MURR fuel assembly. Both of these fuels are high-enriched aluminum-clad uranium aluminide plate type fuel elements similar to the ATR fuel evaluated in this chapter. Since no MIT or MURR fuel elements were included in the drop tests, the following evaluation conservatively estimates a degree of failure and movement of the MIT and MURR Fuel Handling Enclosures (FHE) to develop a worst case pitch expansion of the corresponding fuel elements for evaluation in Section 6.10, *Appendix B: Criticality Analysis for MIT and MURR Fuel*. By conservatively bounding potential damage and evaluating the exceptional worst case pitch expansion of the MIT and MURR fuel elements the ATR FFSC complies with the performance requirements of 10 CFR §71.

2.12.3.1 Structural Design Discussion

A comparison is provided to highlight the similarities and differences between the MIT and MURR designs and the physically tested ATR design. Through this comparison, it is expected that both NCT and HAC testing would result in similar results for the MIT and MURR fuel elements. Similar to the ATR LFPB, the MIT and MURR FHEs are designed to restrict postulated fuel element pitch expansion under the HAC conditions.

The results of NCT conditions on the MIT and MURR payload are assumed to be equivalent to the ATR payload; i.e. there is no damage to the FHE or fuel element under NCT.

For conservatism in evaluating the HAC conditions, the MIT and MURR FHE damage postulated exceeds the results obtained during testing of the ATR payloads. The MIT and MURR FHEs are assumed to separate (fail) and spread apart to permit a worst case reactivity configuration of the fuel elements. The individual fuel plates of the fuel elements are assumed to spread apart uniformly to fill the resulting space.

2.12.3.1.1 Fuel Elements

The ATR FFSC packaging is not modified for the use of the MIT and MURR fuel elements. The MIT and MURR FHE are used in place of the ATR FHE or the LFPB within the ATR FFSC packaging. Similar to the ATR FHE and LFPB, the MIT and MURR FHEs are principally fabricated of aluminum construction and secured with stainless steel locking pins.

The MIT and MURR fuel elements are very similar to the ATR fuel element in design, materials, and fabrication. The weight of the fuel elements are 10 lb, 15 lb, and 25 lb, for the MIT, MURR, and ATR fuel elements respectively. All three fuel elements are fabricated of the same fuel type, aluminum-clad uranium aluminide fuel plates, with all fuel plates swaged into the side plates, and include cast or wrought aluminum end boxes. As such, the structural performance of the MIT and MURR fuel types are anticipated to behave very similarly to the ATR fuel element. Table 2.12.3-1 compares the three fuel element design dimensions. Figure 2.12.3-1 compares the three fuel elements in their overall length and fuel plate length in inches. In this figure, the inside dimension identifies the fuel plate length.

For comparative purposes, an approximate moment of inertia is calculated for all three fuel elements using AutoCAD[®]. The results are presented in Figure 2.12.3-2. The values were determined by taking a cross section of the fuel plate region and selecting the solid boundaries to compute the moments of inertia about the identified axes.

The comparison of the moments of inertia demonstrates that the three fuel elements are similar in stiffness and expected to perform in a similar fashion during NCT and HAC drop events. The length and weight of the fuel elements is clearly bounded by the ATR fuel element. The materials of construction and fabrication techniques are the same for each fuel type. The relatively minor dimensional changes of the ATR fuel element plates as a consequence of the testing identified in Section 2.6, *Normal Conditions of Transport*, and Section 2.7, *Hypothetical Accident Conditions*, further justifies the similar performance of the MIT and MURR fuel elements.

Table 2.12.3-1 –Fuel Element Design

Component	MIT	MURR	ATR
Approximate Weight, lbs	10	15	25
Number of Fuel Plates	15	24	19
Nominal Plate Spacing, in.	.08	.08	.08
Fuel Plate Length, in.	23.00	25.50	49.50
Fuel Plate Thickness, in.	.08	.05	.05, .08, .10
Approximate Fuel Plate Width, in.	2.5	2.0 - 4.3	2.0 – 3.9

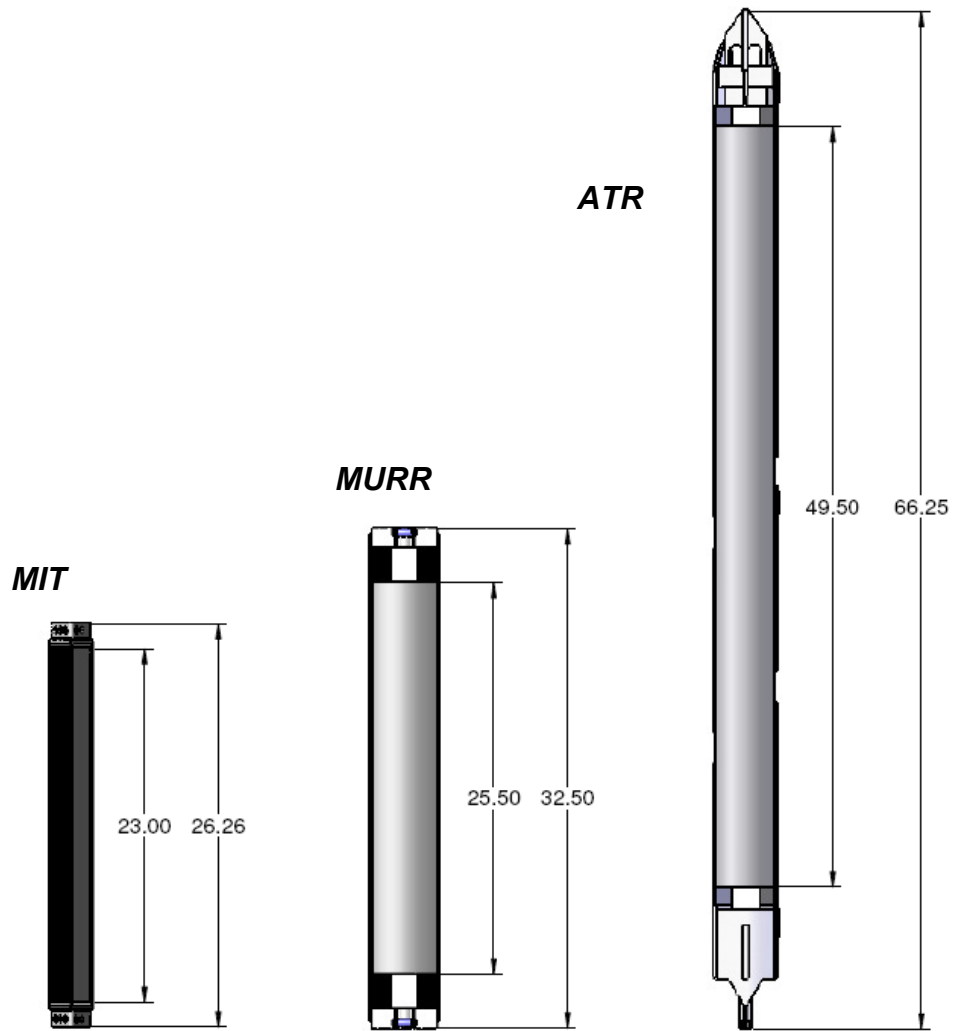


Figure 2.12.3-1 – MIT, MURR, and ATR Fuel Elements

This page left intentionally blank.

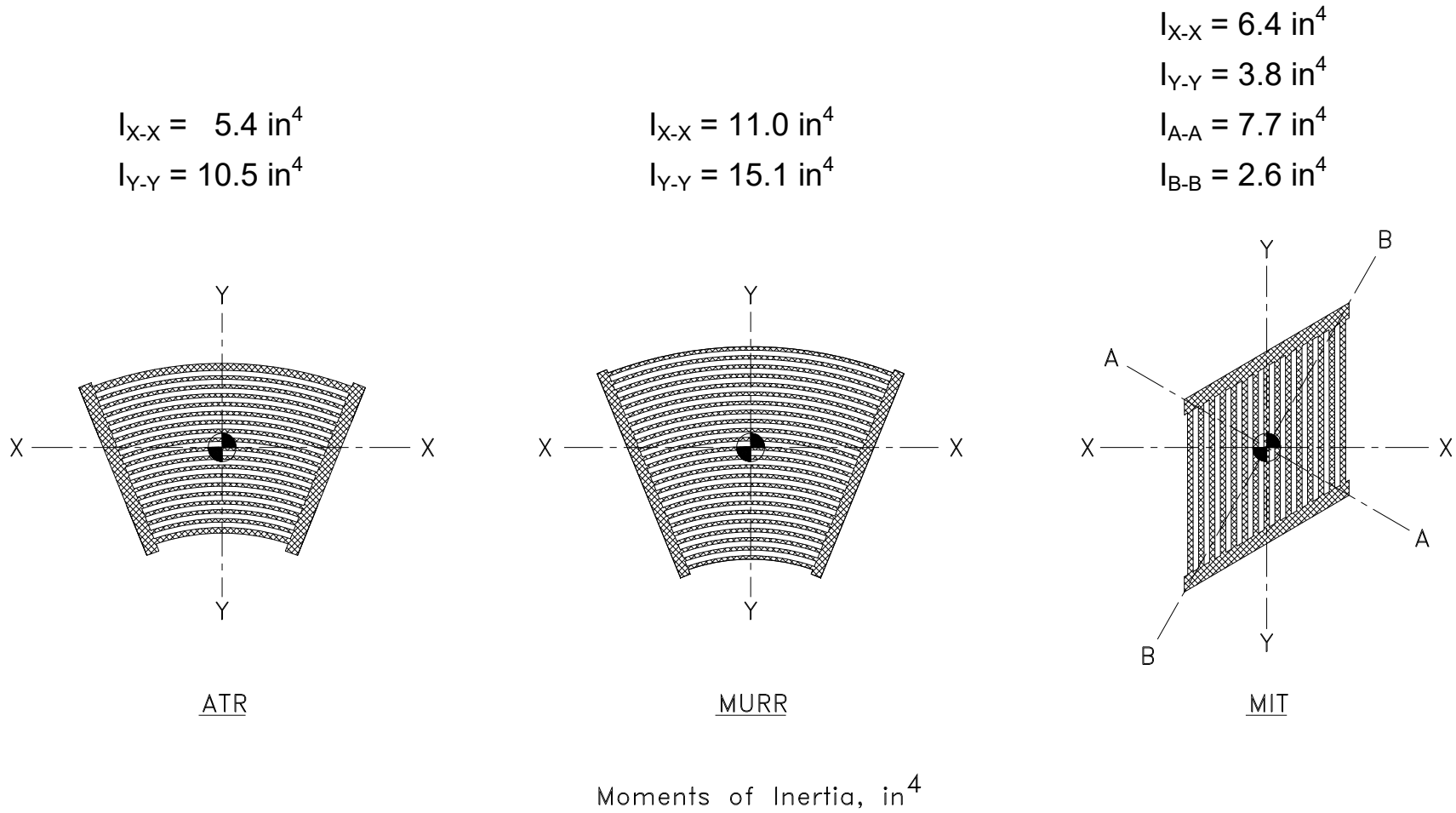


Figure 2.12.3-2 – Fuel Element Moments of Inertia

This page left intentionally blank.

2.12.3.1.2 Fuel Handling Enclosures

The MIT FHE incorporates two end spacers and a two-piece machined aluminum enclosure to protect the MIT fuel element from damage during loading and unloading operations. The enclosure halves are identical segments machined from 6061 aluminum plate. Neoprene rub strips are used to cushion the contact points between the fuel element and enclosure. The end spacers are also fabricated of 6061 aluminum. The end spacers lock the enclosure halves together and are secured using stainless steel ball lock pins. The end spacers also prevent axial movement since the MIT fuel element is much shorter than the package cavity. The weight of the MIT FHE is 25 lb. Figure 2.1-3 illustrates the assembly view of the MIT FHE.

The MURR FHE is designed in the same manner as the MIT FHE. The weight of the MURR FHE is 30 lb. Figure 2.1-4 illustrates the assembly view of the MIT FHE.

The MIT and MURR FHE design is similar to the 30-lb LFPB in that it utilizes machined enclosure halve segments to encase the payload. The use of the enclosure halves makes the MIT and MURR FHEs more robust than the ATR FHE, which weighs 15 lb. The wall thickness of the enclosure halves is 0.19 in compared to the 0.09 in thick sheet used in the ATR FHE. For comparison, the typical machined wall thickness of the LFPB is also 0.19 in thick. The weight of the enclosures and fuel elements are 35 lb, 45 lb, 40 lb, and 50 lb for the MIT payload, MURR payload, ATR payload, and LFPB payload respectively.

Based on the similarity in design and function, the structural and thermal performance of the MIT and MURR FHEs is anticipated to be similar to the physical testing performed using the ATR FHE and LFPB.

2.12.3.1.3 Loose Fuel Plates

MIT and MURR loose fuel plates are not evaluated for use within the LFPB.

2.12.3.2 Allowable Damage

For HAC tests the MIT and MURR fuel elements are anticipated to perform in a similar manner to the ATR fuel element based on the comparable designs and assembly techniques. To conservatively encompass potential damage, the FHE halves are considered to separate while each half is sized at the extreme tolerances to encourage the maximum space around each fuel element. Based on the maximum space developed by the separated FHE, the fuel element plates separate to create a more reactive configuration for the fuel. The proposed pitch expansion greatly exceeds the results of the physical testing performed on the ATR fuel element.

Axial movement of the fuel element within the package inner tube, which occurs by hypothetical neglect of the FHE end spacers, has no adverse effect on the performance of the ATR FFSC. Energy dissipated by failure of the spacers would result in lowering the HAC loads to the MIT and MURR elements. However, the structural tests identified that the ATR fuel element survives the impact loads with damage that has no impact on reactivity. The MURR and MIT fuel elements are of similar materials and of similar construction to the ATR fuel elements. Assuming the spacers to fail with no energy absorption, the impact velocities of the MURR and MIT FHEs on the end fitting of the package would be nearly identical. It is therefore concluded that the damage to MURR and MIT fuel elements is bounded by the damage sustained by the ATR fuel element in the structural tests. However, for conservatism, the fuel plate pitch of the

MURR and MIT elements is set to the condition that results in the worst case reactivity under the volumetric constraints presented by the FHEs.

The HAC criticality array model is a 5x5x1 array of packages and all fuel elements are positioned at the same axial location. The FHE end spacers are conservatively neglected and modeled as water. Axial shifting of fuel elements from the modeled configuration would result in a less reactive condition; therefore, failure of the FHE end spacers is not a criticality concern. For the thermal evaluation, the position of the MIT or MURR fuel element is naturally bounded by the ATR fuel element since its length extends to each end of the package.

The modeled separation of the FHE halves inside the inner tube of the package is determined by using the maximum inner diameter of the package's inner tube and the minimum outer radius of each FHE half as illustrated in Figures 2.12.3-3 and 2.12.3-4. The FHE cavity dimensions are expanded using the maximum tolerance of the parts. Note that this is only hypothetically possible, since this causes the corners of the FHE for both the MIT and MURR to exceed the point of interference with the inner tube wall.

The dimensions for the criticality model of the MIT FHE are determined in the following manner:

- Package inner tube maximum inside diameter: Diameter is specified as 6.0 in. OD X 0.12 in. wall thickness \pm 0.030 in. OD and \pm 10% thickness (per drawing 60501-10 and ASTM A269). Resulting maximum ID is 5.814 in.
- Minimum outside radius of the FHE half: Radius is specified as 2.8 in \pm 0.2 (per drawing 60501-40). Resulting minimum radius is 2.6 in.
- Minimum wall thickness of the FHE half: Wall is specified as 0.19 in \pm 0.06 (per drawing 60501-40). Resulting minimum thickness is 0.13 in.
- Maximum cavity height of the FHE half: Wall height specified as 2.82 in \pm 0.06 (per drawing 60501-40). Resulting maximum height is 2.88 in. (which is greater than the 2.6 maximum radius).
- Maximum cavity width of the FHE half: Wall width specified as 1.62 in \pm 0.06 (per drawing 60501-40). Resulting maximum width is 1.68 in.

The dimensions for the criticality model of the MURR FHE are determined in the following manner:

- Package inner tube maximum inside diameter: Diameter is specified as 6.0 in. OD X 0.12 in. wall thickness \pm 0.030 in. OD and \pm 10% thickness (per drawing 60501-10 and ASTM A269). Resulting maximum ID is 5.814 in.
- Minimum outside radius of the FHE half: Radius is specified as 2.8 in \pm 0.2 (per drawing 60501-50). Resulting minimum radius is 2.6 in.
- Minimum wall thickness of the FHE half: Wall is specified as 0.19 in \pm 0.06 (per drawing 60501-50). Resulting minimum thickness is 0.13 in.
- Maximum cavity height of the FHE half: Wall height specified as 2.00 in \pm 0.06 (per drawing 60501-50). Resulting maximum height is 2.06 in.
- Maximum cavity width of the FHE half: Wall width specified as 1.85 in \pm .06 (per drawing 60501-50). Resulting maximum width is 1.91 in.

The thermal evaluation in Section 3.6, *Thermal Evaluation for MIT, MURR, and Small Quantity Payloads*, makes the following conservative assumptions to bound damage to the fuel elements and FHEs as a result of NCT and HAC events.

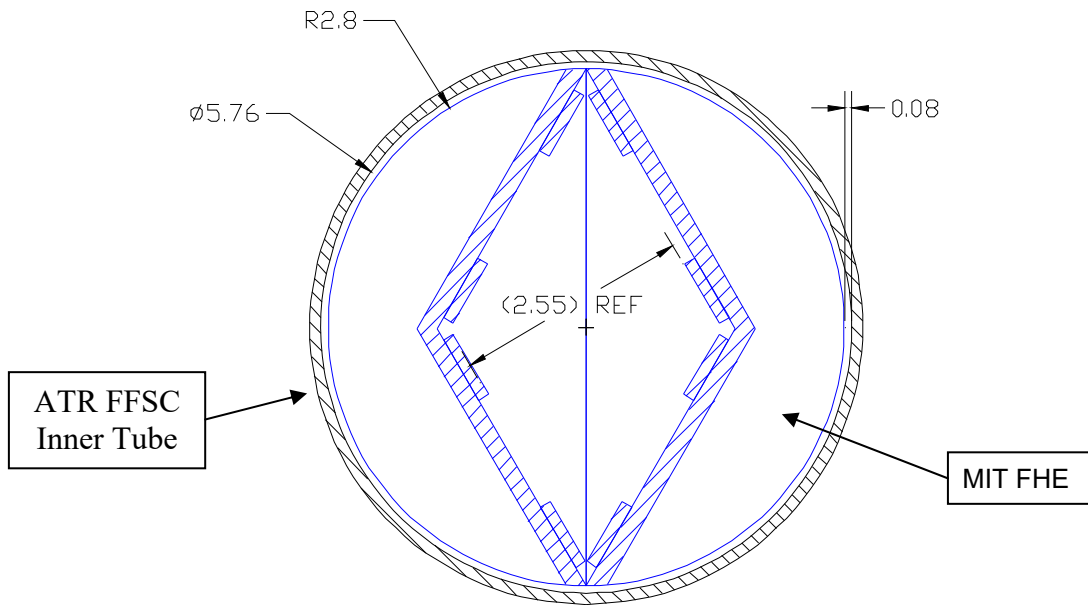
- Idealized contact between the FHE and the package inner tube. The majority of the heat input to the fuel element comes from the radial direction rather than the axial direction. By maximizing the contact, the greatest heat is transferred. Deformation of the payload would have the effect of reducing the contact area, and therefore reducing the conductive heat input.
- Axial movement of the fuel element, as a result of deformation of the FHE end spacers has a negligible effect. The majority of the heat input to the fuel element comes from the radial direction rather than the axial direction (ends). As the fuel element moves closer to the ends of the package the heat input rises. However, the heat input from either end of the package is negligible compared to the heat input received axially from the sides. Furthermore, any credible axial distance of the MIT and MURR fuel elements to the end of the package is bounded by the ATR fuel element.

The criticality evaluation in Section 6.10, *Appendix B: Criticality Analysis for MIT and MURR Fuel*, makes the following conservative assumptions to bound damage to the fuel element as a result of HAC events.

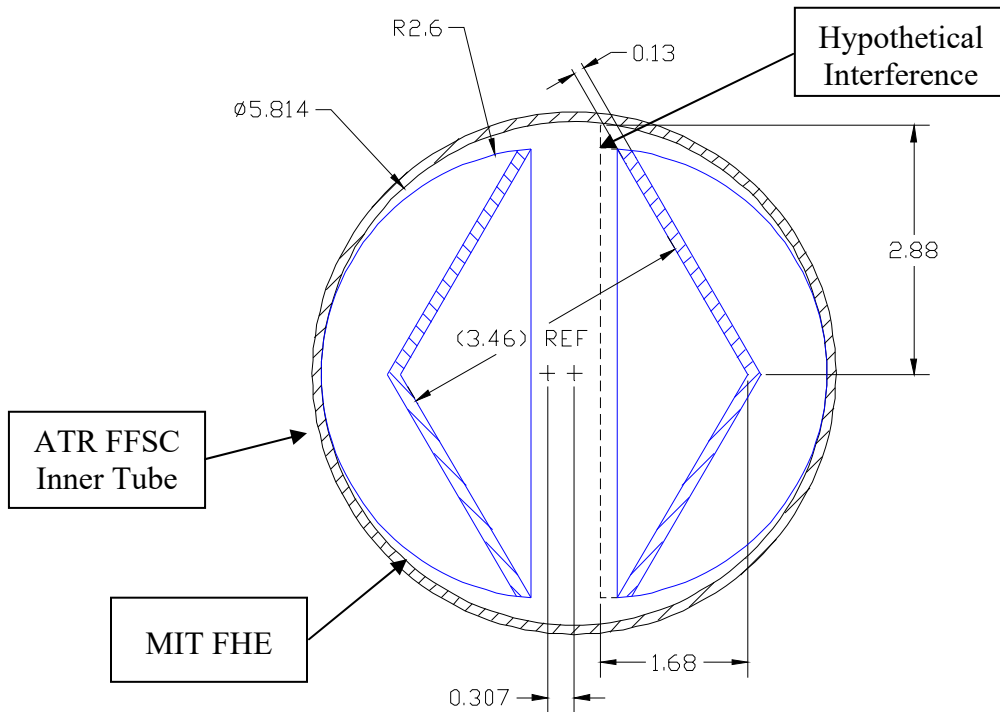
- Neglecting the function of the end spacers, the two halves are pushed apart to the maximum extent to maximize the available space for pitch expansion.
- Although it is not feasible in actual practice to push the FHEs to the center of the array if the two FHE halves are already pushed apart, both the MIT and MURR models are shifted by 0.307-in towards the center of the array.
- Fuel element end boxes are not modeled. For criticality purposes, any amount of damage to the end boxes is acceptable.
- Note that the MIT and MURR FHEs are “sliced off” in the corners because such a translation is not possible without interference.

Due to the conservative assumptions utilized for the thermal and criticality evaluations, the allowable damage to the FHEs is considered severe and therefore far exceeding the physical testing results performed using the ATR fuel element and LFPB payloads covered in Section 2.12.1, *Certification Tests on CTU-1*, and Section 2.12.2, *Certification Tests on CTU-2*.

For containment purposes, the MIT and MURR fuel element plates must remain intact to prevent the fuel meat from within the fuel plate from exiting the package. The MIT and MURR fuel elements are fully supported over the length of the fuel plates by the FHE enclosure halves. The enclosure halves are specifically designed to fully support each fuel element and minimize any deformation or change in the fuel plate geometry. By design the MIT and MURR FHEs are more robust (thicker side walls) than the ATR FHE and therefore provide better support compared to the testing performed using the ATR fuel element and ATR FHE.

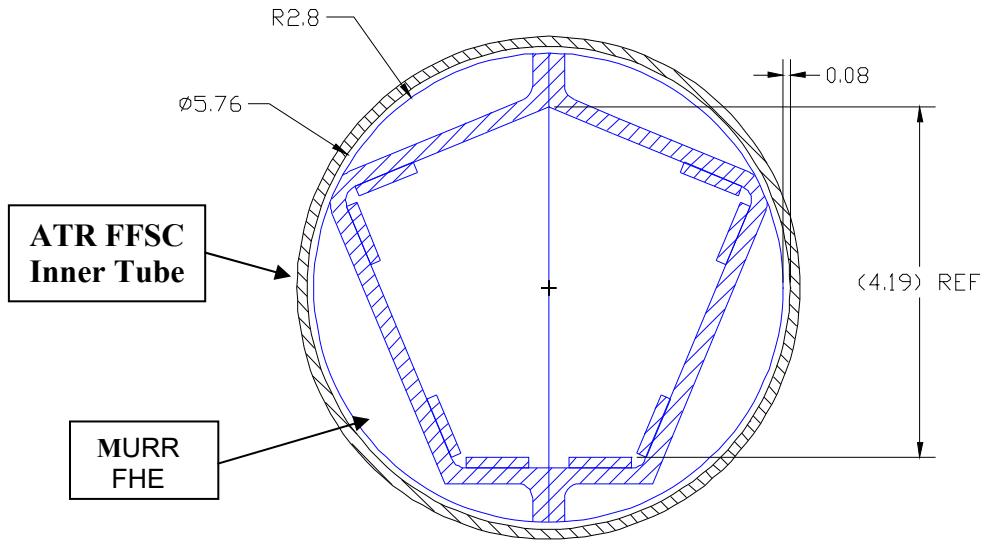


Nominal MIT FHE Dimensions

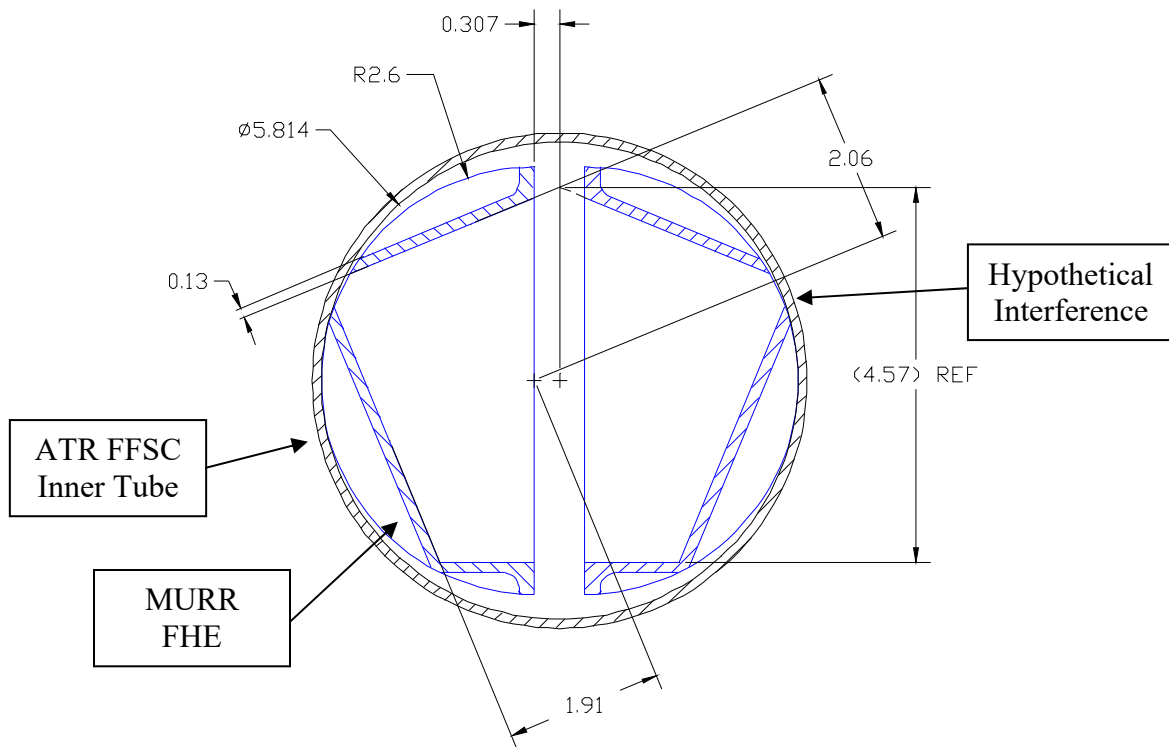


Maximum Tolerances Incorporated to Separate FHE Halves

Figure 2.12.3-3 – MIT FHE Damage



Nominal MURR FHE Dimensions



Maximum Tolerances Incorporated to Separate FHE Halves

Figure 2.12.3-4 – MURR FHE Damage

This page left intentionally blank.

3.0 THERMAL EVALUATION

This chapter identifies and describes the principal thermal design aspects of the ATR FFSC. Further, this chapter presents the evaluations that demonstrate the thermal safety of the ATR FFSC package¹ and compliance with the thermal requirements of 10 CFR 71² when transporting a payload consisting of an assembled, unirradiated fuel element or a payload of loose, unirradiated fuel plates. The payloads are summarized in Table 1.1-1 and described in Section 1.2.2, *Contents*.

Specifically, all package components are shown to remain within their respective temperature limits under the normal conditions of transport (NCT). Further, per 10 CFR §71.43(g), the maximum temperature of the accessible package surfaces is demonstrated to be less than 122 °F for the maximum decay heat loading, an ambient temperature of 100 °F, and no insolation. Finally, the ATR FFSC package is shown to retain sufficient thermal protection following the HAC free and puncture drop scenarios to maintain all package component temperatures within their respective short term limits during the regulatory fire event and subsequent package cool-down.

The analysis in the main body of Chapter 3 pertains only to the ATR HEU fuel element and ATR loose plate basket. The analysis for MIT, MURR, RINSC, Cobra, small quantity payloads, and low enriched uranium fuel elements is contained in Section 3.6, *Thermal Evaluation for MIT, MURR, Cobra, Small Quantity Payloads, and LEU Fuel Elements*.

3.1 Description of Thermal Design

The ATR FFSC package, illustrated in Figure 1.2-1 through Figure 1.2-5 from Section 1.0, *General Information*, consists of three basic components: 1) a Body assembly, 2) a Closure assembly, and 3) either a Fuel Handling Enclosure (FHE) or a Loose Fuel Plate Basket (LFPB). The FHE is configured to house an assembled ATR fuel element, while the LFPB is configured to house loose ATR fuel element plates. The maximum gross weight of the package loaded with an FHE and ATR fuel element is approximately 290 pounds. The maximum gross weight of the package loaded with a LFPB containing its maximum payload is approximately 290 pounds.

The ATR FFSC is designed as a Type AF packaging for transportation of an ATR fuel element or a bundle of loose ATR fuel element plates. The packaging is rectangular in shape and is intended to be transported in racks of multiple packages by highway truck. Since the payload generates essentially no decay heat, the worst case thermal conditions will occur with an individual package fully exposed to ambient conditions. The package performance when configured in a rack of multiple packages will be bounded by that seen for an individual package.

¹ In the remainder of this chapter, the term ‘packaging’ refers to the assembly of components necessary to ensure compliance with the regulatory requirements, but does not include the payload. The term ‘package’ includes both the packaging components and the payload of ATR fuel.

² Title 10, Code of Federal Regulations, Part 71 (10 CFR 71), *Packaging and Transportation of Radioactive Material*, 01-01-21 Edition.

The principal components of the packaging are shown in Figure 1.2-1 and described in more detail below. With the exception of minor components, all steel used in the ATR FFSC packaging is Type 304 stainless steel. Components are joined using full-thickness fillet welds and full and partial penetration groove welds.

3.1.1 Design Features

The primary heat transfer mechanisms within the ATR FFSC are conduction and radiation, while the principal heat transfer from the exterior of the packaging is via convection and radiation to the ambient environment. The Body and Closure assemblies serve as the primary impact and thermal protection for the FHE or the LFPB and their enclosed payloads of an ATR fuel element or loose fuel plates. The FHE and LFPB provide additional thermal shielding of their enclosed payloads during the transient HAC event.

There is no pressure relief system included in the ATR FFSC packaging design. The portions of the packaging that are not directly vented to atmosphere do not contain out-gassing materials. The package insulation is the only non-metallic component located in the enclosed volumes of the package and it is fabricated of a ceramic fiber. The Closure assembly is not equipped with either seals or gaskets so that potential out-gassing of the neoprene material used in ATR fuel tray and the plastic bag material used as a protective sleeve for the fuel element will readily vent without significant pressure build-up in the payload cavity.

The principal thermal design features of each package component are described in the following paragraphs.

3.1.1.1 ATR FFSC Body

The ATR FFSC body is a stainless steel weldment that is approximately 73 inches long and 8 inches square and weighs about 230 lbs (empty). It consists of two nested shells; the outer shell is fabricated of a square stainless steel tube with a 3/16 inch wall thickness, while the inner shell is fabricated from a 6 inch diameter, 0.120 inch wall, stainless steel tube. Three, 1-inch thick stiffening plates (i.e., ribs) are secured to the inner shell by fillet welds at four equally spaced intervals. The ribs are not mechanically attached to the outer shell. Instead, a nominal 0.06 inch air gap exists between the ribs and the outer shell, with a larger nominal gap existing at the corners of the ribs. These design features help to thermally isolate the inner shell from the outer shell during the HAC event.

Further thermal isolation of the inner shell is provided by ceramic fiber thermal insulation which is wrapped around the inner shell between the ribs and by the 28 gauge stainless steel sheet used as a jacket material over the insulation. The insulation is applied in two 0.5-inch thick layers in order to permit over-lapping joints between the layers and prevents direct line-of-sight between the inner shell and the jacket should the insulation shift under normal or accident conditions. The stainless steel jacket maintains the insulation around the inner shell and provides a relatively low emissivity barrier to radiative heat exchange between the insulation and the outer sleeve. The insulation jacket is pre-formed to the design shape and dimensions prior to installation. As such, the potential for inadvertent compression of the insulation during installation is minimized.

Once assembled, the inner shell, ribs, and the jacketed insulation wrap are slid as a single unit into the outer shell and secured to closure plates at both ends by welding. Thermal insulation is

built into the bottom end closure plate of the packaging, while the ATR FFSC closure (see below) provides thermal insulation at the top end closure.

Cross-sectional views showing key elements of the ATR FFSC body are provided in Figure 1.2-2 and Figure 1.2-3. Figure 1.2-2 illustrates a cross sectional view at the top end closure of the package and 1.2-3 presents a similar cross sectional view of the package at the bottom end closure.

3.1.1.2 ATR FFSC Closure

The ATR FFSC closure engages with the body using a bayonet style engagement via four uniformly spaced lugs on the closure that engage with four slots in the mating body feature. The closure incorporates 1 inch of ceramic fiber thermal insulation to provide thermal protection and is designed to permit gas to easily vent through the interface between the closure and the body. The closure weighs approximately 10 pounds and is equipped with a handle to facilitate use with gloved hands.

A cross sectional view of the ATR FFSC closure is illustrated in Figure 1.2-4.

3.1.1.3 Fuel Handling Enclosure (FHE)

The Fuel Handling Enclosure (FHE) is a hinged, aluminum weldment used to protect an ATR fuel element from damage during loading and unloading operations. It is fabricated of thin wall (i.e., 0.09 inch thick) 5052-H32 aluminum sheet and features a hinged lid and neoprene rub strips to minimize fretting of the fuel element side plates where they contact the FHE. The surface of the FHE is neither anodized nor coated, but is left as an 'unfinished' aluminum sheet. Figure 1.2-1 presents an illustration of the FHE. A polyethylene bag is used as a protective sleeve over the ATR fuel element.

3.1.1.4 ATR FFSC Loose Fuel Plate Basket (LFPB)

The Loose Fuel Plate Basket (LFPB) serves to maintain the fuel plates within a defined dimensional envelope during transport. The four identical machined segments are machined from a billet of 6061-T651 aluminum and are joined by threaded fasteners (see Figure 1.2-16). A variable number of ATR fuel plates may be housed in the basket, with the maximum payload weight being limited to 20 lbs. or less. The empty weight of the loose fuel plate basket is approximately 30 lbs. Like the FHE, the surface of the LFPB is neither anodized nor coated, but is left with its 'as machined' finish.

3.1.2 Content's Decay Heat

The ATR FFSC is designed as a Type AF packaging for transportation of an unirradiated ATR fuel element or a bundle of loose, unirradiated ATR fuel plates. The decay heat associated with unirradiated ATR fuel is negligible. Therefore, no special devices or features are needed or utilized in the ATR FFSC packaging to dissipate the decay heat. Section 1.2.2, *Contents*, provides additional details.

3.1.3 Summary Tables of Temperatures

Table 3.1-1 provides a summary of the package component temperatures under normal and accident conditions. The temperatures for normal conditions are based on an analytical model of the ATR FFSC package for extended operation with an ambient temperature of 100°F and a diurnal cycle for the insolation loading. The temperatures for accident conditions are based on an analytical model of the ATR FFSC package with the worst-case, hypothetical pre-fire damage as predicted based on drop tests using full-scale certification test units (CTUs).

The results for NCT conditions demonstrate that significant thermal margin exists for all package components. This is to be expected since the only significant thermal loads on the package arise from insolation and ambient temperature changes. The payload dissipates essentially zero decay heat. Further, the evaluations for NCT demonstrate that the package skin temperature will be below the maximum temperature of 122°F permitted by 10 CFR §71.43(g) for accessible surface temperature in a nonexclusive use shipment when transported in a 100°F environment with no insolation.

The results for HAC conditions also demonstrate that the design of the ATR FFSC package provides sufficient thermal protection to yield component temperatures that are significantly below the acceptable limits defined for each component. While the neoprene rubber and polyethylene plastic material used to protect the ATR fuel element from damage are expected to reach a sufficient temperature level during the HAC fire event to induce some level of thermal degradation (i.e., melting, charring, the chemical breakdown of the materials into 2 or more substances, etc.), the loss of these components is not critical to the safety of the package. Further, the potential combustion of these materials will be restricted due to the lack of available oxygen to the point that any potential temperature rise will be insignificant. See Sections 3.2.2, *Technical Specifications of Components*, 3.4.3.1, *Maximum HAC Temperatures*, and 3.5.3, *Thermal Decomposition/Combustion of Package Organics*, for more discussion.

3.1.4 Summary Tables of Maximum Pressures

Table 3.1-2 presents a summary of the maximum pressures achieved under NCT and HAC conditions. Since the ATR FFSC package is a vented package, both the maximum normal operating pressure (MNOP) and the maximum pressure developed within the payload compartment under the HAC condition are 0 psig.

Although the volume between the outer and inner shells is sealed, it does not contain organic or other materials that may outgas or thermally degrade. Therefore, the maximum pressure that may develop within the space will be limited to that achieved due to ideal gas expansion. The maximum pressure rise under NCT will be less than 4 psig, while the pressure rise under HAC conditions will be 39 psig.

Table 3.1-1 – Maximum Temperatures for NCT and HAC Conditions

Location / Component	NCT Hot Conditions	Accident Conditions	Maximum Allowable ^①	
			Normal	Accident
ATR Fuel Element Fuel Plate	147°F	730°F	400°F	1,100°F
ATR Fuel Element Side Plate	148°F	827°F	400°F	1,100°F
Neoprene Rub Strips/Polyethylene Bag	151°F ^②	1,017°F ^②	225°F	N/A
Fuel Handling Enclosure (FHE)	151°F	1,017°F	400°F	1,100°F
Loose Fuel Plate Basket (LFPB)	151°F ^②	746°F	400°F	1,100°F
Inner Shell	157°F	1,422°F	800°F	2,700°F
Ceramic Fiber Insulation, Body				
- Maximum	185°F	1,460°F	2,300°F	2,300°F
- Average	151°F	1,220°F	2,300°F	2,300°F
Ceramic Fiber Insulation, Closure				
- Maximum	145°F	1,418°F	2,300°F	2,300°F
- Average	144°F	1,297°F	2,300°F	2,300°F
Closure	145°F	1,445°F	800°F	2,700°F
Outer Shell	186°F	1,471°F	800°F	2,700°F

Table Notes:

① Maximum allowable temperatures are defined in Section 3.2.2, *Technical Specifications of Components*.

② Component temperature assumed to be equal to that of the FHE.

Table 3.1-2 – Summary of Maximum Pressures

Condition	Fuel Cavity Pressure	Outer/Inner Shell Cavity Pressure
NCT Hot	0 psi gauge	4 psi gauge
HAC Hot	0 psi gauge	39 psi gauge

3.2 Material Properties and Component Specifications

The ATR FFSC is fabricated primarily of Type 304 stainless steel, 5052-H32 and 6061-T651 aluminum, ceramic fiber insulation, and neoprene rubber. The payload materials include 6061-T6 and/or 6061-0 aluminum, uranium aluminide (UAl_x), and uranium-molybdenum (i.e., U-10Mo in a foil coated with thin zirconium interlayers). A polyethylene plastic bag is used as a protective sleeve over the fuel element.

3.2.1 Material Properties

Table 3.2-1 presents the thermal properties for Type 304 stainless steel and 5052-H32 aluminum from Table TCD of the ASME Boiler and Pressure Vessel Code³. Since the HAC analysis requires thermal properties in excess of the maximum temperature point of 400°F provided in Table TCD for 5052-H32 aluminum, the property values for 1100°F (i.e., the approximate melting point for aluminum) are assumed to be the same as those at 400°F. This approach is appropriate for estimating the temperature rise within the fuel basket during the HAC event since the thermal conductivity of aluminum alloys tends to decrease with temperature while the specific heat tends to increase. The density values listed in the table are taken from an on-line database⁴. Properties between the tabulated values are calculated via linear interpolation within the heat transfer code.

Table 3.2-2 presents the thermal properties for the ATR fuel element. For analysis purposes, the material used for the side plates, covers, and fuel cladding are assumed to be 6061-0 aluminum. The thermal properties for the fuel plates are determined as a composite of the cladding and the fuel core materials based on the geometry data for the ATR fuel element⁵ and the thermal properties for the ATR fuel element materials⁶. The details of the computed values are presented in Section 3.5.2.4, *Determination of Composite Thermal Properties for ATR Fuel Plates*. For simplicity and given the low sensitivity to temperature, a conservatively high, fixed thermal conductivity value is used for the fuel plates in order to maximize the heat transfer into the fuel components during the HAC event. The specific heat values are computed as a function of temperature to more accurately capture the change in thermal mass for the fuel plates during the HAC event.

The thermal properties for the non-metallic materials used in the ATR FFSC are presented in Table 3.2-3. The thermal properties for neoprene rubber are based on the *Polymer Data Handbook*⁷, while the thermal properties for the ceramic fiber insulation are based on the Unifrax Durablanket[®] S insulation product⁸ with a nominal density of 6 lb/ft³. The thermal properties are for the uncompressed material in both cases. Although the package design requires that the insulation blanket be compressed by up to 20% at the quadrant points, ignoring

³ American Society of Mechanical Engineers (ASME) Boiler and Pressure Vessel Code, Section II, *Materials, Part D – Properties*, Table TCD, Material Group J, 2001 Edition, 2002 and 2003 Addenda, New York

⁴ Matweb, Online Material Data Sheets, www.matweb.com.

⁵ *ATR Mark VII Fuel Element Assembly*, INEEL Drawing No. DWG-405400.

⁶ *Thermophysical And Mechanical Properties Of ATR Core Materials*, Report No. PG-T-91-031, August 1991, EG&G Idaho, Inc.

⁷ *Polymer Data Handbook*, Oxford University Press, Inc., 1999.

⁸ Unifrax DuraBlanket S ceramic fiber insulation, Unifrax Corporation, Niagara Falls, NY.

the compression for the purposes of the thermal modeling and using the thermal properties for the uncompressed material at all locations provides a conservative estimate of the package's performance under the HAC condition. This conclusion arises from the fact that the insulation's thermal conductivity decreases with density for temperatures above approximately 500°F (see Table 3.2-3). For example, the thermal conductivity of 8 pcf insulation at 1000°F and 1400°F is 0.0814 and 0.1340 Btu/hr-ft-°F, respectively, versus the 0.0958 and 0.1614 Btu/hr-ft-°F values for 6 pcf insulation at the same temperatures. While compression will increase conductivity below 500°F, ignoring the effects of compression for NCT conditions has an insignificant effect since the peak package temperatures occur in the vicinity of the ribs and are therefore unaffected by a local increase in the thermal conductivity of the insulation. Further, large thermal margins exist for the NCT conditions.

The thermal properties for air presented in Table 3.2-4 are derived from curve fits⁹. Because the thermal conductivity of air varies significantly with temperature, the computer model calculates the thermal conductivity across thin air filled gaps as a function of the mean gap temperature. All void spaces within the ATR FFSC package are assumed to be filled with air at atmospheric pressure.

Table 3.2-5 and Table 3.2-6 present the assumed emissivity (ϵ) for each radiating surface and the solar absorptivity (α) value for the exterior surface. The emissivity of 'as-received' Type 304 stainless steel has been measured¹⁰ as 0.25 to 0.28, while the emissivity of weathered Type 304 stainless steel has been measured¹¹ from 0.46 to 0.50. For the purpose of this analysis, an emissivity of 0.30 is assumed for the emittance from all interior radiating stainless steel surfaces, while the emissivity for the exterior surfaces of the package is assumed to be 0.45. The solar absorptivity of Type 304 stainless steel is approximately 0.52¹². Under HAC conditions, the outside of the package is assumed to attain an emissivity of 0.8 in compliance with 10 CFR §71.73(c)(4) and to have a solar absorptivity of 0.9 to account for the possible accumulation of soot.

The 5052-H32 aluminum sheet used to fabricate the FHE will be left with a plain finish while the 6061-T651 billets used to fabricate the Loose Fuel Plate Basket will have a machined surface. The emissivity for either type of finish can be expected to be low (i.e., 0.10 or lower)¹² however, for conservatism, an emissivity of 0.25¹² representative of a heavily oxidized surface is assumed for this evaluation. The 6061-0 aluminum used for the ATR fuel components are assumed to have a surface coating of boehmite ($\text{Al}_2\text{O}_3\cdot\text{H}_2\text{O}$). A 25 μm boehmite film will exhibit a surface emissivity of approximately 0.92¹³. While a fresh fuel element may have a lower surface emissivity, the use of the higher value will provide a conservative estimate of the temperatures achieved during the HAC event.

⁹ Rohsenow, Hartnett, and Cho, *Handbook of Heat Transfer*, 3rd edition, McGraw-Hill Publishers, 1998.

¹⁰ Frank, R. C., and W. L. Plagemann, *Emissivity Testing of Metal Specimens*. Boeing Analytical Engineering coordination sheet No. 2-3623-2-RF-C86-349, August 21, 1986. Testing accomplished in support of the TRUPACT-II design program.

¹¹ "Emissivity Measurements of 304 Stainless Steel", Azzazy, M., prepared for Southern California Edison, September 6, 2000, Transnuclear File No. SCE-01.0100.

¹² G. G. Gubareff, J. E. Janssen, and R. H. Torborg, *Thermal Radiation Properties Survey*, 2nd Edition, Honeywell Research Center, 1960.

¹³ *Heat Transfer in Window Frames with Internal Cavities*, PhD Thesis for Arild Gustavsen, Norwegian University of Science and Technology, Trondheim, Norway, September 2001.

The ceramic fiber insulation has a surface emissivity of approximately 0.90¹² based on a combination of the material type and surface roughness. The same emissivity is assumed for the neoprene rubber.

3.2.2 Technical Specifications of Components

The materials used in the ATR FFSC that are considered temperature sensitive are the aluminum used for the FHE, the LFPB, and the ATR fuel, the neoprene rubber, and the polyethylene wrap used as a protective sleeve around the ATR fuel element. Of these materials, only the aluminum used for the ATR fuel element is considered critical to the safety of the package. The other materials either have temperature limits above the maximum expected temperatures or are not considered essential to the function of the package.

Type 304 stainless steel has a melting point above 2,700°F⁴, but in compliance with the ASME B&PV Code¹⁴, its allowable temperature is limited to 800°F if used for structural purposes. However, the ASME temperature limit generally applies only to conditions where the material's structural properties are relied on for loads postulated to occur in the respective operating mode or load combination (such as the NCT and HAC free drops). Since the package is vented to atmosphere, no critical structural condition exists following the HAC free drop events and, as such, the appropriate upper temperature limit is 800°F for normal conditions and 2,700°F for accident conditions

Aluminum (5052-H32, 6061-0/6061-T6) has a melting point of approximately 1,100°F⁴ however for strength purposes the normal operational temperature should be limited to 400°F³.

The ceramic fiber insulation has a manufacturer's recommended continuous use temperature limit of 2,300°F⁸. There is no lower temperature limit.

The polyethylene plastic wrap used as a protective sleeve around the ATR fuel element has a melting temperature of approximately 225 to 250°F⁴. For the purposes of this analysis, the lower limit of 225°F is used. As a thermoplastic, the polyethylene wrap will melt and sag onto the fuel element when exposed to temperatures in excess of 250°F. Further heating could lead to charring (i.e., oxidation in the absence of open combustion) and then thermal decomposition into its volatile components. Thermal decomposition will begin at approximately 750°F. Unpiloted, spontaneous ignition could occur at temperatures of approximately 650°F¹⁵ or higher. The plastic wrap is approximately 7 inches wide (when pressed flat), 67.5 inches long, and weights approximately 3 oz. As demonstrated in Section 3.5.3, *Thermal Decomposition/Combustion of Package Organics*, the available oxygen in the package is sufficient for consumption of less than 1% of the polyethylene. Loss of the plastic wrap is of no consequence to the thermal safety of the ATR FFSC since its effect on conductive and radiative heat transfer is negligible.

The neoprene rub strips used to minimize fretting of the fuel element side plates have a continuous temperature rating of 200 to 250°F and a short term (i.e., 0.5 hour or less) temperature

¹⁴ American Society of Mechanical Engineers (ASME) Boiler & Pressure Vessel Code, Section III, *Rules for Construction of Nuclear Facility Components*, Division 1, Subsection NB, *Class 1 Components*, & Subsection NG, *Core Support Structures*, 2001 Edition, 2002 Addendum.

¹⁵ Troitzsch, J., *Plastics Flammability Handbook*, 2nd Edition, Oxford University Press, New York, 1990.

limit of approximately 525°F¹⁶. For the purposes of this analysis, a limit of 225°F is used for NCT conditions, while a peak temperature of 525°F is assumed for HAC conditions before thermal degradation begins. Since neoprene is a thermoset polymer, it will not melt, but decompose into volatiles as it degrades. The same limitation on oxygen affecting the combustion of polyethylene also affects neoprene. As discussed in Section 3.5.3, *Thermal Decomposition/Combustion of Package Organics*, the thermal damage expected for the neoprene material is expected to be limited to potential de-bonding from the FHE surfaces and a very limited thermal decomposition. Loss of the neoprene rub strips is of no consequence to the thermal safety of the ATR FFSC.

The minimum allowable service temperature for all ATR FFSC components is below -40 °F.

¹⁶ Parker O-Ring Handbook, ORD 5700/USA, 2001, www.parker.com.

Table 3.2-1 – Thermal Properties of Package Metallic Materials

Material	Temperature (°F)	Thermal Conductivity (Btu/hr-ft-°F)	Specific Heat (Btu/lb _m -°F)	Density (lb _m /in ³)
Stainless Steel Type 304	70	8.6	0.114	0.289
	100	8.7	0.115	
	200	9.3	0.119	
	300	9.8	0.123	
	400	10.4	0.126	
	500	10.9	0.128	
	600	11.3	0.130	
	700	11.8	0.132	
	800	12.2	0.133	
	1000	13.2	0.136	
	1200	14.0	0.138	
	1400	14.9	0.141	
	1500	15.3	0.142	
Aluminum Type 5052-H32	70	79.6	0.214	0.097
	100	80.8	0.216	
	150	82.7	0.219	
	200	84.4	0.222	
	250	85.9	0.225	
	300	87.2	0.227	
	350	88.4	0.229	
	400	89.6	0.232	
	1100 ^①	89.6	0.232	

Notes:

① Values for 1100°F are assumed equal to values at 400°F.

Table 3.2-2 – Thermal Properties of ATR Fuel Materials

Material	Temperature (°F)	Thermal Conductivity (Btu/hr-ft-°F)	Specific Heat (Btu/lb _m -°F)	Density (lb _m /in ³)
Aluminum Type 6061-0	32	102.3	-	0.0976
	62	-	0.214	
	80	104.0	-	
	170	107.5	-	
	260	109.2	0.225	
	350	109.8	-	
	440	110.4	0.236	
	530	110.4	-	
	620	109.8	0.247	
	710	108.6	-	
	800	106.9	0.258	
	890	105.2	-	
	980	103.4	0.269	
	1080	101.1	0.275	
ATR Fuel Plate 1 ^①	80	60.5	0.177	0.114
	800		0.213	
ATR Fuel Plates 2 and 18 ^①	80	78.5	0.189	0.108
	800		0.228	
ATR Fuel Plates 3,4,16 & 17 ^①	80	76.2	0.182	0.112
	800		0.220	
ATR Fuel Plates 5 to 15 ^①	80	74.6	0.176	0.115
	800		0.212	
ATR Fuel Plate 19 ^①	80	54.5	0.173	0.115
	800		0.209	

Notes:

- ① Values determined based on composite value of aluminum cladding and fuel core material (see Appendix 3.5.2.4). Thermal conductivity value is valid for axial and circumferential heat transfer within fuel plate.

Table 3.2-3 – Thermal Properties of Non-Metallic Materials

Material	Temperature (°F)	Thermal Conductivity (Btu/hr-ft-°F)	Specific Heat (Btu/lb _m -°F)	Density (lb _m /ft ³)	Comments
Neoprene ^①	---	0.11	0.52	76.8	
Ceramic Fiber Insulation ^②	70	0.0196	0.28	6	
	200	0.0238			
	400	0.0343			
	600	0.0499			
	800	0.0703			
	1000	0.0958			
	1200	0.1262			
	1400	0.1614			
	1600	0.2017			
Ceramic Fiber Insulation ^{② ③}	70	0.0300	0.28	8	
	200	0.0313			
	400	0.0369			
	600	0.0463			
	800	0.0620			
	1000	0.0814			
	1200	0.1053			
	1400	0.1340			
	1600	0.1669			

Notes:

- ① Conductivity value represents uncompressed neoprene.
- ② Conductivity values are for uncompressed insulation. Compression of the material will increase the thermal conductivity for temperatures below approximately 500°F where conduction dominates and decrease the thermal conductivity for temperatures above 500°F where heat transfer via radiation dominates.
- ③ 8 pcf ceramic fiber insulation is not used in the ATR FFSC Package. Data is provided for comparison purposes to demonstrate the effect of insulation compression on thermal conductivity.

Table 3.2-4 – Thermal Properties of Air

Temperature (°F)	Density lb _m /in ³ ¹	Specific Heat (Btu/lb _m -°F)	Dynamic Viscosity (lb _m /ft-hr)	Thermal Conductivity (Btu/hr-ft-°F)	Prandtl Number ²	Coef. Of Thermal Exp. (°R ⁻¹) ³
-40	Use Ideal Gas Law w/ Molecular wt = 28.966	0.240	0.03673	0.0121	Compute as Pr = c _p μ / k	Compute as β = 1/(°F+459.67)
0		0.240	0.03953	0.0131		
50		0.240	0.04288	0.0143		
100		0.241	0.04607	0.0155		
200		0.242	0.05207	0.0178		
300		0.243	0.05764	0.0199		
400		0.245	0.06286	0.0220		
500		0.248	0.06778	0.0240		
600		0.251	0.07242	0.0259		
700		0.253	0.07680	0.0278		
800		0.256	0.08098	0.0297		
900		0.259	0.08500	0.0315		
1000		0.262	0.08887	0.0333		
1200		0.269	0.09620	0.0366		
1400		0.274	0.10306	0.0398		
1500		0.277	0.10633	0.0412		

Table Notes:

- 1) Density computed from ideal gas law as $\rho = PM/RT$, where R= 1545.35 ft-lbf/lb-mole-R, T= temperature in °R, P= pressure in lbf/ft², and M= molecular weight of air. For example, at 100°F and atmospheric pressure of 14.69lbf/in², $\rho = (14.69 \cdot 144 \text{ in}^2/\text{ft}^2 \cdot 28.966 \text{ lbm/lb-mole}) / 1545.35 \cdot (100 + 459.67) = 0.071 \text{ lbm/ft}^3 = 4.099 \times 10^{-5} \text{ lbm/in}^3$.
- 2) Prandtl number computed as $Pr = c_p \mu / k$, where c_p = specific heat, μ = dynamic viscosity, and k = thermal conductivity. For example, at 100°F, $Pr = 0.241 \cdot 0.04607 / 0.0155 = 0.72$.
- 3) Coefficient of thermal expansion is computed as the inverse of the absolute temperature. For example, at 100°F, $\beta = 1 / (100 + 459.67) = 0.00179$.

Table 3.2-5 – NCT Thermal Radiative Properties

Material	Assumed Conditions	Assumed Emissivity (ϵ)	Absorptivity (α)
Outer Shell, Exterior Surfaces (Type 304 Stainless Steel)	Weathered	0.45	0.52
Outer Shell, Interior Surface and Inner Shell (Type 304 Stainless Steel)	'As- Received'	0.3	---
Ceramic Fiber Insulation & Neoprene	---	0.90	---
Fuel Handling Enclosure and Loose Fuel Plate Basket (6061-T651 & 5052-H32 Aluminum)	Oxidized	0.25	---
ATR Fuel Side Plates and Fuel Cladding (6061-0 Aluminum)	Boehmite film	0.92	---
Ambient Environment	---	1.00	N/A

Table 3.2-6 – HAC Thermal Radiative Properties

Material	Assumed Conditions	Assumed Emissivity (ϵ)	Absorptivity (α)
Outer Shell, Exterior Surfaces (Type 304 Stainless Steel)	Sooted/Oxidized	0.80	0.90
Outer Shell, Interior Surface and Inner Shell (Type 304 Stainless Steel)	Slightly Oxidized	0.45	---
Ceramic Fiber Insulation & Neoprene	---	0.90	---
Fuel Handling Enclosure and Loose Fuel Plate Basket (6061-T651 & 5052-H32 Aluminum)	Oxidized	0.25	---
ATR Fuel Side Plates and Fuel Cladding (6061-0 Aluminum)	Boehmite film	0.92	---
Ambient Environment	---	1.00	N/A

3.3 Thermal Evaluation for Normal Conditions of Transport

This section presents the thermal evaluation of the ATR FFSC for normal conditions of transport (NCT). Under NCT, the package will be transported horizontally. This establishes the orientation of the exterior surfaces of the package for determining the free convection heat transfer coefficients and insolation loading. While the package would normally be transported in tiered stacks of multiple packages, the evaluation for NCT is conservatively based on a single, isolated package since this approach will yield the bounding maximum and minimum temperatures achieved by any of the packages. Further, the surface of the transport trailer is conservatively assumed to prevent heat exchange between the package and the ambient. Thus, the bottom of the ATR FFSC is conservatively treated as an adiabatic surface.

The details of the thermal modeling used to simulate the ATR FFSC package under NCT conditions are provided in Appendix 3.5.2, *Analytical Thermal Model*.

3.3.1 Heat and Cold

3.3.1.1 Maximum Temperatures

The maximum temperature distribution for the ATR FFSC occurs with a diurnal cycle for insolation loading and an ambient air temperature of 100°F, per 10 CFR §71.71(c)(1). The evaluation of this condition is conducted as a transient using the thermal model of an undamaged ATR FFSC described in Appendix 3.5.2.1, *Description of Thermal Model for NCT Conditions*. Figure 3.3-1 and Figure 3.3-2 illustrate the expected heat-up transient for an ATR FFSC loaded with an ATR fuel element. The transient analysis assumes a uniform temperature condition of 70°F for all components prior to loading and exposure to the specified NCT condition at time = 0. The figures demonstrate that the ATR FFSC package will respond rapidly to changes in the level of insolation and will reach its peak temperatures within the first day or two after loading. Table 3.3-1 presents the maximum temperatures reached for various components of the package. As seen from the table, all components are within their respective temperature limits. Figure 3.3-3 illustrates the predicted temperature distribution within the ATR FFSC package at the time of peak temperature.

The maximum temperature distribution for the ATR FFSC without insolation loads occurs with an ambient air temperature of 100°F. Since the package payload dissipates essentially zero watts of decay heat, the thermal analysis of this condition represents a trivial case and no thermal calculations are performed. Instead, it is assumed that all package components achieve the 100°F temperature under steady-state conditions. The resulting 100°F package skin temperature is below the maximum temperature of 122°F permitted by 10 CFR §71.43(g) for accessible surface temperature in a nonexclusive use shipment.

3.3.1.2 Minimum Temperatures

The minimum temperature distribution for the ATR FFSC occurs with a zero decay heat load and an ambient air temperature of -40°F per 10 CFR §71.71(c)(2). The thermal analysis of this condition also represents a trivial case and no thermal calculations are performed. Instead, it is assumed that all package components achieve the -40°F temperature under steady-state conditions.

As discussed in Section 3.2.2, *Technical Specifications of Components*, the -40°F temperature is within the allowable operating temperature range for all ATR FFSC package components.

3.3.2 Maximum Normal Operating Pressure

The payload cavity of the ATR FFSC is vented to the atmosphere. As such, the maximum normal operating pressure (MNOP) for the package is 0 psig.

While the volume between the outer and inner shells is sealed, it does not contain organic or other materials that may outgas or thermally degrade. Therefore, the maximum pressure that may develop within the space will be limited to that achieved due to ideal gas expansion.

Assuming a temperature of 70°F at the time of assembly and a maximum operating temperature of 190°F (based on the outer shell temperature, see Table 3.3-1, conservatively rounded up), the maximum pressure rise within the sealed volume will be less than 4 psi.

Table 3.3-1 - Maximum Package NCT Temperatures

Location / Component	NCT Hot Conditions	Maximum Allowable^①
ATR Fuel Element Fuel Plate	147°F	400°F
ATR Fuel Element Side Plate	148°F	400°F
Neoprene Rub Strips/Polyethylene Bag	151°F ^②	225°F
Fuel Handling Enclosure (FHE)	151°F	400°F
Loose Fuel Plate Basket (LFPB)	151°F ^②	400°F
Inner Shell	157°F	800°F
Ceramic Fiber Insulation, Body		
- Maximum	185°F	2,300°F
- Average	151°F	2,300°F
Ceramic Fiber Insulation, Closure		
- Maximum	145°F	2,300°F
- Average	144°F	2,300°F
Closure	145°F	800°F
Outer Shell	186°F	800°F

Table Notes:

- ① The maximum allowable temperatures under NCT conditions are provided in Section 3.2.2, Technical Specifications of Components.
- ② Component temperature assumed to be equal to that of the FHE.

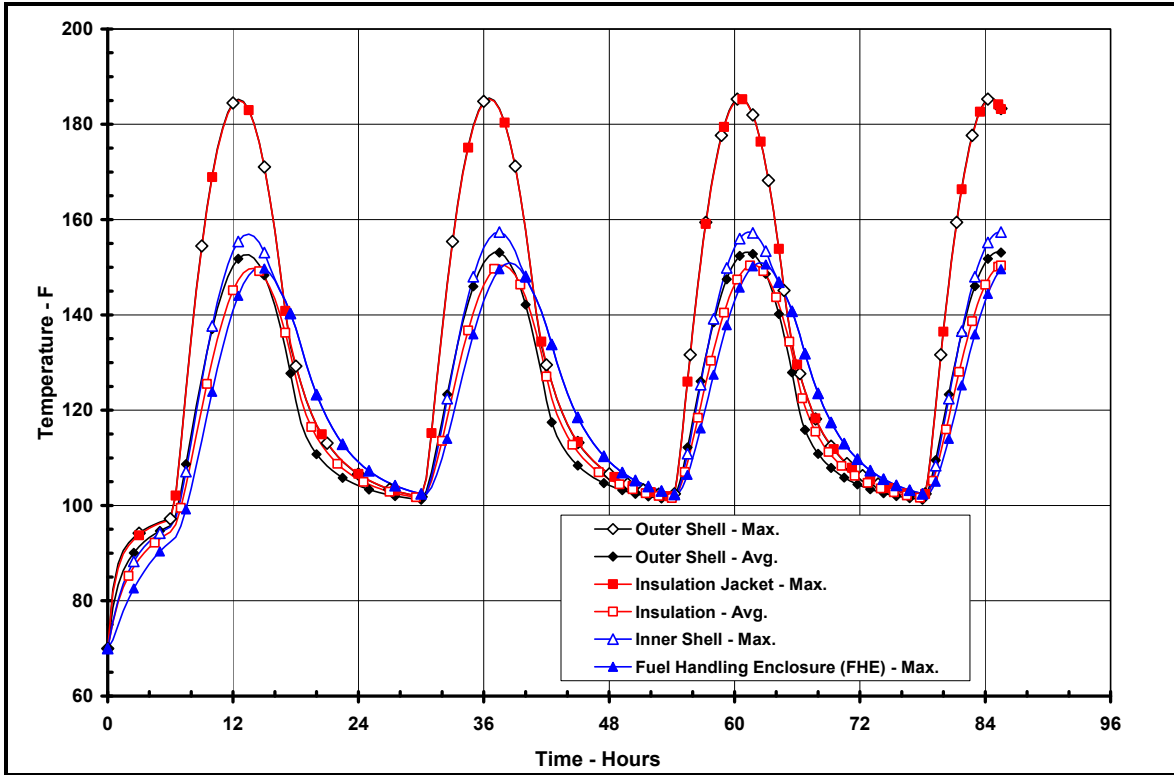


Figure 3.3-1 – ATR FFSC Package Heat-up, NCT Hot Conditions

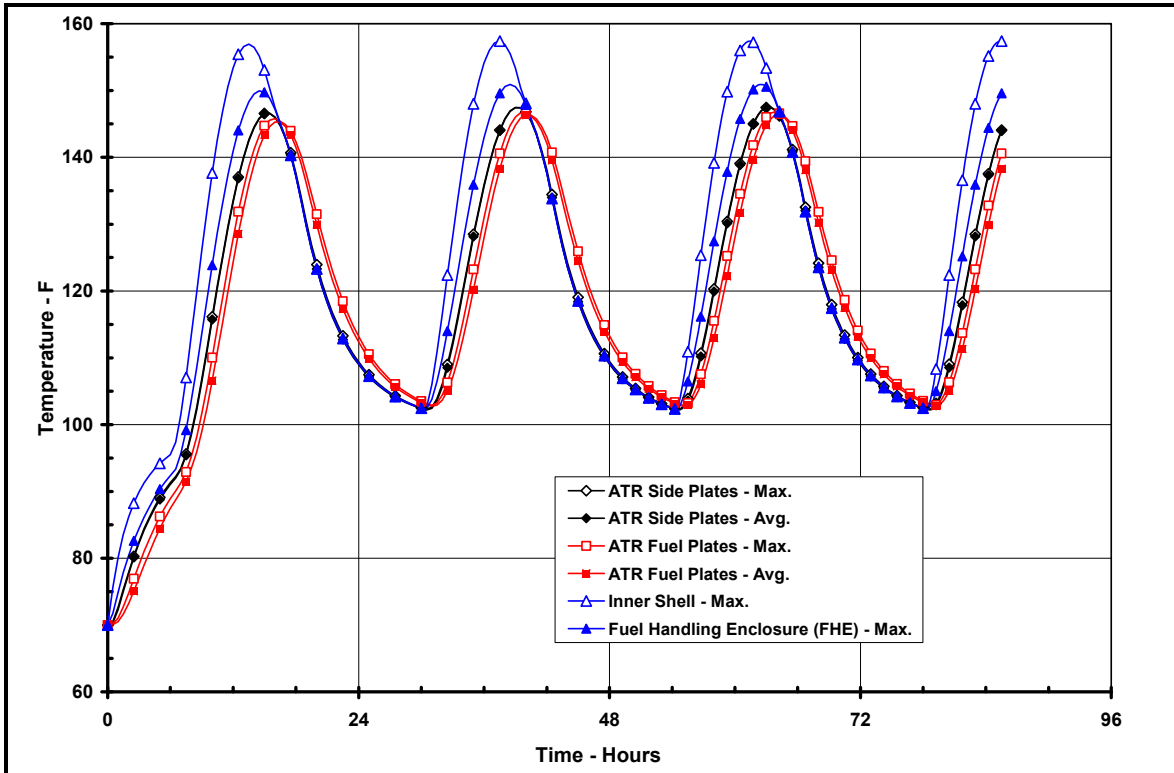


Figure 3.3-2 – ATR Fuel Element Heat-up, NCT Hot Conditions

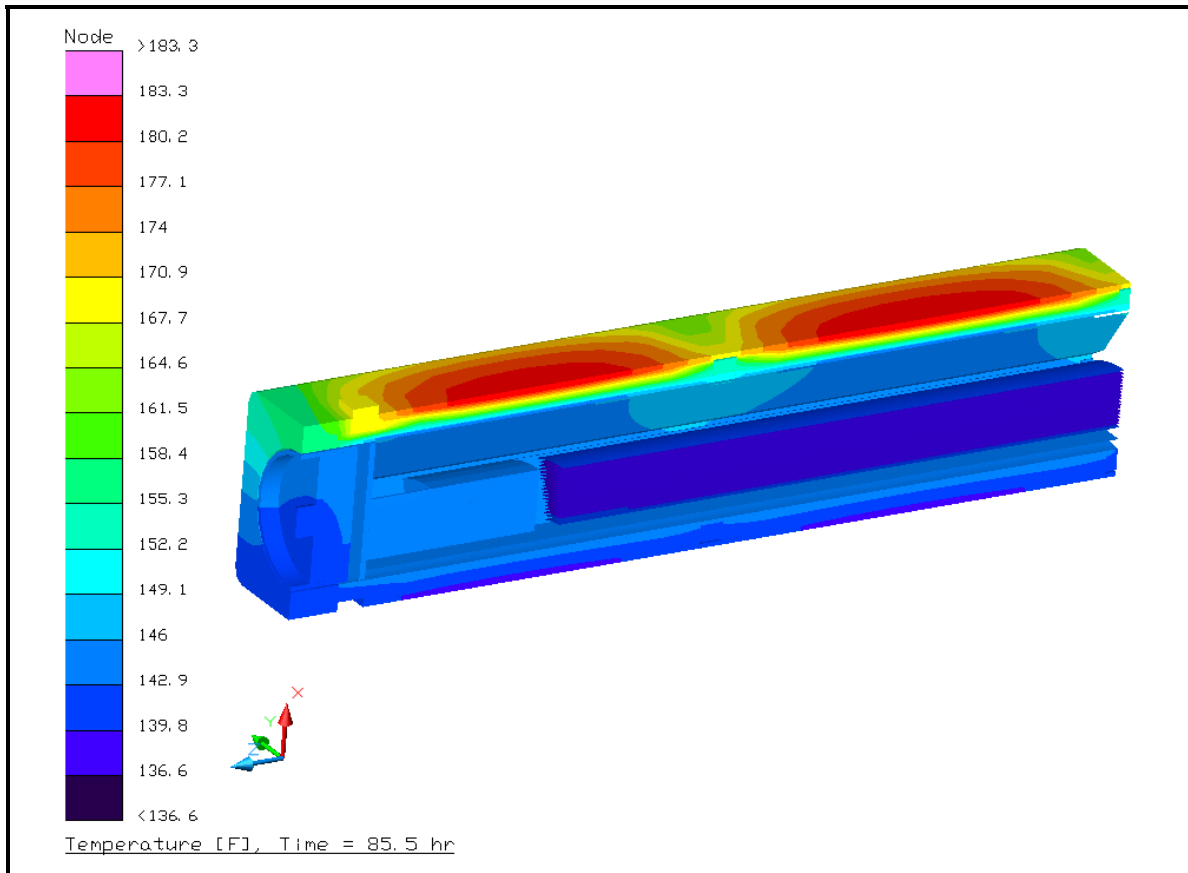


Figure 3.3-3 – Package NCT Temperature Distribution

3.4 Thermal Evaluation for Hypothetical Accident Conditions

This section presents the thermal evaluation of the ATR FFSC package under the hypothetical accident condition (HAC) specified in 10 CFR §71.73(c)(4) based on an analytical thermal model of the ATR FFSC. The analytical model for HAC is a modified version of the quarter symmetry NCT model described in Section 3.5.2.1, *Description of Thermal Model for NCT Conditions*, with the principal model modifications consisting of simulating the expected package damage resulting from the drop events that are assumed to precede the HAC fire and changing the package surface emissivities to reflect the assumed presence of soot and/or surface oxidization.

Physical testing using full scale certified test units (CTUs) is used to establish the expected level of damage sustained by the ATR FFSC package from the 10 CFR 71.73 prescribed free and puncture drops that are assumed to precede the HAC fire event. Appendix 2.12.1, *Certification Tests on CTU-1* and Appendix 2.12.2, *Certification Tests on CTU-2* provide the configuration and initial conditions of the test articles, the test facilities and instrumentation used, and the test results. Section 3.5.2.2, *Description of Thermal Model for HAC Conditions*, provides an overview of the test results, the rationale for selecting the worst-case damage scenario, and the details of the thermal modeling used to simulate the package conditions during the HAC fire event.

3.4.1 Initial Conditions

The initial conditions assumed for the package prior to the HAC event are described below in terms of the modifications made to the NCT thermal model to simulate the assumed package conditions prior to and during the HAC event. These modifications are:

- Simulated the worst-case damage arising from the postulated HAC free and puncture drops as described in Section 3.5.2.2, *Description of Thermal Model for HAC Conditions*,
- Assume an initial, uniform temperature distribution of 100°F based on a zero decay heat package at steady-state conditions with a 100°F ambient with no insolation. This assumption complies with the requirement of 10 CFR §71.73(b)² and NUREG-1609¹⁷,
- Increased the emissivity of the external surfaces from 0.45 to 0.8 to account for possible soot accumulation on the surfaces, per 10 CFR §71.73(c)(4),
- Increased the emissivity of the interior surfaces of the outer shell from 0.30 to 0.45 to account for possible oxidization of the surfaces during the HAC event,

Following the free and puncture bar drops, the ATR FFSC package is assumed come to rest in a horizontal position prior to the initiation of the fire event. Since the package geometry is essentially symmetrical about its axial axis, there are no significant thermal differences whether the

¹⁷ NUREG-1609, *Standard Review Plan for Transportation Packages for Radioactive Material*, §3.5.5.1, U.S. Regulatory Commission, Office of Nuclear Materials Safety and Standards, March 1999.

package is right-side up, up-side down, or even on its end. The potential for the ATR fuel element payload being re-positioned depending upon the package orientation is not significant to the peak temperatures developed under HAC conditions given the modeling approach used to compute the heat transfer from the inner shell to the ATR fuel element. Therefore, the peak package temperatures predicted under this evaluation are representative of those achieved for any package orientation.

3.4.2 Fire Test Conditions

The fire test conditions analyzed to address the 10 CFR §71.73(c) requirements are as follows:

- The initial ambient conditions are assumed to be 100°F ambient with no insolation,
- At time = 0, a fully engulfing fire environment consisting of a 1,475°F ambient with an emissivity of 1.0 is used to simulate the hydrocarbon fuel/air fire event. The assumption of a flame emissivity of 1.0 bounds the minimum average flame emissivity coefficient of 0.9 specified by 10 CFR §71.73(c)(4),
- The convection heat transfer coefficients between the package and the ambient during the 30-minute fire event are based on an average gas velocity¹⁸ of 10 m/sec. Following the 30-minute fire event the convection coefficients are based on still air,
- The ambient condition of 100°F with insolation is assumed following the 30-minute fire event. Since a diurnal cycle is used for insolation, the evaluation assumes that the 30-minute fire begins at noon so as to maximize the insolation heating during the post-fire cool down period. A solar absorptivity of 0.9 is assumed for the exterior surfaces to account for potential soot accumulation on the package surfaces.

The transient analysis is continued for 11.5 hours after the end of the 30-minute fire to ensure that the peak package temperatures are captured.

3.4.3 Maximum Temperatures and Pressure

3.4.3.1 Maximum HAC Temperatures

The outer shell and the ceramic fiber insulation provide thermal protection to the ATR FFSC package during the HAC fire event. The level of thermal protection can be seen via the thermal response curves presented in Figure 3.4-1 and Figure 3.4-2. As illustrated in the figures, while the exterior of the package quickly rises to nearly the temperature of the fire, the heat flow to the FHE and its enclosed ATR fuel element payload is sufficiently restricted that the maximum temperatures of both the FHE and the ATR fuel element are well below the melting point of aluminum. This result occurs despite the conservative assumption of direct contact between the FHE and the inner shell at 3 locations (e.g., the equivalent of four locations for a full model).

¹⁸ Schneider, M.E and Kent, L.A., *Measurements Of Gas Velocities And Temperatures In A Large Open Pool Fire, Heat and Mass Transfer in Fire* - HTD Vol. 73, 1987, ASME, New York, NY.

This level of thermal protections is further illustrated by the perspective views presented in Figure 3.4-3 and Figure 3.4-4 of the temperature distribution in the ATR FFSC package after 30 minutes of exposure to the HAC fire and at the point when the peak ATR fuel element temperature is attained (approximately 22 minutes after the end of the fire). The figures show that the ceramic fiber insulation limits the elevated temperatures resulting from the fire event to regions adjacent to the outer shell. The assumed absence of the ceramic fiber insulation adjacent to the ribs as a result of the pre-fire free drop event can be seen in each figure.

A similar thermal performance is seen for the package when loaded with the Loose Fuel Plate Basket (LFPB). Figure 3.4-5 presents the thermal response curve, while Figure 3.4-6 and Figure 3.4-7 present perspective views of the temperature distribution in the ATR FFSC package after 30 minutes of exposure to the HAC fire and at the point when the peak LFPB temperature is attained (approximately 22 minutes after the end of the fire). A lower maximum temperature is achieved in the LFPB vs. that seen for the FHE because of the higher thermal mass associated with the LFPB. Further, since the LFPB is modeled without its payload of loose fuel plates, these results will bound those seen for a LFPB with a payload.

Table 3.4-1 presents the component temperatures seen prior to the fire, at the end of the 30-minute fire event, and the peak temperature achieved during the entire simulated HAC thermal event. As seen, all temperatures are within their allowable limit. It is expected that the neoprene rub strips and the polyethylene bag used as a protective sleeve for the ATR fuel element will thermally degrade due to the level of temperature achieved. In the case of the polyethylene bag, the bag is expected to melt and sag onto the fuel element when exposed to temperatures in excess of 250°F. Further heating will lead to charring and then thermal decomposition into its volatile components. While spontaneous ignition is unexpected under the unpiloted conditions, the effect would be minimal since, per Section 3.5.3, *Thermal Decomposition/Combustion of Package Organics*, the available oxygen in the package is sufficient for consumption of less than 1% of the polyethylene. As a thermoset polymer, the neoprene is expected to simply decompose into volatiles as it thermally degrades. These components are not critical to the safety of the package and any out-gassing associated with their thermal degradation will not contribute to package pressurization since package is vented.

The results presented above also demonstrate that inclusion of insulation effects prior to the fire would not have affected the safety basis of the design. The low thermal mass of the package effectively mitigates the HAC impact of higher initial component temperatures due to insulation. As seen from Table 3.3-1, consideration of the maximum insulation loading raises the package component temperatures by approximately 50°F above the initial 100°F level assumed by the HAC evaluation. The thermal response curves presented in Figures 3.4-1 and 3.4-2 demonstrate that the fire condition recovers this 50°F temperature difference for the outer components within the first few seconds of fire exposure. Further, since all package components exhibit thermal margins greater than 50°F as shown in Table 3.4-1, the inclusion of insulation effects prior to the fire event would not have impacted the safety basis for the design.

3.4.3.2 Maximum HAC Pressures

The payload cavity of the ATR FFSC is vented to the atmosphere. As such, the maximum pressure achieved under the HAC event will be 0 psig. Section 3.5.3, *Thermal*

Decomposition/Combustion of Package Organics, provides the justification for assuming a 0 psig package pressure for the HAC event.

Although the volume between the outer and inner shells is sealed, it does not contain organic or other materials that may outgas or thermally degrade. Assuming a temperature of 70°F at the time of assembly and a maximum temperature of 1,475°F (based on the outer shell temperature, see Table 3.4-1), the maximum pressure rise within the sealed volume due to ideal gas expansion will be less than 39 psig. This level of pressurization will occur for only a few minutes and then quickly reduce as the package cools.

3.4.4 Maximum Thermal Stresses

The temperature difference between the inner and outer shells during the HAC event (see the average inner and outer shell temperatures presented in Figure 3.4-1) will result in differential thermal expansion between the shells. This differential thermal expansion is expected to peak at approximately 6 minutes after the initiation of fire exposure when the average outer shell temperature is 1,344°F and the average inner shell temperature is 196°F. Based on the differential thermal expansion for Type 304 stainless steel¹⁹ the change in length is computed as:

$$DTE = \Delta L_{OuterShell} - \Delta L_{InnerShell} = [\alpha_{OS}(T_{OS} - 70) - \alpha_{IS}(T_{IS} - 70)]L = 0.9 \text{ inches}$$

where:

$$\alpha_{OS} = 10.7(10^{-6}) \text{ in/in/}^{\circ}\text{F at } 1,300 \text{ }^{\circ}\text{F}$$

$$\alpha_{IS} = 8.9(10^{-6}) \text{ in/in/}^{\circ}\text{F at } 200 \text{ }^{\circ}\text{F}$$

$$T_{OS} = 1,344 \text{ }^{\circ}\text{F}$$

$$T_{IS} = 196 \text{ }^{\circ}\text{F}$$

$$L = 73 \text{ inches (conservatively for both shells)}$$

After 6 minutes of exposure to the fire the difference in shell lengths will decrease as the inner shell heats up. The differential expansion will reach 0-inches approximately 6 minutes after the end of the fire event when the inner and outer shells reach thermal equilibrium and then go negative as the outer shell continues to cool faster than the inner shell. The largest negative thermal differential expansion achieved is approximately 0.22-inches.

The result of this variation in differential thermal expansion may take one of three forms:

- 1) the outer shell buckles outward,
- 2) the outer shell buckles inward, or
- 3) the weld attaching the inner shell to either the closure plate or the bottom end plate will fail and permit the outer shell and the affected plate to move freely.

While in reality, a square tube is likely to buckle inward on two of the four faces and outward on the remaining two faces simultaneously, the two buckling modes are treated independently for the purposes of this evaluation. The possibility of the outer shell buckling outwards is the assumption upon which the thermal modeling presented in Section 3.5.2.2, *Description of*

¹⁹ American Society of Mechanical Engineers (ASME) Boiler and Pressure Vessel Code, Section II, *Materials, Part D – Properties*, 2001 Edition, 2002 and 2003 Addenda, New York, Table TE-1, Group 3. Coefficient B = 8.9×10^{-6} inches/inch/°F at 200°F and 10.7×10^{-6} inches/inch/°F at 1,300°F.

Thermal Model for HAC Conditions is based. This mode is seen as likely given the level of metal softening that will occur with the outer shell quickly reaching over 1,200°F and the expected pressurization of the void space between the inner and outer shells. Buckling the outer shell in this fashion will act to lower the rate of inward heat transfer. As such, ignoring the outer shell's displacement due to differential thermal expansion, as assumed by the HAC thermal modeling, yields conservatively high package temperatures.

The second possibility is that the outer shell buckles inward under the differential thermal expansion. Should this occur, the maximum deflection would be $0.9\text{-inches}/2 = 0.45\text{-inches}$ assuming a zero length deflection and only one buckle along the length of the outer shell. In reality, the actual deflection would measure perhaps 0.33-inches after properly accounting for the curvature in the buckled section. Since this level of deflection would still leave 0.5-inches or more of insulation separating the inner shell from the outer shell, no significant impact on the predicted peak HAC temperatures will occur.

The final possibility which the differential thermal expansion may manifest itself is in the failure of the one of the welds attaching the inner shell to the closure and bottom end plates. If this occurs, besides releasing any potential pressure buildup in the void between the inner and outer shells, the outer shell and the associated end plate will extend away from the inner shell at the point of the weld failure. The size of the gap will maximize at about 0.9-inches and then decrease. Since the insulation jacket is cut out to fit around the hardware used to index the packages to one another, the insulation jacket and the underlying insulation will be pulled in the same direction as the outer shell, thus preventing the creation of a gap between the interface of the insulation wrap and the end plate. Even if such a gap would occur, no direct exposure of cavity within the inner shell to the outer shell surfaces will result since the closure plugs at each end of the package are longer than the predicted movement under differential thermal expansion. Instead, the likely and worst case scenario is that the movement of the outer shell, the insulation jacket, and the insulation will create a gap of approximately 0.9-inches at the interface between the first support rib and the insulation. Combining this gap with an insulation shift of up to 1.75-inches at this same locations due to a pre-fire, 30-foot end drop (see Section 3.5.2.2, *Description of Thermal Model for HAC Conditions*) could result in a scenario where there is a 0.9-inch gap between the support rib and the insulation jacket and up to a $0.9 + 1.75 = 2.65\text{-inch}$ gap between the support rib and the end of the insulation wrap. A sensitivity thermal analysis of this geometry showed that the peak inner shell temperature reported in Table 3.4-1 remained bounding, while the maximum temperature of the ATR fuel element increased by less than 25°F. This modest change in temperature occurs because there is little difference in temperature between the outer shell and the stainless steel insulation wrap. Since this level of temperature increase is well within the thermal margins apparent from Table 3.4-1, the potential thermal impact due to the package geometry displacement under differential thermal expansion is seen as being not significant to the safety of the package.

3.4.5 Accident Conditions for Air Transport of Fissile Material

10 CFR §71.55(f) requires that the package be subcritical subsequent to the application of a series of accident condition tests, including a thermal test. A criticality analysis of the worst-case geometric configuration of the packaging and contents materials is performed in Section 6.7, *Fissile Material Packages for Air Transport*, which considers the presence of all of the

moderating and reflecting material in the package. The tendency of the fire event to decrease the availability of moderating material due to combustion is conservatively neglected. Thus, the effects of the fire test of 10 CFR §71.55(f)(1)(iv) do not need to be specifically evaluated.

Table 3.4-1 – HAC Temperatures

Location / Component	Pre-fire	End of Fire	Peak	Maximum Allowable^①
ATR Fuel Element Fuel Plate	100°F	586°F	730°F	1,100°F
ATR Fuel Element Side Plate	100°F	676°F	827°F	1,100°F
Neoprene Rub Strips/ Polyethylene Bag	100°F	1,016°F	1,017°F	N/A
Fuel Handling Enclosure (FHE)	100°F	1,016°F	1,017°F	1,100°F
Loose Fuel Plate Basket (LFPB)	100°F	584°F	746°F	1,100°F
Inner Shell	100°F	1,422°F	1,422°F	2,700°F
Ceramic Fiber Insulation, Body				
- Maximum	100°F	1,460°F	1,460°F	2,300°F
- Average	100°F	1,220°F	1,220°F	2,300°F
Ceramic Fiber Insulation, Closure				
- Maximum	100°F	1,418°F	1,418°F	2,300°F
- Average	100°F	1,297°F	1,297°F	2,300°F
Closure	100°F	1,445°F	1,445°F	2,700°F
Outer Shell	100°F	1,471°F	1,471°F	2,700°F

Table Notes:

① The maximum allowable temperatures under HAC conditions are provided in Section 3.2.2, Technical Specifications of Components.

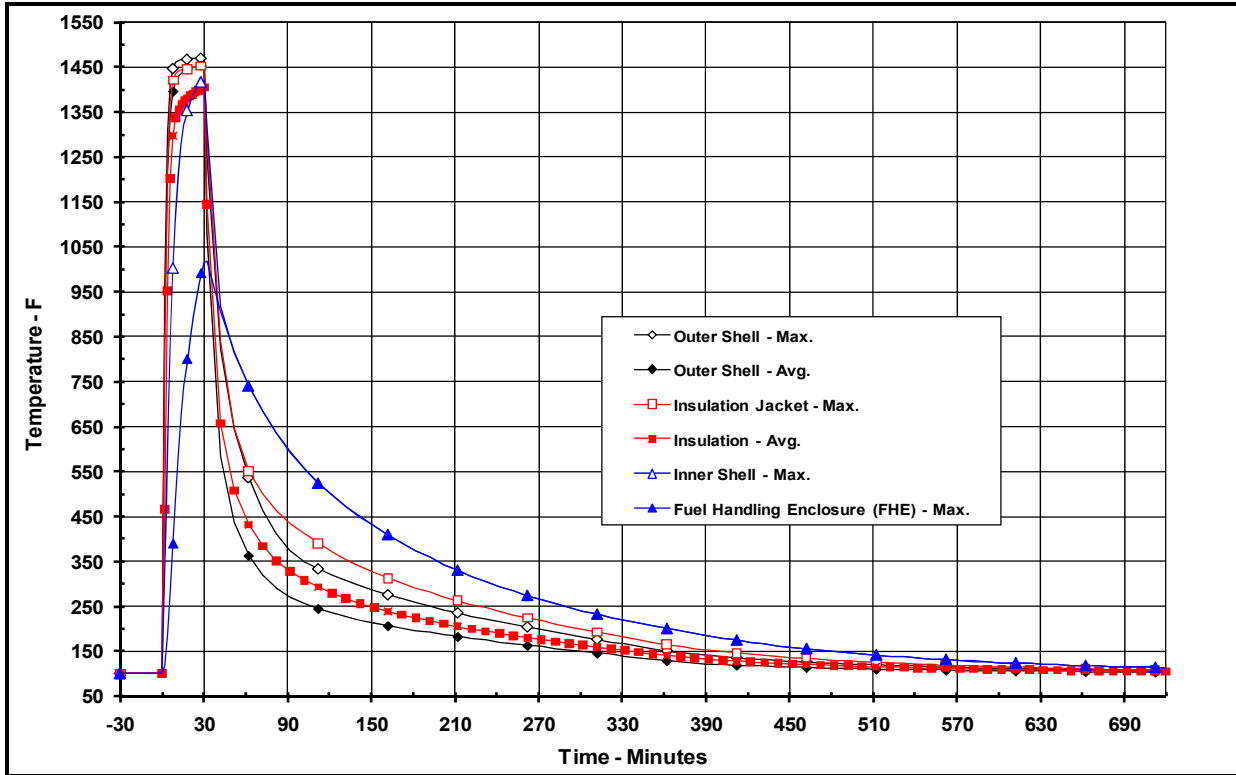


Figure 3.4-1 – ATR FFSC Package Thermal Response to HAC Event

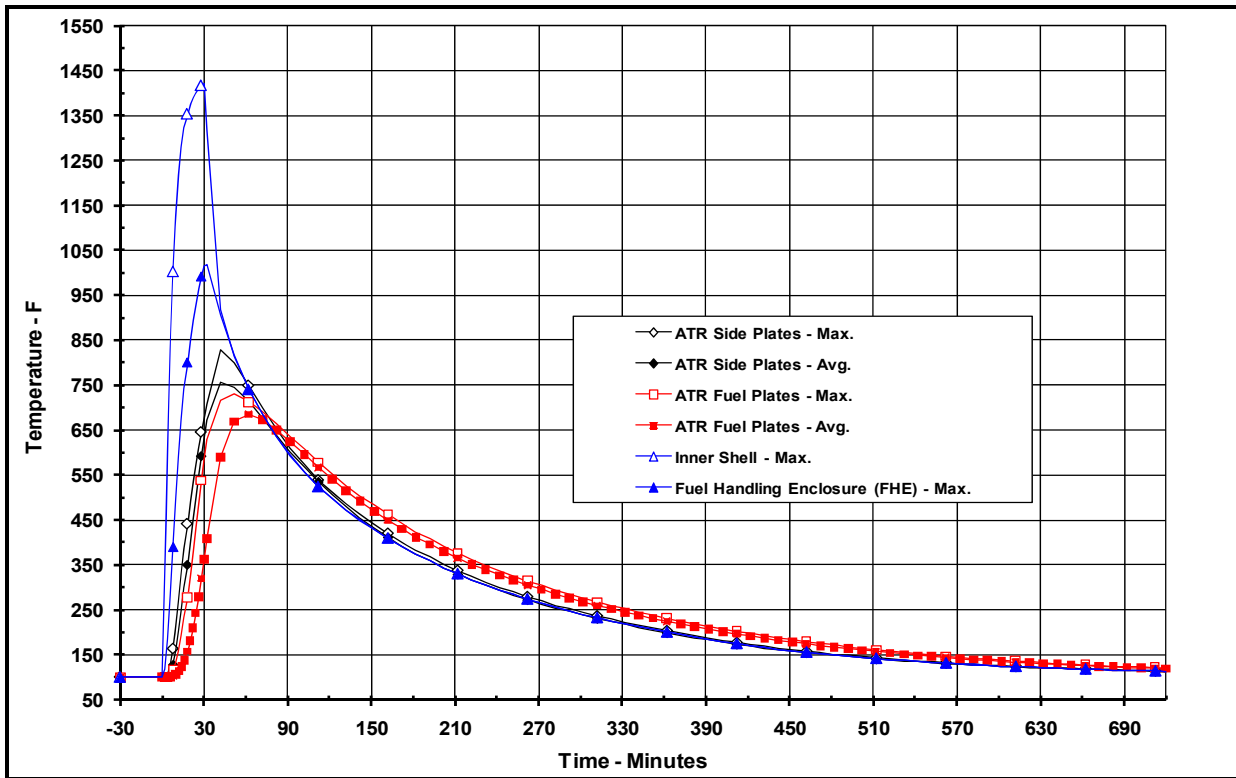
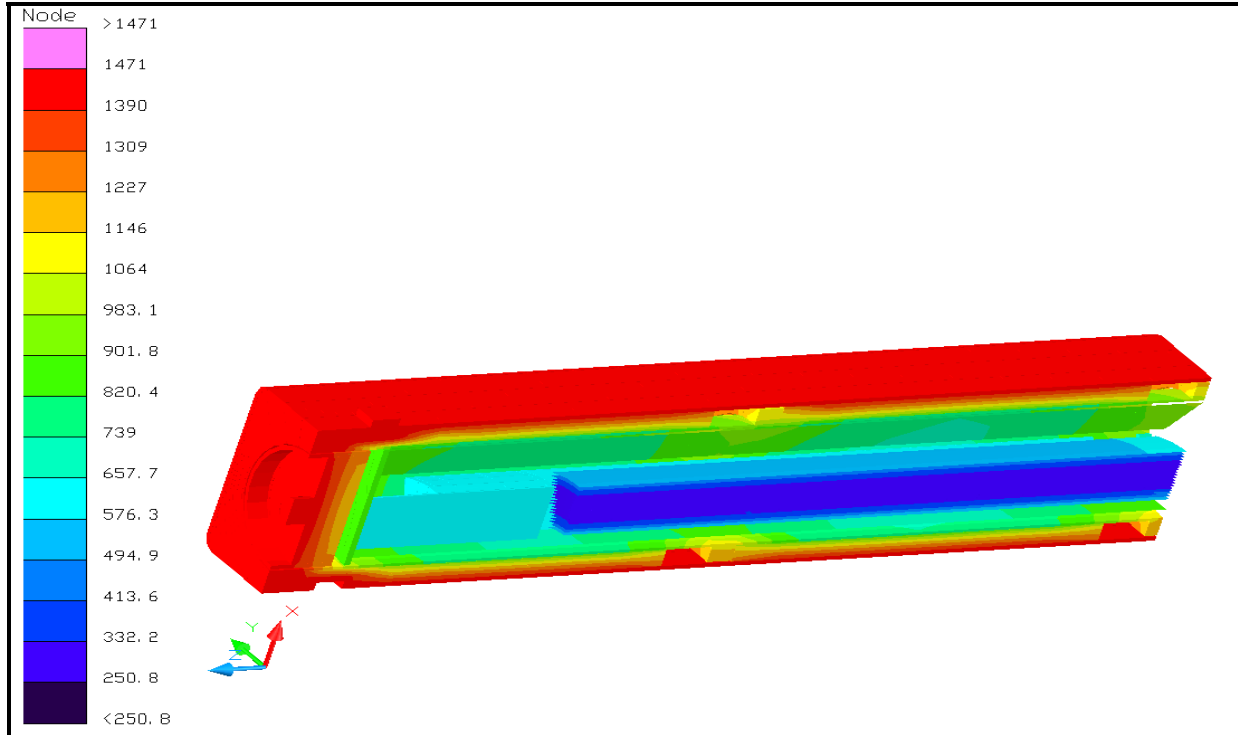
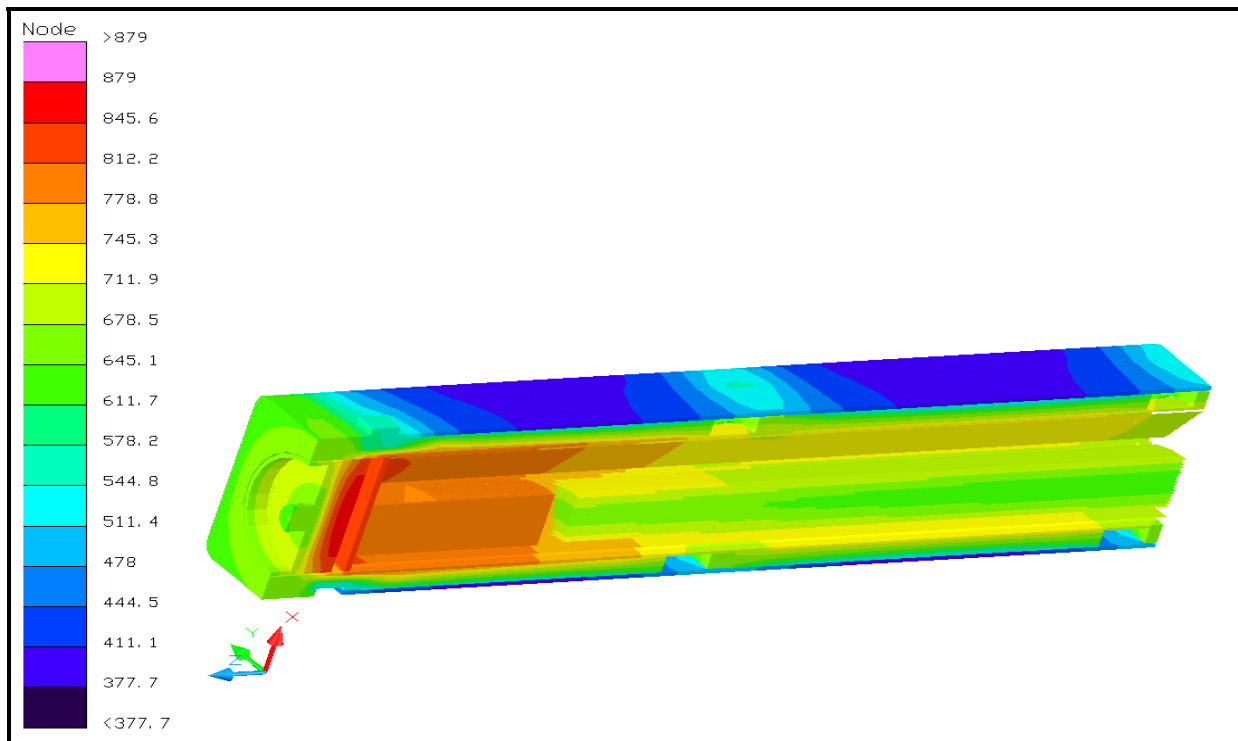


Figure 3.4-2 – ATR Fuel Element Thermal Response to HAC Event



(Note: the positive x-axis is oriented towards the top of the package and the positive z-axis towards the package closure end)

Figure 3.4-3 –Temperature Distribution at End of HAC 30-Minute Fire



(Note: the positive x-axis is oriented towards the top of the package and the positive z-axis towards the package closure end)

Figure 3.4-4 –Temperature Distribution at Peak ATR Fuel Element Temperature

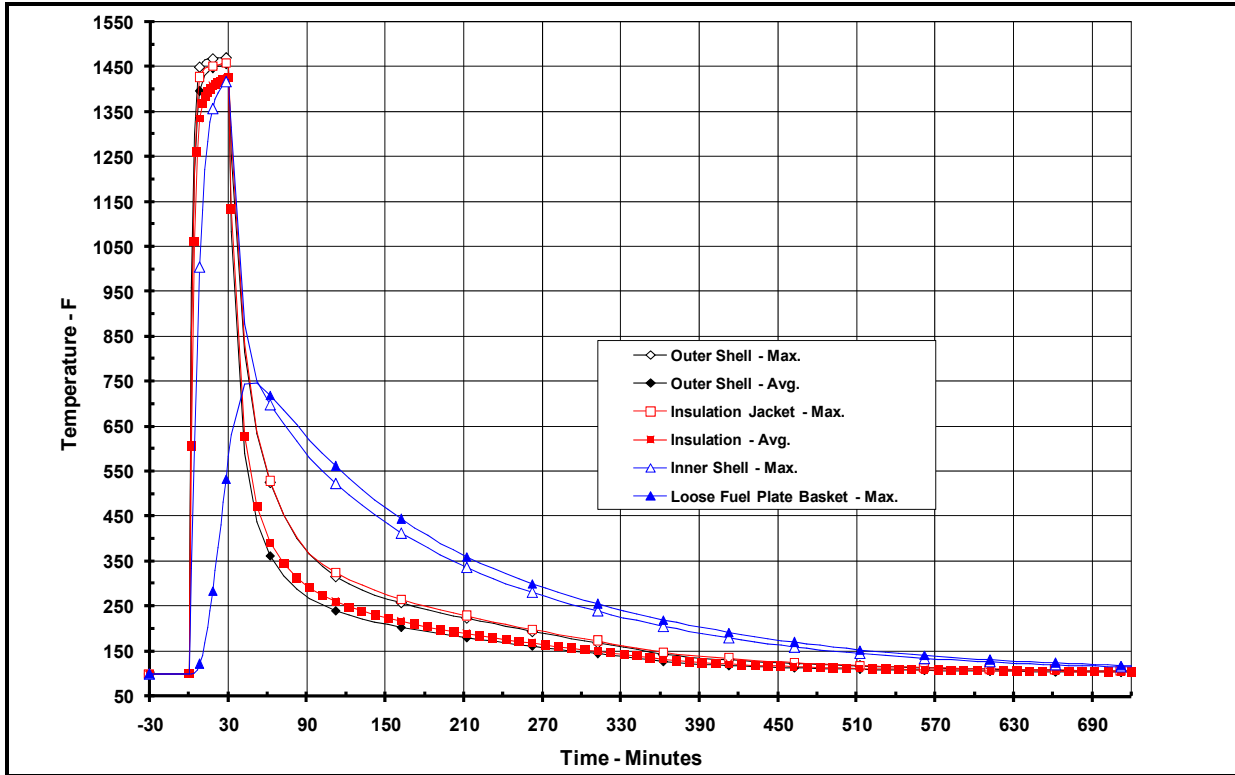
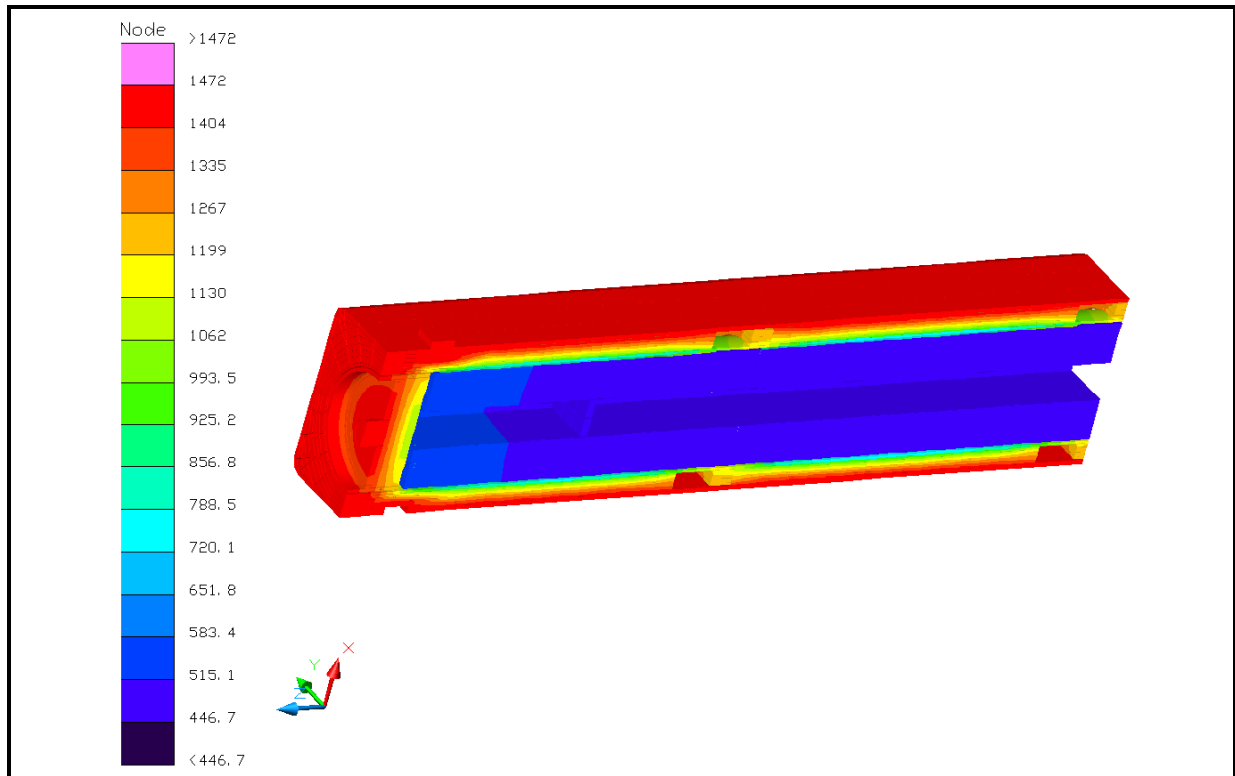
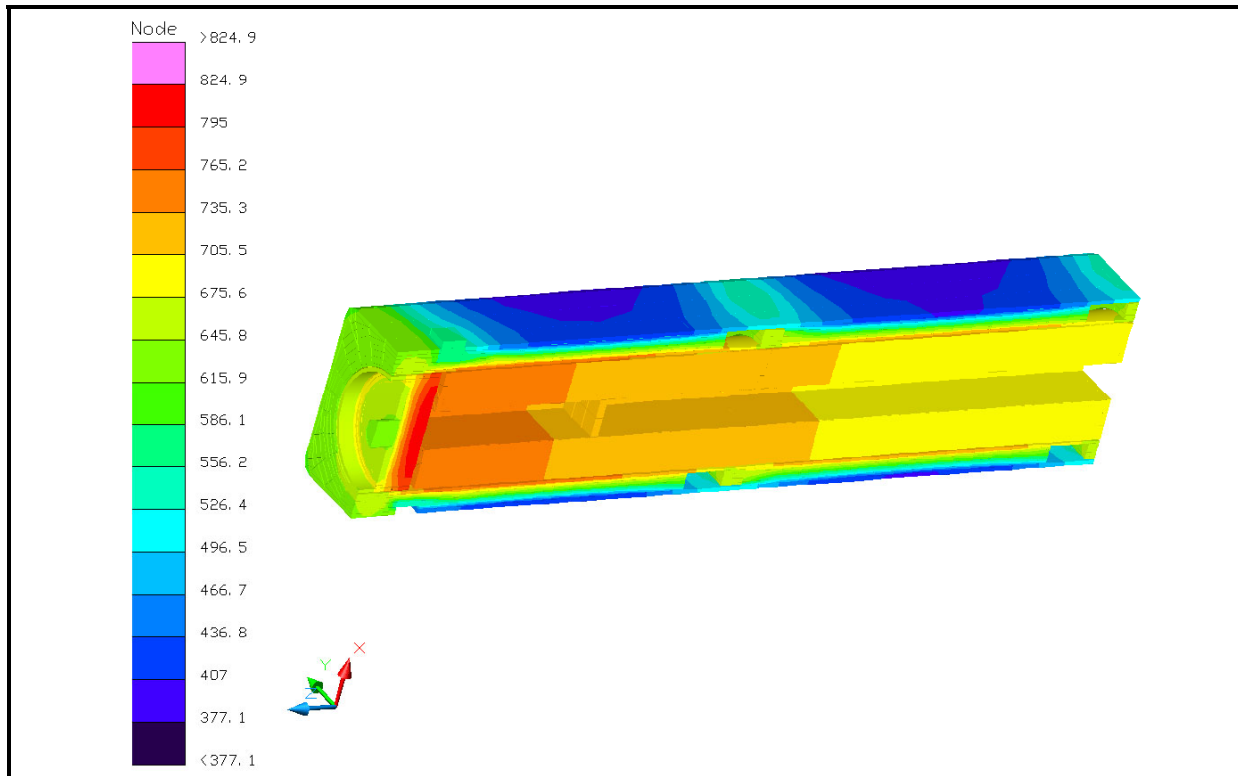


Figure 3.4-5 – ATR FFSC Package with LFPB Thermal Response to HAC Event



(Note: the positive x-axis is oriented towards the top of the package and the positive z-axis towards the package closure end)

Figure 3.4-6 – FFSC-LFPB Temperature Distribution at End of HAC Fire



(Note: the positive x-axis is oriented towards the top of the package and the positive z-axis towards the package closure end)

Figure 3.4-7 – FFSC-LFPB Temperature Distribution at Peak LFPB Temperature

3.5 Appendices

- 3.5.1 Computer Analysis Results
- 3.5.2 Analytical Thermal Model
- 3.5.3 Combustion/Decomposition of Package Organics

3.5.1 Computer Analysis Results

Due to the size and number of the output files associated with each analyzed condition, results from the computer analysis are provided on a CD-ROM.

3.5.2 Analytical Thermal Model

The analytical thermal model of the ATR FFSC package was developed for use with the Thermal Desktop[®]²⁰ and SINDA/FLUINT²¹ computer programs. These programs are designed to function together to build, exercise, and post-process a thermal model. The Thermal Desktop[®] computer program is used to provide graphical input and output display function, as well as computing the radiation exchange conductors for the defined geometry and optical properties. Thermal Desktop[®] is designed to run as an AutoCAD[®] application. As such, all of the CAD tools available for generating geometry within AutoCAD[®] can be used for generating a thermal model. In addition, the use of the AutoCAD[®] layers tool presents a convenient means of segregating the thermal model into its various elements.

The SINDA/FLUINT computer program is a general purpose code that handles problems defined in finite difference (i.e., lumped parameter) and/or finite element terms and can be used to compute the steady-state and transient behavior of the modeled system. Although the code can be used to solve any physical problem governed by diffusion-type equations, specialized functions used to address the physics of heat transfer and fluid flow make the code primarily a thermal code.

The SINDA/FLUINT and Thermal Desktop[®] computer programs have been validated for safety basis calculations for nuclear related projects^{22,23}.

Together, the Thermal Desktop[®] and SINDA/FLUINT codes provide the capability to simulate steady-state and transient temperatures using temperature dependent material properties and heat transfer via conduction, convection, and radiation. Complex algorithms may be programmed into the solution process for the purposes of computing heat transfer coefficients as a function of the local geometry, gas thermal properties as a function of species content, temperature, and pressure, or, for example, to estimate the effects of buoyancy driven heat transfer as a function of density differences and flow geometry.

3.5.2.1 Description of Thermal Model for NCT Conditions

A 3-dimensional, one-quarter symmetry thermal model of the ATR FFSC is used for the NCT evaluation. The model simulates one-quarter of the package, extending from the closure to the

²⁰ Thermal Desktop[®], Versions 4.8 and 5.1, Cullimore & Ring Technologies, Inc., Littleton, CO, 2005/2007.

²¹ SINDA/FLUINT, *Systems Improved Numerical Differencing Analyzer and Fluid Integrator*, Versions 4.8 and 5.1, Cullimore & Ring Technologies, Inc., Littleton, CO, 2005/2007.

²² *Software Validation Test Report for Thermal Desktop[®] and SINDA/FLUINT*, Versions 4.8 and 5.1, Packaging Technology, Inc., File No. TR-VV-05-001, Rev. 1 and Rev. 2.

²³ *Thermal Desktop[®] and SINDA/FLUINT Testing and Acceptance Report*, Version 5.1, AREVA Federal Services, LLC, File No. AFS-TR-VV-006, Rev. 0.

axial centerline of the package. Symmetry conditions are assumed about the package's vertical axis and at the axial centerline. This modeling choice captures the full height of the package components and allows the incorporation of the varying insulation loads that will occur at the top and sides of the package. Program features within the Thermal Desktop[®] computer program automatically compute the various areas, lengths, thermal conductors, and view factors involved in determining the individual elements that make up the thermal model of the complete assembly.

Figure 3.5-1 and Figure 3.5-2 illustrate the 'solid' and 'hidden line' views of the package thermal model. The model simulates one-half of the closure end half of the package (i.e., symmetry is assumed about the package's vertical plane) and extends approximately 36.5 inches in the axial direction (e.g., from closure to the mid-point of the center support rib). As seen from the figure, the modeling captures the various components of the packaging, including the index lug and mating pocket used to align the stacked packages, the recessed exterior surface area of the package closure, the FHE, and the ATR fuel element. Also captured, but not easily seen in the figure due to the scale of the figures, are the nineteen (19) individual fuel plates that comprise the ATR fuel element.

The model is composed of solid and plate type elements representing the various package components. Thermal communication between the various components is via conduction, radiation, and surface-to-surface contact. Since the ATR FFSC Package dissipates essentially no decay heat, the peak temperatures internal to the package are driven by the external heating occurring during NCT and HAC conditions. While the potential for developing convective flows within the air filled cavity between the outer shell and the insulation jacket is small due to the cavity dimensions, if convective heat transfer was to develop it could raise the peak temperatures developed under either NCT or HAC conditions since it would reduce the thermal resistance to heat flowing inward from the outer shell. To address this possibility, the thermal conductivity associated with the air overpack nodes in the lower quadrant of the package are increased by a factor of 2 from that for conduction as a means of simulating the type of enhanced heat transfer that convection would cause. The affected nodes are limited to those in the lower quadrant of the package since, in the assumed horizontal orientation of the package under both NCT and HAC conditions, the buoyancy forces associated with convection will tend to drive the flow in this portion of the package in a circular motion, but would only produce a stratified temperature layer in the upper quadrant. However, since subsequent examination of the temperature distribution at the end of the fire event showed no discernible difference in the insulation jacket temperature between the upper and lower quadrants, it is concluded that the heat transfer within these cavities is dominated by radiation and conduction and the potential for convective heat transfer can be ignored. Despite this conclusion, the factor of 2 has been retained in the models as a conservatism.

A total of approximately 8,050 nodes, 2,800 planar elements, and 3,700 solid elements are used to simulate the modeled components. In addition, one boundary node is used to represent the ambient environment for convection purposes and a second boundary node is used to represent the ambient temperature for the purpose of radiation heat transfer.

Figure 3.5-3 and Figure 3.5-4 illustrate the quarter symmetry thermal models of the FHE and the ATR fuel element. The FHE thermal model uses planar elements to represent the 0.09 inch thick sides of the enclosure, while solid elements are used to represent the 0.25 inch thick end cap.

Heat transfer between the FHE and the inner shell of the package is modeled as a combination of radiation and conduction across the air-filled void space, as well as via direct contact along 3 edges of the FHE. The contact conductance simulates the physical contact between an impact deformed FHE and the inner shell. Figure 3.5-5 illustrates a cross-section through the combined modeling for the inner shell, the FHE, and the ATR fuel element. The left side of the figure illustrates the placement of the thermal nodes (indicated by the small circles) used to simulate each of the components, the use of curved elements to represent the 19 fuel plates, and the assumed points of direct contact between the FHE and the inner shell. The right side of the figure includes depiction of the solid elements that are used to simulate the air voids in and around the FHE. The heat transfer between the FHE and the ATR fuel element is computed as conductance through the 0.125 inch thick neoprene rub strips (see Figure 3.5-5) and radiation and conductance through the air voids.

The heat transfer due to direct contact conservatively assumes the FHE has been deformed as a result of the HAC drop event to create ‘flat’ areas measuring 0.5 inches wide at the lower 2 points of contact, 0.75 inches wide at the top, and extending the entire length of the FHE. Although this type of damage would only occur for the HAC condition (if it occurs at all), it is conservatively assumed for the NCT modeling as well. A conservatively high contact conductance⁹ of 1 Btu/min-in²-°F is assumed.

A detailed model of the ATR fuel element is used to simulate the heat transfer within the fuel element and between the fuel element and the FHE. The detailed thermal model, illustrated in Figure 3.5-4 and Figure 3.5-5, includes a separate representation of each composite fuel plate, the side plates (including the cutouts), and the upper end box casting. Heat transfer between the individual fuel plates is simulated via conduction and radiation across the air space separating the plates. The curvature and separation distance between the plates is based on the information presented in Section 3.5.2.4, *Determination of Composite Thermal Properties for ATR Fuel Plates*. Each quarter segment of the fuel plates is represented by four thermal nodes in the circumferential direction and 16 nodes along its length.

The thermal modeling for the Loose Fuel Plate Basket uses the same model for the ATR FFSC, but replaces the thermal modeling of the FHE and the ATR fuel element with the thermal modeling for the Loose Fuel Plate Basket depicted in Figure 3.5-6. Approximately 500 nodes, 280 planar elements, and 530 solids are used to simulate the basket. Since the payload for the basket may contain a variable number and size of fuel plates, the thermal modeling is based on an empty basket. This approach is conservative since the addition of a payload will serve to increase the thermal mass of the basket and, thus, reduce its temperature rise under the transient conditions associated with the HAC event. Since the unirradiated fuel plates have essentially zero decay heat, there will be no temperature rise between the loose fuel plates and the basket. As such, modeling of the loose fuel plate payload is both unnecessary and conservative for the purposes of this evaluation.

The heat transfer from the exterior surfaces of the ATR FFSC is modeled as a combination of convection and radiation exchange. Appendix 3.5.2.3, *Convection Coefficient Calculation*, presents the methodology used to compute the convection coefficients from the various surfaces. The radiation exchange is computed using a Monte Carlo, ray tracing technique and includes the affect of reflection and/or transmission, according to the optical properties assigned to each surface (see Section 3.2.1, *Material Properties*).

In addition, heating of the exterior surfaces due to solar insolation is assumed using a diurnal cycle. A sine wave model is used to simulate the variation in the applied insolation on the surfaces of the package over a 24-hour period, except that when the sine function is negative, the insolation level is set to zero. The timing of the sine wave is set to achieve its peak at 12 pm and peak value of the curve is adjusted to ensure that the total energy delivered matched the regulatory values. As such, the total energy delivered in one day by the sine wave solar model is given by:

$$\int_{6\text{-hr}}^{18\text{-hr}} Q_{\text{peak}} \cdot \sin\left(\frac{\pi \cdot t}{12\text{-hr}} - \frac{\pi}{2}\right) dt = \left(\frac{24\text{-hr}}{\pi}\right) \cdot Q_{\text{peak}}$$

Using the expression above for the peak rate of insolation, the peak rates for top and side insolation may be calculated as follows:

$$Q_{\text{top}} = \left(800 \frac{\text{cal}}{\text{cm}^2}\right) \cdot \left(\frac{\pi}{24 \text{ hr}}\right) \quad Q_{\text{top}} = 2.68 \frac{\text{Btu}}{\text{hr} \cdot \text{in}^2} = 0.0447 \frac{\text{Btu}}{\text{min} \cdot \text{in}^2}$$

$$Q_{\text{side}} = \left(200 \frac{\text{cal}}{\text{cm}^2}\right) \cdot \left(\frac{\pi}{24 \text{ hr}}\right) \quad Q_{\text{side}} = 0.67 \frac{\text{Btu}}{\text{hr} \cdot \text{in}^2} = 0.0112 \frac{\text{Btu}}{\text{min} \cdot \text{in}^2}$$

Conversion factors of $1 \text{ cal/cm}^2\text{-hr} = 0.0256 \text{ Btu/hr-in}^2$ are used in the above calculations. These peak rates are multiplied by the sine function and the solar absorptivity for Type 304 stainless steel (i.e., 0.52) to create the top and side insolation values as a function of time of day.

3.5.2.2 Description of Thermal Model for HAC Conditions

The thermal evaluations for the hypothetical accident condition (HAC) are conducted using an analytical thermal model of the ATR FFSC. The HAC thermal model is a modified version of the quarter symmetry NCT model described in Section 3.5.2.1, *Description of Thermal Model for NCT Conditions*, with the principal model modifications consisting of simulating the expected package damage resulting from the drop events that are assumed to precede the HAC fire and changing the package surface emissivities to reflect the assumed presence of soot and/or surface oxidization.

Physical testing using full scale certified test units (CTUs) is used to establish the expected level of damage sustained by the ATR FFSC package from the 10 CFR 71.73 prescribed free and puncture drops that are assumed to precede the HAC fire event. Appendix 2.12.1, *Certification Tests on CTU-1* and Appendix 2.12.2, *Certification Tests on CTU-2* document the configuration and initial conditions of the test articles, the test facilities, the instrumentation used, and the test results. The drop tests covered a range of hypothetical free drop orientations and puncture bar drops. The results from both sets of CTU drop tests showed the following:

- 1) The worst case physical damage to the exterior of the package occurs from a CG over corner drop. The resulting damage (depicted in Figure 3.5-7) is thermally insignificant in that there is no breach in the outer shell and the compaction of the underlying insulation is minor and offset by an increase in the gap between the outer shell and the insulation in other areas.
- 2) The oblique, CG over side puncture bar drop caused a 0.5 inch indentation to the side of the package at the center of the impact region and less near the edges. No tearing of the outer shell occurred.
- 3) The end drops caused the ceramic fiber insulation to slide axially between each set of ribs, as depicted in Figure 3.5-9. The amount of re-positioning varied from approximately 1 to 1.75 inches and results in the compression of the insulation in the axial direction by 6 to 10%. No compression or shifting of the insulation in the radial direction was noted from the drop tests. While the insulation jacket showed some crimping at the edges, it was essentially undamaged.

Based on the above observations, the NCT was modified for the HAC evaluations via the following steps:

- 1) A 1.85 inch long segment of insulation was removed between each set of ribs. This degree of insulation re-positioning/compression conservatively bounds the maximum observed distance of 1.75 inches. Heat transfer across the vacated segments of insulation is then computed as radiation and conduction across an air filled space. Figure 3.5-10 illustrates the change made to the NCT thermal model to capture the expected insulation re-positioning. The change in the insulation's thermal conductivity as a result of the compression is conservatively ignored since thermal conductivity decreases with density at temperatures in excess of approximately 500°F (see Table 3.2-3).
- 2) All other geometric aspects of the NCT thermal model are assumed to be unchanged for the HAC evaluations since the observed damage to the outer shell resulting from the free and puncture drops has a superficial impact to the thermal protection offered by the ATR FFSC to the HAC fire event.
- 3) The surface emissivities for the various components of the package are revised as presented in Table 3.2-6 vs. that given in Table 3.2-5.

3.5.2.3 Convection Coefficient Calculation

The convective heat transfer coefficient, h_c , has a form of: $h_c = Nu \frac{k}{L}$, where k is the thermal conductivity of the gas at the mean film temperature and L is the characteristic length of the vertical or horizontal surface.

Natural convection from each surface is computed based on semi-empirical relationships using the local Rayleigh number and the characteristic length for the surface. The Rayleigh number is defined as:

$$Ra_L = \frac{\rho^2 g_c \beta L^3 \Delta T}{\mu^2} \times Pr$$

where:

g_c = gravitational acceleration, 32.174 ft/s ²	β = coefficient of thermal expansion, °R ⁻¹
ΔT = temperature difference, °F	ρ = density of air at the film temperature, lb _m /ft ³
μ = dynamic viscosity, lb _m /ft-s	Pr = Prandtl number = $(c_p \mu) / k$
L = characteristic length, ft	k = thermal conductivity at film temperature
c_p = specific heat, Btu/lb _m -hr-°F	Ra _L = Rayleigh #, based on length 'L'

Note that k, c_p, and μ are each a function of air temperature as taken from Table 3.2-4. Values for ρ are computed using the ideal gas law, β for an ideal gas is simply the inverse of the absolute temperature of the gas, and Pr is computed using the values for k, c_p, and μ from Table 3.2-4. Unit conversion factors are used as required to reconcile the units for the various properties used.

The natural convection from a discrete vertical surface is computed using Equation 6.39 to 6.42 of Rohsenow, et. al.⁹, which is applicable over the range 1 < Rayleigh number (Ra) < 10¹²:

$$Nu^T = \bar{C}_L Ra^{1/4}$$

$$\bar{C}_L = \frac{0.671}{\left(1 + (0.492/Pr)^{9/16}\right)^{4/9}}$$

$$Nu_L = \frac{2.8}{\ln(1 + 2.8/Nu^T)}$$

$$Nu_t = C_t^V Ra^{1/3}$$

$$C_t^V = \frac{0.13 Pr^{0.22}}{\left(1 + 0.61 Pr^{0.81}\right)^{0.42}}$$

$$Nu = \frac{h_c L}{k} = \left[(Nu_L)^6 + (Nu_t)^6 \right]^{1/6}$$

Natural convection from horizontal surfaces is computed from Equations 4.39 and 4.40 of Rohsenow, et. al.⁹, and Equations 3.34 to 3.36 of Guyer²⁴, where the characteristic dimension (L) is equal to the plate surface area divided by the plate perimeter. For a heated surface facing upwards or a cooled surface facing downwards and Ra > 1:

$$Nu = \frac{h_c L}{k} = \left[(Nu_L)^{10} + (Nu_t)^{10} \right]^{1/10}$$

$$Nu_L = \frac{1.4}{\ln\left(1 + 1.677 / \left(\bar{C}_L Ra^{1/4}\right)\right)}$$

²⁴ Guyer, E.C., *Handbook of Applied Thermal Design*, McGraw-Hill, Inc., 1989.

$$\overline{C_L} = \frac{0.671}{\left[1 + (0.492/Pr)^{9/16}\right]^{4/9}}$$

$$Nu_t = 0.14Ra^{1/3}$$

For a heated surface facing downwards or a cooled surface facing upwards and $10^3 < Ra < 10^{10}$, the correlation is as follows:

$$Nu = Nu_L = \frac{2.5}{\ln(1 + 2.5/Nu^T)}$$

$$Nu^T = \frac{0.527}{\left(1 + (1.9/Pr)^{9/10}\right)^{2/9}} Ra^{1/5}$$

The forced convection coefficients applied during the HAC fire event are computed using the relationships in Table 6-5 of Kreith²⁵ for a flat surface, where the characteristic dimension (L) is equal to the length along the surface and the free stream flow velocity is V. The heat transfer coefficient is computed based on the local Reynolds number, where the Reynolds number is defined as:

$$Re_L = \frac{V \times \rho \times L}{\mu}$$

For Reynolds number (Re) $< 5 \times 10^5$ and Prandtl number (Pr) > 0.1 :

$$Nu = 0.664 Re_L^{0.5} Pr^{0.33}$$

For Reynolds number (Re) $> 5 \times 10^5$ and Prandtl number (Pr) > 0.5 :

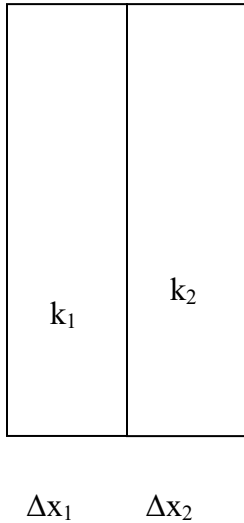
$$Nu = 0.036 Pr^{0.33} [Re_L^{0.8} - 23,200]$$

Given the turbulent nature of the 30-minute fire event, a characteristic length of 0.25 feet is used for all surfaces to define the probable limited distance for boundary growth. The turbulent heat transfer coefficient relationship used for HAC modeling is a modified version of the Colburn relation recommended by the advisory material for the IAEA (see *Advisory Material for the IAEA Regulations for the Safe Transport of Radioactive Material*, TS-G-1.1, Rev. 1, International Atomic Energy Agency, 2008). The same advisory material states that "pool fire gas velocities are generally found to be in the range of 5–10 m/s". The above forced convection relationships yields a convection heat transfer rate of approximately 40 W/m²-K, which matches that obtained with the IAEA recommended Colburn relation and conservatively bounds the experimental values in large pool fires.

²⁵ Kreith, Frank, *Principles of Heat Transfer*, 3rd edition, Harper & Row, 1973.

3.5.2.4 Determination of Composite Thermal Properties for ATR Fuel Plates

The ATR fuel plates are a composite material consisting of a fissile fuel matrix sandwiched within aluminum cladding. For the purposes of this calculation, the fuel composite is treated as a homogenous material with lumped thermal properties as defined below. This modeling approach is justified since the thermal gradient within the fuel element will be very low given that the un-irradiated fuel has essentially no decay heat.



Because of the thinness of the plates, the average conductivity is required only for the axial and circumferential direction. Conductivity through the plates is not required as this analysis assumes a zero temperature gradient in that direction. Mean density and specific heat values are also defined below.

Circumferential and Axial Conductivity

Ignoring the affect of curvature, the heat flow can be written as,

$$q = -\Delta x \Delta z \bar{k} \frac{\Delta T}{\Delta y} = -\Delta x_1 \Delta z k_1 \frac{\Delta T}{\Delta y} - \Delta x_2 \Delta z k_2 \frac{\Delta T}{\Delta y} \quad \text{where}$$

$$\Delta x = \sum_i \Delta x_i$$

From which,

$$\bar{k} = \frac{\Delta x_1 k_1 + \Delta x_2 k_2}{\Delta x}$$

Mean Density

The mean density of the fuel plates is computed from:

$$Mass = \Delta x \Delta y \Delta z \bar{\rho} = \Delta x_1 \Delta y \Delta z \rho_1 + \Delta x_2 \Delta y \Delta z \rho_2, \text{ from which we get } \bar{\rho} = \frac{\Delta x_1 \rho_1 + \Delta x_2 \rho_2}{\Delta x}$$

Mean Specific Heat

In the same manner used to define the mean density, the mean specific heat for the fuel plates is computed as;

$$\bar{\rho} \bar{c}_p \Delta x \Delta y \Delta z = \rho_1 c_{p_1} \Delta x_1 \Delta y \Delta z + \rho_2 c_{p_2} \Delta x_2 \Delta y \Delta z \text{ from which we get, } \bar{c}_p = \frac{\rho_1 c_{p_1} \Delta x_1 + \rho_2 c_{p_2} \Delta x_2}{\bar{\rho} \Delta x}$$

The thermal properties for the individual plates making up the ATR fuel element are computed using the above approach and thermophysical and geometric data^{6,5} for the ATR fuel element.

Based on these data sources, the radius of the inner plate is 3.015 inches, while the radius of the outer plate is 5.44 inches. The gap between the plates is 0.078 inches. The thickness of the aluminum cladding is 0.015 inches.

While the thermal properties for the aluminum cladding and the fissile fuel matrix material will vary with temperature, for the purposes of this evaluation, fixed material properties are assumed in order to simplify the calculation. To provide conservatism for this modeling approach conservatively low value is assumed for the specific heat for each component, while a conservatively high thermal conductivity value is used. This methodology will result in over-predicting the temperature rise within the composite material during the HAC fire event.

The thermal properties used in this calculation are:

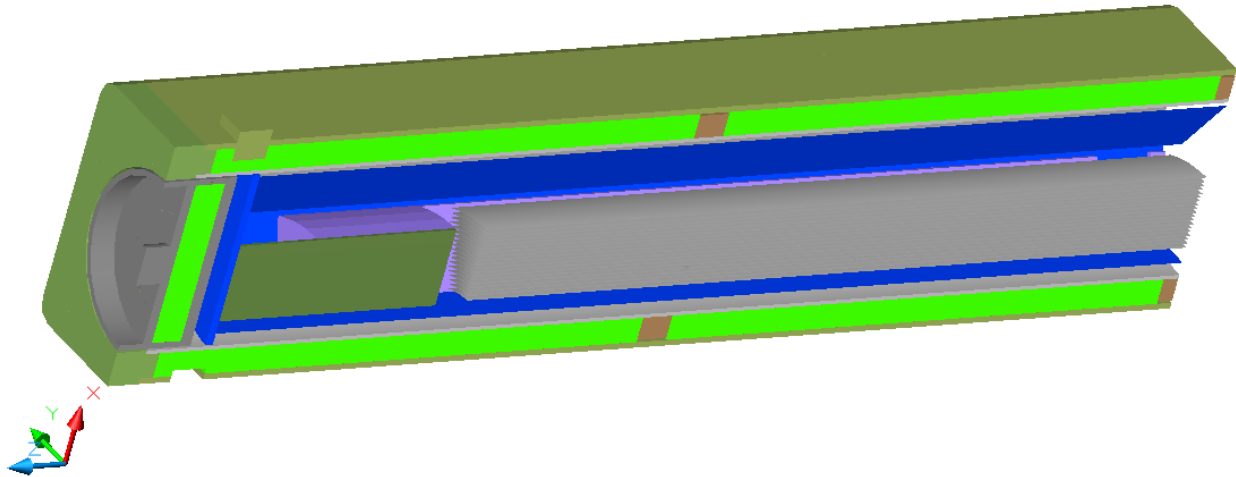
- 1) Aluminum cladding thermal conductivity = 191 W/m-K, conservatively high value from [6], page 18
- 2) Fissile fuel matrix (UAl_x) conductivity:
 - a. 53 W/m-K, conservatively high based on Table 2.3 from [6], at 300K for fuel plates 1, 2, 18, & 19
 - b. 43 W/m-K, conservatively high based on Table 2.3 from [6], at 300K for fuel plates 3, 4, 16, & 17
 - c. 36.1 W/m-K, conservatively high based on Table 2.3 from [6], at 300K for fuel plates 5 to 15
- 3) Aluminum cladding density = 2702 kg/m³, from [6], page 16
- 4) Fissile fuel matrix (UAl_x) density:
 - a. 3409 kg/m³, from [6], Table 2.5, for fuel plates 1, 2, 18, & 19
 - b. 3671 kg/m³, from [6], Table 2.5, for fuel plates 3, 4, 16, & 17
 - c. 3933 kg/m³, from [6], Table 2.5, for fuel plates 5 to 15
- 5) Aluminum cladding specific heat = 896 and 1080 J/kg-K, from [6], Table 3.2, at 300 & 600K, respectively
- 6) Fissile fuel matrix (UAl_x) specific heat:
 - a. 666 & 803 J/kg-K, from [6], Table 2.4, value at 300 & 700K, respectively, for fuel plates 1, 2, 18, & 19
 - b. 616 & 743 J/kg-K, from [6], Table 2.4, value at 300 & 700K, respectively, for fuel plates 3, 4, 16, & 17
 - c. 573 & 692 J/kg-K, from [6], Table 2.4, value at 300 & 700K, respectively, fuel plates 5 to 15

Table 3.5-1 presents the composite thermal conductivity, specific heat, and density values for each of the nineteen (19) fuel plates making up the ATR fuel element. These composite values are based on the thermal property values given above and the geometry depicted in Figure 3.5-11.

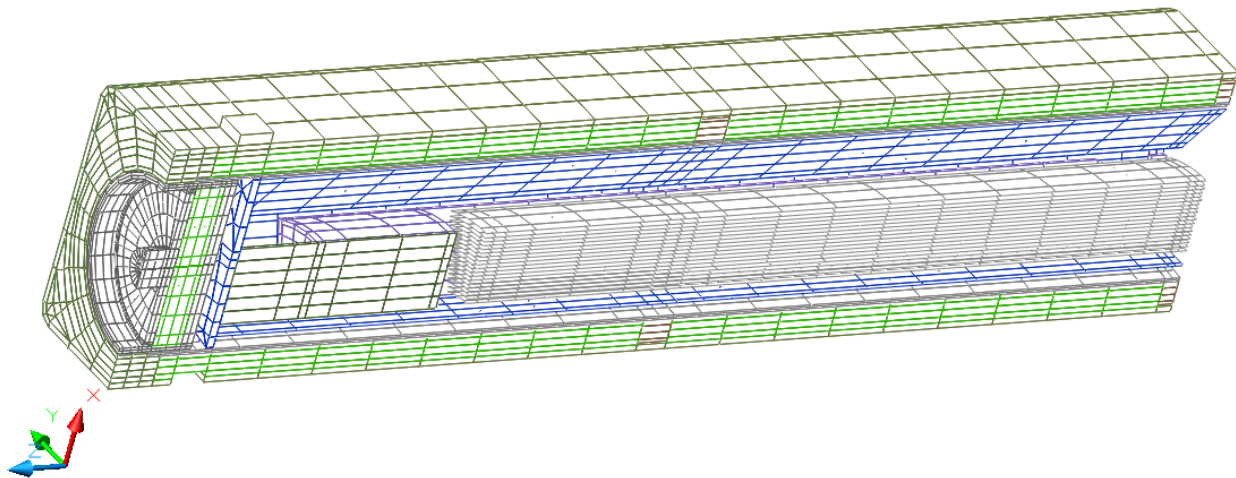
Table 3.5-1 – Composite ATR Fuel Plate Thermal Properties

Plate	Plate Thickness, in	UALx Thickness, in	Circumferential Conductivity (W/m-K)	Inner radius, in	Outer radius, in	Mean radius, in	Mean density, kg/m ³	Mean specific heat, J/(kg K) @ 300 K	Mean specific heat, J/(kg K) @ 700 K
1	0.08	0.05①	104.8	3.015	3.095	3.055	3143.9	740.1	892.3
2	0.05	0.02	135.8	3.173	3.223	3.198	2984.8	790.9	953.5
3	0.05	0.02	131.8	3.301	3.351	3.326	3089.6	762.9	919.8
4	0.05	0.02	131.8	3.429	3.479	3.454	3089.6	762.9	919.8
5	0.05	0.02	129.0	3.557	3.607	3.582	3194.4	736.9	888.9
6	0.05	0.02	129.0	3.685	3.735	3.710	3194.4	736.9	888.9
7	0.05	0.02	129.0	3.813	3.863	3.838	3194.4	736.9	888.9
8	0.05	0.02	129.0	3.941	3.991	3.966	3194.4	736.9	888.9
9	0.05	0.02	129.0	4.069	4.119	4.094	3194.4	736.9	888.9
10	0.05	0.02	129.0	4.197	4.247	4.222	3194.4	736.9	888.9
11	0.05	0.02	129.0	4.325	4.375	4.350	3194.4	736.9	888.9
12	0.05	0.02	129.0	4.453	4.503	4.478	3194.4	736.9	888.9
13	0.05	0.02	129.0	4.581	4.631	4.606	3194.4	736.9	888.9
14	0.05	0.02	129.0	4.709	4.759	4.734	3194.4	736.9	888.9
15	0.05	0.02	129.0	4.837	4.887	4.862	3194.4	736.9	888.9
16	0.05	0.02	131.8	4.965	5.015	4.990	3089.6	762.9	919.8
17	0.05	0.02	131.8	5.093	5.143	5.118	3089.6	762.9	919.8
18	0.05	0.02	135.8	5.221	5.271	5.246	2984.8	790.9	953.5
19	0.1	0.07①	94.4	5.349	5.449	5.399	3196.9	724.3	873.2

① An average UALx thickness of 0.020 inches exists for Plates 1 and 19 vs. the 0.05 and 0.07 inches assumed by this analysis based on the assumption of a constant cladding thickness. However, for the purposes of developing composite fuel plate properties for this evaluation, the UALx thicknesses identified in the table yield conservative bounding thermal property values.

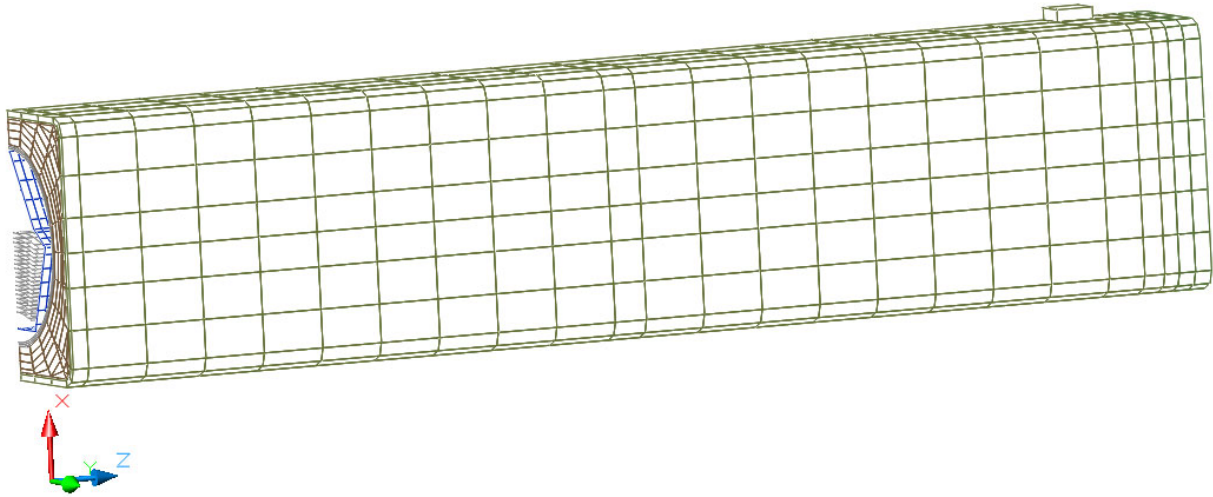


(Note: the positive x-axis is oriented towards the top of the package and the positive z-axis towards the package closure end)



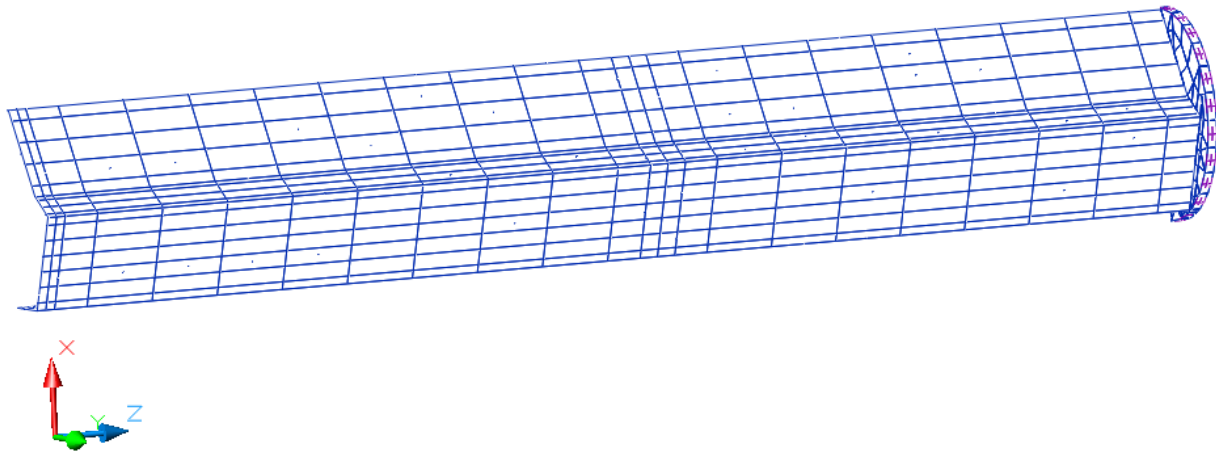
(Note: the positive x-axis is oriented towards the top of the package and the positive z-axis towards the package closure end)

Figure 3.5-1 – ‘Solid’ and & ‘Hidden Line’ Views of Package Quarter Symmetry Thermal Model



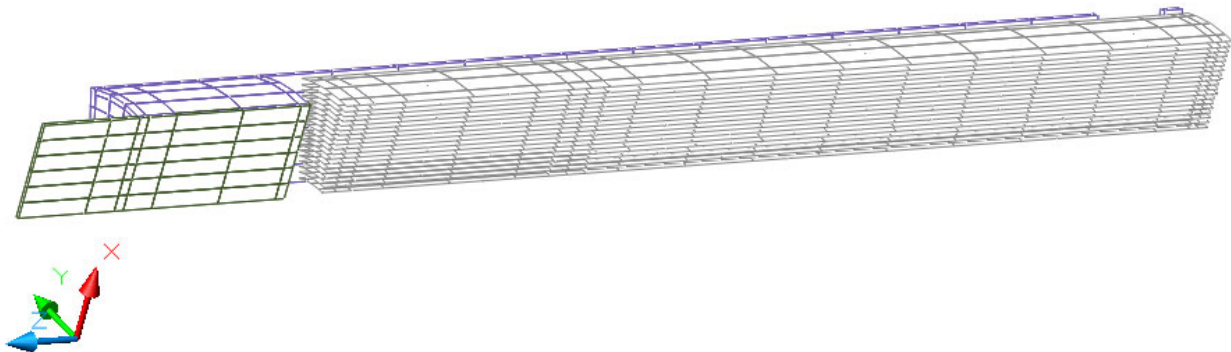
(Note: the positive x-axis is oriented towards the top of the package and the positive z-axis towards the package closure end)

Figure 3.5-2 – Reverse, ‘Hidden Line’ View of Package Quarter Symmetry Thermal Model

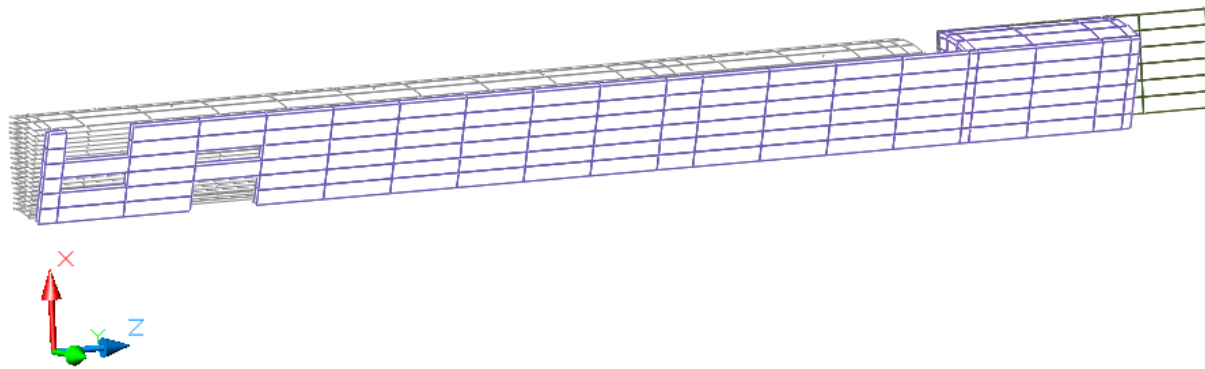


(Note: the positive x-axis is oriented towards the top of the package and the positive z-axis towards the package closure end)

Figure 3.5-3 – Reverse, ‘Hidden Line’ View of FHE Quarter Symmetry Thermal Model



ATR Fuel Element Modeling, View Along Centerline of Element



ATR Fuel Element Modeling, View Along Outside of Element

(Note: the positive x-axis is oriented towards the top of the package and the positive z-axis towards the package closure end)

Figure 3.5-4 – Centerline and Side Views of ATR Fuel Element Thermal Model

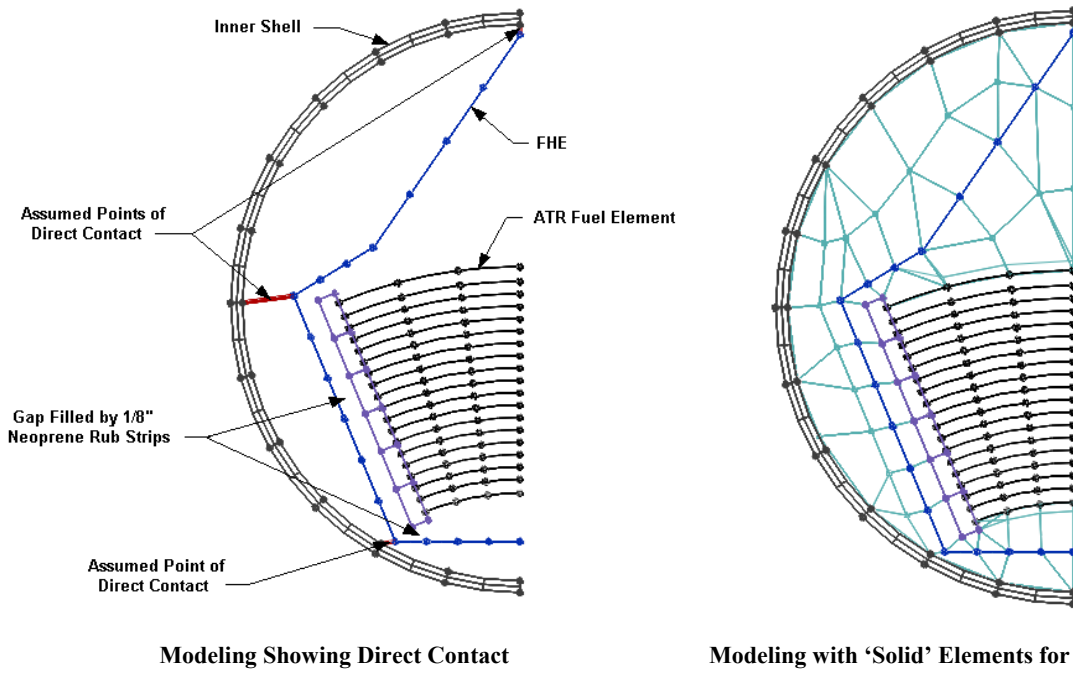
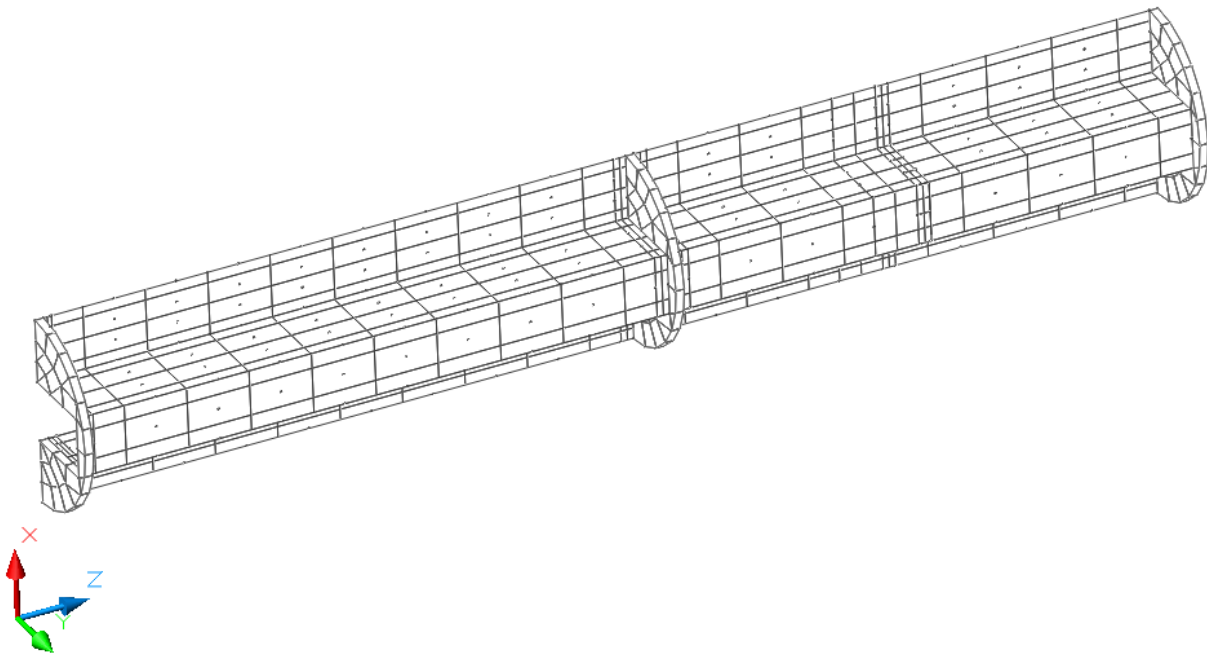


Figure 3.5-5 – Thermal Model of ATR Fuel Element and FHE within Inner Shell



(Note: the positive x-axis is oriented towards the top of the package and the positive z-axis towards the package closure end)

Figure 3.5-6 – Thermal Model of Loose Fuel Plate Basket (LFPB)



Figure 3.5-7 – Worst Case Package Damage Arising from Corner Drop

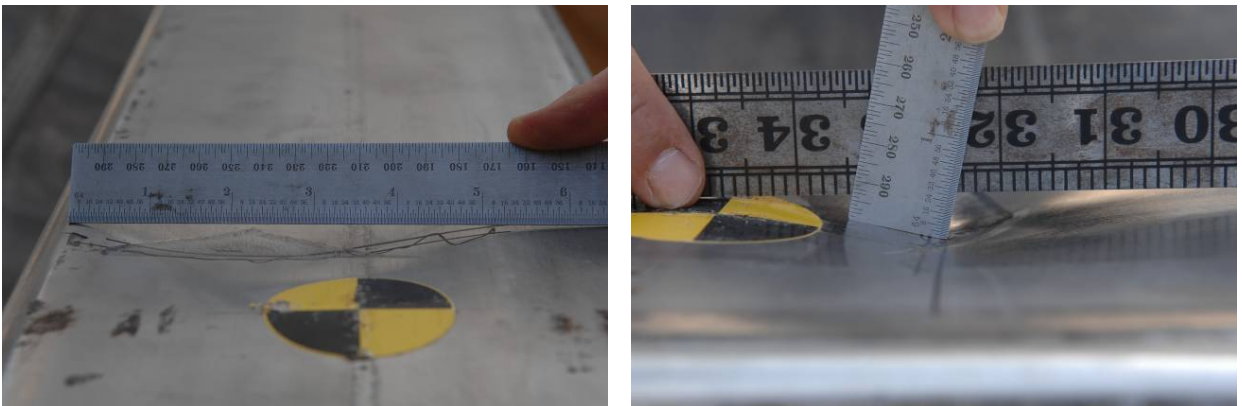
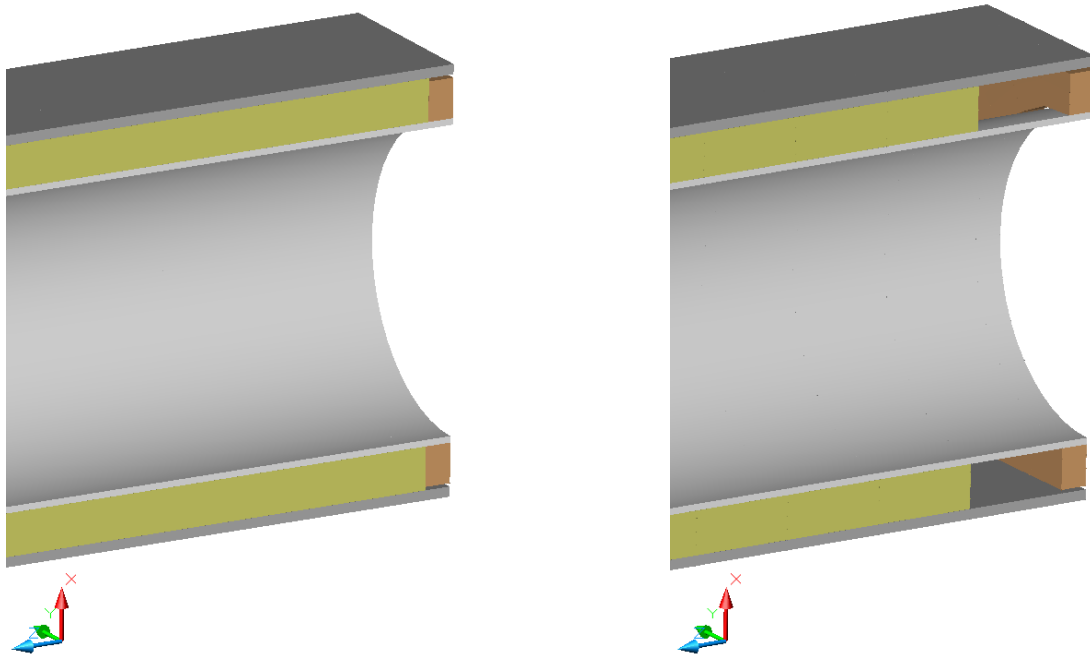


Figure 3.5-8 – Worst Case Package Damage Arising from Oblique Puncture Drop



Figure 3.5-9 – Insulation Re-positioning Arising from End Drop



Insulation Modeling for NCT Conditions

Insulation Modeling for HAC Conditions

Figure 3.5-10 – Thermal Modeling of Insulation Re-positioning for HAC Conditions

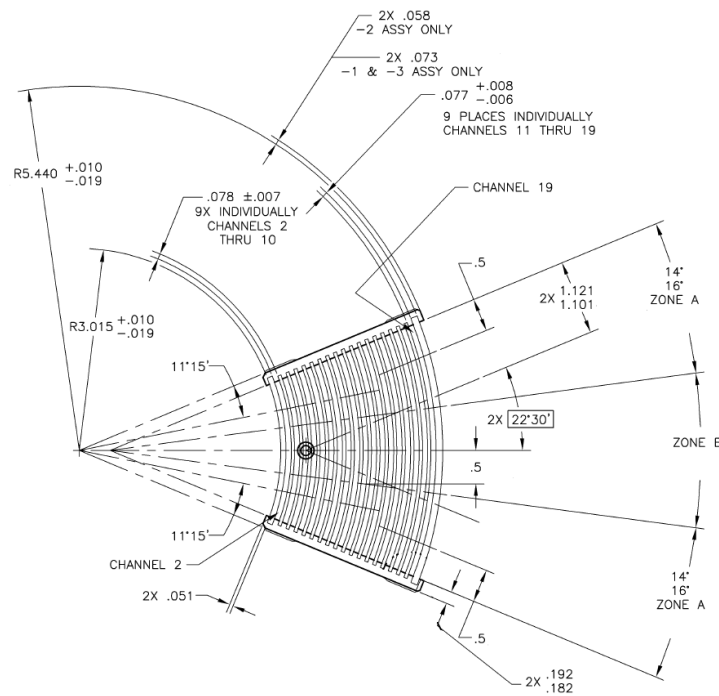


Figure 3.5-11 – ATR Fuel Element Cross Section

3.5.3 Thermal Decomposition/Combustion of Package Organics

The organic material in the ATR FFSC subject to thermal decomposition and/or combustion is limited to polyethylene, neoprene, and the adhesive used to attach the neoprene, as well as a maximum of six pounds of balsa wood or up to 4 kg of cellulosic material. The fuel elements and, optionally, the loose fuel plates are enclosed in polyethylene bags prior to their placement in the FHEs and loose plate basket. The bags serve no safety function beyond providing investment protection of the payload material. Similarly, neoprene (polychloroprene) rub strips are attached via adhesive to the FHEs to provide investment protection against fretting on the elements and loose plates. As such, the loss of the organic material under either NCT or HAC conditions has no safety implication beyond the potential for gas and heat generation. The following sections provide a bounding assessment on the potential safety impact associated with the loss of organic material within the ATR FFSC package.

3.5.3.1 Organic Material Within Package

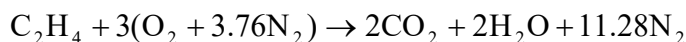
The amount of organic material in the package varies with the payload configuration. While the bounding amount of polyethylene is constant at 200 g, the amount of neoprene varies with payload configuration. The sections below identify the quantity and important thermal properties associated with the organic materials present in the ATR FFSC package.

Polyethylene

Properties of polyethylene related to its thermal decomposition/combustion are as follows:

- a) chemical formulation⁷: $-\text{[CH}_2\text{-CH}_2\text{]}_n\text{-}$,
- b) heat of combustion (ΔH_c)²⁸: 46,500 kJ/kg,
- c) oxygen index^{29,30}: 17.4%,
- d) melting temperature³⁰: 109-135°C
- e) temperature for 1% decomposition³⁰: 275°C
- f) autoignition temperature³¹: 330 to 410°C

Oxygen index (OI) is the minimum oxygen concentration required to support self-sustaining combustion of the polymer. Since piloted conditions do not exist within the ATR FFSC payload cavity, self-sustaining combustion of the polyethylene can't occur when the oxygen concentration drops below 17.4%. Low oxygen concentrations will not only prevent self-sustaining combustion, but will raise the autoignition temperature. Combustion of polyethylene in air is governed by the following equation:



The above equation demonstrates that complete combustion of a mole of polyethylene requires 3 moles of oxygen and, since oxygen constitutes approximately 21% of air, 14.28 moles of air.

²⁸ NUREG-1805, Fire Dynamics Tools, Nuclear Regulatory Commission, Washington, D.C.

²⁹ office.wendallhull.com/matdb/

³⁰ *SFPE Handbook of Fire Protection Engineering*, 3rd Edition, Section 1, Chapter 7, Table 1.7-4, NFPA, 2003.

³¹ *MSDS for Polyethylene*, #1488, prepared by International Programme on Chemical Safety, 2004.

The total quantity of gas generated is 15.28 moles, or an increase of 7% over the original gas quantity existing before combustion. Per SAR section 1.2.2, the amount of polyethylene in the package is limited to 200 g or less. Based on a molecular weight of approximately 28 g/g-mole of polyethylene, the 7.14 g-moles of polyethylene represented by the 200 g would require $7.14 \times 14.28 = 102.0$ g-moles of air for complete combustion.

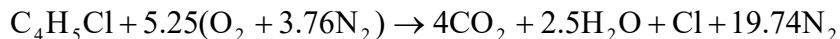
Neoprene

Properties of neoprene (polychloroprene) related to its thermal decomposition/combustion are as follows:

- chemical formulation⁷: $-\text{[CH}_2\text{-Cl-C=CH-CH}_2\text{]}_n-$,
- heat of combustion (ΔH_c)²⁸: 10,300 kJ/kg,
- oxygen index^{29,32}: 32-35% at one atmosphere,
- melting temperature: N/A - thermoset material
- temperature for initial decomposition³⁰: 342°C
- autoignition temperature³²: >380°C in a 21% oxygen concentration environment.

As a thermoset plastic, uncontrolled heating of neoprene will result in reaching the decomposition temperature before the melting point is obtained. The high oxygen index demonstrates why neoprene can't support combustion without an external ignition source. The typical adhesives³³ used to bond the rub strips to the FHEs consist of principally of solvents that outgas during the curing process. The non-volatile components consist of polymers, including polychloroprene, and cure and vulcanization agents. As a result, the cured adhesive layer exhibits properties³³ similar to neoprene.

Combustion of neoprene in air is governed by the following equation:



From the above equation, complete combustion of a mole of neoprene is seen to require 5.25 moles of oxygen and, since oxygen constitutes approximately 21% of air, 24.99 moles of air. The total quantity of gas generated is 27.24 moles, or an increase of 9% over the original gas quantity existing before combustion.

Based on the surface area of rub strips depicted on each SAR drawing, a thickness of 0.125 in, and an adhesive layer thickness of 2 mils, the total quantity of neoprene and neoprene like material used in each FHE is summarized in Table 3.5-2. With a molecular weight of approximately 88.5 g/g-mole of neoprene, the 4.62 g-moles of neoprene represented by the minimum 409 g of neoprene contained within the 60501-40 FHE assembly would require $4.62 \times 24.99 = 115.5$ g-moles of air for complete combustion.

The same limitation on package oxygen that prevents significant combustion of polyethylene will also prevent combustion of the neoprene. This same conclusion applies to the balsa wood and cellulosic material. Further, given the higher oxygen index and autoignition temperature for neoprene versus polyethylene, there is a low probability any neoprene material will be involved in combustion. Instead, it is expected that the only damage to be incurred by the neoprene will

³² *Safe Use of Oxygen and Oxygen Systems*, ASTM, 2nd Edition.

³³ Product and MSDS sheets for 3M™ Spray 80 Neoprene Contact Adhesive or 3M™ Scotch-Weld Neoprene Contact Adhesive 1357.

be a de-bonding from the FHE surfaces and a small amount of thermal decomposition. Since thermal decomposition is an endothermic process, the loss of the material will act to lower the temperatures predicted within the FHE.

3.5.3.2 Air Quantity Within Package

Since the ATR FFSC payload cavity is not sealed, the quantity of gas filling the cavity volume will vary with time as a function of the cavity's bulk gas temperature, the thermal decomposition of the enclosed organic material, and diffusion of gas through the package closure gaps. The following sections address these various mechanisms affecting the air/oxygen content within the package.

Potential Combustion Due to Resident Air Quantity

The ATR FFSC payload cavity has a length of 67.88 in and a diameter of 5.76 in. The gross cavity volume is 1768.8 in³. The ATR fuel element and the ATR FHE have volumes of approximately 155 and 223 in³, based on weights of 25 and 15 lbs, respectively, and mean densities of 0.112 and 0.097 lbs/in³, respectively. The net cavity space is therefore approximately 1,391 in³ (22.8 liters). Table 3.5-3 summarizes the net cavity volume existing for all payload configurations. As seen from the table, only the MIT FHE (SAR drawing 60501-40) loaded with a MIT fuel element results in a larger net cavity volume than the ATR FHE (SAR drawing 60501-30) loaded with an ATR fuel element. Given the substantially higher HAC temperature predicted for the ATR FHE (see Section 3.4, *Thermal Evaluation for Hypothetical Accident Conditions*) versus that for the MIT FHE (see Section 3.6, *Thermal Evaluation for MIT, MURR, Cobra, Small Quantity, and LEU Payloads*) and the larger quantity of neoprene used (see Table 3.5-2), the ATR FHE is the appropriate payload configuration for assessing the thermal safety related to the organic material in the package.

At 100°F, approximately 0.9 g-moles of air are required to fill a 1,391 in³ (22.8 liters) cavity space to a pressure of 14.7 psia, while at 626°F (330°C, i.e., the lower autoignition temperature for polyethylene), the quantity of air required to fill the cavity space drops to approximately 0.5 g-mole. As such, the resident air quantity in the payload cavity is sufficient to support combustion of less than 0.5% of the polyethylene (i.e., 0.5 g-mole/102 g-mole air per 200 g polyethylene). The potential heat release from this quantity of polyethylene is: 0.5% x 200 g x 46,500 kJ/kg = 46,500 J = 44 Btu. Based on a combined ATR payload weight of 40 lbs and a specific heat of approximately 0.2 Btu/lb_m-°F³⁴, the net increase in the mean payload temperature would be less than 6°F even if this heat release occurred instantaneously. The use of the combined payload weight for this calculation is appropriate since the combustion occurs in the vapor space and not on a surface. Further, combustion of the limiting 0.5% of the polyethylene can neither occur instantaneously nor in only one concentrated area since the availability of the oxygen within the cavity will be rate limited by the diffusion process from reaching the potential site(s) of polyethylene combustion. In fact, oxygen diffusion will also prevent the entire resident oxygen quantity from being consumed. As such, the estimated 6°F rise in payload temperature is highly conservative.

³⁴ Approximate specific heat of ATR fuel plates per Table 3.2-2

Given the lower heat of combustion of neoprene versus that for polyethylene and the greater air quantity needed for complete combustion, the potential temperature rise from the combustion of polyethylene bounds that for neoprene by a factor of over 3.

Potential Combustion Due to Air Induced Via Pressure Forces

Once the residual air existing in the payload cavity prior to the start of the HAC event is consumed, further combustion will require additional air to enter the cavity via pressure and diffusion forces. The pressure forces will arise due to the balance between ideal gas expansion/contraction and gas generation within the package versus the pressure resistance associated with gas flow through the gaps around the package closure. Heatup of the package during the 30-minute fire event will result in elevated cavity pressure and a continuous outflow of gas from the cavity. This gas flow will switch to an inflow condition once the peak bulk gas temperature is reached and the package begins to cool down.

While an accurate estimate of the gas flow due to pressure forces requires a detailed modeling of the flow paths and resistance factors, a bounding estimate on the rate of gas flow into the package due to pressure differential can be made by assuming zero vent resistance and zero internal gas generation. These assumptions assure that the minimum gas quantity is achieved at the point where packaging cooling begins, thus maximizing the potential for the reverse gas flow necessary to restore atmospheric pressure within the package.

Assuming that the bulk average gas temperature within the package is represented by the mean of the average temperatures over the length of the package's inner shell and the FHE, the cavity gas quantity within the package can be estimated as a function of time during the HAC transient. Figure 3.5-12 presents the predicted package gas quantity for the HAC transient depicted in Figure 3.4-1 for the ATR fuel element. As seen, the package gas quantity rapidly drops during the 30-minute fire event as the cavity gas expands under HAC heating. Shortly after the cessation of the fire event, the package begins to cool and the gas flow switches to an inflow. However, due to the rate of package cooldown, greater than 10 hours are required to restore the approximately 0.5 g-moles of gas expelled during package heatup. The calculated reverse gas flow peaks at 0.0025 g-moles per minute. The potential polyethylene combustion supported by this flow rate is $0.0025 \text{ g-moles per minute} \times 200 \text{ g polyethylene per } 102 \text{ g-mole air} \times 46,500 \text{ kJ/kg} = 228.1 \text{ J/min} = 0.22 \text{ Btu/min}$. Clearly this flow rate is too low to permit any significant rate of combustion, especially when considering the facts that the reverse gas flowrate decreases rapidly from this peak rate and that accounting for flow resistance through the vent geometry will reduce this potential heat gain even more.

When the above discussion is added to the fact that the oxygen concentration at the start of the inflow condition will be well below the oxygen index of 17.5% required to support combustion, the fact that oxygen diffusion within the package will extend the time for the entering air to reach the site of elevated polyethylene temperatures, and as seen in Figure 3.5-12, that the package temperatures will fall below the lower autoignition temperature for polyethylene after 90 minutes, it is reasonable to conclude that the contribution to package heatup from airflow due to pressure differential is essentially zero.

Potential Combustion Due to Air Induced Via Diffusion

Beside pressure differential, the other force available to drive oxygen inflow to the package cavity is diffusion. Assuming that the oxygen inside the package cavity is consumed as fast as it enters, the rate of oxygen diffusion can be determined via Fick's first law or:

$$J = -\rho \times D \times \frac{\partial w}{\partial y}$$

where: J = mass flux of oxygen per area, g/cm²

D = diffusion coefficient of oxygen in nitrogen, cm²/sec

ρ = density of air, g/cm³

$\frac{\partial w}{\partial y}$ = change in mass fraction of oxygen over diffusion path

While diffusion of oxygen in nitrogen is used to reflect that fact that the environment within the payload cavity is assumed to be oxygen depleted, in reality there is little difference between diffusion in air or nitrogen. The diffusion coefficient is a function of temperature and pressure. Diffusion increases with increasing temperature since the molecules move rapidly and decreases with increasing pressure since higher fluid density increases the number of molecules per unit volume, increasing the number of collisions, thus slowing the speed of transport. The diffusion coefficient for oxygen in air at 1 atm and 25°C is 0.206 cm²/sec³⁵. Since the fluid pressure is assumed to remain near atmospheric throughout the HAC event, there is no need to adjust the diffusion coefficient for pressure effects. However, the temperature of the fluid both within and exterior to the package will increase significantly during the HAC transient, thus necessitating an adjustment³⁶ in the diffusion coefficient via:

$$D_{O-N} = 0.0018583 \sqrt{T^3 \times \left(\frac{1}{M_O} + \frac{1}{M_N} \right)} \times \frac{1}{P \times \sigma_{O-N}^2 \times \Omega_{D,O-N}}$$

where: D = diffusion coefficient of oxygen in air, cm²/sec

T = temperature, K

M = molecular mass of oxygen and nitrogen

P = pressure, atm

Ω_{D,O-N} = collision integral for molecular diffusion of oxygen in nitrogen

σ_{O-N} = collision diameter, Angstroms

From Table E.1 and the equations provided in Transport Phenomena³⁶, M_O = 31.999, M_N = 28.013, σ_O = 3.433, σ_N = 3.667, ε_O/κ = 113, and ε_N/κ = 99.8. σ_{O-N} = 0.5x(3.433 + 3.667) = 3.55. ε_{O-N}/κ = (113 x 99.8)^{0.5} = 106.2. Assuming the maximum flame temperature of 1475°F (1075K), the dimensionless temperature is κT/ε_{O-N} = 1075/106.2 = 10.1. From Table E.2³⁶, Ω_{D,O-N} = 0.741. Thus, D_{O-N} at a pressure of 1 atm and 1475°F is 1.815 cm²/sec.

³⁵ CRC Handbook of Engineering Tables, Dorf, R. editor, CRC Press LLC, 2004.

³⁶ Transport Phenomena, 2nd Ed., Eqn 17.3-12 and Appendix E, Bird, R., Stewart, W, and Lightfoot, E., John Wiley & Sons, Inc., 2002.

The bayonet type closure plug for the ATR FFSC package results in a labyrinth like leakage path (see Figure 3.5-13). To conservatively bound the available leakage area for air exchange via diffusion, the closure plug geometry can be simplified as simply the barrel portion (i.e., flow path over segment A-B, Figure 3.5-13). Per the Table 3.5-4, the maximum diffusion area represented by this flow path is 1.71 in² (11 cm²). Based on the derived diffusion coefficient, an air density of 0.000325 g/cm³ at 1475°F (1075K), and a total diffusion path length of 2.5 in (6.4 cm, i.e., the total length of the closure plug), the maximum diffusion rate during the 30-minute fire event is calculated as:

$$J \times \text{Area} = -0.000325 \text{ g/cm}^3 \times 1.815 \text{ cm}^2/\text{sec} \times \frac{0.21 - 0}{6.4} \times 11 \text{ cm}^2$$

$$J \times \text{Area} = 0.00021 \text{ g/sec} = 0.0004 \text{ g-mole/min}$$

Following the fire event, the ambient temperature will drop to 100°F and the ambient density will rise to 0.001128 g/cm³. The diffusion coefficient for oxygen in air at 1 atm and 25°C is 0.206 cm²/sec³⁵, or approximately 11% of the diffusion coefficient determined for the fire conditions. The net effect of the higher density and lower diffusion coefficient is a diffusion rate of 0.00008 g/sec, or 38% of the rate determined at fire conditions.

Based on the 0.22 Btu/min temperature rise determined in the previous section for the 0.0026 g-mole/min oxygen flow associated with the pressure differential, the 0.0004 g-mole/min oxygen diffusion rate would generate a maximum 0.03 Btu/min temperature rise, dropping to less than 0.013 Btu/min following the end of the fire event. Since accounting for the diffusion resistance within the payload cavity will reduce the potential heat generation rate even more, a reasonable conclusion is that the contribution to package heatup from oxygen diffusion can be ignored.

3.5.3.3 Pressure Loss Across Closure Leakage Path

The ATR FFSC package is not sealed, but uses a bayonet type closure plug that results in a labyrinth like leakage path, see Figure 3.5-13. The size of the various pathways illustrated in the figure are listed in Table 3.5-4. The maximum pressure rise within the package is associated with the minimum flow area and the maximum gas generation and thermal expansion, with the total pressure loss estimated from a summation of the individual pressure losses associated with each portion of the flow path. Normalizing the individual pressure losses to the flow velocity in the A-B channel allows direct addition of the individual loss coefficients and eases the calculation of the pressure loss based on a single flow velocity. The normalizing to flow velocity involves multiplying the calculated loss coefficient by the square of the area ratio.

The entrance loss at the beveled portion of the closure plug can be estimated using a conical inlet with adjoining wall (i.e, Diagram 3-7³⁷). Based on a 15° bevel angle on closure plug and L/D_h > 0.6, the total loss coefficient at the entrance is:

$$\xi_1 = \frac{\Delta P}{0.5 \rho v^2} = 0.13$$

³⁷ *Handbook of Hydraulic Resistance*, 3rd Ed., Idelchik, I.E., Begell House Publishers, 1996.

where v is the flow velocity upstream of the inlet area. This value is conservatively increased to $\xi_1 = 0.50$ for a blunt, flush inlet (Diagram 3-1³⁷). Since the loss coefficient is based on the flow velocity after entering the gap, no adjustment for flow area in A-B is necessary:

$$K_1 = \xi_1 = 0.5$$

The pressure loss associated with flow in the A-B channel is a function of wall friction losses. Given the short path length and smooth wall surfaces, the associated pressure loss will be insignificant and can be ignored.

Flow between B-B' can be approximated as a 90-degree turn with sharp corners (Diagram 6-6³⁷). Here the rectangular side length ratio (a_o/b_o) is equal to $(5.64 \times \pi)/((5.76 - 5.64)/2) = 295.3$ and the ratio of cross section areas (b_1/b_0) is equal to $0.006/0.06 = 0.1$ (based on the minimum gap width after the turn). With these values, the loss factor extrapolated from Diagram 6-6 is $\xi_2 = 3.1$. Given uncertainties in the extrapolation, the computed value is doubled to 6.2 for conservatism³⁸. Since the loss coefficient is based on the flow velocity in the gap approaching the turn, no adjustment for flow area in A-B is necessary:

$$K_2 = \xi_2 = 6.2$$

Flow between B'-E can also be approximated as a 90-degree sharp corner turn (Diagram 6-6³⁷). Again, the rectangular side length ratio (a_o/b_o) is equal to $(5.967 \times \pi)/(0.006 \text{ min gap}) = 3124$ and the ratio of cross section areas (b_1/b_0) is equal to $0.235/0.006 = 39$. With these values, the loss factor can be conservatively estimated from Diagram 6-6 as $\xi_3 = 0.55$. Converting to the loss coefficient based on the gap area for flow path A-B yields:

$$K_3 = \xi_3 \left(\frac{0.45}{0.11} \right)^2 = 9.20$$

Flow between E-F can also be approximated as a sudden expansion with a discharge to ambient. A loss factor of 1 is used to account for these losses. Converting to the loss coefficient based on the gap area for flow path A-B yields:

$$K_4 = \xi_4 \left(\frac{0.45}{1.77} \right)^2 = 0.06$$

The parallel flow path to B'-E consisting of B'-C, C-D, and D-E can be conservatively ignored as its inclusion will serve to lower the estimated total pressure loss. Therefore, a bounding estimate of the total loss factor associated with the minimum expected flow path areas is calculated as $K_1 + K_2 + K_3 + K_4 = 0.5 + 6.2 + 9.2 + 0.06 = 16$.

The pressure loss for flow through the closure plug leakage path can be computed as a function of velocity and density via $\Delta P = 16 \times 0.5 \frac{\rho v^2}{g_c}$. Since mass flow is also a function of velocity and

³⁸ This flow loss is a reasonable upper bound given a worst case assumption that the flow comes to a complete stop before the turn and then needs to re-accelerate into the smaller gap. When adjusted for velocity differences, the flow loss under this worst case scenario would be approximately $(0.45 \text{ in}^2/0.11 \text{ in}^2)^2 \times 0.5 = 8.4$, where 0.5 is the loss factor associated with a blunt inlet fitting.

density, $\dot{m} = \rho \times v \times \text{Area}$, the pressure loss relationship can be re-formulated as a function of mass flow via:

$$\Delta P = 16 \times 0.5 \frac{\rho \left[\dot{m} / (\rho \times \text{Area}) \right]^2}{g_c}$$

where Area is the flow area in the path A-B (0.45 in² minimum) and the density is for the bulk gas temperature. From the data used to develop Figure 3.5-12, the maximum gas flow required to maintain atmospheric pressure within the ATR FFSC cavity due to only ideal gas expansion occurs during package heatup. The peak flowrate of 0.035 g-mole/min occurs approximately 8 minutes after the start of the 30-minute HAC fire and when the bulk gas temperature within the payload cavity has reached 230°F (110°C). Based on a molecular weight of 28.96 g/g-mole for air, the associated mass flow and density are 1.01 g/min (0.00004 lb_m/sec) and the gas density is 0.00091 g/cm³ (0.057 lb_m/ft³). Substituting these values into the above equation yields:

$$\Delta P = 5(10^{-6}) \text{ psi}$$

for the conservative assumption of minimum flow areas within all vent gaps. The pressure loss at nominal gap dimensions will be even lower.

This maximum pressure rise due to thermal expansion of the cavity gas is too low to create an issue. Thermal decomposition of polyethylene and neoprene will generate additional gases that would need to be vented. While only a small fraction of the material is expected to be thermally decomposed due to a combination of the temperature levels achieved and the time above the thermal decomposition temperature level, a bounding maximum pressure rise can be estimated assuming the entire inventory of both polyethylene and neoprene decomposes over a 60 minute period. The potential gas quantity associated with the total decomposition of the 200 g of polyethylene is 200 g/(28 g/g-mole) x 2 g-moles H₂ per g-mole polyethylene = 14.3 g-moles H₂. Similarly, the 1,926 g of neoprene associated with the SAR 60501-70 FHE assembly will generate 1926 g/(88.5 g/g-mole) x (2 g-moles H₂ + 1 g-moles HCl) per g-mole neoprene = 65.3 g-moles H₂ and HCl. The combined gas generation rate is therefore (14.3 + 65.3 g-mole)/60 minutes, or 1.33 g-moles/minute. Alternately, considering the entire mass of neoprene and polyethylene to decompose in 60 minutes gives a mass flow rate of (1,926 + 200)/60 = 35.4 g/min, or 0.0013 lb_m/s. Conservatively assuming the gas is H₂ at a temperature of 1,017 °F from Table 3.1-1, the gas density is 1.1(10⁻⁶) lb_m/in³. Substituting into the equation above yields:

$$\Delta P = 0.16 \text{ psi}$$

For the case of the balsa FHE which weighs a maximum of 6 lb, the mass flow rate is 6/60 = 0.1 lb/min or 0.0017 lb_m/s. Again assuming the same conservatively low gas density, the prior result may be factored by the square of the mass flow rate, yielding:

$$\Delta P = 0.16 \times (0.0017/0.0013)^2 = 0.27 \text{ psi}$$

Four kg of cellulosic material would have a mass flow rate of 0.0024 lb_m/s. Factoring the neoprene result as before yields:

$$\Delta P = 0.16 \times (0.0024/0.0013)^2 = 0.55 \text{ psi}$$

These results are based on three significant conservatisms:

- Minimum flow area in all gaps
- 100% of the mass decomposes to gas (no residue)
- Density of gas minimized (high-temperature hydrogen)

As such, the assumption of a 0 psig pressure throughout the HAC event is valid for the purposes of determining the safety basis of the design.

Based on the level of and type of damage noted in Appendix 2.12.1, *Certification Tests on CTU-1* and Appendix 2.12.2, *Certification Tests on CTU-2*, no change to the net vent areas based on the assumed minimum gaps is expected. Thus the above conclusions remain valid for the damaged package configuration as well.

Table 3.5-2 – Neoprene Quantity Per Assembly

SAR Drawing	Neoprene Surface Area, in ²	Neoprene Volume, in ³	Neoprene Adhesive Volume, in ³	Neoprene Quantity, g [Ⓛ]
60501-10	N/A	N/A	N/A	N/A
60501-20	N/A	N/A	N/A	N/A
60501-30	475	59	1.0	1210 g
60501-40	162	20	0.3	409 g
60501-50	266	33	0.5	676 g
60501-60	547	68	1.1	1393 g
60501-70	748	94	1.5	1926 g

Notes: Ⓛ Based on density of 1.23 g/cm³ (76.8 lb/ft³ per Table 3.2-3)

Table 3.5-3 – Net Cavity Volume vs. Payload Assembly

SAR Drawing	Gross Cavity Volume, in ³	FHE Volume, in ³	Payload Volume, in ³	Net Cavity Volume, in ³	Comments
60501-20	1768.8	307.4 [Ⓛ]	168.1 [Ⓜ]	1293.3	ATR Loose Plate FHE
60501-30	"	154.6 [Ⓝ]	223.2 [Ⓞ]	1390.9	ATR FHE - Design basis selection due to combination of net cavity size and peak HAC temperature for FHE
60501-40	"	256.1 [Ⓟ]	88.5 [Ⓠ]	1424.1	MIT FHE
60501-50	"	307.4 [Ⓡ]	126.1 [Ⓢ]	1335.4	MURR FHE
60501-60	"	286.9 [Ⓣ]	142.9 [Ⓤ]	1339.0	RINSC FHE
60501-70	"	307.4 [Ⓛ]	168.1 [Ⓜ]	1293.3	Small Quantity FHE

Notes: Ⓛ Based on 30 lb weight and density of 0.0976 in³ per Tables 2.1-1 and 3.2-2

Ⓜ Based on 20 lb weight and density of 0.112 in³ per Tables 2.1-1 and 3.2-2

Ⓝ Based on 15 lb weight and density of 0.097 in³ per Tables 2.1-1 and 3.2-1

Ⓞ Based on 25 lb weight and density of 0.112 in³ per Tables 2.1-1 and 3.2-2

Ⓟ Based on 25 lb weight and density of 0.0976 in³ per Tables 2.1-1 and 3.2-2

Ⓠ Based on 10 lb weight and density of 0.113 in³ per Tables 2.1-1 and 3.6-4

Ⓡ Based on 30 lb weight and density of 0.0976 in³ per Tables 2.1-1 and 3.2-2

Ⓢ Based on 15 lb weight and density of 0.119 in³ per Tables 2.1-1 and 3.6-4

Ⓣ Based on 28 lb weight and density of 0.0976 in³ per Tables 2.1-1 and 3.2-2

Ⓤ Based on 17 lb weight and density of 0.119 in³ per Tables 2.1-1 and 3.6-4

Table 3.5-4 – Closure Leakage Path Areas

Flow Path	Inner/Outer Diameter, in	Gap Width/Length, in	Flow Path Area, in ²
A to B	5.64 ± 0.01 5.76 ± 0.06 ^①	1.69	Max: 1.71 Min: 0.45
B to B'	5.70 (mean)	0.006 to 0.03 ^②	Max: 0.54 Min: 0.11
B' to C	5.967 (min)	0.006 to 0.03 ^②	Max: 0.56 Min: 0.11
C to D	6.38 ± 0.02 6.44 ± 0.01	0.281	Max: 0.91 Min: 0.30
D to E	6.21 (mean)	0.006 to 0.03 ^②	Max: 0.59 Min: 0.12
B' to E	5.967 ± 0.01 6.44 ± 0.01	0.281	Max: 1.92 ^③ Min: 1.77 ^③
E to F	5.967 ± 0.01 6.44 ± 0.01	0.56	Max: 1.92 ^③ Min: 1.77 ^③

Notes: ① Tolerance from ASTM A269

② Based on bayonet tab of width of 0.25 in. centered in slot width of 0.281 in., and tolerances of +0.01 on both parts.

③ Based on 40% of gross area accounting for area of bayonet tabs and ignoring additional smaller gaps

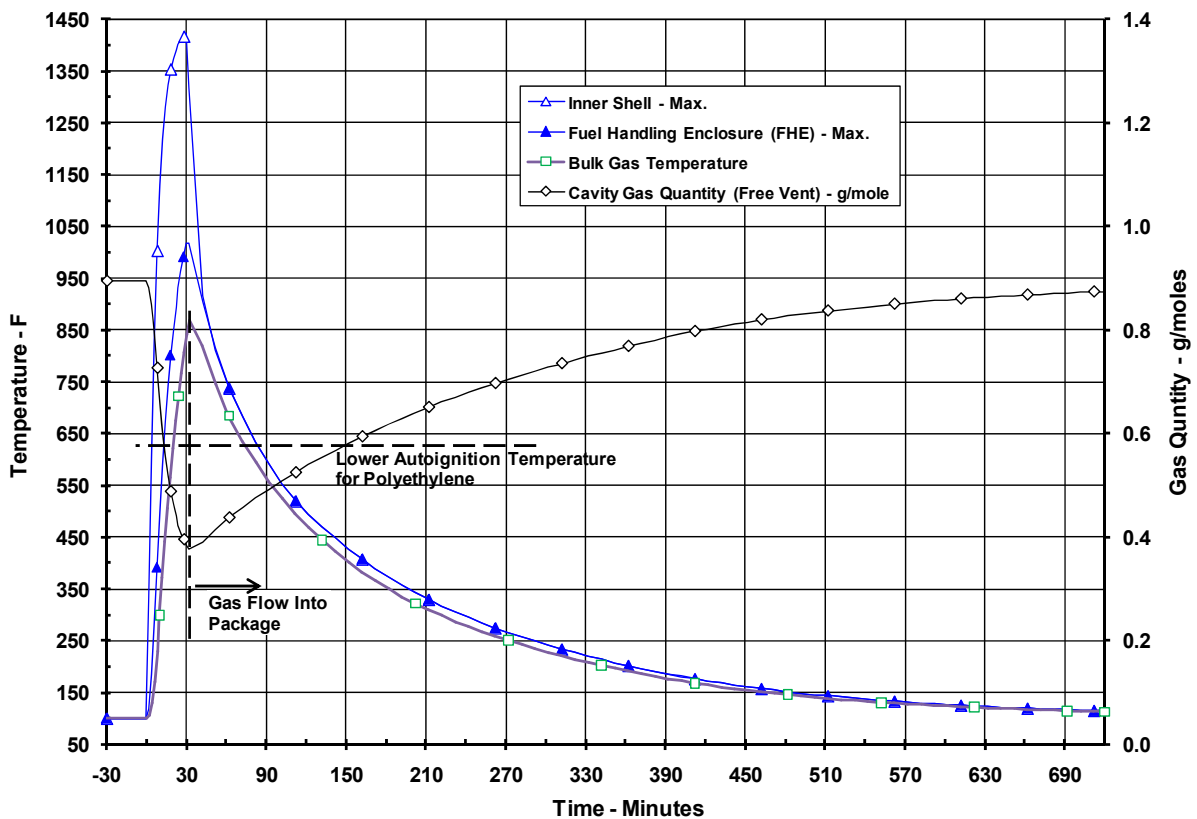
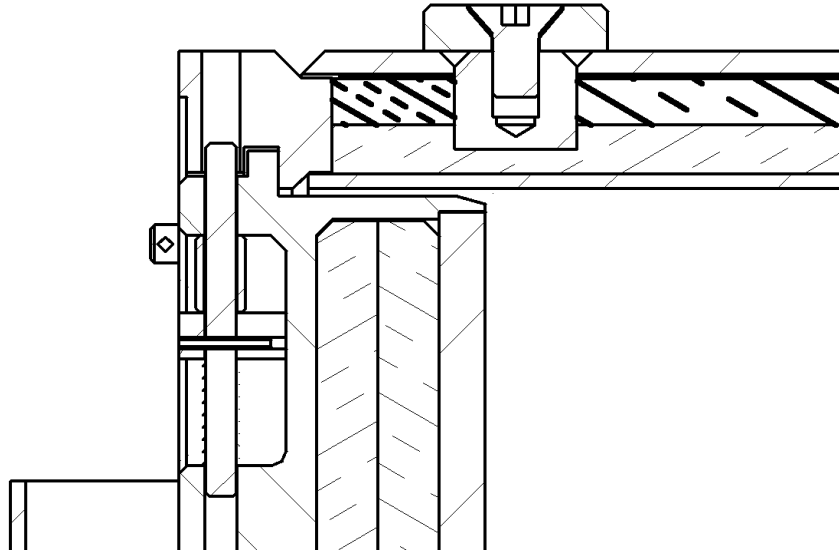
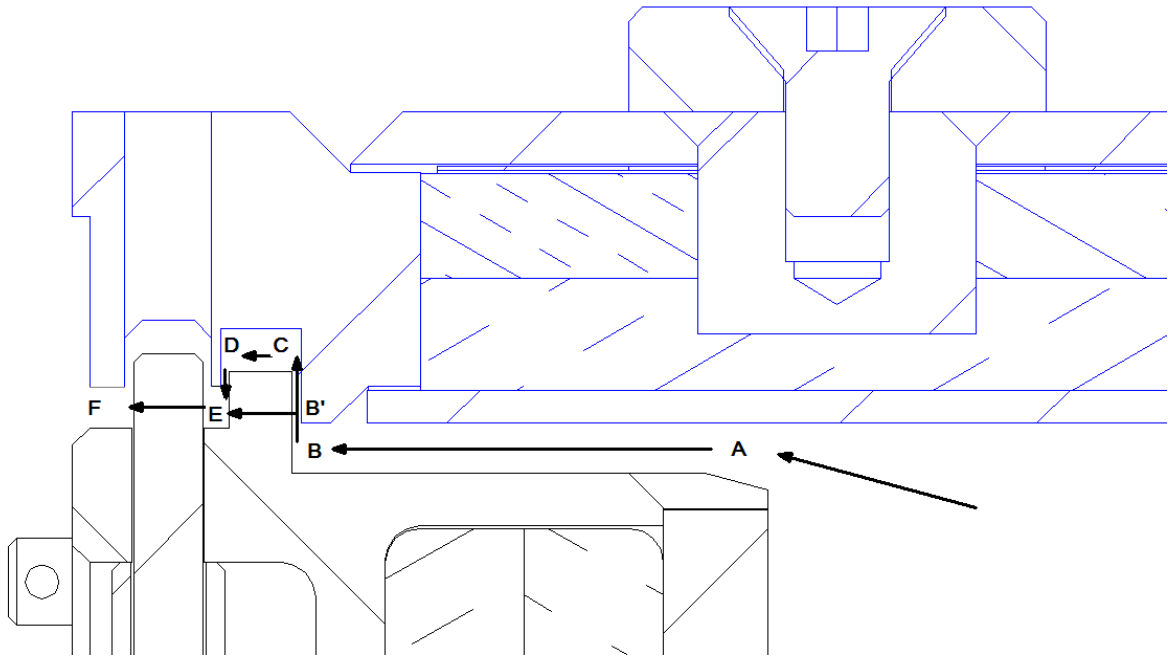


Figure 3.5-12 – Free Vent Gas Flow During HAC Transient



a) Package Closure



b) Enlarged Flow Paths at Package Closure

Figure 3.5-13 – Free Vent Gas Flow Path

3.6 Thermal Evaluation for MIT, MURR, Cobra, Small Quantity, and LEU Payloads

This section identifies and describes the principal thermal design aspects of the ATR FFSC for the transport of one assembled fuel element of the type: MIT HEU, MURR HEU, Cobra, ATR LEU, MIT LEU or DDE, MURR LEU or DDE, NBSR DDE, or small quantity payloads as described in Section 1.2.2.4, *Small Quantity Payload*. The evaluation presented herein demonstrates that the thermal performance of the ATR FFSC when transporting these payloads is bounded by the temperatures reported for the transport of the ATR fuel element payload. Specifically, the evaluations presented herein demonstrate the thermal safety of the ATR FFSC package¹ complies with the thermal requirements of 10 CFR 71² when transporting a payload consisting of either an assembled, unirradiated fuel element, or loose, unirradiated fuel plates, or other small quantity payloads as described in Section 1.2.2, *Contents*.

All package components are shown to remain within their respective temperature limits under the normal conditions of transport (NCT). Further, per 10 CFR §71.43(g), the maximum temperature of the accessible package surfaces is demonstrated to be less than 122 °F for the maximum decay heat loading, an ambient temperature of 100 °F, and no insolation. Finally, the ATR FFSC package is shown to retain sufficient thermal protection following the HAC free and puncture drop scenarios to maintain all package component temperatures within their respective short term limits during the regulatory fire event and subsequent package cool-down.

3.6.1 Description of Thermal Design

The ATR FFSC package, as described and illustrated in Chapter 1.0, *General Information*, consists of three basic components: 1) a Body assembly, 2) a Closure assembly, and 3) either a Fuel Handling Enclosure (FHE) or a Loose Fuel Plate Basket (LFPB). The FHE is configured to house one assembled fuel element or DDE, while the LFPB is configured to house loose fuel element plates. The maximum gross weight of the fully loaded package is approximately 290 lbs.

The ATR FFSC is designed as a Type AF packaging. The packaging is rectangular in shape and is intended to be transported in racks of multiple packages by highway truck. Since the payload generates essentially no decay heat, the worst case thermal conditions will occur with an individual package fully exposed to ambient conditions. The package performance when configured in a rack of multiple packages will be bounded by that seen for an individual package.

The thermal design aspects of the principal components of the packaging are described in more detail in Section 3.1, *Description of Thermal Design*. The paragraphs below present the thermal design features of the various payloads and their associated FHEs.

3.6.2 Fuel Handling Enclosures

Fuel handling enclosures are used with all payloads (except the NBSR DDE), and associated loose fuel element plates. Except as noted, the FHE are machined, two-piece aluminum

enclosures used to protect the fuel element from damage during loading and unloading operations. The FHE consist of two identical segments machined from 6061 aluminum plate or bar stock. The FHE features neoprene rub strips to further protect the fuel. The FHE is neither anodized nor coated, but is left as unfinished aluminum. Spacer weldments on either end of the enclosure halves are used to position and support the FHE within the ATR FFSC cavity. The spacers are also fabricated of 6061 aluminum. A polyethylene bag may be used as a protective sleeve over the fuel elements. The following table presents a directory of figure depictions of the FHE and fuel elements, and design weights of the FHE. Note, the MIT, MURR, and Cobra loose fuel element plates are shipped in the Small Quantity FHE (SQFHE). Loose plates may be shipped with kraft paper and adhesive tape for property protection, and aluminum or cellulosic dunnage, as described in Section 1.2.1.1.8, *Small Quantity Payload FHE*. The FHE used with the ATR LEU fuel element is made of two halves of balsa wood and held together using four straps. The NBSR DDE does not utilize a FHE.

Fuel	Exploded View of FHE	Fuel Element Figure	FHE Design Weight, lb
MIT HEU, LEU, DDE	Figure 1.2-6	Figure 1.2-13	25
MURR HEU	Figure 1.2-7	Figure 1.2-14	30
MURR LEU, DDE	Figure 1.2-18	Figure 1.2-14	21
RINSC	Figure 1.2-8	Figure 1.2-15	28
Small Quantity	Figure 1.2-9	Not shown in figures	30
Cobra	Figure 1.2-10	Figure 1.2-19	28
ATR LEU	Figure 1.2-17	Figure 1.2-12	6

3.6.3 Content’s Decay Heat

The ATR FFSC is designed as a Type AF packaging for transportation of an unirradiated fuel elements or a bundle of loose, unirradiated fuel plates. The decay heat associated with unirradiated fuel is negligible. Therefore, no special devices or features are needed or utilized in the ATR FFSC packaging to dissipate the decay heat. Section 1.2.2, *Contents*, provides additional details regarding the potential contents of the ATR FFSC.

3.6.4 Summary Tables of Temperatures

Table 3.6-1 provides a summary of the maximum package component temperatures achieved under NCT and HAC conditions for either the MIT HEU or MURR HEU fuel element payloads. These temperatures are either bounded by or similar to those reported in Table 3.1-1 for the transport of the ATR HEU fuel element payload. Those values unbounded by the values found in Table 3.6-1 remain well below the maximum allowable temperatures. Based on the results for the MURR fuel element, the maximum temperatures achieved under NCT and HAC conditions for the Cobra fuel element, small quantity payloads (including the RINSC fuel element), and

LEU fuel elements and DDEs are shown by qualitative analysis below to also be bounded by the results presented in Table 3.1-1.

The MIT HEU and MURR HEU payload temperatures for NCT are based on an analytical model of the ATR FFSC package under extended operation with an ambient temperature of 100°F and a diurnal cycle for the insolation loading. The temperatures for HAC are based on an analytical model of the ATR FFSC package with the worst-case, hypothetical pre-fire damage as predicted based on drop tests using full-scale certification test units (CTUs). The ATR FFSC with the Cobra fuel element, small quantity payloads, or LEU fuel elements and DDEs was not specifically modeled as part of this evaluation. Instead, their thermal performance is estimated using a qualitative approach based on the thermal characteristics of the other payloads and their associated thermal performance.

The MIT HEU and MURR HEU payload results for NCT demonstrate that significant thermal margin exists for all package components. This is expected since the only significant thermal loads on the package arise from insolation and ambient temperature changes. The payload dissipates essentially zero decay heat. Further, the evaluations for NCT demonstrate that the package skin temperature will be below the maximum temperature of 122°F permitted by 10 CFR §71.43(g) for accessible surface temperature in a nonexclusive use shipment when transported in a 100°F environment with no insolation. Given the significant thermal margin existing for the other payloads and the similar materials of fabrication, the Cobra fuel element, small quantity payloads, and LEU fuel elements and DDEs are also predicted to exhibit large thermal margins.

The MIT HEU and MURR HEU payload results for HAC conditions demonstrate that the design of the ATR FFSC package provides sufficient thermal protection to yield component temperatures that are significantly below the acceptable limits defined for each component. While the neoprene rubber and polyethylene plastic material used to protect the fuel element from damage are expected to reach a sufficient temperature level during the HAC fire event to induce thermal decomposition, the loss of these components is not critical to the safety of the package. As demonstrated in Section 3.5.3, *Thermal Decomposition/Combustion of Package Organics*, the available oxygen in the package, plus that which may enter the package under pressure differential and gas diffusion forces, is insufficient to result in any significant heat generation due to combustion. Given the similar materials of fabrication and equivalent thermal mass as the MURR payload, the Cobra fuel element, small quantity payloads, and LEU fuel elements and DDEs are also predicted to exhibit large thermal margins under HAC conditions.

3.6.5 Summary Tables of Maximum Pressures

Table 3.6-2 presents a summary of the maximum pressures achieved under NCT and HAC conditions. Since the ATR FFSC package is a vented package, both the maximum normal operating pressure (MNOP) and the maximum pressure developed within the payload compartment under the HAC condition are 0 psig. Section 3.5.3, *Thermal Decomposition/Combustion of Package Organics*, provides the justification for assuming a 0 psig package pressure for the HAC event.

Although the volume between the outer and inner shells is sealed, it does not contain organic or other materials that may outgas or thermally decompose. Therefore, the maximum pressure that may develop within the space will be limited to that achieved due to ideal gas expansion. The

maximum pressure rise under NCT will be less than 4 psig, while the pressure rise under HAC conditions will be 39 psig.

In the remainder of this appendix, the use of the terms MIT and MURR, unless distinguished by the term ‘LEU’, shall be taken to mean MIT HEU and MURR HEU, respectively.

Table 3.6-1 – Maximum Temperatures for NCT and HAC Conditions

Location / Component	NCT Hot Conditions	Accident Conditions	Maximum Allowable ^①	
			Normal	Accident
Fuel Element Fuel Plate	143°F	640°F	400°F	1,100°F
Fuel Element Side Plate	143°F	644°F	400°F	1,100°F
Neoprene Rub Strips/Polyethylene Bag	143°F ^②	710°F	225°F	N/A
Fuel Handling Enclosure (FHE)	143°F	710°F	400°F	1,100°F
Inner Shell	157°F	1,417°F	800°F	2,700°F
Ceramic Fiber Insulation, Body	- Maximum	184°F	2,300°F	2,300°F
	- Average	149°F	2,300°F	2,300°F
Ceramic Fiber Insulation, Closure	- Maximum	145°F	2,300°F	2,300°F
	- Average	143°F	2,300°F	2,300°F
Closure	145°F	1,439°F	800°F	2,700°F
Outer Shell	184°F	1,475°F	800°F	2,700°F

Table Notes:

① Maximum allowable temperatures are defined in Section 3.2.2, *Technical Specifications of Components*.

② Component temperature assumed to be equal to that of the FHE.

Table 3.6-2 – Summary of Maximum Pressures

Condition	Fuel Cavity Pressure	Outer/Inner Shell Cavity Pressure
NCT Hot	0 psi gauge	4 psi gauge
HAC Hot	0 psi gauge	39 psi gauge

3.6.6 Material Properties and Component Specifications

The ATR FFSC is fabricated primarily of Type 304 stainless steel, 5052-H32 and 6061-T651 aluminum, ceramic fiber insulation, and neoprene rubber. The payload materials include 6061-T6 and/or 6061-0 aluminum, uranium aluminide (UAl_x), uranium silicide (U_3Si_2), and uranium molybdenum (U-10Mo in a foil coated with thin zirconium interlayers). A polyethylene plastic bag is used as a protective sleeve over the fuel element.

3.6.6.1 Material Properties

The material specifications for the ATR FFSC package are defined in Section 3.2.1, *Material Properties*. Table 3.6-3 presents the thermal properties for 6061 aluminum used for the MIT and MURR FHEs, as taken from Table TCD of the ASME Boiler and Pressure Vessel Code³. Although the design permits a variety of aluminum tempers to be used, a single data set is provided since the material temper has little to no effect on its thermal properties. Further, because the HAC analysis requires thermal properties in excess of the maximum temperature point of 400°F provided in Table TCD, the property values at 1100°F (i.e., the approximate melting point for aluminum) are assumed to be the same as those at 400°F. This approach is appropriate for estimating the temperature rise within the fuel basket during the HAC event since the thermal conductivity of aluminum alloys tends to decrease with temperature while the specific heat tends to increase. The density values listed in the table are taken from an on-line database⁴. Properties between the tabulated values are calculated via linear interpolation within the heat transfer code.

Table 3.6-4 presents the thermal properties for the MIT and MURR fuel elements. For analysis purposes, the material used for the side plates and end fittings are assumed to be 6061-0 aluminum. The thermal properties for the fuel plates are determined as a composite of the cladding and the fuel core materials based on the geometry data for the MIT and MURR fuel element^{39,40} and the thermal properties for the ATR fuel element materials⁶. This approach is the same as used for the ATR fuel element. The details of the computed values are presented in Appendix 3.6.9.2.3, *Determination of Composite Thermal Properties for MIT and MURR Fuel Plates*. For simplicity, the thermal properties are assumed to be constant with temperature based on the use of conservatively high thermal conductivity and conservatively low specific heat values. This approach maximizes the heat transfer into the fuel components during the HAC event, while under-estimating the ability of the components to store the heat.

The RINSC fuel elements are fabricated with a nominally 0.020-in thick mixture of uranium silicide (U_3Si_2) and aluminum powder as the fuel “meat” and a nominally 0.015-in thick aluminum alloy cladding. The twenty-two (22) flat fuel plates have a 2.8-in width, an overall length of 25-in, and an active fuel region of 22.5 to 24.0-in. These fuel plate meat and cladding thicknesses match those of the interior plates for the ATR fuel element and are similar to those for the MURR fuel plates. The side plates are fabricated of ASTM B 209, aluminum alloy 6061-

³⁹ *Massachusetts Institute of Technology, Test Research Training Reactor 3 Fuel Plate*, EG&G, Idaho, Inc., Drawing No. 410368, Rev. A.

⁴⁰ *University of Missouri at Columbia, Test Research Training Reactor 4 MURR Fuel Plate*, EG&G, Idaho, Inc., Drawing No. 409406, Rev. E.

T6 and 6061-T651 and are approximately 0.188-in thick. This is similar to the side plate thicknesses of the ATR, MIT, and MURR fuel elements.

The thermal conductivity of the RINSC fuel plates are similar to data obtained in the measurements of the thermal conductivities for the uranium aluminide (UAl_x) based fuels⁴¹. Similarly, the thermal mass of the fuel plates are comparable despite the higher density of uranium silicide versus uranium aluminide since the ratio of the specific heats of the two materials is nearly the inverse of the density ratio.

The Cobra fuel elements are fabricated with a nominally 0.025-in thick mixture of Uranium and either aluminum as UAl_x (HEU) or with silicon as U_3Si_2 (LEU) as the fuel “meat” and a nominally 0.014-in thick aluminum alloy cladding. The fuel is constructed using six concentric circular layers of fuel plates, divided into three equal segments by radial, aluminum alloy separator plates. The fuel plates are approximately 38 inches long. The entire fuel element, including aluminum alloy end fittings, is approximately 61 inches long. The diameter of the element (outside edge of the separator plates) is approximately 3.25 inches. The remarks above concerning thermal conductivity and thermal mass for the RINSC fuel elements apply to the Cobra fuel elements as well.

The LEU fuel elements and DDEs are described in Section 3.6.9.2.6, *Determination of Thermal Properties for LEU Fuel Elements*.

The additional small quantity payloads are fabricated as described in Section 1.2.2.4, *Small Quantity Payload*. Small quantity payloads may be shipped with aluminum or cellulosic dunnage.

The thermal properties for air and for the non-metallic materials used in the ATR FFSC are presented in Section 3.2.1, *Material Properties*, as is the assumed emissivity (ϵ) for each radiating surface and the solar absorptivity (α) value for the exterior surface. The 6061-0 aluminum used for the MIT and MURR fuel components are assumed to have a surface coating of boehmite ($Al_2O_3 \cdot H_2O$). A 25 μm boehmite film will exhibit a surface emissivity of approximately 0.92¹³. While a fresh fuel element may have a lower surface emissivity, the use of the higher value will provide a conservative estimate of the temperatures achieved during the HAC event.

3.6.6.2 Technical Specifications of Components

The materials used in the ATR FFSC that are considered temperature sensitive include the aluminum used for the FHEs, the LFPB, and the fuel elements, the neoprene rubber, and the polyethylene wrap used as a protective sleeve around the fuel elements. Of these materials, only the aluminum used for the fuel elements is considered critical to the safety of the package. The other materials either have temperature limits above the maximum expected temperatures or are not considered essential to the function of the package.

Section 3.2.2, *Technical Specifications of Components*, presents the basis for the temperature limits of the various components. These temperature limits are applicable to this safety evaluation as well.

⁴¹ IAEA-TECDOC-643, *Research Reactor Core Conversion Guidebook*, Volume 4: Fuels (Appendices I-K), International Atomic Energy Agency, Vienna, Austria.

Table 3.6-3 – Thermal Properties of Package Metallic Materials

Material	Temperature (°F)	Thermal Conductivity (Btu/hr-ft-°F)	Specific Heat (Btu/lb_m-°F)	Density (lb_m/in³)
Aluminum Type 6061-T651 / T6511	70	96.1	0.214	0.098
	100	96.9	0.216	
	150	98.0	0.220	
	200	99.0	0.222	
	250	99.8	0.224	
	300	100.6	0.227	
	350	101.3	0.230	
	400	101.9	0.231	
	1100 ^①	101.9	0.231	

Notes:

① Values for 1100°F are assumed equal to values at 400°F.

Table 3.6-4 – Thermal Properties of MIT and MURR Fuel Materials

Material	Temperature (°F)	Thermal Conductivity (Btu/hr-ft-°F)	Specific Heat (Btu/lb _m -°F)	Density (lb _m /in ³)
Aluminum Type 6061-0	32	102.3	-	0.0976
	62	-	0.214	
	80	104.0	-	
	170	107.5	-	
	260	109.2	0.225	
	350	109.8	-	
	440	110.4	0.236	
	530	110.4	-	
	620	109.8	0.247	
	710	108.6	-	
	800	106.9	0.258	
	890	105.2	-	
	980	103.4	0.269	
	1080	101.1	0.275	
MURR Fuel Plate ^①	80	57.9	0.165	0.121
	800		0.200	
MIT Fuel Plate ^①	80	72.6	0.176	0.115
	800		0.212	

Notes:

- ① Values determined based on composite value of aluminum cladding and fuel core material (see Appendix 3.5.2.4). Thermal conductivity value is valid for axial and circumferential heat transfer within fuel plate.

3.6.7 Thermal Evaluation for Normal Conditions of Transport

The ATR FFSC with the MIT or MURR fuel element payloads is transported horizontally under normal conditions of transport (NCT). This establishes the orientation of the exterior surfaces of the package for determining the free convection heat transfer coefficients and insolation loading. While the package would normally be transported in tiered stacks of multiple packages, the evaluation for NCT is conservatively based on a single, isolated package since this approach will yield the bounding maximum and minimum temperatures achieved by any of the packages. Further, since the surface of the transport trailer is conservatively assumed to prevent heat exchange between the package and the ambient, the bottom of the ATR FFSC is treated as an adiabatic surface.

The details of the thermal modeling used to simulate the ATR FFSC package under NCT conditions are provided in Appendix 3.5.2, *Analytical Thermal Model*, while details of the thermal modeling of the MIT and MURR FHEs and fuel elements are provided in Appendix 3.6.9.2.1, *Description of MIT and MURR Payload Thermal Models for NCT Conditions*. The ATR FFSC with Cobra fuel elements or small quantity payloads was not specifically modeled as part of this evaluation. Instead, their thermal performance is estimated using a qualitative approach based on the thermal characteristics of the other payloads and their associated thermal performance. See below for the details of this qualitative basis.

3.6.7.1 Heat and Cold

3.6.7.1.1 Maximum Temperatures

The maximum temperature distribution for the ATR FFSC occurs with a diurnal cycle for insolation loading and an ambient air temperature of 100°F, per 10 CFR §71.71(c)(1). The evaluation of this condition is conducted as a transient using the thermal model of an undamaged ATR FFSC described in Appendix 3.6.9.2.1, *Description of MIT and MURR Payload Thermal Models for NCT Conditions*. Figure 3.6-1 illustrates the expected heat-up transient for an ATR FFSC loaded with a MIT fuel element. The transient analysis assumes a uniform temperature condition of 70°F for all components prior to loading and exposure to the specified NCT condition at time = 0.

The figures demonstrate that the ATR FFSC package will respond rapidly to changes in the level of insolation and will reach its peak temperatures within the first day or two after loading. The higher thermal mass of the MIT FHE on a unit length basis versus that of the ATR FHE is reflected in the delayed response of the MIT FHE to changes in the inner shell temperature, whereas the ATR FHE was seen in Figure 3.3-1 to respond more rapidly. A similar temperature response curve is seen for the MURR FHE.

Table 3.6-5 presents the maximum temperatures reached for various components of the package. As seen from the table, all components are within their respective temperature limits. Figure 3.6-2 illustrates the predicted temperature distribution within the ATR FFSC package with a MIT fuel element payload at the end of the evaluated transient heat up period and near the time of peak temperature. Figure 3.6-3 presents the temperature distribution within the ATR FFSC package with a MURR fuel element payload.

The maximum temperature distribution for the ATR FFSC without insolation loads occurs with an ambient air temperature of 100°F. Since the package payload dissipates essentially zero watts of decay heat, the thermal analysis of this condition represents a trivial case and no thermal calculations are performed. Instead, it is assumed that all package components achieve the 100°F temperature under steady-state conditions. The resulting 100°F package skin temperature is below the maximum temperature of 122°F permitted by 10 CFR §71.43(g) for accessible surface temperature in a nonexclusive use shipment.

The ATR FFSC with the small quantity payload was not specifically modeled as part of this evaluation. Instead, its thermal performance is estimated using a qualitative approach based on the thermal characteristics of the other payloads and their associated thermal performance. Using this approach, it is estimated that the maximum temperatures attained for the transportation of the small quantity payload within the ATR FFSC will be bounded by that presented for the MURR payload. This conclusion is based on the facts that the combined weight of the small quantity payload and MURR FHE's with their enclosed fuel elements, plates, or foils are similar (see Section 1.2.2.3, *MURR HEU Fuel Element*, and Section 1.2.2.4, *Small Quantity Payload*), the FHE's are both fabricated of 6061 aluminum, and the fuel elements have similar thermal properties (see Section 3.6.6.1). This conclusion is further supported by the fact that Table 3.6-5 demonstrates that the MIT and MURR fuel elements produce essentially the same peak NCT temperatures despite their design differences. As such, the limited design differences between the MURR and small quantity payloads will not yield a significant difference in their NCT thermal response.

The ATR FFSC with the RINSC fuel element payload and the Cobra fuel element payload are not specifically modeled as part of this evaluation. Instead, their thermal performance is estimated using a qualitative approach based on the thermal characteristics of the other payloads and their associated thermal performance. (See Section 3.6.9.2.4, *Determination of Thermal Properties for RINSC Element*, Section 3.6.9.2.5, *Determination of Thermal Properties for Cobra Element*, and Section 3.6.9.2.6, *Determination of Thermal Properties for LEU Fuel Elements* for details). Using this approach, it is estimated that the maximum temperatures attained for the transportation of the RINSC, Cobra, and LEU fuel elements and DDEs are considered bounded by the analysis of the MURR payload and no additional analysis is required.

3.6.7.1.2 Minimum Temperatures

The minimum temperature distribution for the ATR FFSC occurs with a zero decay heat load and an ambient air temperature of -40°F per 10 CFR §71.71(c)(2). The thermal analysis of this condition also represents a trivial case and no thermal calculations are performed. Instead, it is assumed that all package components achieve the -40°F temperature under steady-state conditions. As discussed in Section 3.2.2, *Technical Specifications of Components*, the -40°F temperature is within the allowable operating temperature range for all ATR FFSC package components.

3.6.7.2 Maximum Normal Operating Pressure

The payload cavity of the ATR FFSC is vented to the atmosphere. As such, the maximum normal operating pressure (MNOP) for the package is 0 psig.

While the volume between the outer and inner shells is sealed, it does not contain organic or other materials that may outgas or thermally decompose. Therefore, the maximum pressure that may develop within the space will be limited to that achieved due to ideal gas expansion. Assuming a temperature of 70°F at the time of assembly and a maximum operating temperature of 190°F (based on the outer shell temperature, see Table 3.6-5, conservatively rounded up), the maximum pressure rise within the sealed volume will be less than 4 psi.

Table 3.6-5 - Maximum Package NCT Temperatures

Location / Component	MIT Fuel Payload	MURR Fuel Payload	Maximum Allowable ^①
Fuel Element Fuel Plate	143°F	142°F	400°F
Fuel Element Side Plate	143°F	142°F	400°F
Neoprene Rub Strips/Polyethylene Bag	143°F ^②	142°F ^②	225°F
Fuel Handling Enclosure (FHE)	143°F	142°F	400°F
Inner Shell	157°F	157°F	800°F
Ceramic Fiber Insulation, Body			
- Maximum	184°F	184°F	2,300°F
- Average	149°F	148°F	2,300°F
Ceramic Fiber Insulation, Closure			
- Maximum	145°F	145°F	2,300°F
- Average	143°F	143°F	2,300°F
Closure	145°F	145°F	800°F
Outer Shell	184°F	184°F	800°F

Table Notes:

- ① The maximum allowable temperatures under NCT conditions are provided in Section 3.2.2, *Technical Specifications of Components*.
- ② Component temperature assumed to be equal to that of the FHE.

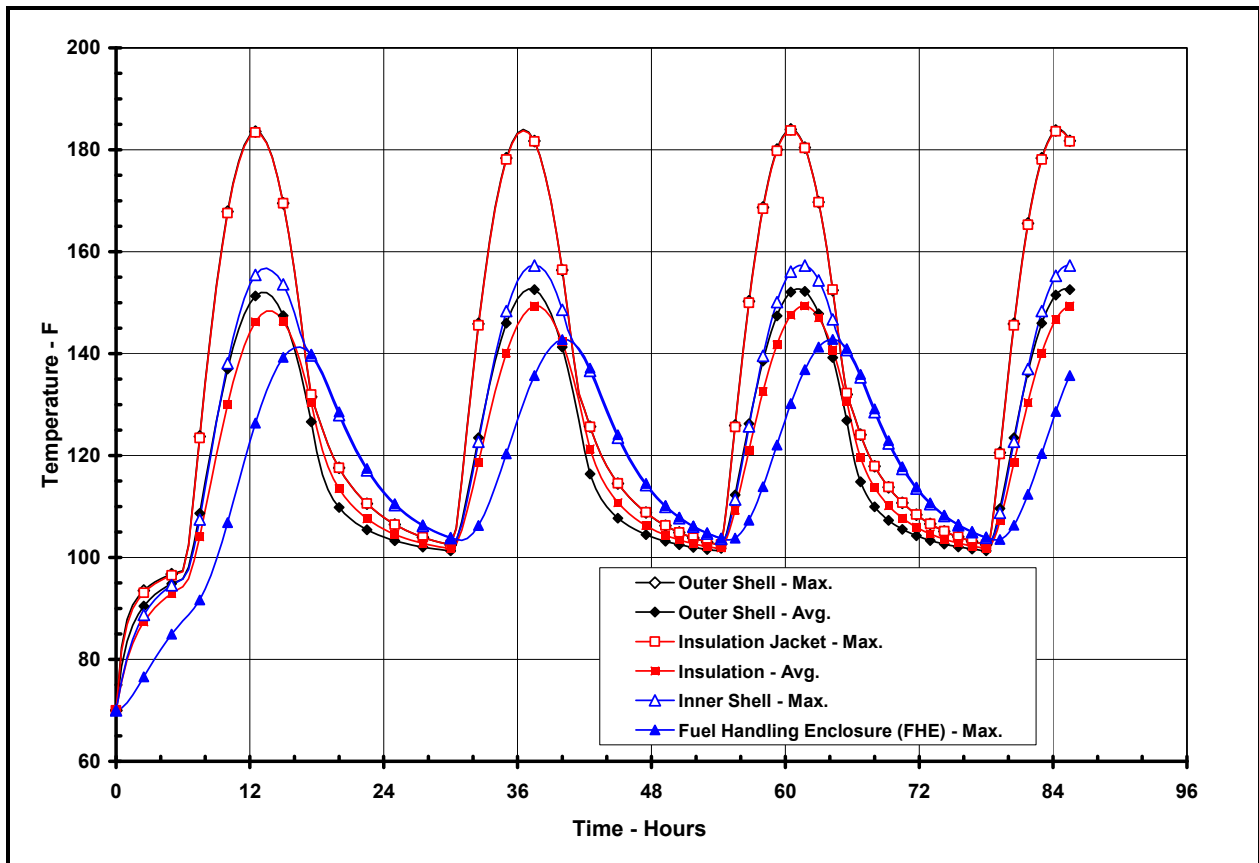


Figure 3.6-1 – ATR FFSC Package Heat-up with MIT Payload, NCT Hot Conditions

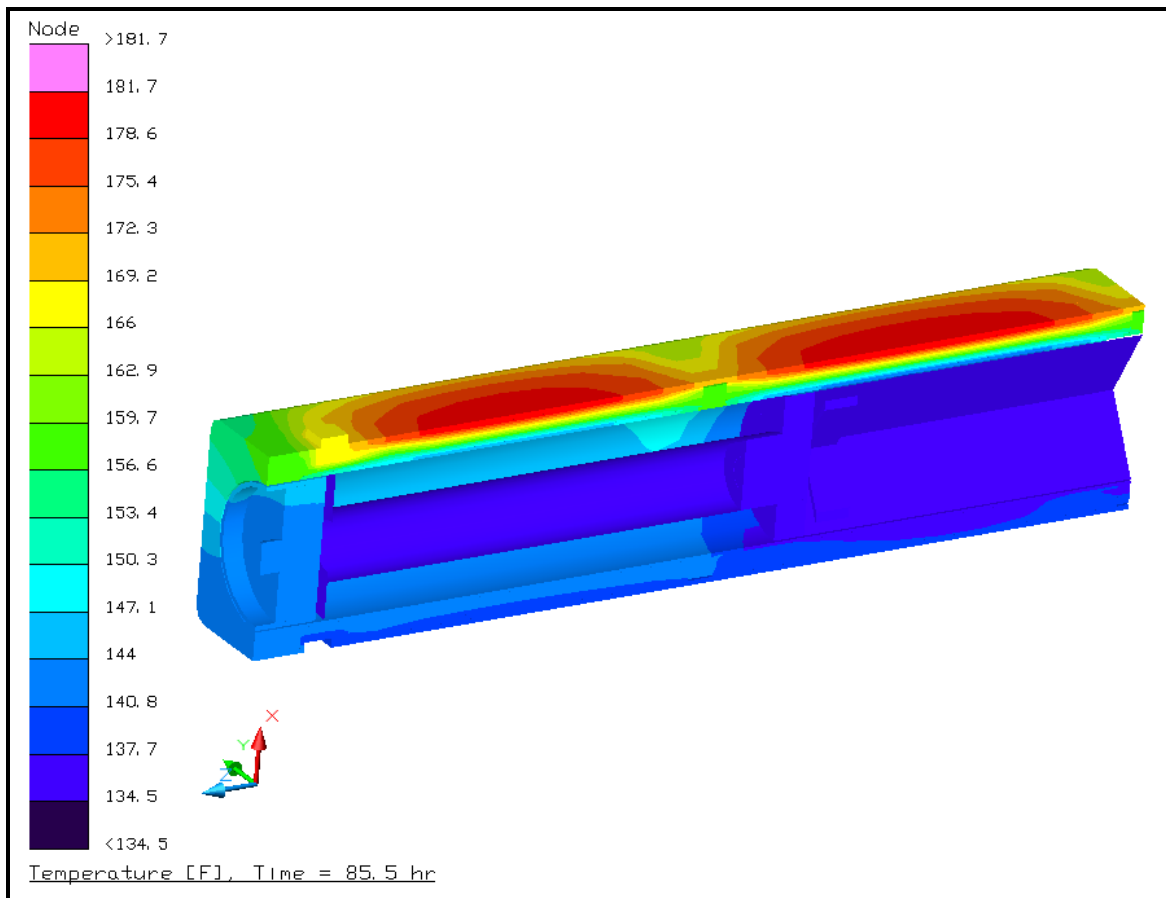


Figure 3.6-2 – Package NCT Temperature Distribution for MIT Payload

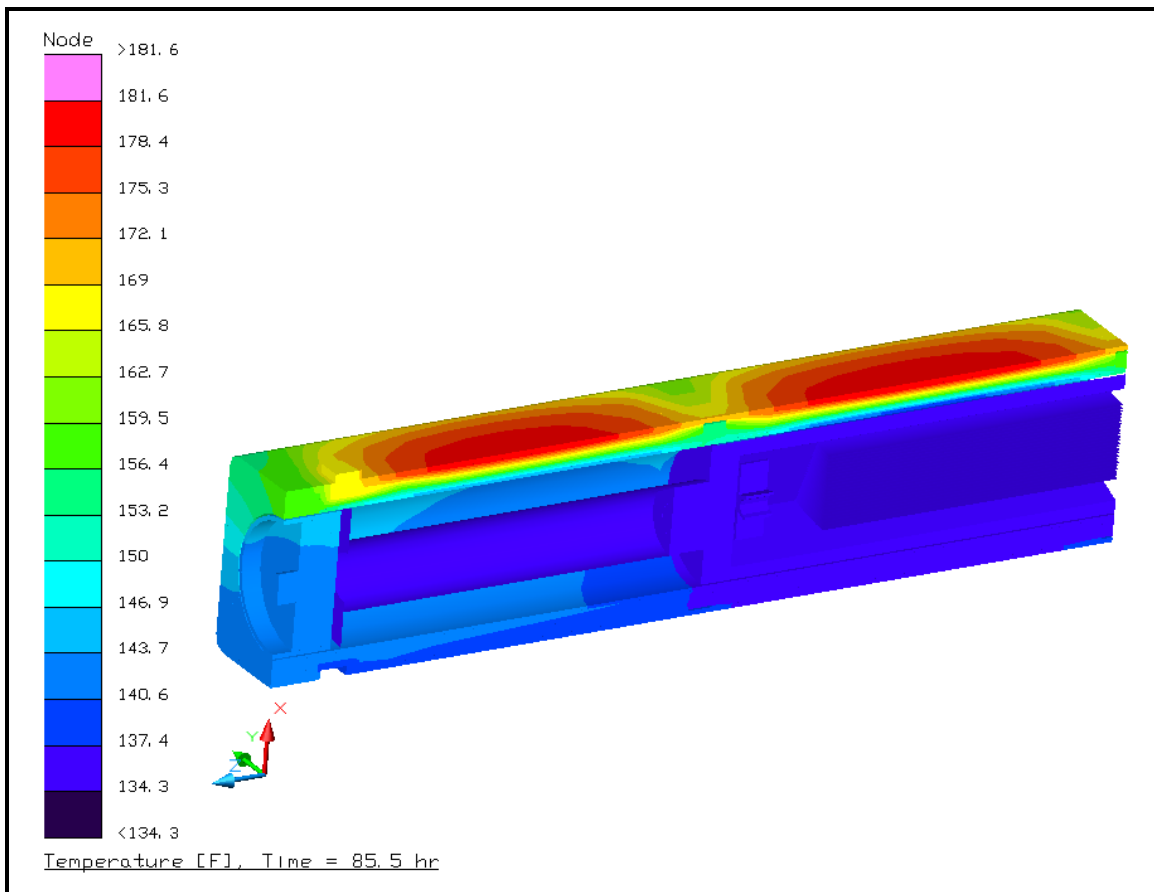


Figure 3.6-3 – Package NCT Temperature Distribution for MURR Payload

3.6.8 Thermal Evaluation for Hypothetical Accident Conditions

This section presents the thermal evaluation of the ATR FFSC package under the hypothetical accident condition (HAC) specified in 10 CFR §71.73(c)(4)² based on an analytical thermal model. The analytical model of the ATR FFSC for HAC is a modified version of the quarter symmetry NCT model described in Appendix 3.5.2.1, *Description of Thermal Model for NCT Conditions*, with the principal model modifications consisting of simulating the expected package damage resulting from the drop events that are assumed to precede the HAC fire and changing the package surface emissivities to reflect the assumed presence of soot and/or surface oxidization. The analytical model of the MIT and MURR fuel elements are the same as those described in Appendix 3.6.9.2.1, *Description of MIT and MURR Payload Thermal Models for NCT Conditions*. The evaluations of the ATR FFSC with a small quantity payload and RINSC and Cobra payloads under HAC conditions are accomplished using a qualitative approach in the same manner as accomplished for NCT conditions (see Section 3.6.7.1.1, *Maximum Temperatures*).

Physical testing using full scale certified test units (CTUs) is used to establish the expected level of damage sustained by the ATR FFSC package from the 10 CFR 71.73 prescribed free and puncture drops that are assumed to precede the HAC fire event. Appendix 3.5.2.2, *Description of Thermal Model for HAC Conditions*, provides an overview of the test results, the rationale for selecting the worst-case damage scenario, and the details of the thermal modeling used to simulate the package conditions during the HAC fire event.

3.6.8.1 Initial Conditions

The initial conditions assumed for the package prior to the HAC event are described below in terms of the modifications made to the NCT thermal model to simulate the assumed package conditions prior to and during the HAC event. These modifications are:

- Simulated the worst-case damage arising from the postulated HAC free and puncture drops as described in Appendix 3.5.2.2, *Description of Thermal Model for HAC Conditions*,
- Assume an initial, uniform temperature distribution of 100°F based on a zero decay heat package at steady-state conditions with a 100°F ambient with no insolation. This assumption complies with the requirement of 10 CFR §71.73(b)² and NUREG-1609¹⁷,
- Increased the emissivity of the external surfaces from 0.45 to 0.8 to account for possible soot accumulation on the surfaces, per 10 CFR §71.73(c)(4),
- Increased the emissivity of the interior surfaces of the outer shell from 0.30 to 0.45 to account for possible oxidization of the surfaces during the HAC event,

Following the free and puncture bar drops, the ATR FFSC package is assumed come to rest in a horizontal position prior to the initiation of the fire event. Given that the package geometry is essentially symmetrical about its axial axis, there are no significant thermal differences whether the package is right-side up, up-side down, or on its side. None of the payloads are expected to be re-positioned as a result of the pre-fire drop and puncture bar events based on the limited damage seen

for the ATR FHE as a result of the drop tests conducted on the ATR FFSC presented in Section 2.12.1, *Certification Tests on CTU-1*, and given the greater robustness of the payload FHEs. However, even if the end spacers are conservatively assumed to buckle as a result of the HAC drop event, no significant temperature increase will occur since direct contact between the FHE and the closure plug will be prevented and because the average radial heat transfer through the sides of the package does not change significantly as a function of axial position. Therefore, the peak package temperatures predicted under this evaluation based on no payload re-positioning or reconfiguration are representative of those achieved for any package orientation and/or credible re-positioning of the enclosed payloads.

3.6.8.2 Fire Test Conditions

The fire test conditions analyzed to address the 10 CFR §71.73(c) requirements are as follows:

- The initial ambient conditions are assumed to be 100°F ambient with no insolation,
- At time = 0, a fully engulfing fire environment consisting of a 1,475°F ambient with an emissivity of 1.0 is used to simulate the hydrocarbon fuel/air fire event. The assumption of a flame emissivity of 1.0 bounds the minimum average flame emissivity coefficient of 0.9 specified by 10 CFR §71.73(c)(4),
- The convection heat transfer coefficients between the package and the ambient during the 30-minute fire event are based on an average gas velocity¹⁸ of 10 m/sec. Following the 30-minute fire event the convection coefficients are based on still air,
- The ambient condition of 100°F with insolation is assumed following the 30-minute fire event. Since a diurnal cycle is used for insolation, the evaluation assumes that the 30-minute fire begins at noon so as to maximize the insolation heating during the post-fire cool down period. A solar absorptivity of 0.9 is assumed for the exterior surfaces to account for potential soot accumulation on the package surfaces.

The transient analysis is continued for 11.5 hours after the end of the 30-minute fire to ensure that the peak package temperatures are captured.

3.6.8.3 Maximum Temperatures and Pressure

3.6.8.3.1 Maximum HAC Temperatures

The thermal performance of the ATR FFSC package loaded with a MIT fuel element payload is summarized in Table 3.6-6, while Table 3.6-7 presents a summation of the results with a MURR fuel element payload. With the exception of the neoprene rub strips and the polyethylene bag used as a protective sleeve around the fuel elements, all other components of the package are seen to remain well below their allowable short term temperature limits. As with the ATR payload, the thermal decomposition of the neoprene strips and polyethylene bag will not impact the safety of the package and any associated out-gassing will not contribute to package pressurization since the package is vented. As demonstrated in Section 3.5.3, *Thermal*

Decomposition/Combustion of Package Organics, the available oxygen in the package is sufficient for consumption of less than 1% of the polyethylene and the quantity of air that enters the cavity under pressure differential and gas diffusion forces is insignificant. The discussion in Section 3.5.3 also provides validation of a 0 psig package pressure for the HAC event.

The outer shell and the ceramic fiber insulation provide thermal protection to the ATR FFSC package during the HAC fire event. The level of thermal protection can be seen via the thermal response curves presented in Figure 3.6-4 and Figure 3.6-5 for the ATR FFSC package loaded with a MIT and MURR fuel element payload, respectively. As seen from the figures, while the exterior of the package quickly rises to nearly the temperature of the fire, the heat flow to the FHE and its enclosed fuel element payloads is sufficiently restricted to limit the maximum temperatures of both the FHE and the fuel element to well below the melting point of aluminum. The higher thermal mass of the MIT and MURR FHEs in comparison with that of the ATR FHE is reflected in their correspondingly slower heat up and longer cool down during the fire transient when compared to that seen in Figure 3.4-1 for the ATR FHE. The higher temperature reached by the MURR FHE versus that seen for the MIT FHE is due to the conservative assumption of direct contact between the FHE and the inner shell along two line locations for the MURR FHE versus one line location for the MIT FHE. Similarly, the difference in the shape of the FHE temperature response curve seen for the MIT FHE between 30 minutes and 60 minutes versus that seen for the MURR FHE for the same time period is related to the fact that the top end of the shorter MIT FHE lies below one of the package's support ribs while the top of the MURR FHE is adjacent to it (see Figures 3.6-6 and 3.6-7).

Although the peak temperature achieved by the MURR FHE is about 20°F hotter than that achieved by the MIT FHE, the peak temperatures reached by the MIT and MURR fuel elements are approximately the same. This results from a combination of the higher thermal mass and greater separation distance between the end of the fuel element and the start fuel plates associated with the MURR fuel element versus that for the MIT fuel element.

The results demonstrate that thermal performance is similar to that achieved with the transport of a LFPB payload (see Section 3.4.3, *Maximum Temperature and Pressure*) due to the fact that these FHE have a thermal mass similar to that of the LFPB. The result of the higher thermal mass is that the MIT and MURR FHEs have a peak temperature that is approximately 300°F cooler than that seen for the ATR FHE and the enclosed fuel elements reach peak temperatures that are 90 to 180°F cooler than that seen for the ATR fuel element. The thermal performance of the ATR FFSC packaging with either the MIT or MURR payload is similar to that seen for the ATR payload.

The results presented above also demonstrate that inclusion of insolation effects prior to the fire would not have affected the safety basis of the design. As documented in Section 3.4.3.1, *Maximum HAC Temperatures*, consideration of the maximum insolation loading raises the package component temperatures by approximately 50°F above the initial 100°F level assumed by the HAC evaluation. Since all package components exhibit thermal margins significantly greater than 50°F, the inclusion of insolation effects prior to the fire event would not have impacted the safety basis for the design.

As with the evaluation for NCT, the thermal performance of the ATR FFSC with the small quantity payload, RINSC, and Cobra fuel elements under HAC conditions was not specifically modeled as part of this evaluation. Instead, based on the similarity between the MURR and small

quantity payloads, the thermal performance is qualitatively estimated to be bounded by that presented for the MURR payload. Since the combined weight of the small quantity payload and MURR FHE's with their enclosed fuel elements, plates, or foils are similar (see Section 1.2.2.3, *MURR HEU Fuel Element*, and Section 1.2.2.4, *Small Quantity Payload*) and the thermal mass of the two payloads are similar, the transient response of the small quantity payload can be expected to be similar to that presented for the MURR payload. This conclusion is further supported by the fact that Table 3.6-6 and Table 3.6-7 show that similar transient results occur for the MIT and MURR fuel element payloads despite their design differences. As such, the limited design differences between the MURR and small quantity payloads will not yield a significant difference in their HAC thermal response. This same logic applies to the RINSC, Cobra, and LEU fuel elements as further discussed in Section 3.6.9.2.4, *Determination of Thermal Properties for RINSC Element*, Section 3.6.9.2.5, *Determination of Thermal Properties for Cobra Element*, and Section 3.6.9.2.6, *Determination of Thermal Properties for LEU Fuel Elements*. Additionally, the SQFHE thermal response without its small quantity payload is expected to be similar with the conservative ATR LFPB thermal response. The empty SQFHE and LFPB are constructed of similar materials and have the same thermal mass of 30 lbs. The LFPB thermal evaluation is conservatively performed without its loose fuel plate payload, see Sections 3.4.3.1 and 3.5.2.1 for discussion of the LFPB thermal evaluation. Therefore, use of the SQFHE for any payload amount up to the maximum loaded SQFHE weight of 50 lbs is bounded by the thermal response of the LFPB evaluation. The addition of any small quantity payload mass to the SQFHE will increase the thermal mass and thereby increase the conservatism of the thermal response with respect to the empty LFPB thermal evaluation results.

3.6.8.3.2 Maximum HAC Pressures

The payload cavity of the ATR FFSC is vented to the atmosphere. As such, the maximum pressure achieved under the HAC event will be 0 psig. Section 3.5.3, *Thermal Decomposition/Combustion of Package Organics*, provides the justification for assuming a 0-psig package pressure for the HAC event.

Although the volume between the outer and inner shells is sealed, it does not contain organic or other materials that may outgas or thermally decompose. Assuming a temperature of 70°F at the time of assembly and a maximum temperature of 1,475°F (based on the outer shell temperature, see Table 3.6-6), the maximum pressure rise within the sealed volume due to ideal gas expansion will be less than 39 psig. This level of pressurization will occur for only a few minutes and then quickly reduce as the package cools.

3.6.8.4 Maximum Thermal Stresses

The ATR FFSC package is fabricated principally of sheet metal and relatively thin structural steel shapes. As such, the thermal stresses developed within each component during the HAC fire event will be low and not significant to the safety of the package.

The temperature difference that exists between the inner and outer shells during the HAC event (see the average inner and outer shell temperatures presented in Figure 3.6-4) will result in differential thermal expansion between the shells. The thermal impact related to the potential package geometry displacement due to this differential thermal expansion was evaluated in

Section 3.4.4, *Maximum Thermal Stresses*, and found not to be significant to the safety of the package.

Table 3.6-6 – HAC Temperatures with MIT Payload

Location / Component	Pre-fire	End of Fire	Peak	Maximum Allowable ^①
MIT Fuel Element Fuel Plate	100°F	345°F	640°F	1,100°F
MIT Fuel Element Side Plate	100°F	346°F	643°F	1,100°F
Neoprene Rub Strips/Polyethylene Bag	100°F	599°F	690°F	N/A
Fuel Handling Enclosure (FHE)	100°F	599°F	690°F	1,100°F
Inner Shell	100°F	1,417°F	1,417°F	2,700°F
Ceramic Fiber Insulation, Body				
- Maximum	100°F	1,462°F	1,462°F	2,300°F
- Average	100°F	1,253°F	1,253°F	2,300°F
Ceramic Fiber Insulation, Closure				
- Maximum	100°F	1,401°F	1,401°F	2,300°F
- Average	100°F	1,233°F	1,233°F	2,300°F
Closure	100°F	1,439°F	1,439°F	2,700°F
Outer Shell	100°F	1,475°F	1,475°F	2,700°F

Table Notes:

- ① The maximum allowable temperatures under HAC conditions are provided in Section 3.2.2, *Technical Specifications of Components*.

Table 3.6-7 – HAC Temperatures with MURR Payload

Location / Component	Pre-fire	End of Fire	Peak	Maximum Allowable ^①
MURR Fuel Element Fuel Plate	100°F	371°F	636°F	1,100°F
MURR Fuel Element Side Plate	100°F	380°F	644°F	1,100°F
Neoprene Rub Strips/Polyethylene Bag	100°F	648°F	710°F	N/A
Fuel Handling Enclosure (FHE)	100°F	648°F	710°F	1,100°F
Inner Shell	100°F	1,417°F	1,417°F	2,700°F
Ceramic Fiber Insulation, Body				
- Maximum	100°F	1,462°F	1,462°F	2,300°F
- Average	100°F	1,222°F	1,222°F	2,300°F
Ceramic Fiber Insulation, Closure				
- Maximum	100°F	1,402°F	1,402°F	2,300°F
- Average	100°F	1,236°F	1,236°F	2,300°F
Closure	100°F	1,439°F	1,439°F	2,700°F
Outer Shell	100°F	1,475°F	1,475°F	2,700°F

Table Notes:

- ① The maximum allowable temperatures under HAC conditions are provided in Section 3.2.2, *Technical Specifications of Components*.

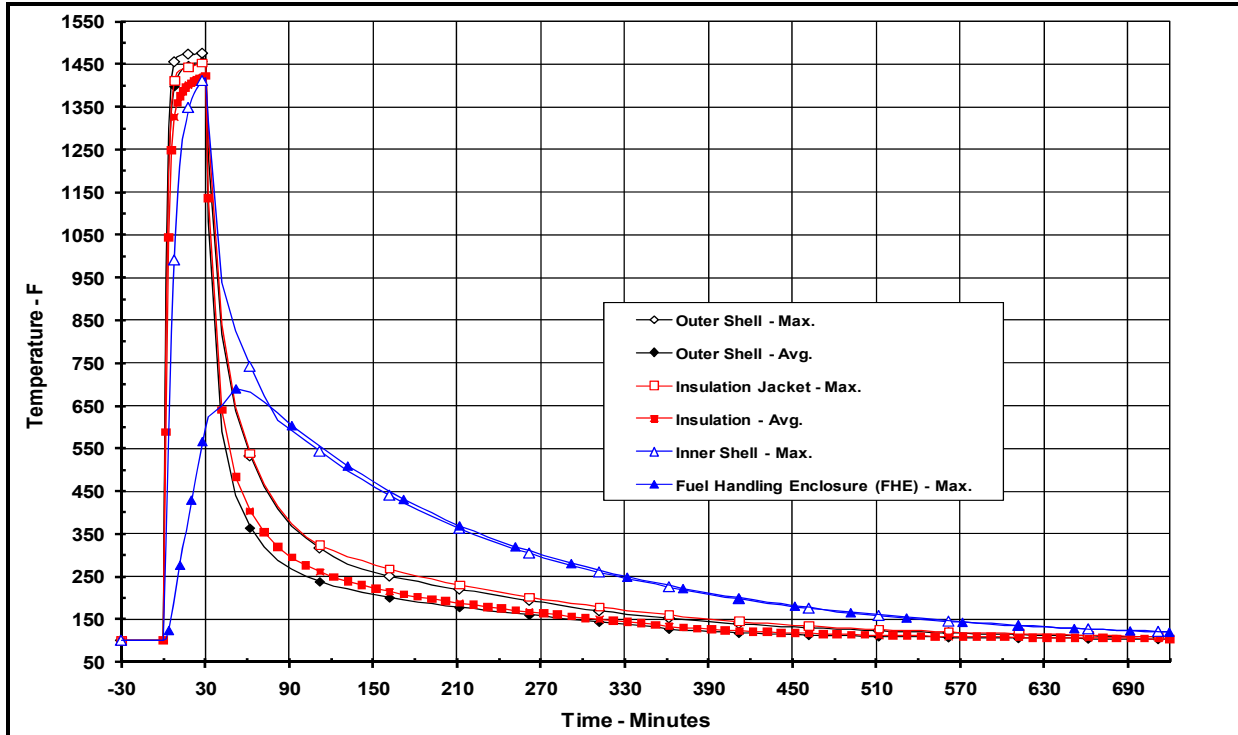


Figure 3.6-4 – ATR FFSC Package Thermal Response to HAC Event with MIT Payload

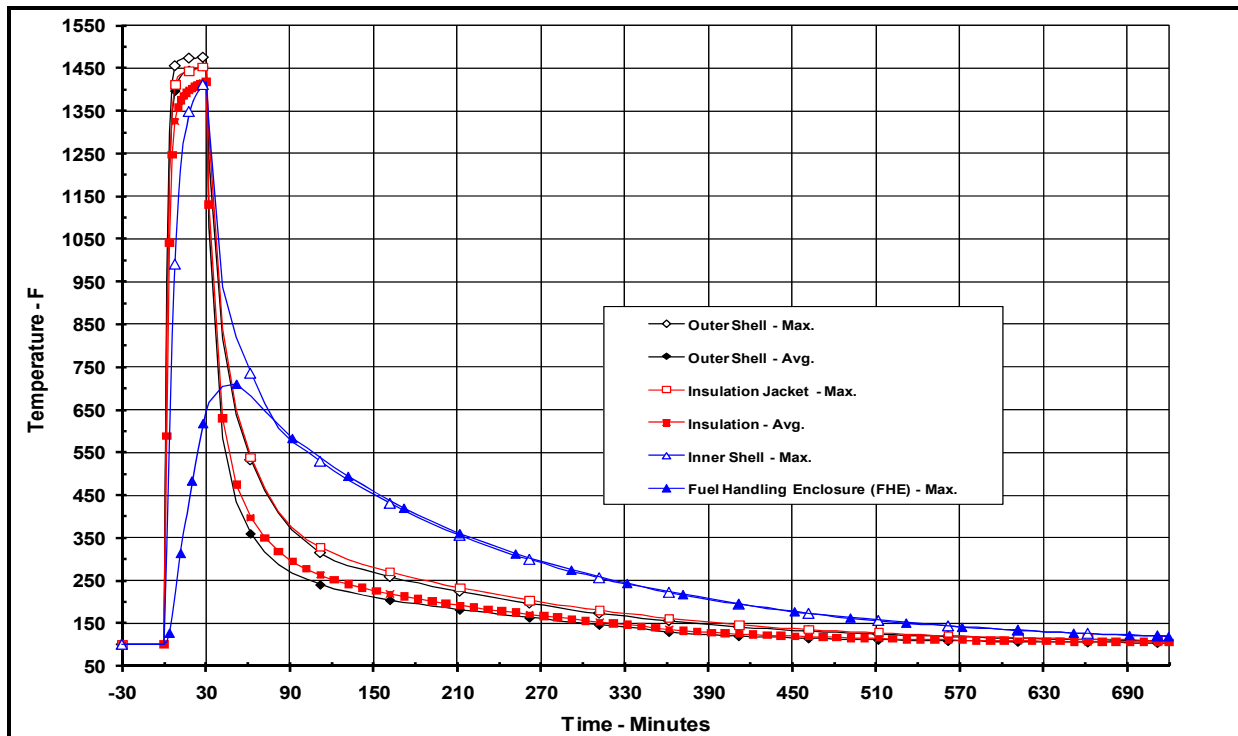
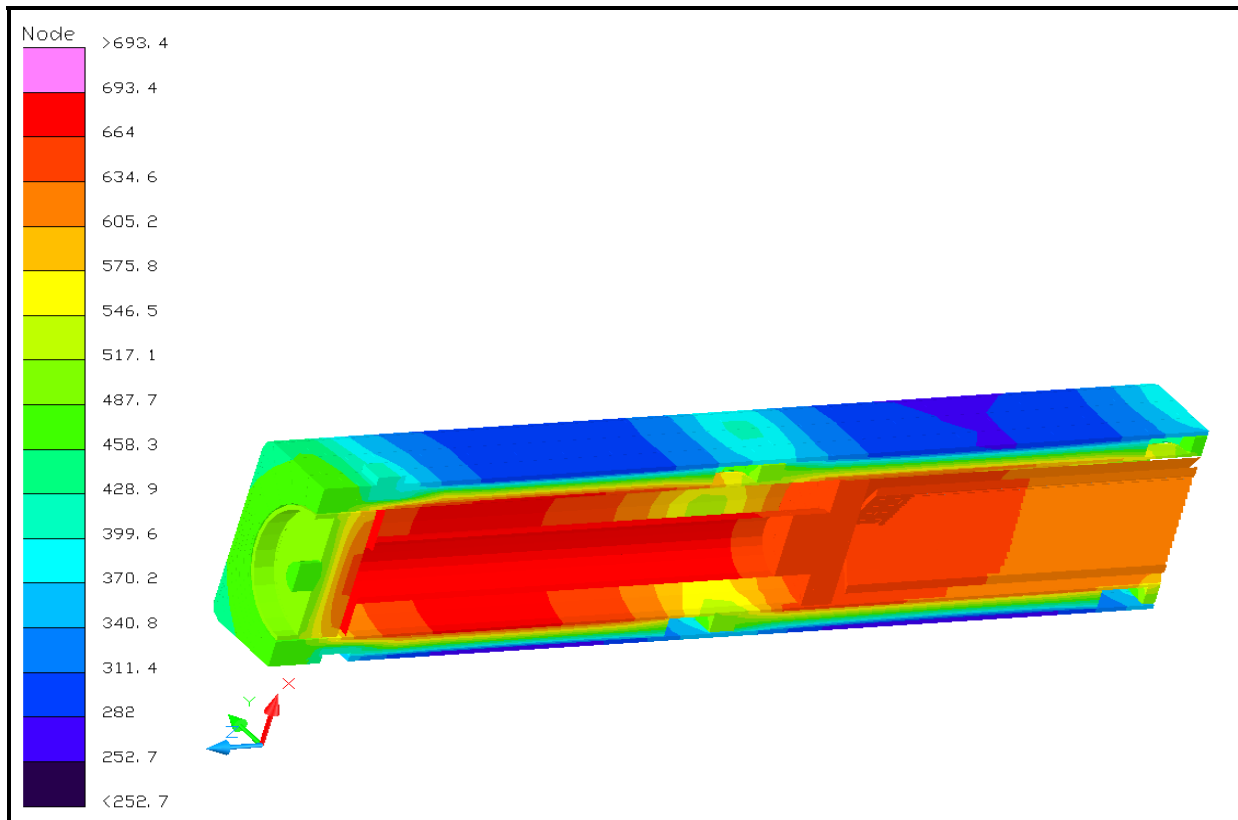
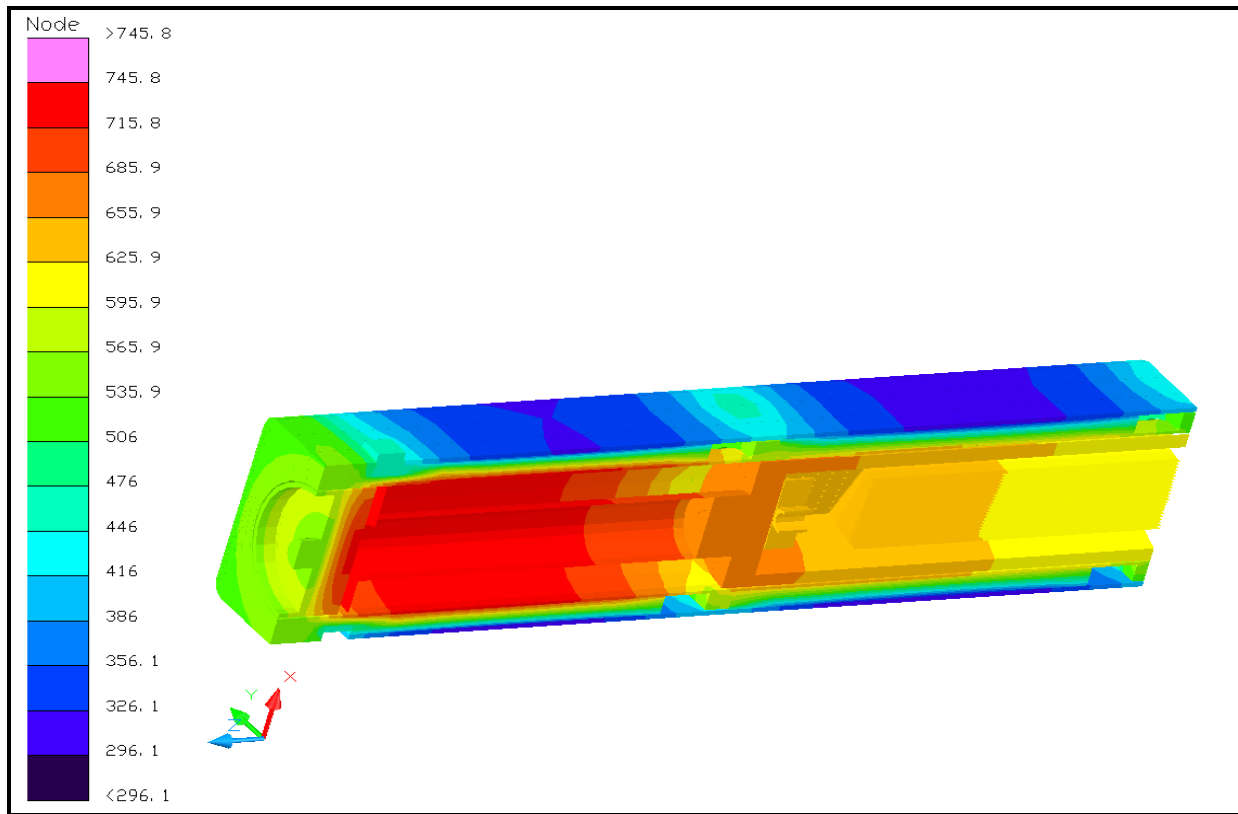


Figure 3.6-5 – ATR FFSC Package Thermal Response to HAC Event with MURR Payload



(Note: the positive x-axis is oriented towards the top of the package and the positive z-axis towards the package closure end)

Figure 3.6-6 –Temperature Distribution at Time of Peak MIT Fuel Element Temperature



(Note: the positive x-axis is oriented towards the top of the package and the positive z-axis towards the package closure end)

Figure 3.6-7 –Temperature Distribution at Time of Peak MURR Fuel Element Temperature

3.6.9 Appendices

3.6.9.1 Computer Analysis Results

3.6.9.2 Analytical Thermal Model

3.6.9.1 Computer Analysis Results

Due to the size and number of the output files associated with each analyzed condition, results from the computer analysis are provided on a CD-ROM.

3.6.9.2 Analytical Thermal Model

The analytical thermal model of the ATR FFSC package and the MIT and MURR fuel element payloads were developed for use with the Thermal Desktop^{®20} and SINDA/FLUINT²¹ computer programs. These programs are designed to function together to build, exercise, and post-process a thermal model. Appendix 3.5.2, *Analytical Thermal Model*, provides an overview of the capability and functionality of these programs. The SINDA/FLUINT and Thermal Desktop[®] computer programs have been validated for safety basis calculations for nuclear related projects²². The ATR FFSC with the small quantity payload was not specifically modeled as part of this evaluation. Instead, its thermal performance is estimated using a qualitative approach based on the thermal characteristics of the other payloads and their associated thermal performance.

3.6.9.2.1 Description of MIT and MURR Payload Thermal Models for NCT Conditions

A 3-dimensional, one-quarter symmetry thermal model of the ATR FFSC is used for the NCT evaluation. The model simulates one-quarter of the package, extending from the closure to the axial centerline of the package. Symmetry conditions are assumed about the package's vertical axis and at the axial centerline. This modeling choice captures the full height of the package components and allows the incorporation of the varying insolation loads that will occur at the top and sides of the package. Program features within the Thermal Desktop[®] computer program automatically compute the various areas, lengths, thermal conductors, and view factors involved in determining the individual elements that make up the thermal model of the complete assembly. Details of the thermal modeling of the ATR FFSC packaging are provided in Appendix 3.5.2.1, *Description of Thermal Model for NCT Conditions*.

A detailed model of the MIT and MURR fuel elements are used to simulate the heat transfer within the fuel elements and between the fuel element and their associated FHEs and spacer weldments. The detailed thermal models, illustrated in Figure 3.6-8 to Figure 3.6-13, include a separate representation of each composite fuel plate, the side plates, and the end fittings. Heat transfer between the individual fuel plates is simulated via conduction and radiation across the air space separating the plates. The curvature and separation distance between the plates is based on the information presented in Appendix 3.6.9.2.3, *Determination of Composite Thermal Properties for MIT and MURR Fuel Plates*.

The thermal modeling for the MIT fuel element and FHE is similar to that described for the ATR fuel element payload. Figure 3.6-8 illustrates the quarter symmetry thermal model of the MIT FHE and one of the two spacer weldments. The FHE thermal model uses planar elements to represent the 0.19 inch thick sides of the enclosure and the 0.25 inch thick elements of the spacer weldment. Solid elements are used to represent the ends of the FHE. Heat transfer between the FHE and the inner shell of the package is modeled as a combination of radiation and conduction across the air-filled void space, as well as via direct contact along 1 edge of the FHE. The contact conductance simulates a conservative idealized physical contact (i.e., a flat, smooth interface and that the FHE is oriented within the package such that the edge is aligned with the vertical axis of the package) between the FHE and the inner shell. Due to the robustness of the MIT FHE, no change to the direct contact between the FHE and the inner shell conservatively assumed for the NCT condition is expected as a result of the HAC drop event.

Figure 3.6-9 illustrates a cross-section through the combined modeling for the inner shell, the FHE, and the MIT fuel element. The left side of the figure illustrates the placement of the thermal nodes (indicated by the small circles) used to simulate each of the components, the use of planar elements to represent the 15 fuel plates, and the assumed points of direct contact between the FHE and the inner shell. The right side of the figure includes depiction of the solid elements that are used to simulate the air voids around the FHE. The heat transfer between the FHE and the MIT fuel element is computed as conductance through the 0.125 inch thick neoprene rub strips and radiation and conductance through the air voids.

Figure 3.6-10 illustrates a side and end view of the thermal model of the MIT fuel element as it would be for a complete fuel element. Approximately 1,140 nodes, 350 planar elements, and 445 solids are used to represent the quarter symmetry thermal model of the MIT fuel element, FHE, and the spacer weldment.

The thermal modeling for the MURR fuel element and FHE is similar to that described above for the MIT fuel element payload. Figure 3.6-11 illustrates the quarter symmetry thermal model of the MURR FHE and one of the two spacer weldments. The FHE thermal model uses planar elements to represent the 0.19 inch thick sides of the enclosure and the 0.25 inch thick elements of the spacer weldment. Solid elements are used to represent the ends of the FHE. Heat transfer between the FHE and the inner shell of the package is modeled as a combination of radiation and conduction across the air-filled void space, as well as via direct contact along 2 edges of the FHE. The contact conductance simulates a conservative idealized physical contact (i.e., a flat, smooth interface and an alignment that places 2 edges of the FHE in contact) between the FHE and the inner shell. Due to the robustness of the MURR FHE, no change to the direct contact between the FHE and the inner shell conservatively assumed for the NCT condition is expected as a result of the HAC drop event.

Figure 3.6-12 illustrates a cross-section through the combined modeling for the inner shell, the FHE, and the MURR fuel element. The left side of the figure illustrates the placement of the thermal nodes (indicated by the small circles) used to simulate each of the components, the use of curved, planar elements to represent the 24 fuel plates, and the assumed points of direct contact between the FHE and the inner shell. The right side of the figure includes depiction of the solid elements that are used to simulate the air voids around the FHE. The heat transfer between the FHE and the MURR fuel element is computed as conductance through the 0.125 inch thick neoprene rub strips and radiation and conductance through the air voids.

Figure 3.6-13 illustrates a side and end view of the quarter symmetry thermal modeling used for the MURR fuel element. Approximately 1,400 nodes, 700 planar elements, and 340 solids are used to represent the quarter symmetry thermal model of the MURR fuel element, FHE, and the spacer weldment.

The heat transfer from the exterior surfaces of the ATR FFSC is modeled in the same manner as that used for the evaluation of the ATR fuel element payload and assumes a combination of convection and radiation exchange. Appendix 3.5.2.3, *Convection Coefficient Calculation*, presents the methodology used to compute the convection coefficients from the various surfaces. The radiation exchange is computed using a Monte Carlo, ray tracing technique and includes the affect of reflection and/or transmission, according to the optical properties assigned to each surface (see Section 3.2.1, *Material Properties*).

In addition, heating of the exterior surfaces due to solar insolation is assumed using a diurnal cycle. The methodology used to simulate and apply the insolation loading is described in Appendix 3.5.2.1, *Description of Thermal Model for NCT Conditions*.

3.6.9.2.2 Description of Thermal Model for HAC Conditions

The thermal evaluations for the hypothetical accident condition (HAC) are conducted in the same manner and using the same methodology as that described in Appendix 3.6.9.2.1, *Description of MIT and MURR Payload Thermal Models for NCT Conditions*. No change to the geometry or position of the MIT and MURR fuel element payloads are expected as a result of the drop and puncture bar events that are assumed to precede the HAC fire event.

3.6.9.2.3 Determination of Composite Thermal Properties for MIT and MURR Fuel Plates

The MIT and MURR fuel plates are a composite material consisting of a fissile fuel matrix sandwiched within aluminum cladding. For the purposes of this calculation, the fuel composite is treated as a homogenous material with lumped thermal properties. The methodology used to compute the composite thermal properties for each fuel element is the same as that described in Appendix 3.5.2.4, *Determination of Composite Thermal Properties for ATR Fuel Plates*.

Each MIT element contains up to 515 g U-235, enriched up to 94 wt.%, which equates to a density of approximately 1.5 g U/cc in the fuel matrix. The thermal properties for the individual plates making up the MIT fuel element are computed using the approach used with the ATR Fuel Plates and the geometric data^{39,42} for the MIT fuel element. Each of the fifteen (15) fuel plates contained in the MIT fuel element has a thickness of 0.08 inches and a width of 2.526 inches. The nominal gap between the plates is 0.078 inches. Since the aluminum cladding contains 110 grooves on each side of the plate, the effective thickness of the cladding is reduced from 0.025 inches to 0.02 inches. Table 3.6-8 presents the composite thermal conductivity, specific heat, and density values for the fuel plates. These composite values are based on the described geometry of the fuel plates and the same thermophysical data⁶ used for the ATR fuel plates.

The thermal properties for the MIT element used are:

- 1) Aluminum cladding thermal conductivity = 191 W/m-K, conservatively high value from [6], page 18
- 2) Fissile fuel matrix (UAl_x) conductivity = 38.5 W/m-K, conservatively high based on Table 2.3 from [6] at 300K for 1.5 g U/cc
- 3) Aluminum cladding density = 2702 kg/m³, from [6], page 16
- 4) Fissile fuel matrix (UAl_x) density = 3846 kg/m³, from [6], Table 2.5 for 1.5 g U/cc
- 5) Aluminum cladding specific heat = 896 & 1080 J/kg-K, from [6], Table 3.2 at 300 & 700K, respectively
- 6) Fissile fuel matrix (UAl_x) specific heat = 587 & 709 J/kg-K, from [6], Table 2.4, value at 300 & 700K, respectively, for 1.5 g U/cc

⁴² Massachusetts Institute of Technology, Test Research Training Reactor 3 Welded Fuel Element Assembly, EG&G Idaho, Inc. Drawing No. DWG-419486, Rev. A.

Each MURR element contains up to 785 g U-235, enriched up to 94 wt.%, which equates to a density of approximately 1.44 g U/cc in the fuel matrix. The thermal properties for the individual plates making up the MURR fuel element are also computed using the approach used with the ATR Fuel Plates and the geometric data^{40,43} for the MURR fuel element. Due to the curved geometry of the twenty-four (24) fuel plates contained in the MURR fuel element, each plate has a different geometry. The inner plate has an inner radius of 2.77 inches and an arc length of 1.993 inches, while the outer plate has an inner radius of 5.76 inches and an arc length of 4.342 inches. The nominal gap between the plates is 0.08 inches. The thickness of the aluminum cladding is 0.01 inches. Table 3.6-9 presents the composite thermal conductivity, specific heat, and density values for the twenty four (24) fuel plates making up the MURR fuel element. These composite values are based on the described geometry of the fuel plates and the same thermophysical data⁶ used for the ATR fuel plates.

The thermal properties for the MURR fuel element used in this calculation are:

- 1) Aluminum cladding thermal conductivity = 191 W/m-K, conservatively high value from [6], page 18
- 2) Fissile fuel matrix (UAl_x) conductivity = 39.8 W/m-K, conservatively high based on Table 2.3 from [6], at 300K for 1.44 g U/cc
- 3) Aluminum cladding density = 2702 kg/m³, from [6], page 16
- 4) Fissile fuel matrix (UAl_x) density = 3793 kg/m³, from [6], Table 2.5 for 1.44 g U/cc
- 5) Aluminum cladding specific heat = 896 & 1080 J/kg-K, from [6], Table 3.2, at 300 & 700K, respectively
- 6) Fissile fuel matrix (UAl_x) specific heat = 596 & 719 J/kg-K, from [6], Table 2.4, value at 300 & 700K, respectively, for 1.44 g U/cc

3.6.9.2.4 Determination of Thermal Properties for RINSC Element

The RINSC fuel elements are fabricated with a nominally 0.020-in thick mixture of uranium silicide (U₃Si₂) and aluminum powder as the fuel “meat” and a nominally 0.015-in thick aluminum alloy cladding. The twenty-two (22) flat fuel plates have a 2.8-in width, an overall length of 25-in, and an active fuel region of 22.5 to 24.0-in. The fuel plate meat and cladding thicknesses match those of the interior plates for the ATR fuel element and are similar to those for the MURR fuel plates. The side plates are fabricated of ASTM B 209, aluminum alloy 6061-T6 and 6061-T651 and are approximately 0.188-in thick. This is similar to the side plate thicknesses of the ATR, MITR, and MURR fuel elements.

The thermal conductivity of the RINSC fuel plates⁴¹ are similar to data obtained in the measurements of the thermal conductivities for the uranium aluminide (UAl_x) based fuels⁶. Similarly, the thermal mass of the fuel plates are comparable despite the higher density of uranium silicide versus uranium aluminide since the ratio of the specific heats of the two materials is nearly the inverse of the density ratio.

⁴³ University of Missouri at Columbia, MURR UAl_x Fuel Element Assembly, EG&G Idaho, Inc. Drawing No. DWG-409407, Rev. N.

The ATR FFSC with the RINSC fuel element payload is not specifically modeled as part of this evaluation. Instead, its thermal performance is estimated using a qualitative approach based on the maximum temperatures attained for the transportation of the MURR fuel element within the ATR FFSC. This conclusion is based on the facts that the combined weight of the RINSC and MURR FHE's with their enclosed fuel elements are the same, the FHE's are both fabricated of 6061 aluminum, and the fuel elements have similar thermal properties (see above). This conclusion is further supported by the fact that the MIT and MURR fuel elements produce essentially the same peak temperatures despite their design differences. As such, the limited design differences between the MURR and RINSC payloads will not yield a significant difference in their thermal response.

3.6.9.2.5 Determination of Thermal Properties for Cobra Element

As with the MURR and MIT fuel elements, the temperature of the Cobra fuel element will vary based on the heat that flows into the ATR FFSC package from insolation (NCT) and the hypothetical fire (HAC). The temperature of the fuel element will depend primarily on the nature of the dominant resistances in the heat path between the fuel and the environment, and on the heat capacity or thermal mass of the package. A comparison can be made between the Cobra fuel element case and the MURR case, whose resulting temperatures are given in Table 3.6-5 (NCT) and Table 3.6-7 (HAC). The dominant resistances consist of the non-metallic links in the heat path from the outside to the inside (such as air gaps and rubber); the resistance through the metallic elements is comparatively negligible (such as steel and aluminum), and will be neglected in what follows. The non-metallic elements in the heat path are:

- The insulation between the inner and outer shells of the package, based on the thermal conductivity, thickness, and area of the insulation
- The air gap between the inner shell and the FHE, based on the radiative heat transfer properties and the area
- The contact conductance of the FHE resting on the inner shell
- The neoprene rubber between the FHE and the fuel element
- The air gap between the FHE and the fuel element
- The contact conductance of the fuel element resting on the rubber

Because the Cobra fuel element is transported within a FHE having a design very similar to that of the MURR fuel element, the dominant heat transfer resistances will be very similar, including the same number and approximate size of air gaps, emissivities, contact conductances, and rubber thickness. The thermal behavior in transient heat transfer also depends on the thermal mass of the components. From Table 2.1-1, the weight of the MURR fuel element and its FHE are 15 lb and 30 lb, respectively, for a total of 45 lb; and the weight of the Cobra fuel element and its FHE are 20 lb and 28 lb, respectively, for a total of 48 lb. Since the heat capacity of all aluminum alloys is very similar, and since the total weight of each fuel element plus FHE is essentially the same, the thermal mass will be essentially the same. Thus, the Cobra fuel element case will have essentially the same thermal behavior in NCT and HAC to the MURR fuel

element case. In addition, the temperatures calculated for the MURR case show significant margins to the limiting temperatures for the various components.

3.6.9.2.6 Determination of Thermal Properties for LEU Fuel Elements

The full size prototype LEU fuel elements and DDEs to be transported in the ATR FFSC are:

- ATR LEU fuel element
- MIT LEU fuel element and DDE
- MURR LEU fuel element and DDE
- NBSR DDE

Each of the LEU fuel elements has the same design as the corresponding HEU fuel element, including bounding dimensions, except for a different number of fuel plates in some cases. The DDEs have the same core design as the corresponding LEU fuel element, differing only in the end structures. The NBSR DDE does not have a corresponding LEU fuel element used in the ATR FFSC, but its materials, construction, and weight are similar to those of the other LEU fuel elements and DDEs.

The U-10Mo fuel meat is an alloy of nominally 10-wt% molybdenum with uranium which is enriched up to 20%. The meat material is clad with a nominal 0.001-inch thick layer of zirconium and with 6061 aluminum alloy. The MIT LEU fuel elements and DDEs are transported within the same FHE as is used for the corresponding HEU fuel elements. The MURR LEU fuel elements and DDEs are transported in a slightly modified FHE. Both are made of solid machined aluminum. The ATR LEU fuel element is transported in a balsa wood FHE, and the NBSR DDE is transported with cellulosic protective material (such as cardboard).

The LEU fuel elements and DDEs are not explicitly modeled for this evaluation, because they are considered to be bounded by the ATR, MIT, and MURR HEU fuel elements which are modeled in this Appendix.

Because all of the payload fuel elements have negligible decay heat, the temperature under NCT will be completely determined by solar loading, and the thermal characteristics of the fuel elements or FHEs will have little influence over the temperature. Under HAC, the heat input is dominated by the hypothetical fire. Because the thermal mass dominates the heat transfer relations, the effect of any differences in the overall conductivity of the fuel elements is negligible. The higher thermal mass of the LEU fuel elements and DDEs serves to damp the thermal transient response in the model compared to the HEU case. The LEU fuel elements are heavier than the corresponding HEU fuel elements by factors of 1.8 (ATR), 1.9 (MIT), and 1.9 (MURR). The DDEs all have weights comparable to the LEU prototypic fuel elements. Thus, all of the LEU payloads are significantly heavier than the current HEU payloads. This will result in a lower peak temperature for the LEU fuel elements and DDEs under HAC.

The thermal decomposition of the balsa wood FHE or the cellulosic material surrounding the NBSR DDE will not have a significant effect on the payload temperature, due to the limited supply of oxygen in the package during the fire, as discussed in Section 3.5.3, *Thermal Decomposition/Combustion of Package Organics*. In addition, the loss of these components is not critical to the safety of the package. Furthermore it is noted that the margin of safety against

melting of the fuel plates is over 300 °F for the ATR HEU element (see Table 3.1-1) and over 400 °F for the MIT/MURR fuel plate (see Table 3.6-1). Thus, the thermal integrity of the LEU fuel elements will be maintained through the HAC fire event.

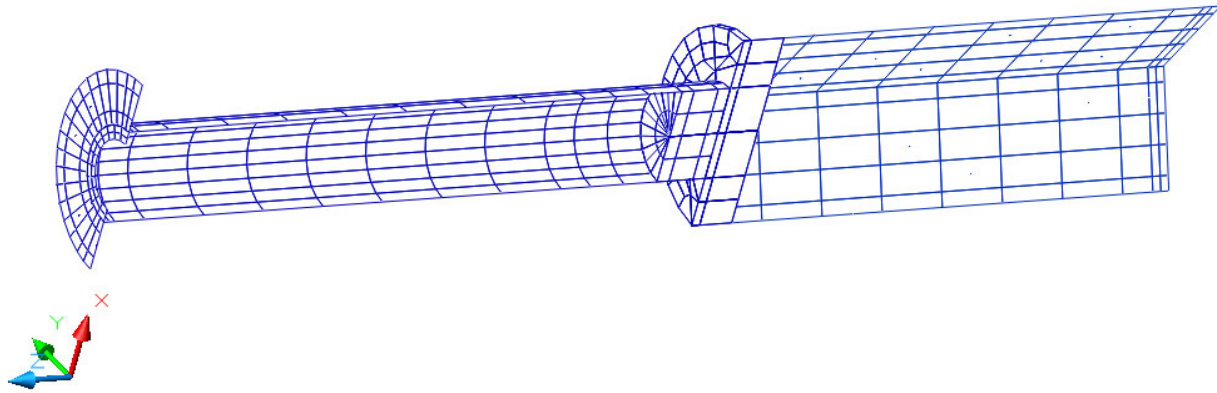
Table 3.6-8 – Composite MIT Fuel Plate Thermal Properties

Plate	Plate Thickness, in	UAlx Thickness, in	Axial and Circumferential Conductivity (W/m-K)	Plate Width, in	Mean density, kg/m ³	Mean specific heat, J/(kg K) @ 300 K	Mean specific heat, J/(kg K) @ 700 K
1 to 15	0.08*	0.03	125.6	2.314	3192.3	736.5	888.4

* - mean plate thickness estimated at 0.07 inches after allowance for ribbing

Table 3.6-9 – Composite MURR Fuel Plate Thermal Properties

Plate	Plate Thickness, in	UAlx Thickness, in	Axial and Circumferential Conductivity (W/m-K)	Inner radius, in	Outer radius, in	Plate Arc Length, in	Mean density, kg/m ³	Mean specific heat, J/(kg K) @ 300K	Mean specific heat, J/(kg K) @ 700 K
1	0.05	0.03	100.3	2.77	2.82	1.993	3288.8	692.6	835.2
2	0.05	0.03	100.3	2.9	2.95	2.095	3288.8	692.6	835.2
3	0.05	0.03	100.3	3.03	3.08	2.197	3288.8	692.6	835.2
4	0.05	0.03	100.3	3.16	3.21	2.300	3288.8	692.6	835.2
5	0.05	0.03	100.3	3.29	3.34	2.402	3288.8	692.6	835.2
6	0.05	0.03	100.3	3.42	3.47	2.504	3288.8	692.6	835.2
7	0.05	0.03	100.3	3.55	3.6	2.606	3288.8	692.6	835.2
8	0.05	0.03	100.3	3.68	3.73	2.708	3288.8	692.6	835.2
9	0.05	0.03	100.3	3.81	3.86	2.810	3288.8	692.6	835.2
10	0.05	0.03	100.3	3.94	3.99	2.912	3288.8	692.6	835.2
11	0.05	0.03	100.3	4.07	4.12	3.014	3288.8	692.6	835.2
12	0.05	0.03	100.3	4.2	4.25	3.116	3288.8	692.6	835.2
13	0.05	0.03	100.3	4.33	4.38	3.218	3288.8	692.6	835.2
14	0.05	0.03	100.3	4.46	4.51	3.321	3288.8	692.6	835.2
15	0.05	0.03	100.3	4.59	4.64	3.423	3288.8	692.6	835.2
16	0.05	0.03	100.3	4.72	4.77	3.525	3288.8	692.6	835.2
17	0.05	0.03	100.3	4.85	4.9	3.627	3288.8	692.6	835.2
18	0.05	0.03	100.3	4.98	5.03	3.729	3288.8	692.6	835.2
19	0.05	0.03	100.3	5.11	5.16	3.831	3288.8	692.6	835.2
20	0.05	0.03	100.3	5.24	5.29	3.933	3288.8	692.6	835.2
21	0.05	0.03	100.3	5.37	5.42	4.035	3288.8	692.6	835.2
22	0.05	0.03	100.3	5.5	5.55	4.137	3288.8	692.6	835.2
23	0.05	0.03	100.3	5.63	5.68	4.239	3288.8	692.6	835.2
24	0.05	0.03	100.3	5.76	5.81	4.342	3288.8	692.6	835.2



(Note: the positive x-axis is oriented towards the top of the package and the positive z-axis towards the package closure end)

Figure 3.6-8 – ‘Hidden Line’ View of MIT FHE and Spacer Quarter Symmetry Thermal Model

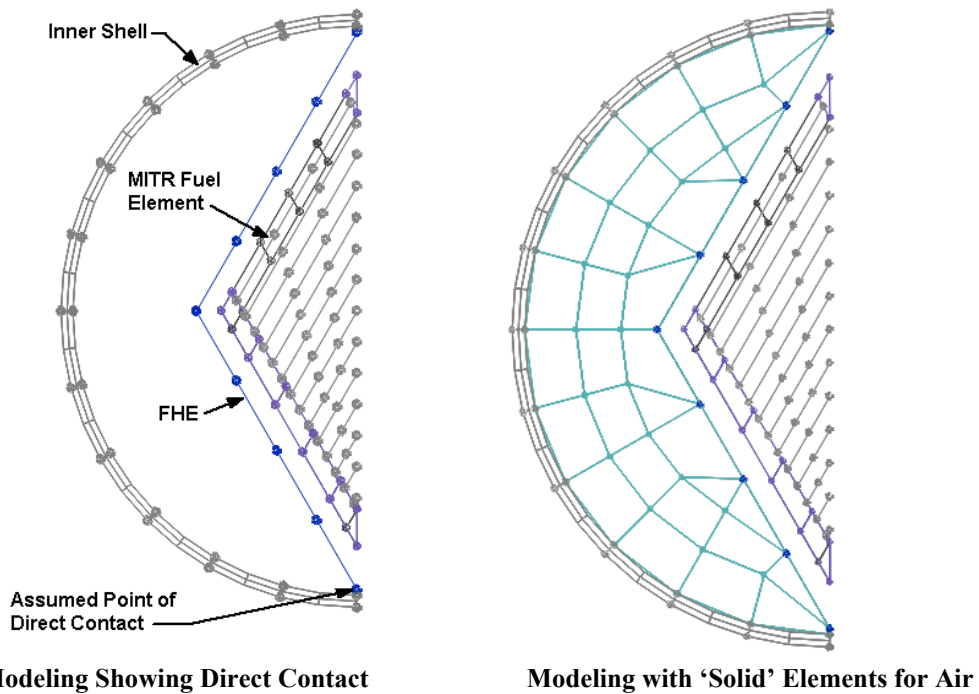
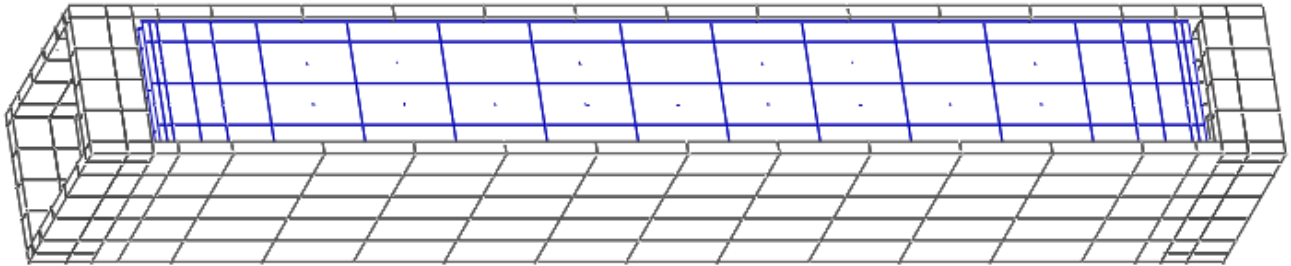
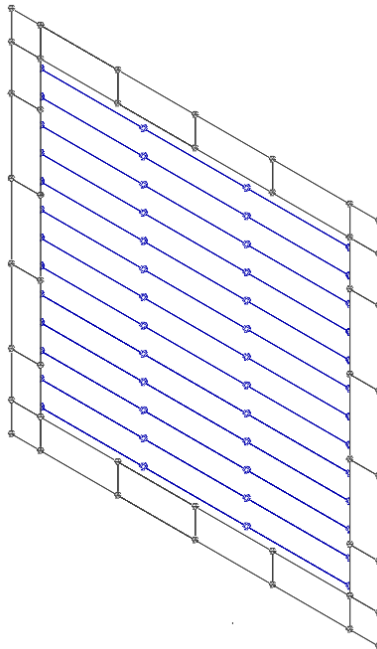


Figure 3.6-9 – Thermal Model of MIT Fuel Element and FHE within Inner Shell

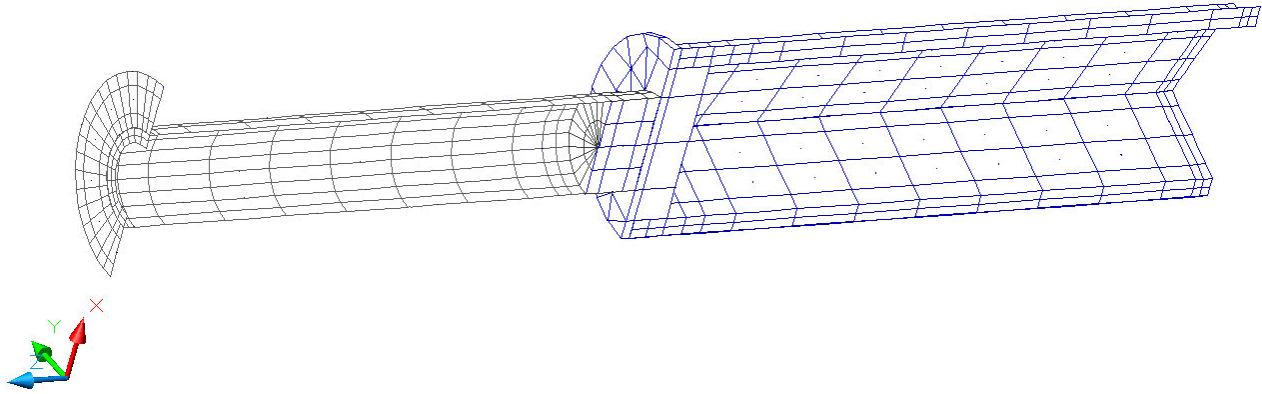


MIT Fuel Element Model, Side View of Full Element



MIT Fuel Element Model, End View of Full Element

Figure 3.6-10 – Side and End Views of MIT Fuel Element Thermal Model



(Note: the positive x-axis is oriented towards the top of the package and the positive z-axis towards the package closure end)

Figure 3.6-11 – ‘Hidden Line’ View of MURR FHE and Spacer Quarter Symmetry Thermal Model

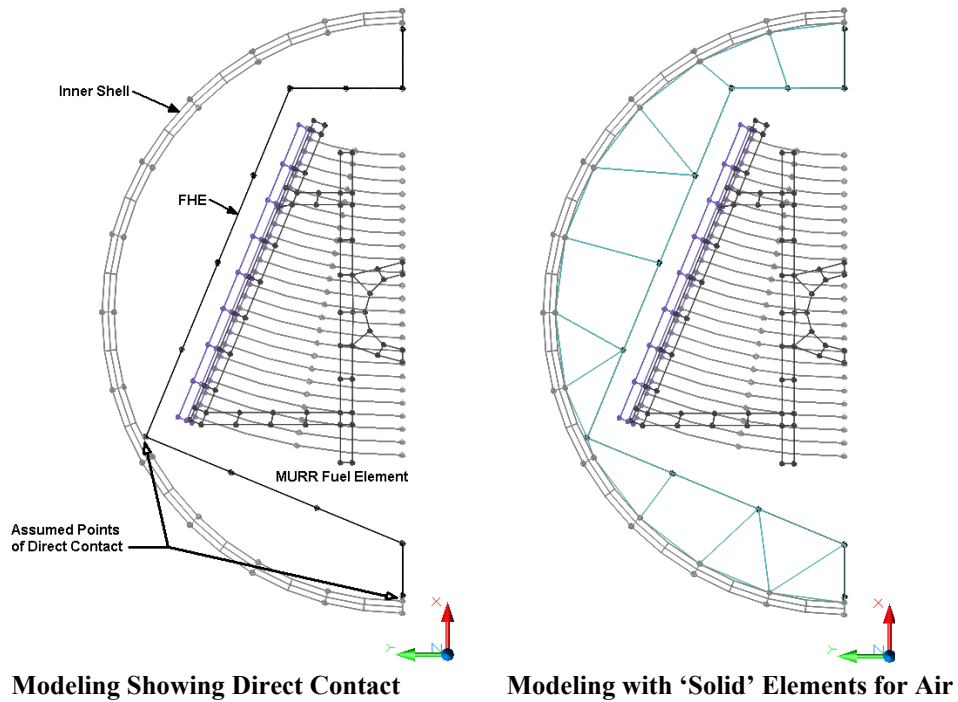
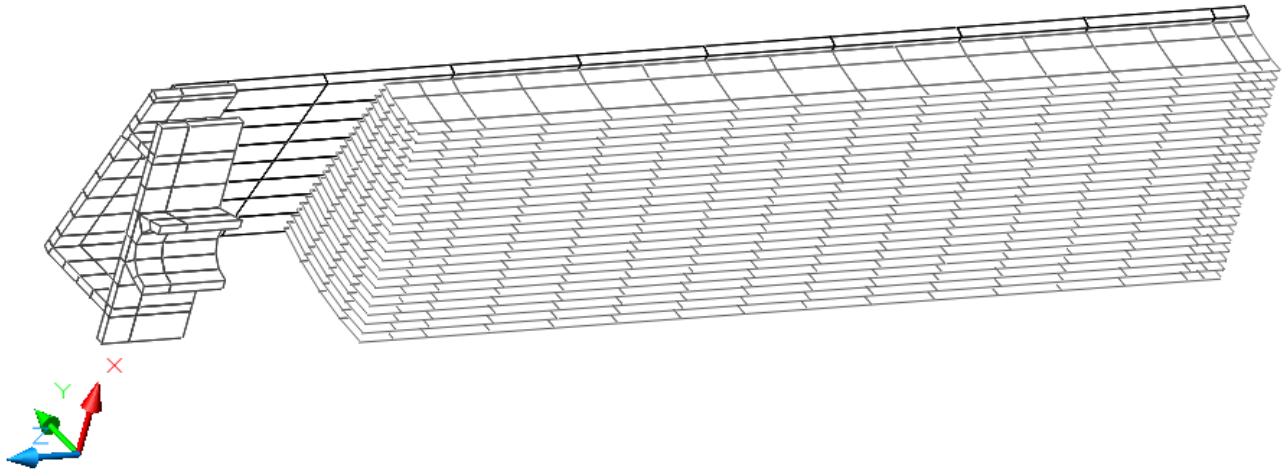
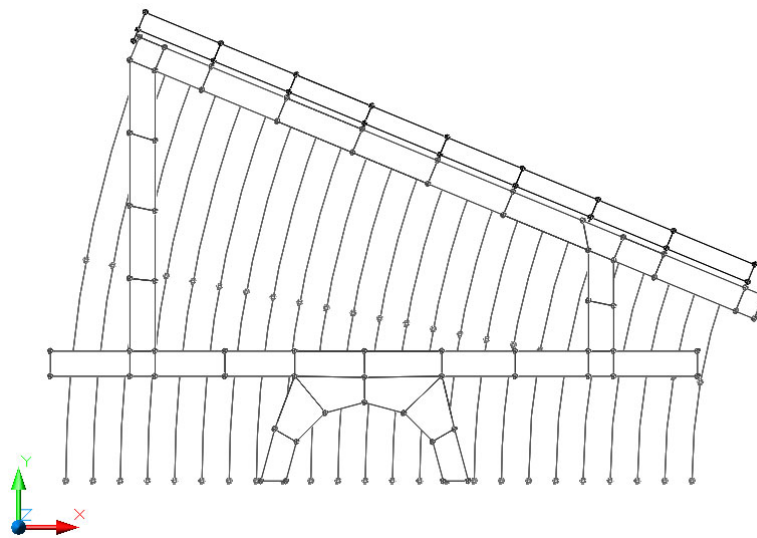


Figure 3.6-12 – Thermal Model of MURR Fuel Element and FHE within Inner Shell



MURR Fuel Element Model, Side View of Quarter Symmetry Model



MURR Fuel Element Model, End View of Quarter Symmetry Model

Figure 3.6-13 – Side and End Views of MURR Fuel Element Thermal Model

This page left intentionally blank.